THE UNIVERSITY *of* EDINBURGH

Structure, magnetic and electronic properties of new 1111-type and 42622-type transition metal-based oxyarsenides.

Karolina Kasperkiewicz

Doctor of Philosophy
University of Edinburgh

2014

Declaration

I do hereby declare that I composed this thesis myself and that all research detailed within it, unless otherwise stated, is my own. This work has not been submitted for any other degree or professional qualification than this doctorate. Some of the research herein has already been published; these publications are included in the appendix.

Karolina Kasperkiewicz

February 2014

Acknowledgments

I would like to express my deepest gratitude to my supervisor Professor John Paul Attfield for his support and guidance through the whole time of research and then writing my thesis. He helped me to go through the hardest times and always offered me his helping hand. I would also like to express my thanks to my first supervisor, Dr Serena Margadonna, for allowing me to work on this interesting project and for her guidance towards my future career. Her help and input was invaluable in the discussion and interpretation of the collected data.

I would like to thank Jane Pancheva for her help with synthesising some of the samples presented in Chapter 5. I also owe a debt of gratitude to Dr Anna Kusmartseva and Dr Dmitry Sokolov for their help, fruitful discussions and the PPMS and high pressure measurements presented in Chapters 4 and 5. Anna not only helped out with the experiments, but along with my other two friends from the lab, Andrea and Christina, supported me and helped to make my time during the PhD research very memorable – thank you all for that!

I would also like to thank my parents for their support and faith in me and to all my family and friends for believing in my talents. Finally big thanks go to my fiancé, who was always there for me, supported in moments of doubt and helped every single day by giving me motivation and a helping hand.

Abstract

Discovery of high-temperature superconductors aroused a great interest in studies on these materials. In 1987 an yttrium-based compound YBCO (Yttrium-Barium-Copper-Oxide) was synthesised with T_c at 93 K. It was immediately evident that the BCS theory does not explain the pairing mechanism in these oxide-based superconductors, which predicted that a maximum T_c of about 30 K could be achieved. Layered copper oxides were for a long time the most studied high-T_c superconductors. With the discovery, at the beginning of 2008, by Kamihara of a new non-cuprate high-T_c superconductor a different path of studies had opened.

This family of quaternary oxyarsenides $LaO_{1-x}F_xFeAs$ was surprising due to the presence of Fe, which should lead to long-range magnetic order suppressing superconductivity. Although the parent compound LaFeAsO is not superconducting, electron doping (by partial substitution of O^{2-} with F^-) leads to superconductivity with T_c of 26 K. Since these discoveries there has been extensive research on the family of rare-earth quaternary oxypnictides with general formula REFaAsO (RE = La, Sm, Ce, Nd, Pr, Gd, Tb, Dy) and with T_c reaching 55 K for electron doped SmFeAsO.

A study of new NdFeAsO family with Sr doping on Nd site was conducted. Synthesis of $Nd_{1-x}Sr_xFeAsO$ compounds and their further characterisation revealed that hole doping in these materials is a successful route to achieve superconductivity. Partial substitution of Nd^{3+} by Sr^{2+} with small doping level (x = 0.05) shows semiconducting type behaviour, while increasing doping level leads to the emergence of metallic conductivity and with level of doping 20% obtaining superconductivity at T_c = 13.5 K. These materials adopt a simple tetragonal crystal structure (space group *P4/nmm*), which undergoes a structural phase transition on cooling to orthorhombic symmetry (space group *Cmma*). The changes of structural, electronic and magnetic properties with doping level show very different behaviour – non-symmetric to the electron doped side of the phase diagram.

The family of Fe-As based superconductors has expanded further by the discoveries of $A_{1-x}A'_xFe_2As_2$ (A = Alkaline Earth, A' = Alkali metal), LiFeAs and NaFeAs phases, $Sr_3Sc_2Fe_2As_2O_5$. A series of iron-based oxyarsenides with general formula $Sr_4M^1{}_2O_6M^2{}_2As_2$ (M^1 = Sc, Cr, V; M^2 = Fe, Co, Ni) was synthesised and their structure was studied using powder X-ray and neutron diffraction. These materials adopt tetragonal crystal structure (space group *P4/nmm*) in analogy with REFeAsO systems. The Fe-As planes are sandwiched between perovskite K_2NiF_4-type oxide layers of $Sr_4M_2O_6$ (M^I = Sc, Cr, V), the large size of which creates a large distance between Fe-As planes. In spite of structural analogy with REFeAsO these new materials show a different behaviour from REFeAsO, which is absence of a structural phase transition on cooling. Both $Sr_4V_2O_6Fe_2As_2$ and $Sr_4Sc_2O_6Ni_2As_2$ compounds are superconducting without doping with T_c at 28 K and 2.5 K respectively. Neither $Sr_4Sc_2O_6Fe_2As_2$ nor $Sr_4Cr_2O_6Fe_2As_2$ show these properties, but are good parent compounds for doping, which may lead to producing compounds that achieve superconductivity. Further research was made with synthesising doped $Sr_4Cr_2O_6Fe_2As_2$ with doping on Fe site with Co. The structure and magnetic and electrical properties of these compounds were studied and proved to show superconducting behaviour with T_c up to 17.5 K for 5% Co doping.

Table of contents

Abstract iv

Table of contents v

List of Tables x

List of Figures xii

List of Abbreviations xxv

CHAPTER 1 1

Structure, magnetic and electronic properties of new transition metal-based oxyarsenides. 1

1.1. Introduction. 1

1.2. Superconductivity. 2

1.2.1. London equation. 4

1.2.2. The Ginzburg-Landau model. 5

1.2.3. BCS theory and Cooper pairs. 7

1.2.4. Type-II superconductors. 9

1.3. High temperature superconductors. 11

1.4. Rare-earth transition metal oxyarsenides. 12

1.4.1. Superconducting properties. 14

1.4.2. 11 materials. 16

1.4.3. 122 materials. 16

1.4.4. 111 materials. 18

1.4.5. 1111 materials. 19

1.4.6. 42622 materials. 21

1.4.7. Comparison between oxyarsenides and cuprates. 21

1.5. Bibliography. 23

CHAPTER 2 33
Experimental techniques. 33
2.1. Introduction. 33
2.2. Powder diffraction. 34
2.2.1. Theory of powder diffraction. 34
2.2.1.1. Bragg's Law. 36
2.2.2. Equations. 39
2.2.3. Laboratory X-ray instruments. 40
2.2.4. Synchrotron X-ray. 40
2.2.4.1. Theory of synchrotron X-ray. 40
2.2.4.2. Instruments. 41
2.2.4.3. Beamlines. 42
2.2.5. Neutron diffraction. 44
2.2.5.1. Theory of neutron diffraction. 44
2.2.5.2. Source of neutrons. 46
2.2.5.3. Instruments. 47
2.2.6. Data analysis and treatment. 48
2.2.6.1. The Rietveld method. 48
2.2.6.2. Peak shape. 49
2.2.6.3. Background intensity. 51
2.2.6.4. Indicators of fit. 51
2.2.6.5. GSAS computer programme package. 52
2.3. Magnetic measurements and SQUID. 52
2.3.1. Magnetism in metals. 57
2.4. Electrical resistivity measurements using a PPMS. 58
2.5. Bibliography. 60
CHAPTER 3 62
Synthesis of hole doped rare-earth iron oxyarsenides
$Nd_{1-x}Sr_xFeAsO$ ($0 < x \leq 0.2$). 62
3.1. Introduction. 62
3.2. Electron and hole doping in REFeAsO. 64

3.3. Experimental work. 65
3.4. Results. 66
3.4.1. Structural properties. 66
3.4.2. Magnetic properties. 78
3.4.3. Electrical resistivity. 82
3.5. Discussion. 84
3.6. Conclusions. 86
3.7. Bibliography. 87
CHAPTER 4 89
Synthesis of $Sr_4M^{I}_2O_6M^{II}_2As_2$ (M^{I} = Sc, V, Cr; M^{II} = Fe, Co, Ni). 89
4.1 Introduction. 89
4.2. $Sr_4Sc_2O_6M_2As_2$ (M = Fe, Co, Ni) parent compounds. 91
4.2.1. Experimental. 91
4.2.2. Results. 93
4.2.2.1. Structural properties. 93
4.2.2.2. Magnetic properties. 107
4.2.2.3. Resistivity measurements. 108
4.3. $Sr_4M_2O_6Fe_2As_2$ (M = Cr, V) parent compounds. 110
4.3.1. Introduction. 110
4.3.2. Experimental. 110
4.3.3. Results. 112
4.3.3.1. Structural properties. 112
4.3.3.2. Magnetic properties. 126
4.3.3.3. Electrical properties. 128
4.4. Discussion. 131
4.5. Conclusions. 135
4.6. Bibliography. 136
CHAPTER 5 138
Synthesis of $Sr_4Cr_2O_6Fe_{2-x}Co_xAs_2$ ($0 < x < 2$). 138
5.1. Introduction. 138
5.2. Experimental. 140

5.3. Results. **142**
5.3.1. Structural properties. 142
5.3.2. Magnetic susceptibility. 150
5.3.3. Electrical resistivity. 153
5.4. Conclusion. **157**
5.5. Bibliography. **158**
CHAPTER 6 159
Conclusions and future directions. 159
List of conferences and experiments attended 163
Reprint of Publications. 164

List Of Tables

Table 2.1. The seven crystal systems with minimum symmetry requirements. 35

Table 3.1. Masses of starting materials used to prepare different compositions of $Nd_{1-x}Sr_xFeAsO$. 66

Table 3.2. Refined structural parameters and bond lengths (Å) and angles (°) for $Nd_{1-x}Sr_xFeAsO$ with x = 0.05, 0.1 and 0.2 obtained from Rietveld refinements of the synchrotron X-ray diffraction data at room temperature. Estimated errors in the last digits are given in parentheses. The schematic diagram of the structure is shown in Figure 3.1. 70

Table 3.3. Refined structural parameters and bond lengths (Å) and angles (°) for $Nd_{1-x}Sr_xFeAsO$ with x = 0.05, 0.1 and 0.2 obtained from Rietveld refinements of the synchrotron X-ray diffraction data at temperature 5 K. Estimated errors in the last digits are given in parentheses. 76

Table 4.1. Refined structural parameters and bond lengths (Å) and angles (°) for $Sr_4Sc_2O_6Fe_2As_2$, $Sr_4Sc_2O_6Co_2As_2$ and $Sr_4Sc_2O_6Ni_2As_2$ obtained from Rietveld refinements of the synchrotron X-ray diffraction data at room temperature. Estimated errors in the last digits are given in parentheses. 96

Table 4.2. Refined structural parameters and bond lengths (Å) and angles (°) for $Sr_4Sc_2O_6Fe_2As_2$, $Sr_4Sc_2O_6Co_2As_2$ and $Sr_4Sc_2O_6Ni_2As_2$ obtained from Rietveld refinements of the synchrotron X-ray diffraction data at 20 K. Estimated errors in the last digits are given in parentheses. 101

Table 4.3. Refined structural parameters and bond lengths (Å) and angles (°) for $Sr_4Cr_2O_6Fe_2As_2$, $Sr_4V_2O_6Fe_2As_2$ made with V_2O_5 and $Sr_4V_2O_6Fe_2As_2$ made with V_2O_3 obtained from Rietveld refinements of the synchrotron X-ray diffraction data at room temperature. Estimated errors in the last digits are given in parentheses. 114

Table 4.4. Refined structural parameters and bond lengths (Å) and angles (°) for $Sr_4Cr_2O_6Fe_2As_2$ and $Sr_4V_2O_6Fe_2As_2$ obtained from Rietveld refinements of the synchrotron X-ray diffraction data at 5 K. Estimated errors in the last digits are given in parentheses. 118

Table 5.1. Masses of starting materials used to prepare different compositions of $Sr_4Cr_2O_6Fe_{2-x}Co_xAs_2$. 141

Table 5.2. Refined structural parameters and bond lengths (Å) and angles (°) for chosen samples of $Sr_4Cr_2O_6Fe_{2-x}Co_xAs_2$ with x = 0.05, 0.15, 0.25, 1 and 2 obtained from Rietveld refinements of the synchrotron X-ray diffraction data at room temperature. Estimated errors in the last digits are given in parentheses. 146

Table 5.3. Values of superconducting transition temperatures and diamagnetic shielding fractions with increased cobalt doping level in $Sr_4Cr_2O_6Fe_{2-x}Co_xAs_2$. 153

List Of Figures

Figure 1.1. a) A plot of resistivity, ρ, versus temperature, T, comparing the behaviour of a superconductor (with its critical temperature) and a normal metal, b) Temperature dependence of the critical field. 3

Figure 1.2. Comparison of type I and type II superconductors: a) Magnetisation, M, as a function of applied field, H b) Temperature dependence of the critical field. 10

Figure 1.3. Crystal structure of the iron-based superconductors: a) 11, b) 32522, c) 1111, d) 111, e) 122 and f) 42622 families. 13

Figure 1.4. Experimentally determined phase for $Ba(Fe_{1-x}Co_x)_2As_2$. 17

Figure 1.5. Experimentally determined phase for $NaFe_{1-x}Co_xAs$. 18

Figure 1.6. Experimentally determined phase for: a) $LaFeAsO_{1-x}F_x$, b) $SmFeAsO_{1-x}F_x$ and c) $CeFeAsO_{1-x}F_x$. 20

Figure 2.1. Illustration of the reflection from waves on two lattice planes used for the derivation of Bragg's law. 37

Figure 2.2. a) The geometry of the Debye-Scherrer camera and b) scattered beams originating from a powder sample with Debye-Scherrer cones shown. 38

Figure 2.3. Principal structures of a synchrotron - here ESRF, Grenoble. 41

Figure 2.4. Beamline in ESRF, Grenoble. 42

Figure 2.5. High resolution powder diffractometer at ID31 beamline (a), the same diffractometer with cryostat mounted (b) and schematic diagram of multianalyser stage (c). 43

Figure 2.6. Variation of neutron scattering lengths with atomic number. 45

Figure 2.7. Instrument layout for a) D2B and b) D20. 47

Figure 2.8. Schematic diagram of the arrangement of magnetic moments in different types of magnetism. 53

Figure 2.9. Variation of magnetic susceptibility with temperature. 55

Figure 2.10. Graphical illustration of the Curie-Weiss law. 56

Figure 2.11. Schematic diagram of the four-probe method. 59

Figure 3.1. Schematic diagram of the room temperature tetragonal structure of the first discovered rare–earth quaternary oxypnictide – LaFeAsO. 63

Figure 3.2. Schematic diagram of the room temperature tetragonal structure of the $Nd_{1-x}Sr_xFeAsO$ system. 67

Figure 3.3. Final observed (blue circles), calculated (red solid line), and difference (lower green solid line) plots for the Rietveld refinement of $Nd_{0.948}Sr_{0.052}FeAsO$ at RT. Tick marks show the reflection positions. The refinement proceeded with the main phase in the *P4/nmm* space group. The refined lattice constants are a = 3.97171(2) Å and c = 8.57316(6) Å. The agreement factors are R_{wp} = 6.50%, R_{exp} = 3.80%. The X-ray wavelength is 0.4030068 Å. Inset shows zoom in on the 20 to 35 2θ data range. 68

Figure 3.4. Final observed (blue circles), calculated (red solid line), and difference (lower green solid line) plots for the Rietveld refinement of $Nd_{0.909}Sr_{0.091}FeAsO$ at RT. Tick marks show the reflection positions. The refinement proceeded with the main phase in the *P4/nmm* space group. The refined lattice constants are a = 3.97334(2) Å and c = 8.58077(6) Å. The agreement factors are R_{wp} = 6.71%, R_{exp} = 4.34%. The X-ray wavelength is 0.4030068 Å. Inset shows zoom in on the 20 to 35 2θ data range. 69

Figure 3.5. Final observed (blue circles), calculated (red solid line), and difference (lower green solid line) plots for the Rietveld refinement of $Nd_{0.79}Sr_{0.21}FeAsO$ at RT. Tick marks show the reflection positions. The refinement proceeded with the main phase in the *P4/nmm* space group. The refined lattice constants are a = 3.97773(2) Å and c = 8.64147(8) Å. The agreement factors are R_{wp} = 6.42%, R_{exp} = 4.11%. The X-ray wavelength is 0.4030068 Å. Inset shows zoom in on the 20 to 35 2θ data range. 69

Figure 3.6. Evolution of the room temperature tetragonal lattice constants as a function of Sr^{2+} doping level ***x*.** Unit cell vector '*a*' is plotted against the left-hand scale; '*c*' against the right-hand scale. The lines are guides to the eye. 71

Figure 3.7. Schematic diagram of the **(a)** AsF_4 and **(b)** $FeAs_4$ units. The values of the bond distances and angles reported refer to the x = 0.05 composition. 72

Figure 3.8. Diagram of the evolution of distances between a) Fe-As, b) Fe-Fe and angles between c) Fe-As-Fe, d) Fe-As-Fe and e) thickness of Fe-As layer in $Nd_{1-x}Sr_xFeAsO$. 73

Figure 3.9. Final observed (blue circles), calculated (red solid line), and difference (lower green solid line) plots for the Rietveld refinement of $Nd_{0.948}Sr_{0.052}FeAsO$ at 5 K. Tick marks show the reflection positions. The refinement proceeded with the main phase in the *Cmma* space group. The refined lattice constants are a = 5.59862(1) Å, b = 5.62133(1) Å and c = 8.53437(2) Å. The agreement factors are R_{wp} = 5.25%, R_{exp} = 3.04%. The X-ray wavelength is 0.4030068 Å. Inset shows zoom in on the 20 to 35 2θ data range. 74

Figure 3.10. Final observed (blue circles), calculated (red solid line), and difference (lower green solid line) plots for the Rietveld refinement of $Nd_{0.909}Sr_{0.091}FeAsO$ at 5 K. Tick marks show the reflection positions. The refinement proceeded with the main phase in the *Cmma* space group. The refined lattice constants are a = 5.59930(2) Å, b = 5.62358(1) Å and c = 8.54437(2) Å. The agreement factors are

R_{wp} = 5.87%, R_{exp} = 3.85%. The X-ray wavelength is 0.4030068 Å. Inset shows zoom in on the 20 to 35 2θ data range. 74

Figure 3.11. Final observed (blue circles), calculated (red solid line), and difference (lower green solid line) plots for the Rietveld refinement of $Nd_{0.79}Sr_{0.21}FeAsO$ at 5 K. Tick marks show the reflection positions. The refinement proceeded with the main phase in the *Cmma* space group. The refined lattice constants are a = 5.60451(2) Å, b = 5.62914(1) Å and c = 8.60519(2) Å. The agreement factors are R_{wp} = 4.99%, R_{exp} = 3.29%. The X-ray wavelength is 0.4030068 Å. Inset shows zoom in on the 20 to 35 2θ data range. 75

Figure 3.12. Temperature evolution of the lattice constants for $Nd_{1-x}Sr_xFeAsO$: green circles, blue diamonds and red squared refer to compositions with x = 0.05, 0.1 and 0.2, respectively. 77

Figure 3.13. On the left: temperature evolution of the volume for $Nd_{1-x}Sr_xFeAsO$: green circles, blue diamonds and red squared refer to compositions with x = 0.05, 0.1 and 0.2, respectively. On the right: thermal response of the structural parameters describing the $FeAs_4$ tetrahedra - Fe-As bond distances and Fe-As-Fe exchange angle. 78

Figure 3.14. Evolution of effective magnetic moment per mol of sample against the doping level of Sr. 79

Figure 3.15. Temperature evolution diagram of $\chi_M * T$ for different compositions of $Nd_{1-x}Sr_xFeAsO$: black, green, red and blue marks refer to composition with x = 0, 0.05, 0.1 and 0.2 respectively. 80

Figure 3.16. Low field superconducting transition of $Nd_{0.8}Sr_{0.2}FeAsO$. 81

Figure 3.17. The temperature evolution of the resistivity for the different compositions of $Nd_{1-x}Sr_xFeAsO$: blue, red and black marks refer to compositions

with x = 0, 0.05 and 0.2 respectively. The inset illustrates the superconducting transition. 82

Figure 3.18. Temperature evolution of the derivative of the resistivity curves for different compositions of $Nd_{1-x}Sr_xFeAsO$: black, red and blue marks refer to composition with x = 0.05, 0.1 and 0.2 respectively. 83

Figure 3.19. Comparison of T_c in electron doped and hole doped NdFeAsO. 85

Figure 4.1. Schematic diagram of the room temperature tetragonal structure of $Sr_4Cr_2O_6Fe_2As_2$. 90

Figure 4.2. Final observed (blue circles), calculated (red solid line), and difference (lower green solid line) plots for the Rietveld refinement of 42622-Fe at RT. Tick marks show the reflection positions. The refinement proceeded with the main phase in the *P4/nmm* space group. The X-ray wavelength is 0.4030068 Å. Inset shows zoom in on the 20 to 40 2θ data range. 94

Figure 4.3. Final observed (blue circles), calculated (red solid line), and difference (lower green solid line) plots for the Rietveld refinement of 42622-Co at RT. Tick marks show the reflection positions and are from top to bottom: $Sr_4Sc_2O_6Co_2As_2$, SrO and CoAs. The refinement proceeded with the main phase in the *P4/nmm* space group. The X-ray wavelength is 0.4030068 Å. Inset shows zoom in on the 20 to 40 2θ data range. 94

Figure 4.4. Final observed (blue circles), calculated (red solid line), and difference (lower green solid line) plots for the Rietveld refinement of 42622-Ni at RT. Tick marks show the reflection positions. The refinement proceeded with the main phase in the *P4/nmm* space group. The X-ray wavelength is 0.4030068 Å. Inset shows zoom in on the 20 to 35 2θ data range. 95

Figure 4.5. Schematic diagram of the room temperature tetragonal structure of the $Sr_4Sc_2O_6Fe_2As_2$ system. 97

Figure 4.6. Schematic diagram of the **(a)** $FeAs_4$ unit and **(b)** the tetrahedron with detailed two-fold (α) and tetra-fold (β) As-Fe-As angles. The values of the angles reported refer to the $Sr_4Sc_2O_6Co_2As_2$ sample. 98

Figure 4.7. Dependence of the *a* and *c* axes and As-M^{II}-As angles versus ionic radii of transition metals (M^{II} = Ni, Co and Fe) in $Sr_4Sc_2O_6Fe_2As_2$, $Sr_4Sc_2O_6Ni_2As_2$ and $Sr_4Sc_2O_6Co_2As_2$. 99

Figure 4.8. Final observed (blue circles), calculated (red solid line), and difference (lower green solid line) plots for the Rietveld refinement of 42622-Fe at 5 K. Tick marks show the reflection positions. The refinement proceeded with the main phase in the *P4/nmm* space group. The X-ray wavelength is 0.4030068 Å. Inset shows zoom in on the 20 to 35 2θ data range. 102

Figure 4.9. Final observed (blue circles), calculated (red solid line), and difference (lower green solid line) plots for the Rietveld refinement of 42622-Co at 20 K. Tick marks show the reflection positions and are from top to bottom: $Sr_4Sc_2O_6Co_2As_2$, SrO and CoAs. The refinement proceeded with the main phase in the *P4/nmm* space group. The X-ray wavelength is 0.4030068 Å. Inset shows zoom in on the 20 to 35 2θ data range. 102

Figure 4.10. Final observed (blue circles), calculated (red solid line), and difference (lower green solid line) plots for the Rietveld refinement of 42622-Ni at 5 K. Tick marks show the reflection positions. The refinement proceeded with the main phase in the *P4/nmm* space group. The X-ray wavelength is 0.4030068 Å. Inset shows zoom in on the 20 to 35 2θ data range. 103

Figure 4.11. On the left: temperature evolution of the lattice constants for 42622-Sc: green and red circles refer to the *a* and *c* lattice constants, respectively. On the right: temperature evolution of the volume of 42622-Sc. 103

Figure 4.12. On the left: temperature evolution of the lattice constants for 42622-Co: green and red circles refer to the *a* and *c* lattice constants, respectively. On the right: temperature evolution of the volume for 42622-Co. 104

Figure 4.13. On the left: temperature evolution of the lattice constants for 42622-Ni: green and red circles refer to the *a* and *c* lattice constants, respectively. On the right: temperature evolution of the volume for 42622-Ni. 104

Figure 4.14. On the left: temperature evolution of the two-fold and tetra-fold angles for 42622-Sc: red and blue circles refer to α and β angles, respectively. On the right: temperature evolution of the Fe-As distance and the slab thickness for that composition. 105

Figure 4.15. On the left: temperature evolution of the two-fold and tetra-fold angles for 42622-Co: red and blue circles refer to α and β angles, respectively. On the right: temperature evolution of the Co-As distance and the slab thickness for that composition. 105

Figure 4.16. On the left: temperature evolution of the two-fold and tetra-fold angles for 42622-Ni: red and blue circles refer to α and β angles, respectively. On the right: temperature evolution of the Ni-As distance and the slab thickness for that composition. 105

Figure 4.17. Raw neutron data of $Sr_4Sc_2O_6Co_2As_2$ performed at D20 showing the difference between 100 K and 2 K data. 106

Figure 4.18. Temperature evolution diagram of χ_M for $Sr_4Sc_2O_6Fe_2As_2$ sample. The inset shows the superconducting transition for $Sr_4Sc_2O_6Ni_2As_2$. 107

Figure 4.19. Temperature dependence of the inverse magnetic susceptibility for $Sr_4Sc_2O_6Co_2As_2$, the black line corresponds to the fit to Curie-Weiss law. 108

Figure 4.20. Temperature dependence of the resistivity of $Sr_4Sc_2O_6Fe_2As_2$. 109

Figure 4.21. Schematic diagram of the room temperature tetragonal structure of the $Sr_4V_2O_6Fe_2As_2$ system. 115

Figure 4.22. Final observed (blue circles), calculated (red solid line), and difference (lower green solid line) plots for the Rietveld refinement of 42622-Cr at RT. Tick marks show the reflection positions and are from top to bottom: $Sr_4Cr_2O_6Fe_2As_2$, SrO and FeAs. The refinement proceeded with the main phase in the *P4/nmm* space group. The X-ray wavelength is 0.4030068 Å. Inset shows zoom in on the 20 to 40 2θ data range. 116

Figure 4.23. Final observed (blue circles), calculated (red solid line), and difference (lower green solid line) plots for the Rietveld refinement of 42622-V made with V_2O_5 at RT. Tick marks show the reflection positions. The refinement proceeded with the main phase in the *P4/nmm* space group. The X-ray wavelength is 0.4030068 Å. Inset shows zoom in on the 20 to 40 2θ data range. 116

Figure 4.24. Final observed (blue circles), calculated (red solid line), and difference (lower green solid line) plots for the Rietveld refinement of 42622-V made with V_2O_3 at RT. Tick marks show the reflection positions and are from top to bottom: $Sr_4V_2O_6Fe_2As_2$, FeAs and Sr_2VO_4. The refinement proceeded with the main phase in the *P4/nmm* space group. The X-ray wavelength is 0.4030068 Å. Inset shows zoom in on the 20 to 40 2θ data range. 117

Figure 4.25. On the left: temperature evolution of the lattice constants for 42622-Cr: green and red circles refer to the *a* and *c* lattice constants, respectively. On the right: temperature evolution of the volume for 42622-Cr. 119

Figure 4.26. On the left: temperature evolution of the two-fold and tetra-fold angles for 42622-Cr: red and blue circles refer to α and β angles, respectively. On the right: temperature evolution of the Fe-As distance and the slab thickness for that composition. 119

Figure 4.27. Final observed (blue circles), calculated (red solid line), and difference (lower green solid line) plots for the Rietveld refinement of 42622-Cr at 5 K. Tick marks show the reflection positions and are from top to bottom: $Sr_4Cr_2O_6Fe_2As_2$, SrO and Si powder. The refinement proceeded with the main phase in the *P4/nmm* space group. The X-ray wavelength is 0.4030068 Å. Inset shows zoom in on the 20 to 37 2θ data range. 120

Figure 4.28. Final observed (blue circles), calculated (red solid line), and difference (lower green solid line) plots for the Rietveld refinement of 42622-V at 5 K. The tick marks show the reflection positions and are from top to bottom: $Sr_4V_2O_6Fe_2As_2$ and Si powder. The refinement proceeded with the main phase in the *Cmma* space group. The X-ray wavelength is 0.4030068 Å. Inset shows zoom in on the 15 to 30 2θ data range. 120

Figure 4.29. On the left: temperature evolution of the lattice constants for 42622-V: green and red circles refer to the *a* and *c* lattice constants, respectively. On the right: temperature evolution of the volume for 42622-V. 121

Figure 4.30. On the left: temperature evolution of the two-fold and tetra-fold angles for 42622-V: red and blue circles refer to α and β angles, respectively. On the right: temperature evolution of the Fe-As distance and the slab thickness for that composition. 122

Figure 4.31. Example of peak splitting evolution with temperature observed in synchrotron X-ray experiment for sample 42622-V. 122

Figure 4.32. Raw neutron data of $Sr_4V_2O_6Fe_2As_2$ performed at D20 showing the difference between 100 K and 2 K data. 123

Figure 4.33. Neutron powder diffraction data of Cr-42622 collected on the D20 beamline at 2 K, showing magnetic peaks. 124

Figure 4.34. Temperature evolution of magnetic peaks from neutron powder diffraction data on Cr-42622, collected on the D20 beamline between 2 K and 100 K. 124

Figure 4.35. Final observed (blue circles), calculated (red solid line), and difference (lower green solid line) plots for the Rietveld refinement of neutron data of 42622-Cr at RT collected on D2B beamline. Tick marks show the reflection positions and are from top to bottom: $Sr_4Cr_2O_6Fe_2As_2$, SrO and FeAs. The refinement proceeded with the main phase in the *P4/nmm* space group. The wavelength used is 1.5943 Å. 125

Figure 4.36. Final observed (blue circles), calculated (red solid line), and difference (lower green solid line) plots for the Rietveld refinement of neutron data of 42622-Cr at 2 K collected on D2B beamline. Tick marks show the reflection positions and are from top to bottom: $Sr_4Cr_2O_6Fe_2As_2$, SrO and FeAs. The refinement proceeded with the main phase in the *P4/nmm* space group. The wavelength used is 1.5943 Å. Inset shows the graphic representation of the fitted magnetic structure. 126

Figure 4.37. Temperature evolution diagram of χ_M for $Sr_4Cr_2O_6Fe_2As_2$. Inset shows the temperature dependence of inverse magnetic susceptibility. 127

Figure 4.38. Temperature evolution diagram of χ_M for $Sr_4V_2O_6Fe_2As_2$ sample made with V_2O_5. The inset shows the superconducting transitions in V-42622 sample made with V_2O_3 with and without oxygenation of the sample. 128

Figure 4.39. Temperature dependence of resistivity of $Sr_4Cr_2O_6Fe_2As_2$ in ambient pressure and at 22 kbar. 129

Figure 4.40. An overview of the temperature dependence on resistivity for $Sr_4Cr_2O_6Fe_2As_2$ at different pressures. 130

Figure 4.41. Temperature dependence of resistivity for $Sr_4V_2O_6Fe_2As_2$. 131

Figure 4.42. Comparison of all 42622 samples' lattice strain as a function of the transition metals size difference-from left to right the data represents samples made with these metals respectively: Cr-Fe, V-Fe, Sc-Fe, Sc-Co, Sc-Ni. 132

Figure 4.43. Comparison of all 42622 samples' α and β angles as a function of the transition metals size difference-from left to right the data represents samples made with these metals respectively: Cr-Fe, V-Fe, Sc-Fe, Sc-Co, Sc-Ni. 133

Figure 4.44. Comparison of all 42622 samples' slab thickness and transition metals distances as a function of the transition metals size difference-from left to right the data represents samples made with these metals respectively: Cr-Fe, V-Fe, Sc-Fe, Sc-Co, Sc-Ni. 133

Figure 5.1. Final observed (blue circles), calculated (red solid line), and difference (lower green solid line) plots for the Rietveld refinement of $Sr_4Cr_2O_6Fe_{1.95}Co_{0.05}As_2$ at RT. Tick marks show the reflection positions and are from top to bottom: the main phase, 8% SrO and 12% FeAs. The refinement proceeded with the main phase in the *P4/nmm* space group. The X-ray wavelength is 0.4030068 Å. Inset shows zoom in on the 20 to 40 2θ data range. 142

Figure 5.2. Final observed (blue circles), calculated (red solid line), and difference (lower green solid line) plots for the Rietveld refinement of $Sr_4Cr_2O_6Fe_{1.9}Co_{0.1}As_2$ at RT. Tick marks show the reflection positions and are from top to bottom: the main phase, 6% SrO and 8% FeAs. The refinement proceeded with the main phase in the *P4/nmm* space group. The X-ray wavelength is 0.4030068 Å. Inset shows zoom in on the 20 to 40 2θ data range. 143

Figure 5.3. Final observed (blue circles), calculated (red solid line), and difference (lower green solid line) plots for the Rietveld refinement of $Sr_4Cr_2O_6Fe_{1.85}Co_{0.15}As_2$ at RT. Tick marks show the reflection positions and are from top to bottom: the main phase, 2.5% SrO and 8.5% FeAs. The refinement proceeded with the main phase in the *P4/nmm* space group. The X-ray wavelength is 0.4030068 Å. Inset shows zoom in on the 20 to 40 2θ data range. 143

Figure 5.4. Final observed (blue circles), calculated (red solid line), and difference (lower green solid line) plots for the Rietveld refinement of $Sr_4Cr_2O_6Fe_{1.75}Co_{0.25}As_2$ at RT. Tick marks show the reflection positions and are from top to bottom: the main phase, 4% SrO and 10% FeAs. The refinement proceeded with the main phase in the *P4/nmm* space group. The X-ray wavelength is 0.4030068 Å. Inset shows zoom in on the 20 to 40 2θ data range. 144

Figure 5.5. Final observed (blue circles), calculated (red solid line), and difference (lower green solid line) plots for the Rietveld refinement of $Sr_4Cr_2O_6FeCoAs_2$ at RT. Tick marks show the reflection positions and are from top to bottom: the main phase, 8% SrO, 4% FeAs and 3% CoAs. The refinement proceeded with the main phase in the *P4/nmm* space group. The X-ray wavelength is 0.4030068 Å. Inset shows zoom in on the 20 to 40 2θ data range. 144

Figure 5.6. Final observed (blue circles), calculated (red solid line), and difference (lower green solid line) plots for the Rietveld refinement of $Sr_4Cr_2O_6Fe_{0.5}Co_{1.5}As_2$ at RT. Tick marks show the reflection positions and are from top to bottom: the main phase, 10% SrO, 5% FeAs and 3% CoAs. The refinement proceeded with the main phase in the *P4/nmm* space group. The X-ray wavelength is 0.4030068 Å. Inset shows zoom in on the 20 to 40 2θ data range. 145

Figure 5.7. Final observed (blue circles), calculated (red solid line), and difference (lower green solid line) plots for the Rietveld refinement of $Sr_4Cr_2O_6Co_2As_2$ at RT. Tick marks show the reflection positions and are from top to bottom: the main phase, 12% SrO, 7% CoAs and 2% Co_2As_3. The refinement proceeded with the main phase in the *P4/nmm* space group. The X-ray wavelength is 0.4030068 Å. Inset shows zoom in on the 20 to 40 2θ data range. 145

Figure 5.8. Schematic diagram of the room temperature tetragonal structure of the $Sr_4Cr_2Fe_{2-x}Co_xAs_2O_6$ system. The particular arrangement shown is $Sr_4Cr_2Fe_{1.75}Co_{0.25}As_2O_6$. 147

Figure 5.9. Evolution of the room temperature tetragonal lattice constants as a function of Co^{3+} doping level x in $Sr_4Cr_2O_6Fe_{2-x}Co_xAs_2$**.** The lines are guides to the eye. 148

Figure 5.10. Evolution of the room temperature tetrahedral angle and Fe-As bond as a function of Co^{3+} doping level x in $Sr_4Cr_2O_6Fe_{2-x}Co_xAs_2$**.** The lines are guides to the eye. 149

Figure 5.11. Evolution of the room temperature tetragonal lattice constants as a function of percentage of parent lattice constants in $Sr_4Cr_2O_6Fe_{2-x}Co_xAs_2$**.** The lines are guides to the eye. 149

Figure 5.12. Temperature dependence of magnetic susceptibility measured at 10 kOe for the $Sr_4Cr_2O_6Fe_{2-x}Co_xAs_2$ series. 150

Figure 5.13. Temperature dependence of inverse magnetic susceptibility for the $Sr_4Cr_2O_6Fe_{2-x}Co_xAs_2$ series. The solid line is a fit to the Curie-Weiss law. 151

Figure 5.14. Evolution of the superconducting transition with the doping level in $Sr_4Cr_2O_6Fe_{2-x}Co_xAs_2$**.** 152

Figure 5.15. Evolution of the superconducting transition temperatures with the doping level in $Sr_4Cr_2O_6Fe_{2-x}Co_xAs_2$**.** The lines are guides to the eye. 152

Figure 5.16. Temperature dependence of the resistivity for $Sr_4Cr_2O_6Fe_{1.9}Co_{0.1}As_2$ measured at different pressures. 154

Figure 5.17. Temperature dependence of the resistivity for $Sr_4Cr_2O_6Fe_{1.85}Co_{0.15}As_2$ measured at different pressures. The bottom picture shows a close-up of measurements done at higher pressures. 155

Figure 5.18. Comparison of different temperature dependence of the resistivities for different samples of $Sr_4Cr_2O_6Fe_{2-x}Co_xAs_2$ measured at 22 kbar for the parent compound and $x = 0.1$ and 26 kbar for $x = 0.15$. 156

List of Abbreviations

AC	Alternating Current
AE	Alkaline Earth
BCS	Badeen Cooper Schrieffer theory
cgs	Centimetre-Gram-Second
Cr-42622	Sr4Cr2O6Fe2As2
DC	Direct Current
ESRF	European Synchrotron Radiation Facility
FC	Field Cooled
FWHM	Full Width at Half Maximum
GL	Ginzburg Landau
GSAS	General Structure Analysis System
HOPG	Highly Oriented Pyrolytic Graphite
ILL	Institute Laue Langevin
MPMS	Magnetic Property Measurement System
MRI/NMR	Magnetic Resonance Imaging / Nuclear Magnetic Resonance
PC	Personal Computer
PPMS	Physical Property Measurement System
PSD	Position Sensitive Detector
RE	Rare Earth
REO	Rare Earth Oxide
RT	Room Temperature
SDW	Spin Density Wave
SQUID	Superconducting Quantum Interference Device
XRPD	X-Ray Powder Diffraction
ZFC	Zero Field Cooled
ZFC/FC	Zero Field Cooled / Field Cooled
V-42622	Sr4V2O6Fe2As2

Chapter 1

Structure, magnetic and electronic properties of new transition metal-based oxyarsenides.

1.1. Introduction.

Modern technology, with its constant drive towards miniaturisation and effectiveness of materials, demands the research of new compounds that can be useful in this process. Over the past two decades a huge proportion of the interest in such new materials has been in high temperature superconductors. Their unique property of conducting electrical current with no resistivity has been known since the early 20th century[1], but only the discovery that such properties can be obtained at relatively high temperatures sparked the race to discover the best superconductors with as high transition temperatures as possible.

Superconductors have a wide usage in constructing powerful electromagnets (which are used for example in MRI/NMR machines and in particles accelerators), in digital circuit development and in most sensitive magnetometers. But the potential usage for future high temperature superconductors is much larger: lower power electric motors, transmitting electric power, new types of computers, magnetic levitation, and nanoscale technology. The other important factor in developing new superconducting materials is also trying to fully understand the mechanisms behind superconductivity, which is something that still fires up the scientific community.

The first high temperature superconductors discovered were ceramic materials - cuprates. The first one was $La_{2-x}Ba_xCuO_4$, discovered in 1986[1], and its transition temperature in the 30 K range was such a breakthrough that the authors of this discovery, Karl Müller and Johannes Bednorz, were awarded a Nobel Prize in Physics the following year. That discovery opened a huge field for research to synthesise new types of high temperature superconductors.

The aim of this research was to synthesise new materials that would be suitable parent compounds for further doping. The effects of doping were investigated in order to examine the possibility of producing new superconducting materials. The work started by synthesising samples from the 1111 family of iron-based oxyarsenides, as this was the first reported family of such materials to produce superconductors. Later the research shifted towards other families, and the final work was focused on the largest family known, the 42622 family of iron-based oxyarsenides. In this thesis, the synthesis and characterisation of new 1111-type and 42622-type materials will be presented alongside the structural, magnetic and electronic properties observed in those materials. A concise theoretical background of the aforementioned properties and interactions will be provided, in addition to a review of the different families of previously discovered transition metal-based oxyarsenides.

1.2. Superconductivity.

Superconductivity was first observed by Heike Kamerlingh Onnes in 1911[2]. He discovered that upon cooling with liquefied helium, the electrical resistance of some metals (mercury, lead and tin) vanishes at very low temperatures and retains no resistance at even lower temperatures. It was the first time that this new type of material classification based on conductivity arose, which was completely different from the already well known conductors, insulators and semiconductors. Newly discovered techniques for achieving very low temperatures were an important factor which allowed research in this new field of superconducting materials.

Superconductivity is a phenomenon occurring in certain materials where zero resistivity, and therefore a lack of Joule heating, is observed below a specific critical temperature, T_c. This means that an electric current can be carried in such materials without any energy loss. The other important property of superconductors is perfect diamagnetism, which means that the superconducting material excludes magnetic fields from penetrating the material and also expels magnetic flux from its interior. Both of these properties can be destroyed when either a sufficiently high magnetic field, critical field H_c, is applied, or the current passing through exceeds a critical

current value. Another interesting property which superconductors show is the Josephson effect. This is a phenomenon of a zero voltage supercurrent, which can flow across a Josephson junction. This is a device consisting of two strongly superconducting materials separated by a 'weak link', which could be a thin insulating layer, a weakly superconductive metal or a short discontinuity in the superconductor itself. Superconductivity can also be induced by high pressures, which force normally insulating materials to become metallic and show signs of superconductivity.

All metallic materials show a steady drop in resistivity with decreasing temperature and it reaches a limiting value, known as the residual resistivity, at absolute zero. In superconductors there is a clear drop in resistance at the critical temperature T_c, specific for each material (Figure 1.1a).

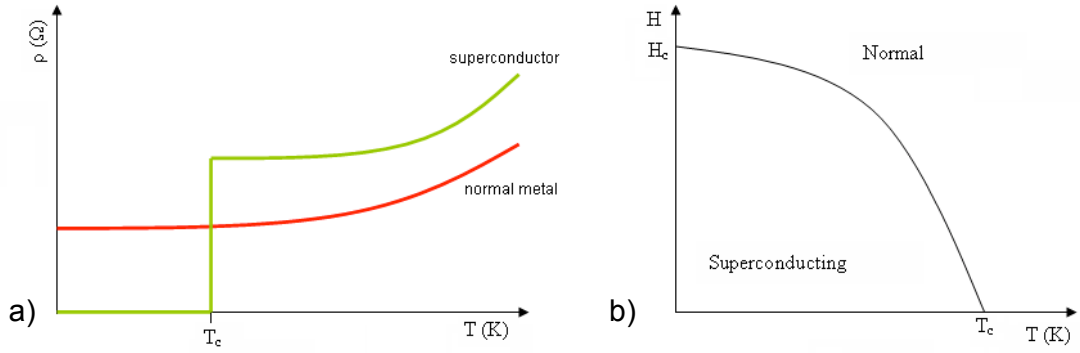

Figure 1.1. a) A plot of resistivity, ρ, versus temperature, T, comparing the behaviour of a superconductor (with its critical temperature) and a normal metal, **b)** Temperature dependence of the critical field**.**

Perfect diamagnetism of superconductors was first discovered in 1933 by Walther Meissner and Robert Ochsenfeld. They found that if a superconductor at a normal state is placed in a weak magnetic field upon cooling below its critical temperature, it shows a spontaneous expulsion of that magnetic field. The Meissner effect does not eject the magnetic field completely, instead there is a small amount of material on the outside penetrated by the field, described as London penetration depth, λ. That value is usually very small, in the region of 1000 Å and it depends on the geometry of the material. The Meissner effect is what indicates the existence of the critical magnetic field above which the superconductivity will be destroyed. It relates to the free-energy difference per unit volume between the normal (f_n) and superconducting (f_s)

states in zero field. This thermodynamic critical field gives a clear relationship between the energy associated with holding the field out against the magnetic pressure with the condensation energy[2]:

$$\frac{H_c^2(T)}{8\pi} = f_n(T) - f_s(T) \qquad \text{Equation 1.1}$$

This also shows that T_c of a superconductor depends on the presence of a magnetic field and that dependency can be described by a parabola (Figure 1.1b)[3].

1.2.1. London equation.

Since the first discovery of superconductivity and the Meissner effect there was a need to find the mechanism behind these discoveries. The first such theory was developed in 1935 by two brothers: Fritz and Heinz London. They based their theory on the model of superfluid ^{4}He and made an assumption that in the sample the total electron density, n_t, can be divided into a normal part, n_n, and superfluid part, n_s:

$$n_t = n_n + n_s \qquad \text{Equation 1.2}$$

These superconducting electrons would move without resistivity while normal ones would still behave as if their resistivity was finite. During movement the superfluid electrons would 'short circuit' the normal ones making the total resistivity of the material equal to zero[4].

They proposed two equations that would describe the microscopic electric and magnetic fields:

$$E = \frac{\partial}{\partial t}(\Lambda j_s) \qquad \text{Equation 1.3}$$

$$B = -c\Lambda(\nabla \times j_s)$$ Equation 1.4

where E and B are electric and magnetic field respectively, j_s is the superconducting current density and Λ can be described as:

$$\Lambda = \frac{4\pi\lambda^2}{c^2} = \frac{m}{n_s e^2}$$ Equation 1.5

Here e is the charge of the electron, m is the electron mass and λ is the penetration depth[2]. Out of these equations the penetration depth can be calculated as:

$$\lambda = \sqrt{\frac{m}{\mu_0 n_s e^2}}$$ Equation 1.6

The London equations explain the Meissner effect and can be written as an equation relating electrical current density within a superconductor and the magnetic vector potential, A:

$$j_s = -\frac{n_s e^2}{m} A$$ Equation 1.7

The following years brought more accurate theories explaining the superconducting mechanism but the London equations still remain its simplest description.

1.2.2. The Ginzburg-Landau model.

In 1950 Vitaly Lazarevitch Ginzburg and Lev Landau established their mathematical theory that would describe the superconducting phase transition in terms of thermodynamics.

Landau postulated that second-order phase transitions involve a change in the symmetry of the whole system. Based on that prediction they introduced an order parameter, ψ, which is a complex pseudo-wavefunction describing the

superconducting electrons[2]. The density of these electrons (or London superfluid density) can be described as:

$$n_s = |\psi(x)|^2 \qquad \text{Equation 1.8}$$

The order parameter characterizes the superconducting state by assuming that above the critical temperature the order parameter is equal to zero and that when the material becomes superconducting the parameter is nonzero. Taking into account the order parameter, the London equation is given by[4]:

$$j_s = -\frac{(2e)^2}{m^*}|\psi|^2 A \qquad \text{Equation 1.9}$$

where m^* is the Ginzburg-Landau (GL) effective mass equal to two bare electron mass.

The theory introduced a new parameter, called the Ginzburg-Landau coherence length, $\xi(T)$, which characterizes the superconductor:

$$\xi(T) = \sqrt{\frac{\hbar^2}{2m^*|a(T)|}} \qquad \text{Equation 1.10}$$

where a is a GL phenomenological constant. The Ginzburg-Landau coherence length is an important parameter which shows the distance from the surface over which the order parameter has recovered back to nearly its bulk value[5]. Near T_c the coherence length diverges and is characterized by a critical exponent of ½:

$$\xi(T) = \xi(0)|t|^{-\frac{1}{2}} \qquad \text{Equation 1.11}$$

where t is called reduced temperature and is equal to:

$$t = \frac{T - T_c}{T_c}$$ Equation 1.12

The Ginzburg-Landau theory was first introduced as a phenomenological model but later it was also derived from further theories which gave a microscopic interpretation of its parameters[6].

1.2.3. BCS theory and Cooper pairs.

The first microscopic theory of superconductivity was described in 1957 by John Bardeen, Leon Cooper and Robert Schrieffer, and is therefore known as the BCS theory. It uses quantum mechanical techniques and treats all electrons as a one-coupled system.[7]

This theory is based on a hypothesis by Herbert Frölich in 1950 about a weak effective attraction between electrons near the Fermi surface. It might seem like a surprising idea considering that bare electrons repel each other with electrostatic Coulomb force, as they have charges of the same sign. But in metals electrons have slightly different properties and behave as quasiparticles, which is an excitation state of a solid consisting of moving electrons and an exchange correlation hole which surrounds them. Following that idea Cooper concentrated on the interaction of two electrons outside of the Fermi surface. He showed that if there is at least one pair of electrons with an attractive interaction between them, it makes the Fermi sea of electrons unstable. These two electrons can be paired up in a superconducting state due to electron-phonon interactions, and these electron pairs are called Cooper pairs. The electrons in a Cooper pair are coupled over a typical distance of 100 nm, which is also called a correlation length, and such pairs are dynamically bonded, which means they break up and form new pairs all the time. The Cooper pairs are considered bosons, with zero overall spin and are individual change carriers. All of the properties of Cooper pairs favour low temperatures for their formation[7-8].

Finally, the last step in forming the full BCS theory was to write down a wave function that included many paired up particles near the Fermi surface:

$$\left|\Psi_{BCS}\right\rangle = \prod_{k>k_F}\left(u_k^* + v_k^* P_k^+\right)\prod_{k'>k_F}\left(u_{k'}^* P_{k'} + v_{k'}^*\right)\psi_($$

Equation 1.13

Where P is the Cooper pair creation operator. u^*_k and v^*_k are given by:

$$u_k^* = \frac{1}{1+\left|\alpha_k\right|^2}$$

Equation 1.14

$$v_k^* = \frac{\alpha_k}{1+\left|\alpha_k\right|^2}$$

Equation 1.15

where α_k are parameters in k-space to maximise the total energy.

The BCS gap equation uses the gap parameter, Δ:

$$\Delta = \left|g_{eff}\right|^2 \sum_k \frac{\Delta}{2E_k}$$

Equation 1.16

Where g_{eff} is a constant connected to the electron-phonon interaction. This equation gives the BCS value of the gap parameter at zero temperature:

$$\left|\Delta\right| = 2\hbar\omega_D e^{-\frac{1}{\lambda}}$$

Equation 1.17

Here λ is a coupling constant and $\hbar\omega_D$ is the Debye energy. This shows that energy in superconductors is on a lower scale than the Debye energy, and it explains why critical temperatures in superconductors are so much lower in value than typical energy scales in metals.[4] The BCS gap equation gives equation for T_c when $\Delta \rightarrow 0$:

$$k_B T_c = 1.13\hbar\omega_D e^{-\frac{1}{\lambda}}$$

Equation 1.18

The BCS theory predicts the existence of an energy gap of 2Δ in superconductors at the Fermi level, which separates the occupied and unoccupied states:

$$2\Delta(T=0) = 3.52 k_B T_c \qquad \text{Equation 1.19}$$

This prediction was proven experimentally while the BCS theory was being developed. From this equation it was predicted that it would not be possible to gain a T_c above 30 K. The experiments proved also that this gap arises from electron-phonon coupling and is proportional to the order parameter ψ.[2]

The BCS theory also explained the isotope effect (with exceptions):

$$T_c \propto M^{-\alpha} \qquad \text{Equation 1.20}$$

Which says that the superconducting transition temperature depends on the mass of the crystal lattice ions, M.

The BCS theory explains the mechanisms behind superconductivity of low temperature superconductors and the previously mentioned theories and properties of superconductors. However, it does not explain the mechanisms of high temperature superconductors, as this theory did not allow for the possibility of superconductivity above 30 K.

1.2.4. Type-II superconductors.

Another great discovery took place in 1957 – Alexei Alexeyevich Abrikosov investigated the Ginzburg-Landau theory and predicted that from an energy point of view there is a possibility of the London penetration depth, λ, being larger than the Ginzburg-Landau coherence length, ξ. In GL theory, typical superconductors have the ratio $\lambda/\xi < 1$. This is true for traditional metallic superconductors, but since discoveries of superconductors with unexpected properties, it became obvious that there is another class of superconductors. Abrikosov named the superconductors which followed GL theory type I superconductors to distinguish them from the new type II. He found out that in type II superconductors a magnetic field can enter the superconductor in the form of vortices, which makes these superconductors exhibit an imperfect Meissner effect. The magnetic field is channelled through a vortex core,

which is essentially a normal metal but with a property that allows the whole material to retain its superconducting properties.

In type I superconductors the magnetic field inside the material remains zero until a critical field, H_c, is applied, destroying the superconductivity. That transition is very sharp and beyond that point the Meissner effect disappears. Type II superconductors however, have two such critical fields, H_{c1} and H_{c2}, labelled as the lower and upper critical fields, respectively. Below H_{c1} the material behaves like a type I superconductor but when H_{c2} is reached the magnetic flux starts to enter the material and the superconductor is in the vortex state of both normal and superconducting regions (Figure 1.2).

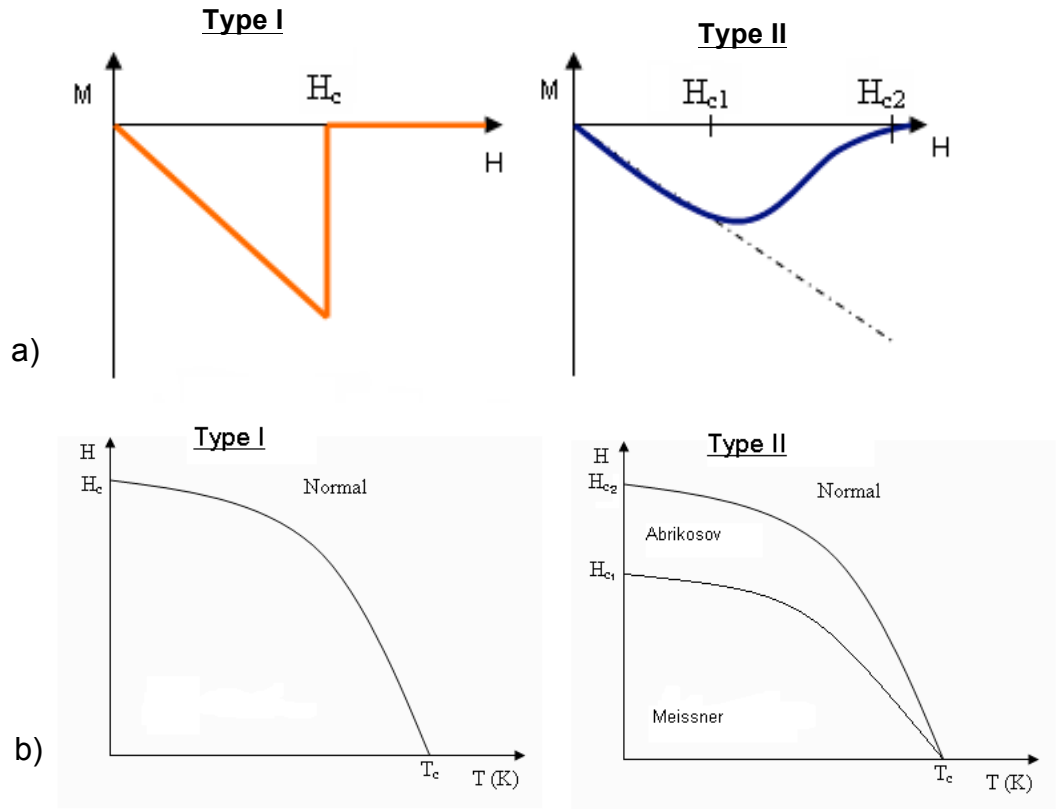

Figure 1.2. Comparison of type I and type II superconductors: **a)** Magnetisation, *M*, as a function of applied field, *H;* **b)** Temperature dependence of the critical field**.**

1.3. High temperature superconductors.

Up until 1986 the main research on superconductors was concentrated on mono-element materials and alloys, and the highest recorded superconducting transition temperature was 22.3 K for the metallic alloy Nb_3Ge[9]. It was far away from the 77 K goal, which is the boiling point of nitrogen and indicates the widespread usefulness of superconducting materials for economical reasons. After the discovery of cuprates in 1986[1] as high temperature superconductors, a huge interest in this new type of superconductors emerged with the aim of discovering materials which are still superconducting above 77 K. For more than twenty years researchers were working on synthesising new cuprates with high temperature superconducting transitions. Very quickly, researchers achieved a transition temperature above 77 K with $YBa_2Cu_3O_{7-x}$ in 1987, showing superconductivity at 93 K at ambient pressure[10]. The highest recorded transition temperature for cuprates is 138 K at ambient pressure[11] for $HgBa_2Ca_2Cu_3O_8$ and 166 K at high pressure[12] for fluorinated $HgBa_2Ca_2Cu_3O_8$. In 1991 fullerides stroked another wave of interest in researchers searching for high temperature superconductors when potassium doped C_{60} showed superconductivity below 18 K[13]. The highest recorded superconducting transition temperature for fullerides are 33 K at ambient pressure for Cs_2RbC_{60}[14] and 38 K at high pressure for Cs_3C_{60}[14-15]. Other examples of high temperature superconductors discovered in the last three decades, which are worth mentioning, are barium bismuthates and nitride halides. Barium bismuthates, $BaBiO_3$, have a perovskite structure and were shown to be superconducting upon suppression of charge order with a highest T_c of 30 K, when K was substituted for Ba[16, 17]. Nitride halides, MNX (M = Zr or Hf, X = Cl, Br, I), are structured by insulating planes, which can be electron doped by intercalation of metals (usually alkali) into their structures, or by halogen deficiency leading to superconductivity. The highest T_c observed in this family was 26.0 K for $Ca_{0.11}(THF)_yHfNCl$, which was intercalated by not only an alkaline earth metal (here Ca), but also by solvent molecules (here tetrahydrofuran – THF)[18, 19]. Finally, a very important compound is magnesium diboride, MgB_2, which was discovered to be superconducting in 2001. It reaches a T_c of 39 K and it is almost a perfect BCS superconductor[18, 20].

The main characteristic of the cuprate systems is their layered perovskite structure of copper oxide layers sandwiched between metals layer. All cuprates show metallic type conductivity at room temperature. They are brittle, which makes them difficult to use in large scale technologies. Copper ions in Cu-O layers are a mixture of Cu^{+} and Cu^{2+} ions, leading to mixed valency of copper in these systems. The superconductivity occurs in doped parent materials: either electron doped or hole doped. Doping in cuprates can take place in the Cu-O layer by incorporating oxygen vacancies, or in metal layer by using different elements to induce electron or hole doping.[8]

1.4. Rare-earth transition metal oxyarsenides.

Since 1986 most of the research in high temperature superconductors was concentrated mainly on cuprates and fullerides. However, both of these materials are difficult to synthesise in useful forms for use on a large scale, so there was still a need for new types of superconducting materials. Finally in 2008 a Japanese team under Prof. Hideo Hosono reported a new iron-based superconductor, a fluorine doped LaFeAsO[21] with T_c = 26 K. That discovery started a race towards achieving the highest T_c in iron-based superconductors and opened new possibilities as a suitable starting point for developing new superconducting samples.

Very quickly after the discovery of the 1111 family (the name is taken from the general formula of REFeAsO or AEFeAsO, where RE = rare earth metal and AE = alkaline earth metal) there have been a lot of different types of iron-based materials found to be superconducting. Only three months after report by Kamihara et al.[21], a discovery of a new 122 family of $AEFe_2As_2$ was announced by Rotter et al.[22], with a potassium doped $BaFe_2As_2$ showing a T_c of 38 K. The next families of iron-based superconducting materials are the 111 family of AEFeAs, where AE = Na, Li, K[23,24], 11 family with FeSe structure[25] (where the lack of toxic arsenic is beneficial), 32522 family of $AE_3TM_2O_5Fe_2As_2$ where AE = Sr and transition metal, TM = Sc[26]. The latest discovery of the 42622 family of $AE_4TM_2O_6Fe_2As_2$ (AE = Sr and TM = Sc, V,

Cr, Mg[27,28,29,30,31]) shows an even more complicated structure that can lead to superconductivity (Figure 1.3).

A lot of the properties of these new iron-based systems are comparable to those found in similarly structured cuprates[32]. Also during research for possible new iron-based superconductors, cuprates were a good starting point for trying to synthesise their iron analogues. All of the iron-based materials show a layered structure, usually with an Fe-As layer sandwiched between oxide layers. The Fe-As layer is where conductivity takes place, while the oxide layer acts as a charge reservoir. The exception here is the structurally simplest family of 11, where there is no oxide layer at all. The crystal structure of all these families at room temperature is tetragonal, and most undergo a tetragonal to orthorhombic (T→O) structural phase transition upon cooling. A lot of the parent compounds in all the iron-based superconductors show a spin density wave (SDW) anomaly which is suppressed with doping of the parent material.

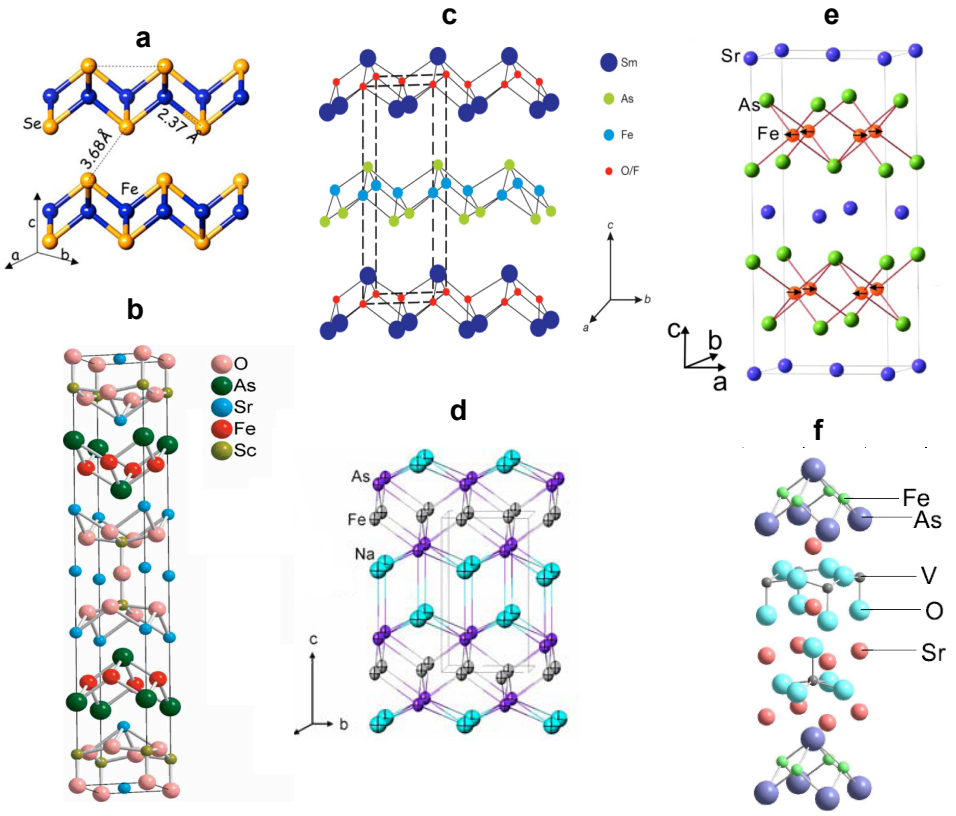

Figure 1.3. Crystal structure of the iron-based superconductors: a) 11, b) 32522, c) 1111, d) 111, e) 122 and f) 42622 families. [33, 34, 35, 36, 37, 38.]

In all of the iron-based superconductors, a very important part in achieving a high critical temperature of superconducting transition is played by the twofold As-Fe-As angle[39] (ideally 109.47º) and the distance between the conducting Fe-As layer and charge reservoir oxide layer. Varying these two structural properties in order to get the best compromise between layer distance and As-Fe-As angle was an important focus when designing new superconducting materials[40].

1.4.1. Superconducting properties.

There are a few known ways to induce superconductivity[41] in otherwise non-superconducting parent materials. The most common way is by chemical doping. Either electron or hole doping can be achieved by the partial replacement of a particular atom or by creating an atom deficiency in the material. The other method includes using high pressures to induce superconductivity or to raise T_c in an already superconducting sample.

The first reported electron doping in iron-based superconductors was done on a LaOFeAs sample in February 2008[21]. Fluorine doping on the oxygen site in $LaFeAsO_{1-x}F_x$ with $x = 0.11$ gave a T_c of 26 K. There was also a clear decrease in lattice constants with F^- substitution to the O^{2-} site, which indicates an induced chemical pressure inside the structure and proves the role that the distance between layers plays towards achieving superconductivity. Later it was shown that by applying a hydrostatic pressure of 3 GPa on $LaFeAsO_{0.89}F_{0.11}$, the T_c can be raised from 26 K to 43 K[42], proving that high pressure can play an important role in the pursuit of high superconducting transition temperatures.

Shortly after that, new compounds with different rare earth metals were produced where fluorine doping was proven to give positive results, with superconductivity quickly reaching a T_c of 43 K in $SmFeAsO_{1-x}F_x$ with $x = 0.15$[35]. It was also realised that during the synthesis, the nominal fluorine amount might be lower due to fluorine escape, essentially making some of the oxygen sites vacant. In order to investigate such a possibility, oxygen deficient samples of $REFeAsO_{1-x}$ (RE = Nd, Pr, La, Gd,

Ce and Sm)[43,44,45,46] were produced using hydrostatic pressure and achieved superconductivity up to 55 K in $SmFeAsO_{1-x}$[43]. Due to making them at high pressures, these samples show a different crystal structure from those made at ambient pressure, and have their As-Fe-As twofold angle closer to the ideal tetrahedron value of 109.47º. Making the same, fluorine free and oxygen deficient samples at ambient pressure has proven this as such materials do not exhibit any signs of superconducting transition. Another example of atom deficiency comes in the 11 family, where although there is no oxide layer, vacancies in the Se site have led to superconductivity in $FeSe_{1-x}$ with $T_c = 8$ K for 12% vacancy[33].

New structures were also investigated with the first-reported hole doped $BaFe_2As_2$, showing superconductivity at 38 K with 40% Ba^{2+} substitution by K^+ and then in potassium doped $SrFe_2As_2$ with T_c being also 38 K[48]. Another example of hole doping in the 122 family comes with sodium substitution on the calcium site in $CaFe_2As_2$, which showed a T_c of 26 K[49]. Hole doping has been proven to be a successful route towards achieving superconductivity in the 1111 family as well. Despite the fact that first hole doping on the RE site in LaFeAsO by calcium ions did not lead to superconductivity, strontium doping has been a success with T_c of 26 K in $La_{1-x}Sr_xFeAsO$ and $Pr_{1-x}Sr_xFeAsO$ with $T_c = 16.3$ K[50].

Another route to chemical doping has been taken by substituting the iron atoms with different transition metals such as Co, Ni, Ru, Rh, Pd, Mn and Ir[51]. It has been seen in the 1111 family (for example cobalt doped $NdFe_{1-x}Co_xAsO$ with T_c = 16.5 K[52] and $CaFe_{1-x}Co_xAsF$ with $T_c = 22$ K), 122 family ($Ba(Fe_{1-x}Co_x)_2As_2$ with T_c of 22 K, $Ba(Fe_{1-x}Ru_x)_2As_2$ with T_c of 22 K[53] or $Ba(Fe_{1-x}Ni_x)_2As_2$ with T_c of 21 K[54]) and 11 family with Co and Ni doping ($T_c = 10$ K in both cases[55]).

Some of the iron-based materials show superconductivity as parent compounds, without any need for doping. Most of these samples do not include arsenic in their structure and instead have other, non-toxic elements like selenium or phosphorus. The simplest example is FeSe with T_c of 13.4 K[56], which can be increased up to 37 K with pressure. Another family that shows superconducting properties without doping is 111 with LiFeAs ($T_c = 18$ K[24, 36]) and NaFeAs ($T_c = 12$ K[24]). In the 1111 family an example is LaFePO with $T_c = 6.6$ K[57], and finally in the biggest family, 42622, there

is $Sr_4Sc_2O_6Fe_2P_2$ with T_c = 17 K[58] and the nickel based (with no iron in the structure) $Sr_4Sc_2O_6Ni_2P_2$ (T_c = 3.3 K) and $Sr_4Sc_2O_6Ni_2As_2$ (T_c = 2.7 K)[59].

Results of doping at pnictide site in FeSe with Te and S (T_c = 15.3 K and 15.5 K respectively[33, 55]) have also been reported. Another substitution was reported on the transition metal site in the 42622 family and 32522 family (Ti doped $RE_4Sc_{2-x}Ti_xO_6Fe_2As_2$ and $RE_3Sc_{2-x}Ti_xO_5Fe_2As_2$ (RE = Ca, Sr) with a maximum onset of T_c reaching 45 K[60]).

1.4.2. 11 materials.

This is the structurally simplest binary family amongst iron-based superconductors. It consists only of Fe-Se layers and is very sensitive to stoichiometry. The parent compound is non-superconductive and exhibits a SDW state. The crystal structure is tetragonal made of $FeSe_4$ tetrahedra, which are identical to the Fe-As layers in other iron arsenide families. A structural phase transition to orthorhombic is present upon cooling[61]. The superconductivity can be enhanced by Se deficiency and can reach a T_c of 13.5 K at ambient pressure. It has been clearly seen that using high pressure on superconducting samples in this family induces a raise of T_c up to 37 K at 7 GPa[25, 56].

Another successful route towards achieving superconductivity in this system is doping on the Se site with Te[33]. This material shows a change in crystal structure from tetragonal to triclinic with Te doping even at room temperature, and reaches a higher T_c than in samples that are only Se deficient, 15.2 K for 50% Te substitution[33].

Doping on the Fe site with both Ni and Co, while the Se amount was non-deficient, has been reported[55]. These samples show a superconducting transition at 10 K for only 5% doping with Ni and Co.

1.4.3. 122 materials.

There have been a lot of different compositions of materials found within the 122 family. Aside from the previously mentioned $REFe_2As_2$ phases (RE = Sr, Ba, Ca, Eu)[49, 64-74] and their successors, which were doped with K, Cs or Na (on RE

site)[37,49,75-78] or Mn, Co, Ru or Ni (on Fe site)[53,54,79-81] others include samples where Fe is substituted with a non-magnetic metal (Ir or Ru)[53,82] or where Fe is completely exchanged for a different metal: $SrRu_2As_2$[83], $SrNi_2As_2$[84], $SrRh_2As_2$[85], $BaNi_2As_2$[86], $BaRu_2As_2$[83,85] and $BaRh_2As_2$[87]. There have also been reports of samples synthesised without the toxic arsenic by replacing it with phosphorus ($BaRh_2P_2$, $BaNi_2P_2$ or $BaIr_2P_2$)[88-90] or with germanium ($SrNi_2Ge_2$ and $SrPd_2Ge_2$)[91,92]. All these iron- or arsenic-free materials show low-temperature superconductivity (T_c between 0.3 K and 3 K).

The 122 family is another example where a structural phase transition occurs upon cooling: from tetragonal *I4/mmm* at room temperature to orthorhombic *Fmmm* at low temperatures. In this family a magnetic phase transition into a SDW state can be observed in parent compounds, and both structural and magnetic phase transitions appear at the same temperature in un-doped samples. With doping those transitions no longer occur at the same temperature, and the magnetic transition comes later than the structural transition upon cooling. The interesting thing about this system is the coexistence of both the SDW and the superconducting states (Figure 1.4) for some doping levels, while with increased doping the SDW is gradually suppressed, which is quite different from other iron-based families of superconductors.

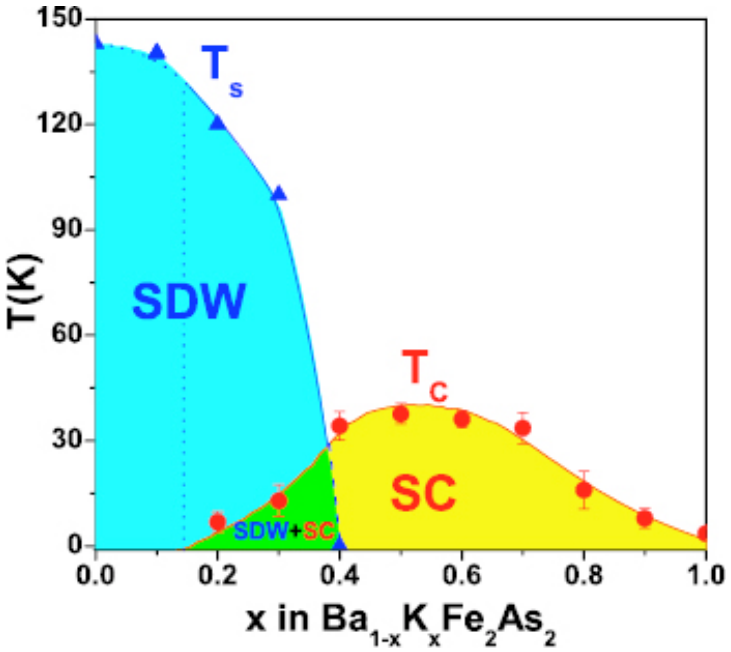

Figure 1.4. Experimentally determined phase diagram for $Ba(Fe_{1-x}Co_x)_2As_2$.[93]

1.4.4. 111 materials.

The crystal structure of this family consists of Fe-As layers with just a cation of an alkaline metal sandwiched between them, making it quite a simple structure. The 111 family members consist mostly of NaFeAs and LiFeAs and arsenic-free LiFeP[69,95,96]. It was the first family to have reported superconductivity in the un-doped parent compounds: LiFeAs has T_c of 18 K[36,97], NaFeAs has $T_c = 9$ K[53,98], while LiFeP shows $T_c = 6$ K[99]. Other members include sodium deficient and cobalt or nickel doped NaFeAs where T_c reaches 21 K for $NaFe_{0.975}Co_{0.025}As$[100].

Both LiFeAs and LiFeP display similar behaviour, with no structural or magnetic phase transition and both show bulk superconductivity in stoichiometric form. However, all of the sodium compounds show different properties with magnetic ordering around 40 K and superconductivity at low temperatures (Figure 1.5). The SDW and superconducting states are coexistent in the parent compound as in some cases of 122 family members. Again all sodium samples show a structural phase transition that occurs around the magnetic one, from tetragonal *P4/nmm* to orthorhombic *Cmma*.

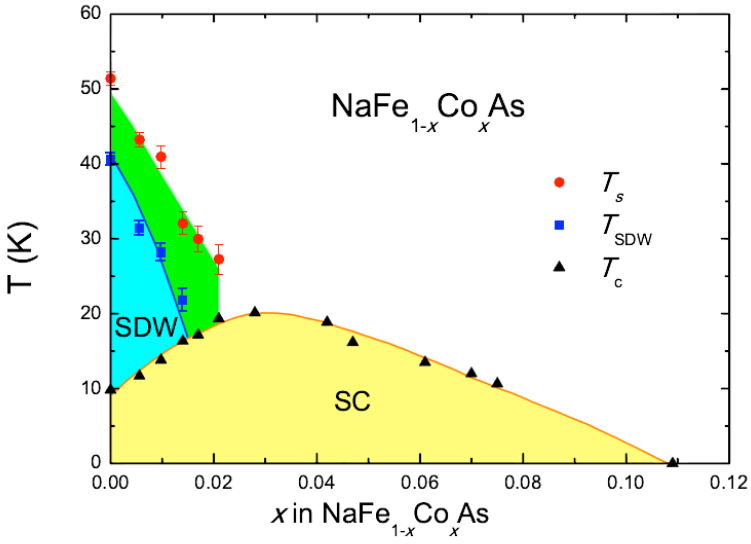

Figure 1.5. Experimentally determined phase diagram for $NaFe_{1-x}Co_xAs$.[100]

1.4.5. 1111 materials.

The 1111 family was the first discovered among all iron-based superconductors, so it is also the most studied family with the biggest variety of compositions. All of the members of this family have a tetragonal ZrCuSiAs-type structure and upon cooling they undergo a structural phase transition T→O from *P4/nmm* to an orthorhombic *Cmma* space group. Parent compounds exhibit a SDW ordering around 150 K, which is at a much higher temperature than other families mentioned. Both magnetic and structural transitions occur in parent compounds at similar, but not precisely the same, temperatures [35,74,101-105].

Upon doping the magnetic ordering is usually suppressed and superconductivity emerges, but in some cases the structural transition vanishes with doping as well. There are many different variations of that behaviour, as in some compounds the SDW and structural transition disappears abruptly with a specific level of doping (for example in fluorine doped LaFeAsO, Figure 1.6 a), for some the magnetic ordering and superconducting state coexists for some region of doping (SmFeAsO, Figure 1.6 b) and finally for others the magnetic ordering decreases slowly down to zero with doping and just then the superconductivity emerges (CeFeAsO, Figure 1.6 c).

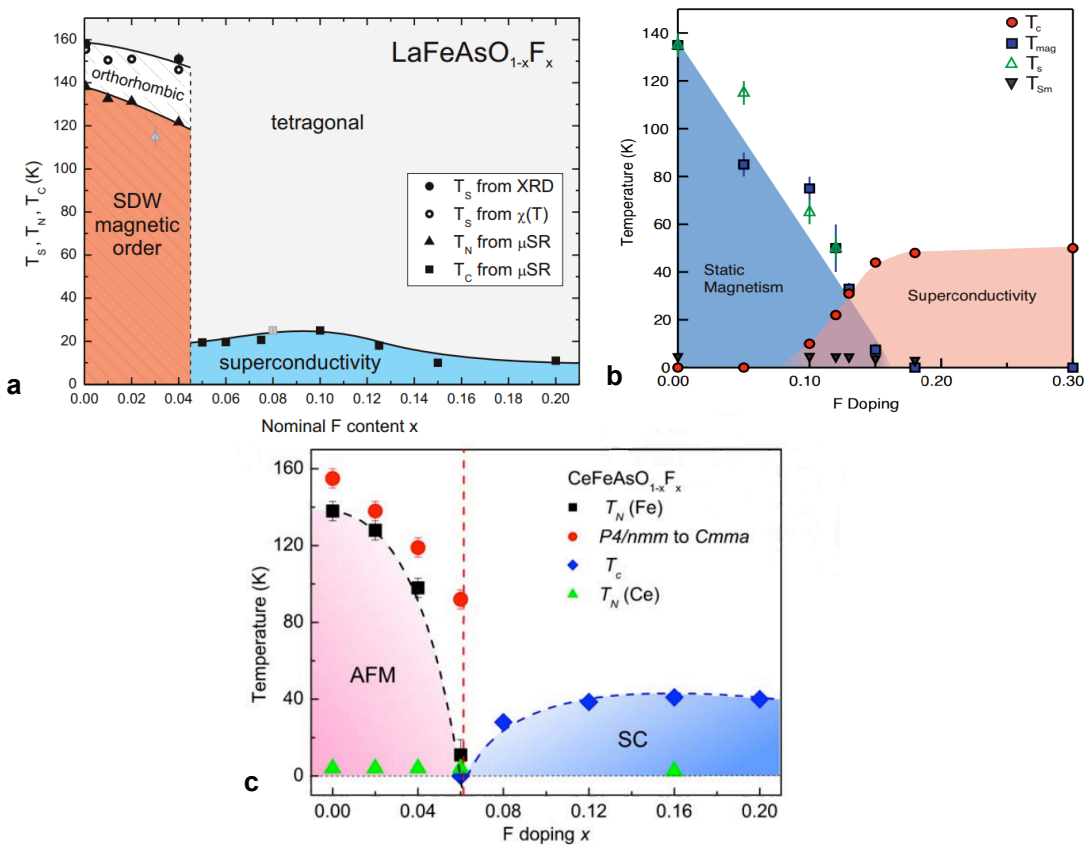

Figure 1.6. Experimentally determined phase diagrams for: a) $LaFeAsO_{1-x}F_x$,[106] b) $SmFeAsO_{1-x}F_x$[107] and c) $CeFeAsO_{1-x}F_x$[108].

The oxygen-free 1111 compounds, REFeAsF (RE = Sr, Ca, Ba, Eu)[51,105,109-112] are isostructural with the aforementioned oxypnictides. Either doping on the Fe site with Co or on the divalent RE metal site with a trivalent ion (like La, Pr, Sm or Nd)[51,111-114] leads to achieving superconductivity with T_c as high as 57.4 K for $Ca_{0.4}Nd_{0.6}FeAsF$[111]. This system also shows a SDW state and a structural phase transition upon cooling like the oxygen containing members of the 1111 family. Here the superconducting and magnetic states can coexist for specific region of doping and a structural phase transition is seen upon cooling from tetragonal to orthorhombic.

1.4.6. 42622 materials.

The 32522 family and 42622 (often abbreviated as 21311) family have the most complex and largest structures amongst the iron-based superconductors. $Sr_3Sc_2O_5Fe_2As_2$ is an example from the 32522 family that is not superconducting as a parent compound[38,115,116], but shows a superconducting state when Ti dopes the Sc site, achieving T_c of around 20 K with a Ti concentration between 60-70%[24]. No magnetic or structural transitions have been reported for this family.

Much more research has gone into the 42622 family of $AE_4TM_2O_6Fe_2As_2$ (AE = Sr, Ca and TM = Sc, V, Cr, Mg, Al)[58,117-122]. Apart from $Sr_4V_2O_6Fe_2As_2$, none of the parent compounds show superconductivity without doping. As in other families, arsenic-free compounds have also been synthesised with phosphorus substituting As -$Sr_4Sc_2O_6Fe_2P_2$[123,124], which is superconducting as a parent compound reaching T_c of 17 K[125] or oxygen deficient $Ca_4Al_2O_{6-x}Fe_2P_2$ with T_c = 17.1 K[126].

Doping in the 42622 family can be achieved by partial substitution on the transition metal site by Ti[24,127], by partial or full substitution on the iron site with Ni or Co, or finally by synthesising oxygen deficient samples. The last case was a successful route to creating a superconducting sample in $Sr_4V_2O_{6-x}Fe_2As_2$ with reported T_c = 37 K at ambient pressure[38]. A full exchange of iron for nickel leads to superconducting samples with both As and P: $Sr_4Sc_2O_6Ni_2As_2$ with T_c = 2.7 K and $Sr_4Sc_2O_6Ni_2P_2$ with T_c = 3.3 K[58]. High pressure has an interesting effect on different members of this family; in the case of $Sr_4V_2O_6Fe_2As_2$ the critical temperature rises to 46 K, but at 4 GPa the T_c of $Sr_4Sc_2O_6Fe_2P_2$ is suppressed down to 5 K at 4 GPa[117].

There has not been any report of any structural phase transitions among the 42622 family. No SDW ordering has been reported, and only in the case of $Sr_4Cr_2O_6Fe_2As_2$ has an antiferromagnetic ordering of Cr^{3+} ions been noticed below 36 K[31].

1.4.7. Comparison between oxyarsenides and cuprates.

As mentioned before, research into new oxyarsenides uses previously discovered cuprates as a template for creating similarly structured oxyarsenside compounds, in the hope that high temperature superconductivity will be present due to the structural

similarity. There are many analogous properties between the two groups that make this possible. The main similarity is within the structure itself: both the aforementioned oxyarsenides and cuprates exhibit a layered structure. Cuprates consist of layers of copper oxide with a perovskite-like structure. Between them are positively charged ions, usually of an alkaline earth metal or a rare earth metal. Finally, layers of metal oxide, connected to the copper oxide planes, act as the charge reservoir. In oxyarsenides, the main structure usually consists of FeAs layers (although sometimes As can be replaced with other non-toxic elements such as P, Se), which can be separated by various additional layers of either metal cations or oxide layers. The oxyarsenides show a much larger variety in their structural composition, and in the sizes and the types of layers sandwiched between the FeAs planes[17].

The next similarity between cuprates and oxyarsenides is the fact that usually the parent compounds do not show superconducting properties, but below a critical temperature exhibit antiferromagnetic behaviour. The nature of this antiferromagnetism in the parent compounds is different between them – cuprates show alternating spins in all dimensions, while oxyarsenides have antiparallel spins in one direction, but usually exhibit stripes of aligned spins along at least one of the others. It is also worth noting the close proximity of both antiferromagnetism and superconductivity in both groups when discussing their similarities[128].

Finally, both cuprates and most oxyarsenides can have superconductivity induced by either hole or electron doping. In the case of oxyarsenides, electron doping is more common and usually leads to higher superconducting transition temperatures than those where hole doping is used. In cuprates, however, hole doping is more common. This can be achieved by either increasing the oxygen quantity, by cation substitution or by band overlap (the last option is rare, but is used in the well known $YBa_2Cu_3O_7$ compound, which has the highest T_c of 93 K). Electron doping is also possible, usually by reduction of Cu^{2+}, but the results are not as successful as those of hole doping[129]. An example of an electron doped cuprate is $M_{2-x}Ce_xCuO_4$ (M = La, Nd, Pr, Sm, Eu) with the maximum T_c of 32 K for $La_{1.91}Ce_{0.09}CuO_4$[130].

1.5. Bibliography.

1. Bednorz, J. G.; Müller, K. A., *Z. Physik B - Condensed Matter* **1986,** *64* (2), 189-193.
2. Tinkham, M., *Introduction to Superconductivity*. DOVER PUBN Incorporated: 2004.
3. Smart, L. E.; Moore, E. A., *Solid State Chemistry: An Introduction, Third Edition*. Taylor & Francis: 2005.
4. Annett, J. F., *Superconductivity, Superfluids and Condensates*. OUP Oxford: 2004.
5. Rose-Innes, A. C.; Rhoderick, E. H., *Introduction to superconductivity*. Pergamon Press: 1978.
6. Tilley, D. R.; Tilley, J., *Superfluidity and Superconductivity*. Adam Hilger: 1990.
7. Rosenberg, H. M., *The Solid State: An Introduction to the Physics of Solid*. Oxford University Press: 1995.
8. Guinier, A.; Jullien, R.; Crystallography, I. U. o., *The solid state: from superconductors to superalloys*. International Union of Crystallography: 1989.
9. Gavaler, J. R., *Applied Physics Letters* **1973,** *23* (8), 480-482.
10. Wu, M. K.; Ashburn, J. R.; Torng, C. J.; Hor, P. H.; Meng, R. L.; Gao, L.; Huang, Z. J.; Wang, Y. Q.; Chu, C. W., *Physical Review Letters* **1987,** *58* (9), 908.
11. Schilling, A.; Cantoni, M.; Guo, J. D.; Ott, H. R., *Nature* **1993,** *363* (6424), 56-58.
12. Chu, C. W.; Gao, L.; Chen, F.; Huang, Z. J.; Meng, R. L.; Xue, Y. Y., *Nature* **1993,** *365* (6444), 323-325.
13. Hebard, A. F.; Rosseinsky, M. J.; Haddon, R. C.; Murphy, D. W.; Glarum, S. H.; Palstra, T. T. M.; Ramirez, A. P.; Kortan, A. R., *Nature* **1991,** *350* (6319), 600-601.
14. Tanigaki, K.; Ebbesen, T. W.; Saito, S.; Mizuki, J.; Tsai, J. S.; Kubo, Y.; Kuroshima, S., *Nature* **1991,** *352* (6332), 222-223.

15. Ganin, A. Y.; Takabayashi, Y.; Khimyak, Y. Z.; Margadonna, S.; Tamai, A.; Rosseinsky, M. J.; Prassides, K., *Nature Materials* **2008,** *7* (5), 367-371.
16. Tang, H.Y.; Chen, W.L.; Wen, W.J.; Wu, M.K.;, Norton, M.L., MRS Proceedings, **1992**, 275, 891.
17. Parinov, I.A., *Microstructure and Properties of High-Temperature Superconductors,* Springer: 2007.
18. Attfield, J.P., *Journal of Materials Chemistry*, **2011**, 21, 4756-4764.
19. Zhang, S.; Tanaka, M.; Zhu, H.; Yamanaka, S., *Superconductor Science and Technology,* **2013,** 26 (8), 085015.
20. Nagamatsu, J.; Nakagawa, N.; Muranaka, T.; Zenitani, Y.; Akimitsu, J., *Nature***, 2001,** 410, 63.
21. Kamihara, Y.; Watanabe, T.; Hirano, M.; Hosono, H., *Journal of the Amerisan Chemical Society* **2008,** *130* (11), 3296-3297.
22. Rotter, M.; Tegel, M.; Johrendt, D., *Physical Review Letters,* **2008**, 101 (10), 107006.
23. Parker, D. R.; Pitcher, M. J.; Baker, P. J.; Franke, I.; Lancaster, T.; Blundell, S. J.; Clarke, S. J., *Chemical Communications,* **2009,** (16), 2189-2191.
24. Chu, C. W.; Chen, F.; Gooch, M.; Guloy, A. M.; Lorenz, B.; Lv, B.; Sasmal, K.; Tang, Z. J.; Tapp, J. H.; Xue, Y. Y., *Physica C: Superconductivity 469* (9–12), 326-331.
25. Margadonna, S.; Takabayashi, Y.; McDonald, M. T.; Kasperkiewicz, K.; Mizuguchi, Y.; Takano, Y.; Fitch, A. N.; Suard, E.; Prassides, K., *Chemical Communications* **2008,** (43), 5607-5609.
26. Zhu, X.; Han, F.; Mu, G.; Zeng, B.; Cheng, P.; Shen, B.; Wen, H.-H., *Physical Review B,* **2009,** *79* (2), 5.
27. Ogino, H.; Katsura, Y.; Horii, S.; Kishio, K.; Shimoyama, J.-I., *Superconductor Science and Technology,* **2009,** *22*, 13.
28. Sato, S.; Ogino, H.; Kawaguchi, N.; Katsura, Y.; Kishio, K.; Shimoyama, J.-I., *Superconductor Science and Technology,* **2010**, 045001, 11.
29. Zhu, X.; Han, F.; Mu, G.; Cheng, P.; Shen, B.; Zeng, B.; Wen, H.-H., *Physical Review B***, 2009**, 79 (22).

30. Xie, Y. L.; Liu, R. H.; Wu, T.; Wu, G.; Song, Y. A.; Tan, D.; Wang, X. F.; Chen, H.; Ying, J. J.; Yan, Y. J.; Li, Q. J.; Chen, X. H., *Europhysics Letters,* **2009,** *86*, 9.

31. Tegel, M.; Hummel, F.; Su, Y.; Chatterji, T.; Brunelli, M.; Johrendt, D., *Europhysics Letters,* **2010,** *89* (37006), 6.

32. Wen, H.-H., *Advanced Materials* **2008,** 20(19), 3764-3769.

33. Yeh, K. W.; Hsu, H. C.; Huang, T. W.; Wu, P. M.; Huang, Y. L.; Chen, T. K.; Luo, J. Y.; Wu, M. K., *Journal of the Physical Society of Japan 77SC* (Supplement C), 19.

34. Zhu, X.; Han, F.; Mu, G.; Zeng, B.; Cheng, P.; Shen, B.; Wen, H.-H., *Physical Review B* **2009,** *79* (2), 5.

35. Chen, X. H.; Wu, T.; Wu, G.; Liu, R. H.; Chen, H.; Fang, D. F., *Nature* **2008,** *453* (7196), 761-762.

36. Tapp, J. H.; Tang, Z.; Lv, B.; Sasmal, K.; Lorenz, B.; Chu, P. C. W.; Guloy, A. M., *Physical Review B* **2008,** *78* (6), 060505.

37. Rotter, M.; Pangerl, M.; Tegel, M.; Johrendt, D., *Angewandte Chemie International Edition* **2008,** *47* (41), 7949-7952.

38. Zhu, X.; Han, F.; Mu, G.; Cheng, P.; Shen, B.; Zeng, B.; Wen, H.-H., arXiv:0904.1732,**2009**.

39. Mizuguchi, Y.; Hara, Y.; Deguchi, K.; Tsuda, S.; Yamaguchi, T.; Takeda, K.; Kotegawa, H.; Tou, H.; Takano, Y.,*Superconductor Science and Technology,* **2010,** 23 (5), 054013.

40. Matsuishi, S.; Inoue, Y.; Nomura, T.; Yanagi, H.; Hirano, M.; Hosono, H., *Journal of the American Chemical Society* **2008,** *130* (44), 14428-14429.

41. Huang, X. Q., arXiv:1001.5067, **2010**.

42. Takahashi, H.; Igawa, K.; Takahashi, Y.; Arii, K.; Okada, H.; Kamihara, Y.; Hirano, M.; Hosono, H.; Matsubayashi, K.; Uwatoko, Y.; Nakano, S.; Kikegawa, T., *Journal of Physics: Conference Series,* **2009,** *150* (5), 052257.

43. Ren, Z.-A.; Che, G.-C.; Dong, X.-L.; Yang, J.; Lu, W.; Yi, W.; Shen, X.-L.; Li, Z.-C.; Sun, L.-L.; Zhou, F.; Zhao, Z.-X., *Europhysics Letter,* **2008,** *83* (1), 17002.

44. Rotundu, C. R.; Keane, D. T.; Freelon, B.; Wilson, S. D.; Kim, A.; Valdivia, P. N.; Bourret-Courchesne, E.; Birgeneau, R. J., *Physical Review B,* **2009,** *80* (14), 144517.

45. Zhao, J.; Huang, Q.; de la Cruz, C.; Lynn, J. W.; Lumsden, M. D.; Ren, Z. A.; Yang, J.; Shen, X.; Dong, X.; Zhao, Z.; Dai, P., *Physical Review B,* **2008,** *78* (13), 132504.

46. Yang, J.; Li, Z.-C.; Lu, W.; Yi, W.; Shen, X.-L.; Ren, Z.-A.; Che, G.-C.; Dong, X.-L.; Sun, L.-L.; Zhou, F.; Zhao, Z.-X., *Superconductor Science and Technology,* **2008,** *21* (8), 082001.

47. F.C. Hsu, J.Y. Luo, K.W. Yeh, T.K. Chen, T.W. Huang, Wu, Phillip M., Y.C. Lee, Y.L. Huang, Y.Y. Chu, D.C. Yan, M.K. Wu, *Proceedings of the National Academy of Sciences,* 2008, volume 105, 14262.

48. Chen, G.-F.; Li, Z.-C.; Li, G.; Hu, W.-Z.; Dong, J.; Zhou, J.; Zhang, X.-D.; Zheng, P.; Wang, N.-L.; Luo, J.-L., *Chinese Physics Letters* **2008,** *25* (9), 3403.

49. Shirage, P. M.; Miyazawa, K.; Kito, H.; Eisaki, H.; Iyo, A., *Applied Physics Express 1* (8), 081702.

50. Wen, H. H.; Mu, G.; Zhu, X. Y.; Cheng, P.; Fang, L.; Han, F.; Zeng, B.; Shen, B., *Physica C: Superconductivity* **2009,** *469* (15–20), 894-897.

51. Marcinkova, A.; Grist, D. A. M.; Margiolaki, I.; Hansen, T. C.; Margadonna, S.; Bos, J.-W. G., *Physical Review B,* **2010**, 81 (6), 064511.

52. Matsuishi, S.; Inoue, Y.; Nomura, T.; Yanagi, H.; Hirano, M.; Hosono, H., *Journal of the American Chemical Society* **2008,** *130* (44), 14428-14429.

53. Paular, S.; Sharma, S.; Bharathi, A.; Satya, A. T.; Chandra, S.; Hariharan, Y.; Sundar, C. S., *arXiv:0902.2728v3*.

54. Li, L. J.; Luo, Y. K.; Wang, Q. B.; Chen, H.; Ren, Z.; Tao, Q.; Li, Y. K.; Lin, X.; He, M.; Zhu, Z. W.; Cao, G. H.; Xu, Z. A., *New Journal of Physics* **2009,** *11* (2), 025008.

55. Mizuguchi, Y.; Tomioka, F.; Tsuda, S.; Yamaguchi, T.; Takano, Y., *Journal of the Physical Society of Japan 78* (7), 074712.

56. Margadonna, S.; Takabayashi, Y.; Ohishi, Y.; Mizuguchi, Y.; Takano, Y.; Kagayama, T.; Nakagawa, T.; Takata, M.; Prassides, K., *Physical Review B* **2009,** *80* (6), 064506.

57. Hamlin, J. J.; Baumbach, R. E.; Zocco, D. A.; Sayles, T. A.; Maple, M. B., *Journal of Physics: Condensed Matter* **2008,** *20* (36), 365220.

58. Ogino, H.; Matsumura, Y.; Katsura, Y.; Ushiyama, K.; Horii, S.; Kishio, K.; Shimoyama, J.-i., *Superconductor Science and Technology,* **2009**, 22 (7), 075008.

59. Matsumura, Y.; Ogino, H.; Horii, S.; Katsura, Y.; Kishio, K.; Shimoyama, J.-I., *Applied Physics Express 2,* **2009**, 063007.

60. Chen, G. F.; Xia, T.-L.; Yang, H. X.; Li, J. Q.; Zheng, P.; Luo, J. L.; Wang, N. L., *Superconductor Science and* Technology, **2009**, 22 (7), 072001.

61. Xia, Y.; Huang, F.; Xie, X.; Jiang, M., *Europhysics Letters* **2009,** *86* (3), 37008.

62. Matsuishi, S.; Inoue, Y.; Nomura, T.; Yanagi, H.; Hirano, M.; Hosono, H., *Journal of the American Chemical Society* **2008,** *130* (44), 14428-14429.

63. Jesche, A.; Caroca-Canales, N.; Rosner, H.; Borrmann, H.; Ormeci, A.; Kasinathan, D.; Klauss, H. H.; Luetkens, H.; Khasanov, R.; Amato, A.; Hoser, A.; Kaneko, K.; Krellner, C.; Geibel, C., *Physical Review B* **2008,** *78* (18), 180504.

64. Zhao, J.; Ratcliff, W.; Lynn, J. W.; Chen, G. F.; Luo, J. L.; Wang, N. L.; Hu, J.; Dai, P., *Physical Review B* **2008,** *78* (14), 140504.

65. Jeevan, H. S.; Hossain, Z.; Kasinathan, D.; Rosner, H.; Geibel, C.; Gegenwart, P., *Physical Review B* **2008,** *78* (5), 052502.

66. Tegel, M.; Rotter, M.; Weiss, V.; Schappacher, F. M.; Pöttgen, R.; Johrendt, D., Prof. Dr . *Journal of Physics: Condensed Matter* **2008,** *20* (45), 452201;

67. Canfield, P. C.; Budko, S. L., *Annual Review of Condensed Matter Physics,* **2010**, vol.1, 27-50.

68. Huang, Q.; Qiu, Y.; Bao, W.; Green, M. A.; Lynn, J. W.; Gasparovic, Y. C.; Wu, T.; Wu, G.; Chen, X. H., *Physical Review Letters 101* (25).

69. Miyake, T.; Nakamura, K.; Arita, R.; Imada, M., *Journal of the Physical Society of Japan,* **2010**, 79, 044705.

70. Chu, C. W.; Lorenz, B., *Physica C: Superconductivity 469* (9–12), 385-395.

71. Jesche, A.; Caroca-Canales, N.; Rosner, H.; Borrmann, H.; Ormeci, A.; Kasinathan, D.; Klauss, H. H.; Luetkens, H.; Khasanov, R.; Amato, A.; Hoser, A.; Kaneko, K.; Krellner, C.; Geibel, C., *Physical Review B* **2008,** *78* (18), 180504.

72. Chu, C.-W.; Chaudhury, R. P.; Chen, F.; Gooch, M.; Guloy, A. M.; Lorenz, B.; Lv, B.; Sasmal, K.; Tang, Z.; Wang, L.; Xue, Y.-Y., *Journal of the Physical Society of Japan* **2008,** *77*, 72-77.

73. Li, H.; Tian, W.; Zarestky, J. L.; Kreyssig, A.; Ni, N.; Bud'ko, S. L.; Canfield, P. C.; Goldman, A. I.; McQueeney, R. J.; Vaknin, D., *Physical Review B* **2009,** *80* (5), 054407.

74. Krellner, C.; Caroca-Canales, N.; Jesche, A.; Rosner, H.; Ormeci, A.; Geibel, C., *Physical Review B* **2008,** *78* (10), 100504.

75. Torikachvili, M. S.; Bud'ko, S. L.; Ni, N.; Canfield, P. C., *Physical Review B* **2008,** *78* (10), 104527.

76. Sasmal, K.; Lv, B.; Lorenz, B.;.Guloy, A.; Chen, F.; Xue, Y.-Y.; Chu, C.-W., *Physical Review Letters***, 2008,** 101(10), 107007.

77. Zhao, L.; Liu, H.-Y.; Zhang, W.-T.; Meng, J.-Q.; Jia, X.-W.; Liu, G.-D.; Dong, X.-L.; Chen, G.-F.; Lou, J.-L.; Wang, N.-L.; Lu, W.; Wang, G.-L.; Zhou, Y.; Zhu, Y.; Wang, X.-Y.; Xu, Z.-Y.; Chen, C.-T.; Zhou, X.-J., *Chinese Physics Letters* **2008,** *25* (12), 4402;

78. Ivanovskii, A. L., *Journal of Structural Chemistry* **2009,** *50* (3), 539-551

79. Ning, F. L.; Ahilan, K.; Imai, T.; Sefat, A. S.; McGuire, M. A.; Sales, B. C.; Mandrus, D.; Cheng, P.; Shen, B.; Wen, H.-H., *Physical Review Letters,* **2010,** 104(3), 037001.

80. Kumar, N.; Nagalakshmi, R.; Kulkarni, R.; Paulose, P. L.; Nigam, A. K.; Dhar, S. K.; Thamizhavel, A., *Physical Review B* **2009,** *79* (1), 012504.

81. Kasinathan, D.; Ormeci, A.; Koch, K.; Burkhardt, U.; Schnelle, W.; Leithe-Jasper, A.; Rosner, H., *New Journal of Physics* **2009,** *11* (2), 025023.

82. Han, F.; Zhu, X.; Cheng, P.; Mu, G.; Jia, Y.; Fang, L.; Wang, Y.; Luo, H.; Zeng, B.; Shen, B.; Shan, L.; Ren, C.; Wen, H.-H., *Physical Review B* **2009,** *80* (2), 024506.

83. Nath, R.; Singh, Y.; Johnston, D. C., *Physical Review B* **2009,** *79* (17), 174513.

84. Mewis, A.; Distler, A., *Zeitschrift für Naturforschung* **1980,** *35* (b), 391-393.

85. Shein, I. R.; Ivanovskii, A. L., *Central European Journal of Physics* **2009**, 8.

86. Ronning, F.; Kurita, N.; Bauer, E. D.; Scott, B. L.; Park, T.; Klimczuk, T.; Movshovich, R.; Thompson, J. D., *Journal of Physics: Condensed Matter* **2008,** *20* (34), 342203.

87. Singh, Y.; Lee, Y.; Nandi, S.; Kreyssig, A.; Ellern, A.; Das, S.; Nath, R.; Harmon, B. N.; Goldman, A. I.; Johnston, D. C., *Physical Review B* **2008,** *78* (10), 104512.

88. Hirai, D.; Takayama, T.; Higashinaka, R.; Aruga-Katori, H.; Takagi, H., *Journal of the Physical Society of Japan 78* **2009**, 023706.

89. Mine, T.; Yanagi, H.; Kamiya, T.; Kamihara, Y.; Hirano, M.; Hosono, H., *Solid State Communications* **2008,** *147* (3–4), 111-113.

90. Shein, I. R.; Ivanovskii, A. L., *Journal of Experimental and Theoretical Physics Letters,* **2009,** *89* (7), 357-361.

91. Shein, I. R.; Ivanovskii, A. L., *Solid State Communications,* **2010,** 150(3-4), 152-156.

92. Rozsa, S.; Schuster, H.-U., *Zeitschrift für Naturforschung,* **1981,** *86b*, 1668-1670.

93. Chen, H.; Ren, Y.; Qiu, Y.; Bao Wie; Liu, R.H.; Wu, G.; Wu, T.; Xie, Y.L.; Wang, X.F.; Huang, Q.; Chen, X.H., *Europhysics Letters,* **2009**, *85* (1), 17006.

94. Wang, X. F.; Wu, T.; Wu, G.; Liu, R. H.; Chen, H.; Xie, Y. L.; Chen, X. H. *New Journal of Physics*, **2009**, 11, 045003.

95. Zhang, X.; Wang, H.; Ma, Y., *Journal of Physics: Condensed Matter* **2010,** *22* (4), 046006.

96. Li, Y. F.; Liu, B. G., *European Physical Journal B,* **2009,** *72* (2), 153-157.

97. Wang, X. C.; Liu, Q. Q.; Lv, Y. X.; Gao, W. B.; Yang, L. X.; Yu, R. C.; Li, F. Y.; Jin, C. Q., *Solid State Communications* **2008,** *148* (11–12), 538-540.

98. Parker, D. R.; Pitcher, M. J.; Baker, P. J.; Franke, I.; Lancaster, T.; Blundell, S. J.; Clarke, S. J., *Chemical Communications* **2009,** (16), 2189-2191.

99. Deng, Z.; Wang, X. C.; Liu, Q. Q.; Zhang, S. J.; Lv, Y. X.; Zhu, J. L.; Yu, R. C.; Jin, C. Q., *Europhysics Letters* **2009,** *87* (3), 37004.

100. Wang, A. F.; Luo, X. G.; Yan, Y. J.; Ying, J. J.; Xiang, Z. J.; Ye, G. J.; Cheng, P.; Li, Z. Y.; Hu, W. J.; Chen, X. H., *Physical Review B* **2012,** *85* (22), 224521.

101. Yang, J.; Li, Z.-C.; Lu, W.; Yi, W.; Shen, X.-L.; Ren, Z.-A.; Che, G.-C.; Dong, X.-L.; Sun, L.-L.; Zhou, F.; Zhao, Z.-X., *Superconductor Science and Technology* **2008,** *21* (8), 082001.

102. Li, Y.; Tong, J.; Tao, Q.; Feng, C.; Cao, G.; Xu, Z.-a.; Chen, W.; Zhang, F.-c., *New Journal of Physics,* **2010,** 12, 083008.

103. Yang, Y.; Hu, X., arXiv:1003.0592, **2010**.

104. Felner, I.; Pal, A.; Nowik, I.; Yamaura, K.; Takayama-Muromachi, E.; Awana, V. P. S., *Physical Review B* **2010,** *81* (212501), 10.

105. Xiao, Y.; Su, Y.; Mittal, R.; Chatterji, T.; Hansen, T.; Price, S.; Kumar, C. M. N.; Persson, J.; Matsuishi, S.; Inoue, Y.; Hosono, H.; Brueckel, T., *Physical Review B,* **2010**, 81, 094523.

106. Luetkens, H.; Klauss, H. H.; Kraken, M.; Litterst, F. J.; Dellmann, T.; Klingeler, R.; Hess, C.; Khasanov, R.; Amato, A.; Baines, C.; Kosmala, M.; Schumann, O. J.; Braden, M.; Hamann-Borrero, J.; Leps, N.; Kondrat, A.; Behr, G.; Werner, J.; Buchner, B., *Nature Materials* **2009,** *8* (4), 305-309.

107. Drew, A. J.; Niedermayer, C.; Baker, P. J.; Pratt, F. L.; Blundell, S. J.; Lancaster, T.; Liu, R. H.; Wu, G.; Chen, X. H.; Watanabe, I.; Malik, V. K.; Dubroka, A.; Rossle, M.; Kim, K. W.; Baines, C.; Bernhard, C., *Nature Materials* **2009,** *8* (4), 310-314.

108. Jun, Z.; Huang, Q.; Clarina de la, C.; Shiliang, L.; Lynn, J. W.; Chen, Y.; Green, M. A.; Chen, G. F.; Li, G.; Li, Z.; Luo, J. L.; Wang, N. L.; Pengcheng, D., *Nature Materials* **2008,** *7* (12), 953-959.

109. Tegel, M.; Johansson, S.; Weiss, V.; Schellenberg, I.; Hermes, W.; Pöttgen, R.; Johrendt, D., *Europhysics Letters ,* **2008,** *84* (67007), 5.

110. Zhu, L.-F.; Liu, B.-G., *Europhysics Letters,* **2009,** *85* (6), 67009.

111. Cheng, P.; Shen, B.; Mu, G.; Zhu, X.; Han, F.; Zeng, B.; Wen, H.-H.,*Europhysics Letters* **2009,** *85* (6), 67003.

112. Wu, G.; Xie, Y.; Chen, H.; Zhong, M.; Liu, R.; Shi, B.; Li, Q.; Wang, X.; Wu, T.; Yan, Y.; Ying, J.; Chen, X., *Chinese Science Bulletin,* **2009,** *54* (11), 1872-1875.

113. Pal, A.; Mehdi, S. S.; Husain, M.; Gahtori, B.; Awana, V. P. S., *Journal of Applied Physics* **2011,** *110* (10), 103913-6.

114. Xiao, Y.; Su, Y.; Mittal, R.; Chatterji, T.; Hansen, T.; Kumar, C. M. N.; Matsuishi, S.; Hosono, H.; Brueckel, T., *Physical Review B* **2009,** *79* (6), 060504.

115. Kotegawa, H.; Kawazoe, T.; Tou, H.; Murata, K.; Ogino, H.; Kishio, K.; Shimoyama, J.-I., *arXiv:0908.1469,* **2009**.

116. Zhu, W. J.; Hor, P. H., *Journal of Solid State Chemistry* **1997,** *134* (1), 128-131.

117. Kotegawa, H.; Kawazoe, T.; Tou, H.; Murata, K.; Ogino, H.; Kishio, K.; Shimoyama, J.-I., *Journal of the Physical Society of Japan,* **2009,** *78* (123707), 4.

118. Lee, K.-W.; Pickett, W. E., *Europhysics Letters,* **2010**, 89(5), 57008.

119. Tegel, M.; Hummel, F.; Lackner, S.; Schellenberg, I.; Pöttgen, R.; Johrendt, D., *Zeitschrift für anorganische und allgemeine Chemie,* **2009,** *635* (13-14), 2242-2248.

120. Ogino, H.; Katsura, Y.; Horii, S.; Kishio, K.; Shimoyama, J.-i., *Superconductor Science and Technology,* **2009,** *22*, 13;

121. Zhang, Y.-L.; Zhang, J.-H.; Tao, X.-M.; Tan, M.-Q., *Superconductor Science and Technology,* **2011,** *24* (10), 105014.

122. Xie, Y. L.; Liu, R. H.; Wu, T.; Wu, G.; Song, Y. A.; Tan, D.; Wang, X. F.; Chen, H.; Ying, J. J.; Yan, Y. J.; Li, Q. J.; Chen, X. H., *Europhysics Letters,* **2009,** *86*, 9.

123. Shein, I. R.; Ivanovskii, A. L., arXiv:0903.4038, **2009**.

124. Yates, K. A.; Usman, I.; Morrison, K.; Moore, J. D.; Gilbertson, A. M.; Caplin, A. D.; Cohen, L. F., *Superconductor Science and Technology 23* (2), 11.

125. Ogino, H.; Matsumura, Y.; Katsura, Y.; Ushiyama, K.; Horii, S.; Kishio, K.; Shimoyama, J.-i., *Superconductor Science and Technology* **2009,** *22* (7), 075008.

126. Shirage, P. M.; Kihou, K.; Lee, C.-H.; Kito, H.; Eisaki, H.; Iyo, A., *Applied Physics Letters* **2010,** *97* (17), 172506.

127. Shein, I. R.; Ivanovskii, A. L., *Central European Journal of Physics* **2009**, 8.

128. Kresin, V.Z.; Morawitz, H.; Wolf, S.A., Superconducting State: Mechanisms and Properties, OUP Oxford: 2013.

129. Brinkman, A.; Hilgenkamp, H., Physica C: Superconductivity, 2005, 42 (3-4), 0921.

130. Krockenberger, Y.; Kurian, J.; Winkler, A.; Tsukada, A.; Naito, M.; Alff, L., *Physical Review B* **2008,** *77* (6), 060505.

Chapter 2

Experimental techniques.

2.1. Introduction.

The research presented in this work is mostly concentrated on structural, magnetic and electronic properties of the newly discovered 1111-type and 42622-type iron-based superconducting materials. In order to study these families in the solid state, numerous techniques have been used and are described within this chapter. The main interest was to describe the structure of the produced samples, which was achieved by use of X-ray powder diffraction (XRPD). Initial XRPD measurements on all samples were performed using laboratory Bruker D8 AXS, Bruker D8 Advance and Bruker D2 Phaser diffractometers. More detailed experiments on structure determination with use of variable temperatures were done at the European Synchrotron Radiation Facility (ESRF) in Grenoble, France. Another important facility used for both detailed crystal and magnetic structure determination in samples is the Institute Laue Langevin (ILL) in Grenoble, France. Further measurements investigating superconducting and magnetic properties of the researched materials were performed using Quantum Design Magnetic Property Measurement System (MPMS), which contains a Superconducting Quantum Interference Device (SQUID). Finally, superconducting and electronic properties were measured on a Quantum Design Physical Property Measurement System (PPMS). All of the techniques and facilities used will be described in detail, as well as the theoretical background on which they are based. In addition, the theoretical aspects of experimental data analysis and computer software programs used will also be described in this chapter.

2.2. Powder diffraction.

2.2.1. Theory of powder diffraction.

Powder diffraction is very powerful technique widely used to characterize polycrystalline materials. It is mostly used where single crystals are not available. In a single crystal diffraction measurement it is necessary to rotate the crystal in the radiation source in order to generate the complete diffraction pattern[1]. In powder diffraction, the sample is ideally made up of a huge number of small crystallites, which have random orientation so there is always some part of the material that fulfils the orientation requirements for the measurement. This method raises some technical problems as well, for example the size of grains must be very small (preferably below 10 μm) because bigger crystals may give problematic data to analyse.

The characteristic property of crystalline materials is their regularly repetitive pattern in all three dimensions. These patterns may consist of a repeating molecule, group of molecules, group of atoms or ions. The simplest repeating object or group of objects within the structure are referred to as unit cells. Unit cells are imaginary geometrical parallelepiped shapes which are defined by three vectors: *a, b* and *c*, which lie along the *x, y* and *z* axes respectively. Dimensions of unit cells are represented by the lengths of these three vectors *a, b* and *c*. There are seven crystal lattice systems that class crystals according to the relationships between dimensions of the unit cell and the angles (α,β,γ) between the vectors making it as shown in Table 2.1.

Unit cells are three-dimensional objects that can be classified into three main types - primitive (P), body centred (I) and face centred (F), depending on the distribution of lattice points in the unit cell. The Primitive (P-type) unit cell has one lattice point in each of its corners, I-type has also lattice points located in the corners, but also one additional point in the centre of the unit cell, and F-type has lattice points in all the corners and in the centre of each of unit cells' faces. The F-type also includes unit cells which have lattice points in the corners and only in the centre of one of its faces – such types are named after the location of that lattice point: A-type

when the lattice point is located on the face represented by *b* and *c* vectors, B-type when the lattice point is located on the face represented by *a* and *c* vectors and finally C-type when the lattice point is located on the face represented by *a* and *b* vectors. The combination of these four types of unit cells with seven crystal lattice systems (Table 2.1) gives 14 permissible Bravais lattices.

Table 2.1. The seven crystal systems with minimum symmetry requirements[2].

System	Unit cell	Minimum symmetry requirements	Bravais Lattices
Triclinic	$\alpha\neq\beta\neq\gamma\neq90°$ $a\neq b\neq c$	None	P
Monoclinic	$\alpha=\gamma=90°$ $\beta\neq90°$ $a\neq b\neq c$	One twofold axis or one symmetry plane	P, C
Orthorhombic	$\alpha=\beta=\gamma=90°$ $a\neq b\neq c$	Any combination of three mutually perpendicular twofold axes or planes of symmetry	P, I, F, C
Trigonal / Rhombohedral	$\alpha=\beta=\gamma\neq90°$ $a=b=c$	One threefold axis	P
Hexagonal	$\alpha=\beta=90°$ $\gamma=120°$ $a=b\neq c$	One sixfold axis or one sixfold improper axis	P
Tetragonal	$\alpha=\beta=\gamma=90°$ $a=b\neq c$	One fourfold axis or one fourfold improper axis	P, I
Cubic	$\alpha=\beta=\gamma=90°$ $a=b=c$	Four threefold axes at 109°28’ to each other	P, I, F

In powder diffraction, it is useful to discuss lattice planes which are defined by three noncollinear lattice points in a crystal[3]. The lattice plane equation:

$$hx + ky + lz = m \qquad \text{Equation 2.1.}$$

shows a plane at a distance m from its origin. The *h, k, l* constants are called Miller indices. These indices are given by the ratios between the plane interception point with the crystal axis, and the lattice parameter of the unit cells: $h=a/x$, $k=b/y$ and $l=c/z$. The Miller parameters are often written as a set of three integers (*hkl*). For any plane that never intercepts one of the crystallographic axes, the corresponding Miller index will be 0.

A very useful concept in diffraction theory is the reciprocal lattice, introduced by P. Ewald. It associates every Bravais lattice with a reciprocal lattice. The reciprocal lattice points are combined with real lattice parameters by these relationships:

$$a^* = \frac{bc\sin\alpha}{a\cdot(b\times c)} = \frac{bc\sin\alpha}{V}$$
$$b^* = \frac{ac\sin\beta}{b\cdot(c\times a)} = \frac{ac\sin\beta}{V}$$
$$c^* = \frac{ab\sin\gamma}{c\cdot(a\times b)} = \frac{ab\sin\gamma}{V} \qquad \text{Equation 2.2.}$$

These relationships satisfy the following conditions[4]:

$$a^*\cdot b = a^*\cdot c = b^*\cdot a = b^*\cdot c = c^*\cdot a = c^*\cdot b = 0$$
$$a^*\cdot a = b^*\cdot b = c^*\cdot c = 1 \qquad \text{Equation 2.3.}$$

The reciprocal lattice vectors can only be linear combinations of a^*, b^* and c^* with *h, k, l* coefficients, which are always integers[5]:

$$\tau = ha^* + kb^* + lc^* \qquad \text{Equation 2.4.}$$

2.2.1.1. Bragg's Law.

Diffraction is the bending of waves around an obstacle. All types of waves, including electromagnetic waves such as X-rays, can be diffracted. It is the basis of several powerful methods for the determination of molecular structure[6]. The size of an object around which a wave diffracts has to be comparable with the wavelength of the wave. In crystal structures, distances between atoms or ions are of an order of 1 Å, therefore radiation of that wavelength is used to determine the dimensions in solid materials. The wavelengths of both X-rays and neutrons beams are therefore in the correct order of magnitude for structure determination measurements.

In diffraction the waves penetrate the crystal deeply, reflecting the beam on various lattice planes. If there are only two planes, *A* and *B*, which are separated by a

distance *d*, then the difference in the waves' path will be equal to $BC + BD = 2d\sin\theta$, where θ is the angle between the primary beam and the lattice plane (Figure 2.1). If that path difference is a multiple of the wavelength, then a maximum positive interference spot is observed[4].

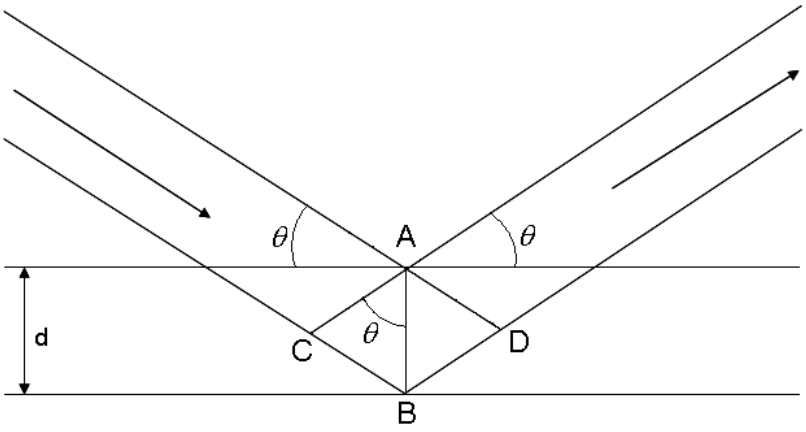

Figure 2.1. Illustration of the reflection from waves on two lattice planes used for the derivation of Bragg's law.

This is the definition of Bragg's law:

$$2d\sin\theta = n\lambda \qquad \text{Equation 2.5.}$$

where n is an integer which defines the order of reflection or diffraction, and λ is the wavelength used.

All of the samples mentioned in this thesis were measured using a fixed wavelength and by moving the detectors, different *d*-spacings were obtained. In this case, Bragg's equation can be given as:

$$\lambda = 2d_{hkl}\sin\theta \qquad \text{Equation 2.6.}$$

And the *d*-spacing in the tetragonal crystallographic lattice can be calculated as:

$$\frac{1}{d^2} = \frac{h^2 + k^2}{a^2} + \frac{l^2}{c^2} \qquad \text{Equation 2.7.}$$

This technique for measuring polycrystalline powders with a fixed wavelength was developed by Debye and Scherrer. It assumes that the varied θ reflections from all the randomly oriented crystallites within the powder will reflect at the appropriate Bragg angle. In three dimensions, the diffracted X-rays of the reflection *hkl* gives coaxial cones which are called Debye-Scherrer cones[7] (Figure 2.2). The huge advantage of this method is that only small amounts of powder are needed for the measurement[8,9].

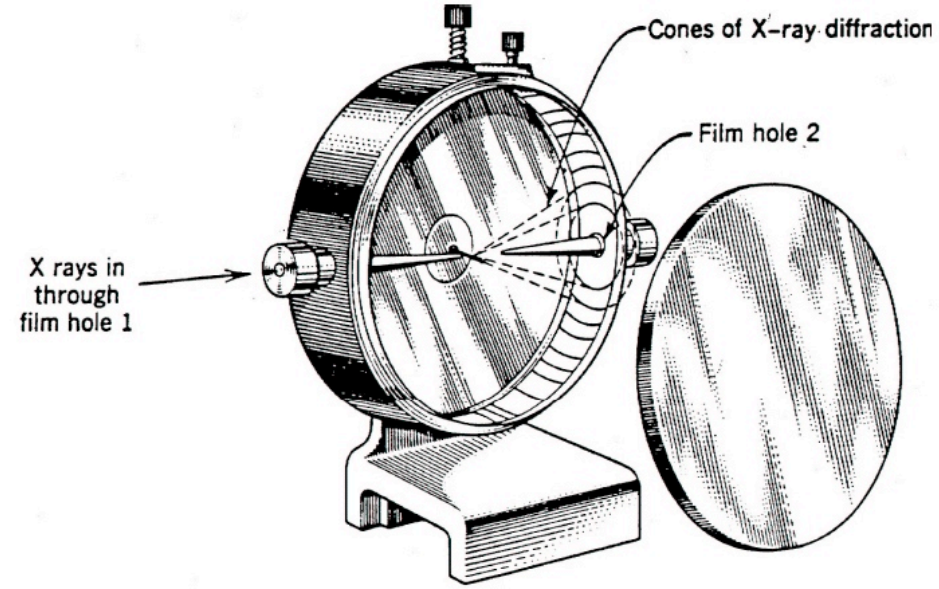

a)

b)

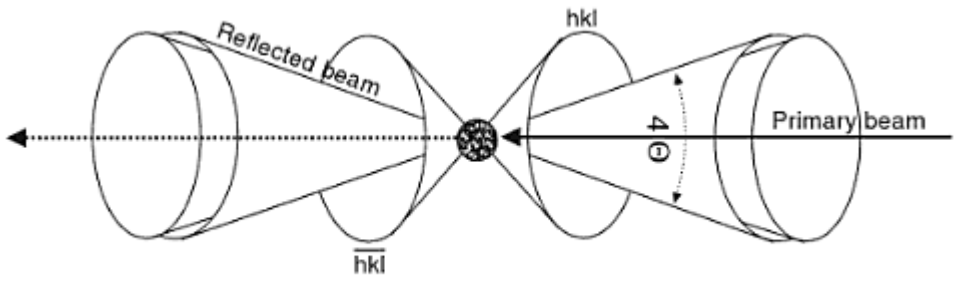

Figure 2.2. a) The geometry of the Debye-Scherrer camera[9] and b) scattered beams originating from a powder sample with Debye-Scherrer cones shown[7].

2.2.2. Equations.

There are two important factors to take into account when describing the crystal structure: structure factor, F_{hkl}, and the intensity of Bragg's reflection, I_{hkl}. The structure factor takes into account contributions from different atoms, and is proportional to the atomic scattering factors of the atoms[8]:

$$structure\ \ factor\ \ F_{hkl} = \frac{amplitude\ \ scattered\ \ by\ \ the\ \ atoms\ \ in\ \ the\ \ unit\ \ cell}{amplitude\ \ scattered\ \ by\ \ an\ \ electron}$$

or more detailed:

$$F_{hkl} = \sum_j f_j(\theta) \cdot \exp\left(-8\pi^2 U_j \sin^2\theta/\lambda^2\right) \cdot \exp\left[2\pi i\left(hx_j + ky_j + lz_j\right)\right]$$

Equation 2.8.

where

U_j = displacement parameter used to account for the thermal motion of atoms in a solid

x_j. y_j. z_j = fractional coordinates of atom j in the unit cell

h, k, l = the Miller indices for the reflection

$f_j(\theta)$ = atomic scattering factor for atom j with the Bragg angle θ, defined as:

$$atomic\ \ scattering\ \ factor\ \ f_j = \frac{amplitude\ \ scattered\ \ by\ \ an\ \ atom}{amplitude\ \ scattered\ \ by\ \ an\ \ electron}$$

or more detailed:

$$f_j = f_0 + f' + f''$$

Equation 2.9.

where f_0 is dependent on the scattering angle θ, and f' and f'' are real and anomalous dispersion terms[10].

The intensity of a Bragg reflection is proportional to the square of F_{hkl}:

$$I_{hkl} \propto F_{hkl}^2$$ Equation 2.10.

2.2.3. Laboratory X-ray instruments.

The first quality checks on all the samples mentioned in this thesis were performed on laboratory Bruker D8 AXS, Bruker D8 Advance and Bruker D2 Phaser diffractometers. Most of these measurements were done using flat-plate mounted samples and some, for better quality, in 0.5 mm sealed quartz capillaries. The X-rays used in these diffractometers are produced in a sealed tube that produces electrons by electrical potential (in case of the aforementioned instruments it is 60 kV) which then interacts with a copper anode source producing X-rays. The radiation output from this mechanism exhibits a series of intense and sharp maxima that correspond to the electrons from higher orbitals dropping in energy, taking the place of ionized electrons from core atomic orbital, emitting radiation while they do so. This radiation has a specific frequency and wavelength. Only a single wavelength is required for diffraction therefore the beam of radiation falls on a single crystal monochromator (in this case germanium) so only $K_{\alpha 1}$ wavelength is used with a length of 1.54056 Å[1,8,11]. For data collection, all diffractometers use a position sensitive detector (PSD). The position sensitive detectors serve as a means to detect and count photons from the X-rays, which excite electrons in the detector material. This allows the scattering data to be collected and analysed. The PSD used in powder X-ray diffraction must be moved during the data collection in order to scan the whole scattering area[4].

2.2.4. Synchrotron X-ray.

2.2.4.1. Theory of synchrotron X-ray.

A much higher intensity of X-rays than that produced in a laboratory diffractometer can be achieved in a synchrotron. A synchrotron is a type of cyclic particle accelerator where electrons are travelling around a vacuumed circular ring (so called storage ring) with speeds close to the speed of light (299 792 458 ms^{-1}). The synchrotron uses a varied magnetic field and a varied frequency-applied electric

field to accelerate particles in a linear accelerator (linac) and then again in a circular (booster synchrotron) one before they are injected into the storage ring where bending magnets are used to keep particles travelling in the ring (Figure 2.3). Synchrotron radiation is extremely intense, around 100-10000 times more intense than the $K_{\alpha 1}$ radiation from a diffractometer's X-ray tube. It is also highly collimated which allows for much higher 2θ resolution. Also the wavelength is not fixed like in a copper source anode, but can be tailored to the particular required wavelength depending on the experiments conducted. Synchrotron radiation is produced as a result of the continuous inward radial acceleration and covers a wavelength range from infrared to very short X-ray wavelengths. With the use of monochromators, a specific wavelength is reflected out of the storage ring to be used for measurement purposes. The other difference between synchrotron radiation and diffractometer X-ray tube is that radiation from a synchrotron is wholly polarized in the plane of the storage ring while in an X-ray tube it is almost entirely unpolarized[8,12,13].

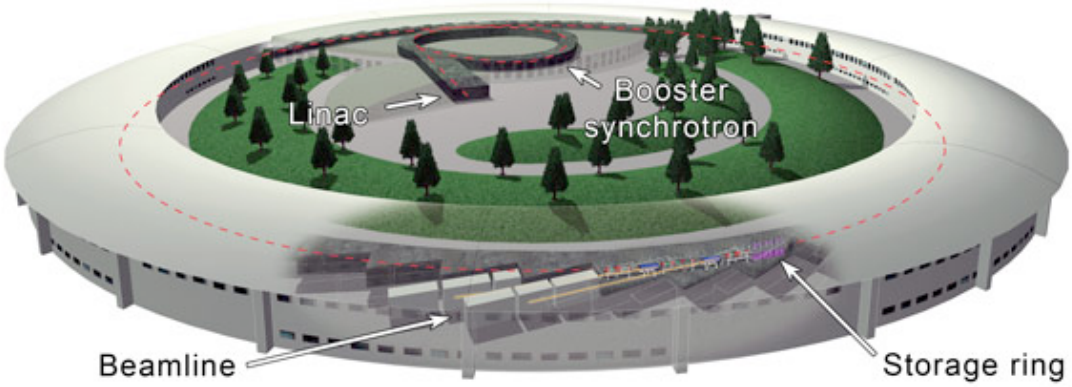

Figure 2.3. Principal structures of a synchrotron ring - here ESRF, Grenoble[14].

2.2.4.2. Instruments.

The European Synchrotron Radiation Facility (ESRF) in Grenoble, France is one of the largest 3rd generation synchrotron light sources. It can accelerate electrons up to 6 GeV and has a circumference of 844.4 m. In ESRF the electrons reach 0.9999999964 of the speed of light, so each electron travels around the storage ring in 2.82 μs, corresponding to a current of 5.688×10^{-14} A. The normal operating current in the ESRF is 200 mA[12]. Each beam of X-rays from the synchrotron source is

guided through a set of lenses and instruments called a beamline, where the X-rays illuminate and interact with samples of the material being studied. There are around 50 beamlines altogether in ESRF, each specialising in a different technique (Figure 2.4).

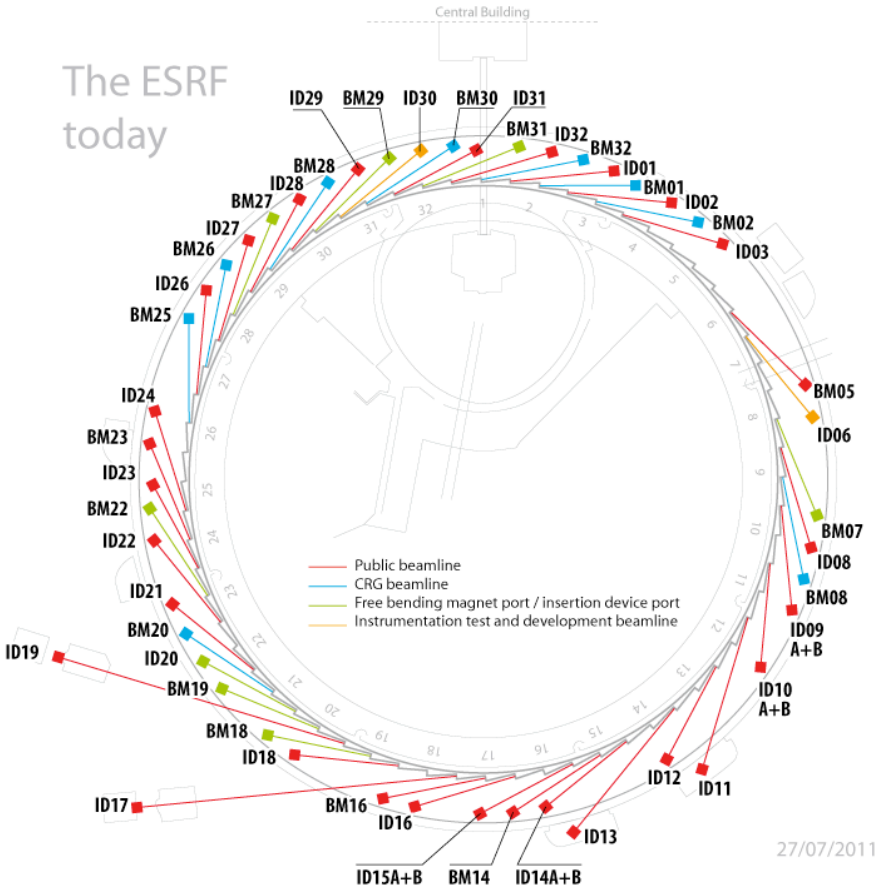

Figure 2.4. Beamline in ESRF, Grenoble[14].

2.2.4.3. Beamlines.

ID31 beamline in ESRF is used for high resolution powder diffraction. It is optimised for capillary samples and the wavelength is optimised for maximum intensity. The X-rays produced cover the entire range of energies from 5 keV to 60 keV (2.48 Å to 0.21 Å in wavelength). The beam monochromator is a double-crystal with Si 111 crystals. The beamline is equipped with nine Si 111 analyser crystals and detectors with channels separated by approximately 2° intervals (Figure 2.5 c). Powder samples are mounted in capillaries on the diffractometer axis with a high

speed capillary spinner (1200 rpm). For low temperature measurements, a low temperature liquid-He cryostat was used to cool samples down to 2 K and the usual capillary size used was 0.3 or 0.5 mm. In the case of low temperature measurements, the capillaries were not sealed but were left open at one end to provide easy flow of helium gas inside the capillary and a homogenous cooling process of the measured samples.

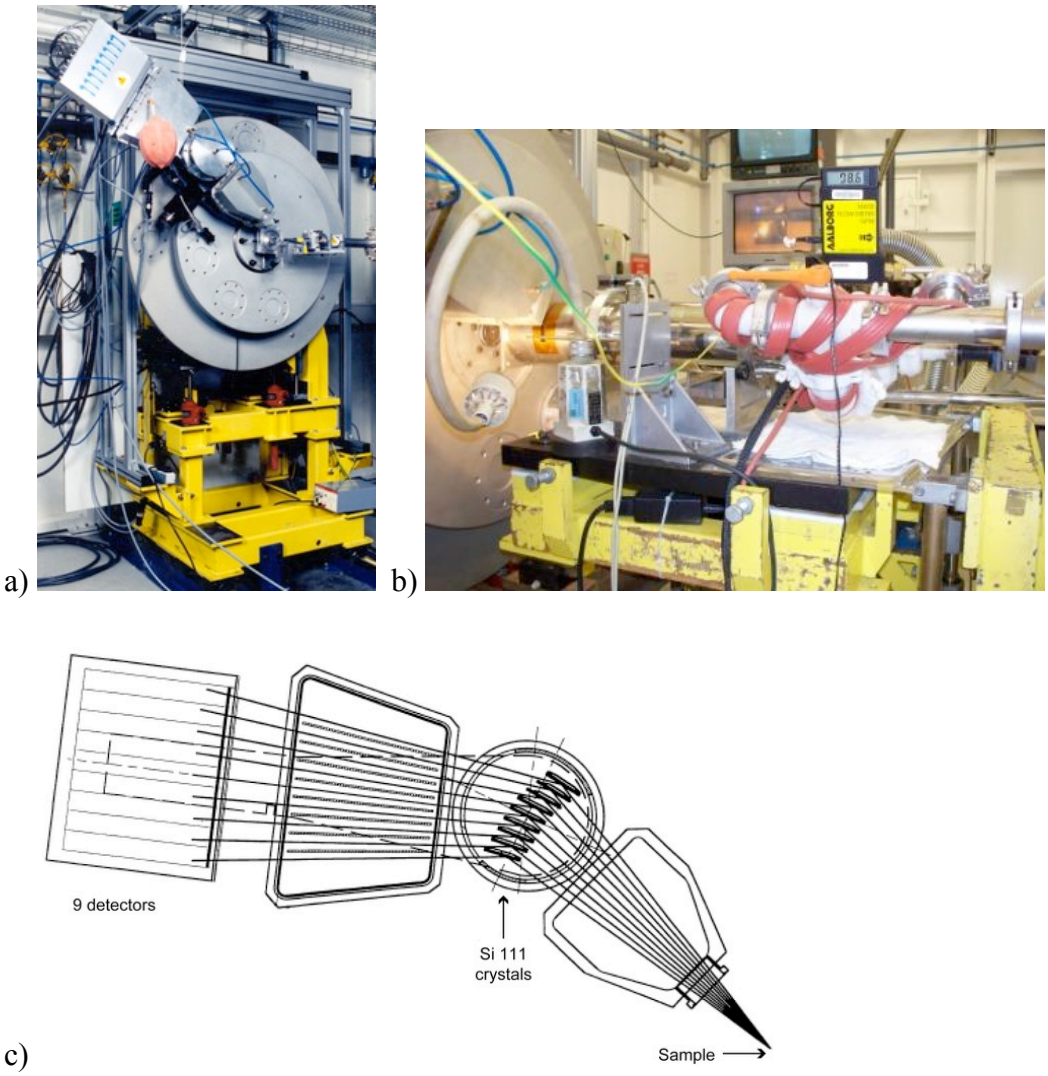

Figure 2.5. High resolution powder diffractometer at ID31 beamline[14] (a), the same diffractometer with cryostat mounted (b) and schematic diagram of multianalyser stage[15] (c).

2.2.5. Neutron diffraction.

2.2.5.1. Theory of neutron diffraction.

X-rays are useful in crystal structure determination because of their wavelength, which is on a similar scale to the distances between the atoms in measured molecules, or groups of atoms or ions. The X-ray scattering is done by electrons in atoms and depends strongly on the number of electrons contained within the atom. In other words, big atoms (like iron, arsenic or strontium) have a higher scattering power than lighter atoms, where the scattering power can be very small (oxygen, nitrogen or especially hydrogen).

The wavelength and momentum of a neutron is described by the de Broglie relationship:

$$\lambda = \frac{h}{p} = \frac{h}{mv}$$ Equation 2.11.

where:

p = the momentum of the particle

h = Planck's constant

m = mass of the neutron

v = velocity of the neutron.

Neutrons used in diffraction have a similar wavelength range to X-rays, so they can be diffracted by crystals[1,16]. Neutron radiation penetrates the materials quite well and its interactions with atoms are weak when compared to X-rays. The scattering is not dependent upon the density of the electron cloud, as the beam penetrates much deeper and is scattered by nuclei and magnetic moments. That is why the diffraction intensity is also much weaker than that seen with X-ray diffraction. The scattering involves the nuclei of atoms and the neutron beam, which means that the scattering power does not depend on the number of electrons anymore, but on properties of the

nucleus itself. There is no simple correlation between atomic number of an element and its scattering power (Figure 2.6).

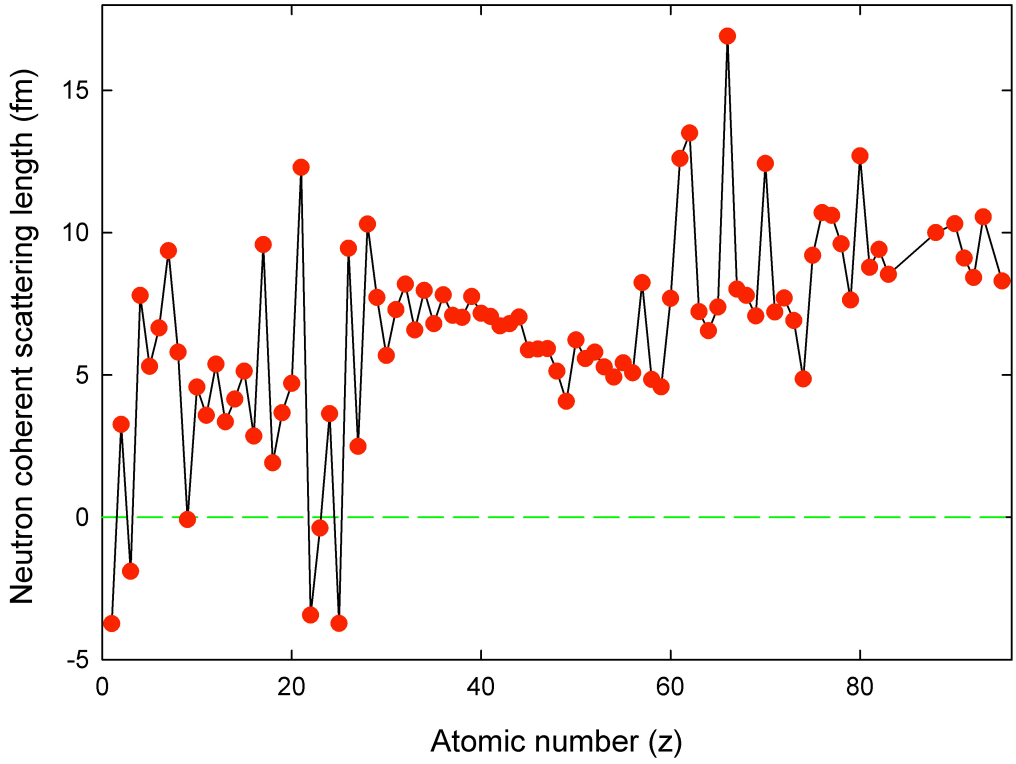

Figure 2.6. Variation of neutron scattering lengths with atomic number[17].

In the case of neutron diffraction, a very important property that can be measured is the identification of light elements, but also of different isotopes, as different isotopes of the same element have different scattering factors. In X-ray diffraction, light atoms are difficult to locate in the crystal structure precisely when in the presence of heavy atoms, so neutron diffraction is a much better technique for this. Another advantage of neutrons over X-rays is that scattering is by the nucleus, meaning that it locates the nucleus instead of the electron density[10,13]. Another important feature of neutron diffraction is its ability to distinguish between atoms with a similar atomic number, which can be very useful in determining the structure of complex materials with many similar atoms, and with possible mixed atom occupancies in the atom sites of a crystal structure.

Finally, the neutron beam can interact not only with the nucleus, but also with unpaired electrons in the sample. This interaction, called magnetic scattering, is due to magnetic dipole interaction between neutron magnetic moments and magnetic moments from the unpaired electrons. When the temperature falls below a certain value, magnetic moments will order themselves in the compound and that can emerge as new information in the collected neutron diffraction data. There are two possibilities of how that can be observed: when the magnetic reflections overlap with the nuclear ones, the collected data can show an increase of those particular peaks; otherwise new additional magnetic peaks may be seen below the ordering temperature[17].

2.2.5.2. Source of neutrons.

A neutron beam can be generated in two ways: either by spallation or by a nuclear reactor. Spallation produces pulsed beam of neutrons, which includes thermal and epithermal neutrons. During the process a heavy metal target is bombarded with a high energy beam of protons, releasing neutrons from the target core. The most common technique using spallation is time-of-flight[4]. In the nuclear reaction method of producing neutrons, fusion is still not a fully controllable technique, so nuclear fission is the most common way of generating neutron beams in nuclear reactors and is also a cheaper technique than spallation. In the nuclear reactor, fission traditionally takes place using uranium fuel[18]:

$$^{235}_{92}U + n \rightarrow nuclei + 200MeV + 2.5n \qquad \text{Equation 2.12.}$$

The produced neutrons have high energy, and are slowed down to thermal energies by passing through a moderator (usually graphite) where they collide with the moderator material until reaching a momentum of 5.2×10^{-24} $kgms^{-1}$. That corresponds to a wavelength of around 100 pm, which can be used for structure diffraction and is of a similar wavelength to X-rays[6]. This technique produces a steady-state source of neutrons with high flux and steady rate.

The Institut Laue-Langevin (ILL) in Grenoble, France is a research centre in which all neutrons are generated in its high flux nuclear reactor. It produces the most

intense continuous neutron flux in the world in the moderator region: 1.5×10^{15} neutrons $s^{-1}cm^{-2}$, with a thermal power of 58.3 MW[19].

2.2.5.3. *Instruments.*

All neutron diffraction experiments mentioned in this thesis were conducted on two of ILL instruments: D2B and D20 (Figure 2.7.).

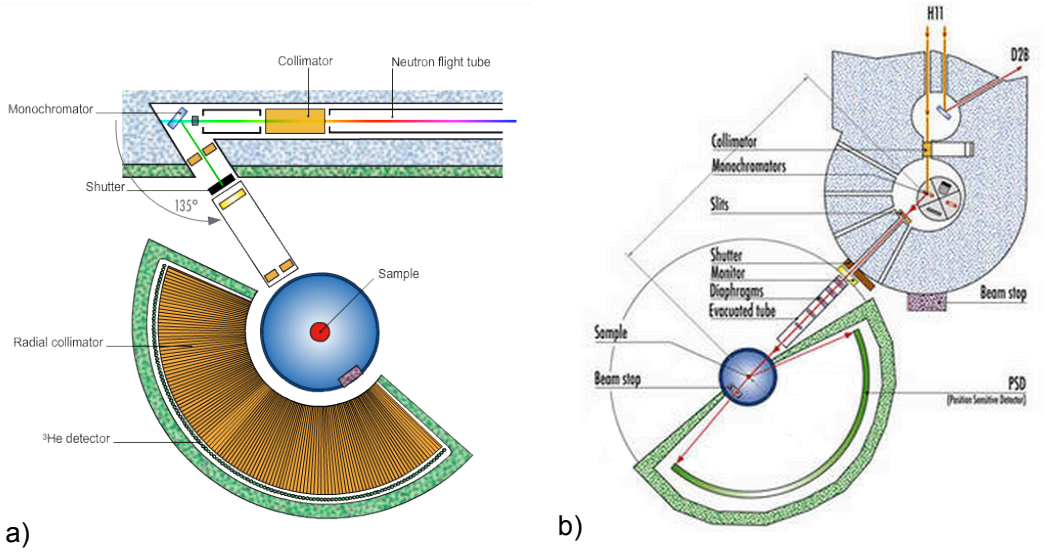

Figure 2.7. Instrument layout for a) D2B[20] and b) D20[21].

D2B is a powder diffractometer with very high resolution and a built-in high flux option. The resolution of this diffractometer is limited only by the powder particle size. D2B has a germanium monochromator with a large take-off angle of 135°. The monochromator is 300 mm high and it focuses vertically onto about 50 mm. The diffractometer is equipped with 128 ^{3}He 200 mm high detectors and collimators. It covers 160° in 2θ, so to achieve the full diffraction pattern it needs 25 steps of 0.05° in 2θ as the 128 detectors are spaced at 1.25° intervals. D2B can measure crystals with very large *d*-spacings as it can change the wavelengths between 1.05 Å and 6 Å. The samples measured for the purpose of this thesis were sealed in vanadium cylindrical cans, and a cryostat was used to cool them to 1.5 K.

D20 is a high intensity two-axis diffractometer with extremely high neutron flux, and it has a variable resolution. It is equipped with four monochromators: two copper, one germanium and one Highly Oriented Pyrolytic Graphite (HOPG) (002).

They provide wavelengths in a region between 0.82 Å and 2.41 Å. The variable take-off angles (up to 120°) of the monochromators make the diffractometer even more flexible. The position sensitive detector is filled with a mixture of ^3He and CH_4 and covers 153.6° in 2θ. The resolution is slightly lower than on D2B, but D20 has the fastest counting rate and can measure smaller volumes of samples. All samples measured on D20 were using the same vanadium cans as in the case of D2B and a cryostat was used to cool them down to 1.7 K.

2.2.6. Data analysis and treatment.

2.2.6.1. The Rietveld method.

In order to analyse the data from powder diffraction, the Rietveld method is used to refine the crystal structure. It is the most widely used method for powder diffraction. The Rietveld method is based on optimising the degree of fit between the calculated and observed powder diffraction pattern using least-squares refinement. The method was developed by Hugo Rietveld in 1969[22]. This is the most widely used method for powder diffraction data analysis. The function minimised in the least-squares refinement, M, is based on a difference between the observed diffraction pattern intensity (y^{obs}) and calculated data (y^{calc}):

$$M = \sum_i W_i \left(y_i^{obs} - \frac{1}{c} y_i^{calc} \right)^2$$

Equation 2.13.

W_i is a least-squares weight factor and c is an overall scale factor. The method does not allocate any of the observed intensities to particular Bragg reflections, and is not sensitive for overlapping of reflections as in other methods. In order to overcome the aforementioned problems this method needs a reasonably good model of the structure as a starting point, which will then be refined to match the experimental data. In other words, it is not a structure solution method but a structure refinement method[23].

In powder diffraction, many crystallites can diffract at a certain point, and all Bragg reflections contribute to the observed intensity in the particular point of the

diffraction pattern. The other contribution to the intensities comes from the background, so the observed intensity equation is:

$$y_i^{obs} = \sum_i y_i^{Bragg} + y_i^{background}$$

Equation 2.14.

The calculated intensities are determined from the model of the structure given as a starting point. During the refinement process there are a number of factors that can be varied in order to achieve the best fit, and consequently the best structure analysis for the given diffraction data. These factors can be divided into two groups:

a) Structural parameters, which can be unit cell dimensions, fractional coordinates, isotropic or anisotropic temperature factors, or site occupancies.

b) Profile parameters, which include diffractometer parameters, background, peak asymmetry or half-width parameters.

2.2.6.2. Peak shape.

The first usage of the Rietveld method was for neutron powder diffraction, because most neutron diffraction profiles can be described using the symmetric Gaussian function. The lower resolution of neutron diffractometers compared to X-rays and contributions from the instrument itself influence the width and shape of peak lines[24]. The peak shape function used in constant wavelength neutron experiments can be described using an almost fully Gaussian function[25], which is here additionally modified for peak asymmetry, A_s:

$$H(\Delta T) = N\left(1 - \frac{\Delta T' |\Delta T| A_s}{\tan\theta}\right)\exp\frac{-\Delta T'^2}{2\sigma^2}$$

Equation 2.15.

where: N is the normalization factor, ΔT is the difference between the reflection position and the profile point, $\Delta T'$ is the modified 2θ difference and σ^2 is the variance of the peak. This varies with 2θ, and can be described as:

$$\sigma^2 = U\tan^2\theta + V\tan^2\theta + W + \frac{F}{\tan^4\theta}$$ Equation 2.16.

The expression $U\tan^2\theta + V\tan^2\theta + W$ is also known as the Full Width at Half Maximum (FWHM) of the Gaussian function. All profile coefficients (U, V, W, F and A_s) are refinable parameters in the Rietveld method to achieve the best fit of the Gaussian function to the profile data.

In the case of X-rays, which have a much better resolution, more detail observation of individual contributions to the line shape can be done. Therefore, there was a need to develop better functions to describe the shape of diffraction lines. The function widely used and considered to be the best at the moment for constant wavelength X-ray diffraction is the pseudo-Voigt function, $F(\Delta T')$[24,26,27].

$$F(\Delta T') = \eta L(\Delta T', \Gamma) + (1-\eta)G(\Delta T', \Gamma)$$ Equation 2.17.

The pseudo-Voigt function was developed by Thompson, Cox and Hastings[28] and uses a weighted sum of both Gaussian (G) and Lorentzian (L) functions. The mixing factor, η, is a function of the Gaussian FWHM's σ^2 and the Lorentzian coefficient, γ, the formulae of which are shown below:

$$\sigma^2 = U\tan^2\theta + V\tan^2\theta + W + \frac{P}{\cos^2\theta}$$ Equation 2.18.

$$\gamma = X\tan\theta + \frac{Y}{\cos\theta}$$ Equation 2.19.

In these equations P is the Scherrer coefficient for Gaussian broadening, and X and Y are the Lorentzian Scherrer broadening and strain broadening respectively. All of these parameters are refinable in the Rietveld method to give the best peak shape. The mixing parameter depends on the width of both Gaussian and Lorentzian functions and appropriate fractions of each are used ($\eta = 0$ for fully Gaussian and $\eta = 1$ for fully Lorentzian contribution). The pseudo-Voigt function gives a much better fit when using X-ray data or any other asymmetric profile data.

2.2.6.3. *Background intensity.*

There are three ways for obtaining the background intensity:

- a specific background function,

- a table of background intensities which the user provides,

- user-selected points in the diffraction pattern and a linear interpolation between them.

Regardless of which method is used, it should always be refined (unless there are some specific reasons not to) together with the structural and profile parameters.

2.2.6.4. *Indicators of fit.*

As the main objective of the Rietveld method is to refine the parameters in order to minimise the M function (as defined in equation 2.13), there are numerical methods to check the agreement between the observed and calculated profiles, referred to as R-factors. One of the most regarded R-factors is the one that reflects the M function being minimised:

$$R_{wp} = \sqrt{\frac{\sum_i W_i \left(y_i^{obs} - y_i^{calc}\right)^2}{\sum_i W_i \left(y_i^{obs}\right)^2}} \qquad \text{Equation 2.20.}$$

Other R-factors that are closer to single-crystal diffraction refinements are the R-Bragg (R_B) and R-structure factor (R_F). Both are based on the intensities (I^{obs} and I^{calc}) assigned to Braggs reflections, deduced with the use of the given model:

$$R_B = \frac{\sum_k \left| I_k^{obs} - I_k^{calc} \right|}{\sum_k I_k^{obs}} \qquad \text{Equation 2.21.}$$

$$R_F = \frac{\sum_k \left| \sqrt{I_k^{obs}} - \sqrt{I_k^{calc}} \right|}{\sum_k \sqrt{I_k^{obs}}}$$ Equation 2.22.

2.2.6.5. GSAS computer programme package.

All powder diffraction data treatment and analysis presented in this thesis was done using the General Structure Analysis System (GSAS) package[25]. GSAS is a set of computer programmes written in Fortran, which is designed to handle a specific task or calculation. It was developed to use on both PC with Microsoft Windows and Linux based operating systems. The version used was equipped with a graphical user interface, EXPGUI[29]. GSAS can handle powder diffraction refinements for multiple phases present in the measured samples, and also can perform combined refinements of X-ray and neutron diffraction data.

2.3. Magnetic measurements and SQUID.

All materials respond, in one way or another, to an applied external magnetic field. There are five main types of magnetism: diamagnetism, paramagnetism, ferromagnetism, antiferromagnetism and ferrimagnetism. Apart from diamagnetism, which is due to paired electrons in closed shells, all other types are an effect of unpaired electrons. Diamagnetism is a much weaker form of magnetism than the other types mentioned, and all materials are diamagnetic. In the presence of a magnetic field, diamagnetism acts to oppose the external magnetic field and is antiparallel to it. Materials that exhibit the other forms of magnetism are considered as magnetic materials. In magnetic materials, the magnetic moments align differently to the applied external magnetic field according to their type of magnetism, as illustrated in Figure 2.8:

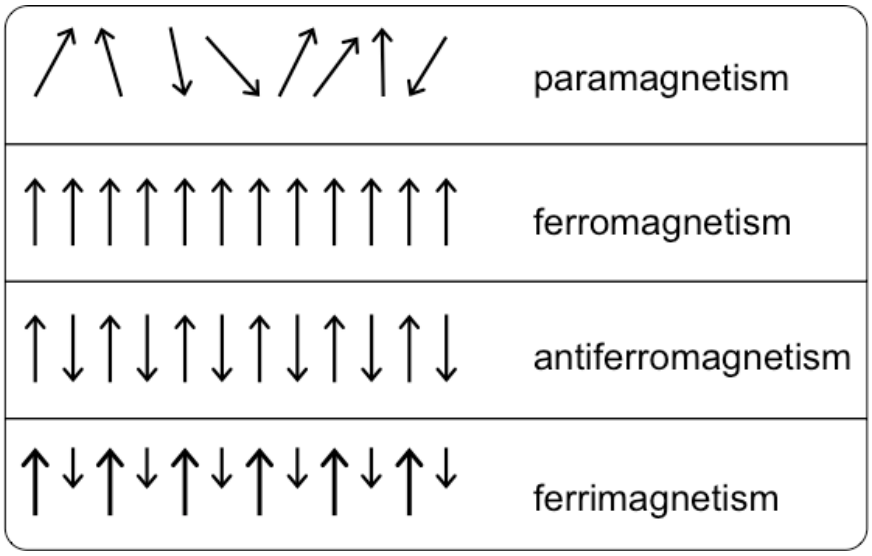

Figure 2.8. Schematic diagram of the arrangement of magnetic moments in different types of magnetism[30].

In paramagnetism the magnetic moments have a random arrangement. In both ferromagnetism and antiferromagnetism, the electron arrangement is ordered; all magnetic moments are parallel in ferromagnetism and antiparallel in antiferromagnetism. Finally, ferrimagnetism is when the magnetic moments are arranged antiparallelly to one another and also of a different magnitude[30].

The density of a magnetic field is known as the magnetic flux density (B). In a vacuum it is proportional to the magnetic field (H) by the magnitude of permeability of free space, μ_0:

$$B = \mu_0 H$$

Equation 2.23.

The magnetic flux density can change when a magnetic material is placed in the magnetic field. If a material is diamagnetic B will decrease, and if the material is paramagnetic then B will increase. In that case, the expression for B is given as:

$$B = \mu_0 (H + M)$$

Equation 2.24.

M is magnetisation (magnetic moment per unit of volume) and is usually discussed in terms of the magnetic susceptibility, χ, which is a dimensionless value:

$$\chi = \frac{M}{H}$$ Equation 2.25.

When dealing with magnetism in samples with a molar volume, V_m, molar magnetic susceptibility is often used:

$$\chi_m = \frac{\chi}{V_m}$$ Equation 2.26.

In solids, which contain metals with isolated unpaired electrons, magnetic moments, μ, are important, and are used to describe the molar magnetic susceptibility as follows:

$$\chi_m = \frac{N_A \mu_0}{3kT} \mu^2$$ Equation 2.27.

Where N_A is Avogadro's number, k_B is Boltzmann's constant and T is the temperature in Kelvin.

Finally, magnetism in samples can also be discussed in terms of the effective magnetic moment, μ_{eff}:

$$\mu_{eff} = 2.828\sqrt{\chi_m T}$$ Equation 2.28.

The number 2.828 is a consequence of fundamental constants in the cgs (centimetre-gram-second) unit system used and allows the μ_{eff} to be expressed in the unit of Bohr magnetons (μ_B).

In paramagnetic materials the interplay between unpaired electrons on different atoms and the randomizing effect of thermal energy can lead to temperature dependence. This temperature dependence is described by the Curie law:

$$\chi = \frac{C}{T}$$ Equation 2.29.

where C is the Curie constant given by:

$$C = \frac{N\mu_B^2\mu_{eff}^2}{3k}$$ Equation 2.30.

and temperature (T) is expressed in Kelvin. If there is a cooperative behaviour between those unpaired electrons, a change in temperature dependence can be seen, and that changeover is associated with characteristic temperatures[2,6,30], for ferromagnetism, the characteristic temperature is the Curie temperature, T_C, and for antiferromagnetism, this is the Néel temperature, T_N. The temperature dependences of magnetic susceptibility in paramagnetic, ferromagnetic and antiferromagnetic materials are illustrated in Figure 2.9.

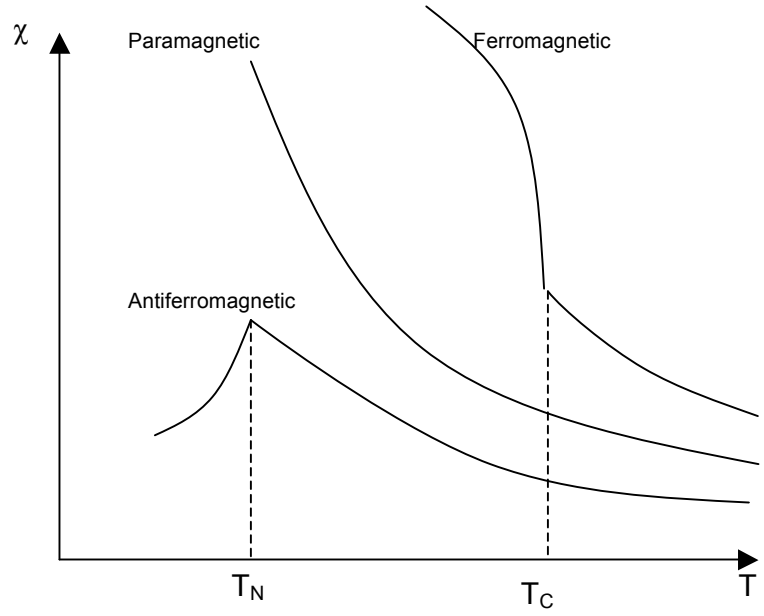

Figure 2.9. Variation of magnetic susceptibility (χ) with temperature (T).

In these cases, the behaviour in high temperature is best described by the Curie-Weiss law:

$$\chi = \frac{C}{T - \theta}$$ Equation 2.31.

θ is the Weiss constant, which is determined by an extrapolation to zero of the paramagnetic regime of the inverse susceptibility plot versus temperature. If by such extrapolation $\theta = 0$, this indicates a simple paramagnetic material. A positive value

of θ indicates ferromagnetism, and $\theta < 0$ indicates antiferromagnetism (Figure 2.10). In an ideal case the Weiss constant is equal to the Curie temperature, $\theta = T_C$, for ferromagnetism and for antiferromagnetism the Weiss constant is equal to the Néel temperature, $\theta = -T_N$.

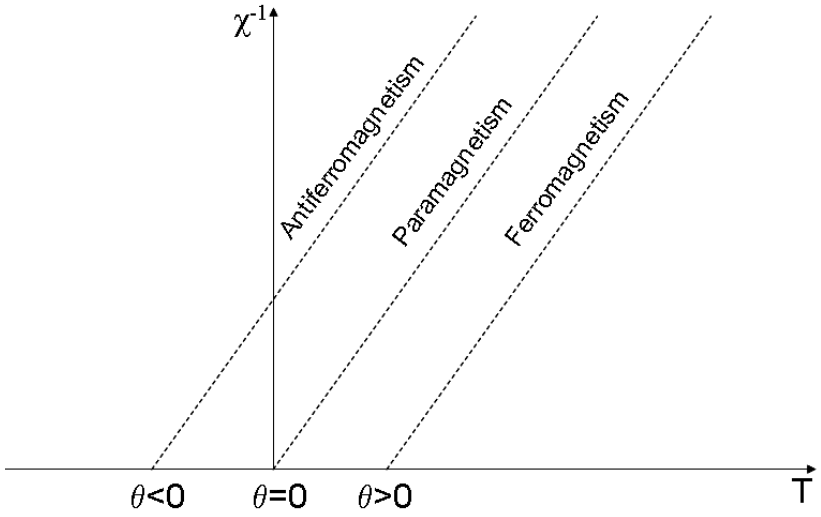

Figure 2.10. Graphical illustration of the Curie-Weiss law.

In order to measure bulk magnetic properties of all the samples presented in this thesis a magnetometer - the Quantum Design Magnetic Properties Measurement System (MPMS) was used. This contained a Superconducting Quantum Interference Device (SQUID). A SQUID is a very sensitive device that measures the sample's magnetisation up to 10^{-8} emu. It does not detect the magnetic field from the sample, but uses superconducting loops containing Josephson junctions to measure how much the sample changes the magnetic flux[31].

In a SQUID magnetometer, the sample is passed in discrete steps through superconducting detecting coils that act like very sensitive quantum interferometer. If a sample is magnetic it will interfere with the magnetic flux through the superconducting sensing ring. That would induce a supercurrent, which by changing the flux in the SQUID produces an output signal, recorded as a sample position. A computer programme analyses the response curve to derive a corresponding magnetic moment. The values of molar magnetic susceptibility can then be measured

using values of magnetisation per mass, m, molecular weight (M_w) and applied magnetic field (H):

$$\chi_m = \frac{m}{M_w H}$$ Equation 2.32.

SQUID can be used in two modes: DC and AC. Direct-current (DC) magnetometry, in which a constant magnetic field is used to magnetize the sample, establishes the equilibrium value of the magnetization in a sample. The two main measurements used to characterize magnetic samples are magnetisation as a function of temperature, *M(T)*, and magnetisation as a function of applied magnetic field, *M(H)*. In alternating-current (AC) magnetic measurements, the sample moment is time dependent and therefore it provides information about the dynamics of the magnetisation.

2.3.1. Magnetism in metals.

The previous section concentrated on magnetism with localised magnetic moments, which have specific distances between each other. Metals, however, have delocalised electrons, which can move freely across the material. These itinerant electrons are either spin-up or spin-down and when a magnetic field is applied their energy will be either lowered or raised, depending on their spin. This paramagnetic susceptibility is called Pauli paramagnetism. When describing magnetism in metals it is useful to introduce the Fermi surface. In *k*-space, the set of points with energy equal to the chemical potential is called the Fermi surface and the Fermi energy, E_F, is defined as

$$E_F = \frac{\hbar^2 k_F^2}{2m_e}$$ Equation 2.33.

where k_F is the Fermi wave vector and m_e is the electron mass. A lot of important properties of materials depend on the density of states at the Fermi level, which can be obtained as

$$g(E_F) = \frac{m_e k_F}{(\pi\hbar)^2}$$ Equation 2.34.

which shows that it is proportional to electron's mass[27].

Under certain conditions a spontaneous ferromagnetism can occur in metals. It happens when electrons from one spin band move to another and change their spins. It is not a favourable process from the point of view of energy, but in some materials this may be outweighed by useful benefits from the interaction of the magnetisation with the molecular field. This spontaneous ferromagnetism is possible if the density of states at the Fermi level is large. When it occurs, a strong Coulomb interaction is present and the electron gas is unstable against it.

These interactions between electrons can lead to the spontaneous development of an oscillatory static magnetisation in the material. Depending on the wavevector of such magnetisation, a ferromagnetic or antiferromagnetic order could develop. In the particular case of the wavevector being equal to $2k_F$, a deformation of electron energy opens up an energy gap and leads to an instability called the spin-density wave. Such instability lowers the total energy of the system. It can be measured by various methods; in this work it was detected by temperature dependent resistivity measurements.

2.4. Electrical resistivity measurements using a PPMS.

In order to measure the electrical resistivity a four-probe technique was used with a Physical Property Measurement System (PPMS). In the four-probe method, a small polycrystalline bar of the sample was used and four wires (copper or gold) were connected to it. Two of the wires were current contacts, connected at the ends of the bar, and two were voltage contacts, connected at the centre of the bar. The wires were usually attached using silver epoxy, which is very conductive adhesive, although in some cases graphite paste or golden plating of the bar was used when the silver epoxy caused the sample to disintegrate. The measurements were done by running a constant current through the sample and measuring the drop of potential in the middle two voltage wires (Figure 2.11).

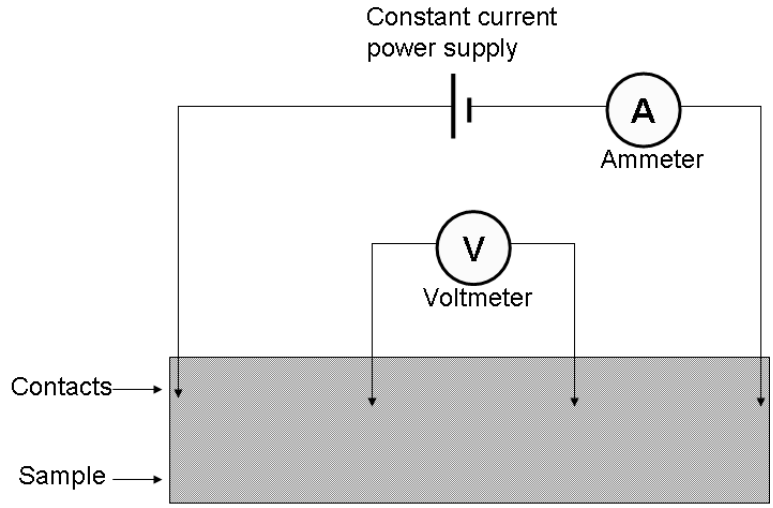

Figure 2.11. Schematic diagram of the four-probe method.

The resistivity of the sample, ρ, can be calculated from the measured resistance, R:

$$\rho = \frac{RA}{l}$$ Equation 2.35.

where A is the area of the measured bar of the sample in cm^2, resistance, R, is measured in Ω and l is the distance between the two inner voltage wires in cm. All resistivity measurements presented in this thesis were collected while varying the temperature between 2 K and 300 K, both on cooling and heating to confirm no temperature hysteresis.

2.5. Bibliography.

1. Clegg, W. *Crystal Structure Determination*; Oxford University Press, Incorporated, **1998**.
2. Smart, L. E.; Moore, E. A. *Solid State Chemistry: An Introduction, Third Edition*; Taylor & Francis, **2005**.
3. Shmueli, U. Theories and Techniques of Crystal Structure Determination; OUP Oxford, **2007**.
4. Giacovazzo, C. *Fundamentals of Crystallography*; Oxford University Press, Incorporated, **2002**.
5. Ashcroft, N. W.; Mermin, N. D. *Solid state physics*; Saunders College, **1976**.
6. Atkins, P. W. *Physical chemistry.* ; Oxford University Press, **1994**.
7. Dinnebier, R. E.; Billinge, S. J. L. *Powder Diffraction: Theory and Practice*; Royal Society of Chemistry, **2008**.
8. Hammond, C. The Basics of Crystallography and Diffraction; OUP Oxford, **2009**.
9. Klein, C.; Hurlbut, C. S. *Manual of Mineralogy (after James D. Dana)*; Wiley, **1999**.
10. Baruchel, J. Neutron and synchrotron radiation for condensed matter studies: Applications to solid state physics and chemistry; Springer-Verlag, **1994**.
11. Cullity, B. D. *Elements of X Ray Diffraction*; BiblioBazaar, **2011**.
12. Bish, D. L.; Post, J. E. *Modern powder diffraction*; Mineralogical Society of America, **1989**.
13. Baianu, I. C., Advanced Techniques and Applications: X-ray and Neutron Diffraction, **2010**.
14. in *http://www.esrf.eu*, 16/02/2013.
15. Hodeau, J.-L.; Bordet, P.; Anne, M.; Prat, A.; Fitch, A. N.; Dooryhee, E.; Vaughan, G.; Freund, A. K., *Proc. SPIE 3448, Crystal and Multilayer Optics* 353, **1998**.
16. Rosenberg, H. M. The Solid State: An Introduction to the Physics of Solid; Oxford University Press, **1995**.
17. Chatterji, T. *Neutron Scattering from Magnetic Materials*; Elsevier Science, 2005.

18. Choppin, G. R.; Liljenzin, J. O.; Rydberg, J. *Radiochemistry and nuclear chemistry [electronic resource]*; Butterworth-Heinemann, **2002**.
19. in http://www.ill.eu/reactor-environment-safety/high-flux-reactor/technical-characteristics/, 05/04/2013.
20. in http://www.ill.eu/fr/instruments-support/instruments-groups/instruments/d2b/fonctionnement/simulated-experiment/ 10/03/2014.
21. in http://www.ill.eu/fr/instruments-support/instruments-groups/instruments/d20/description/instrument-layout/ 10/03/2014.
22. Rietveld, H. Journal of Applied Crystallography **1969**, 2, 65.
23. Young, R. A. *The Rietveld Method*; Oxford University Press on Demand, **1995**.
24. Young, R. A.; Wiles, D. B. *Journal of Applied Crystallography* **1982**, *15*, 430.
25. Larson, A. C.; Von Dreele, R. B., *General Structure Analysis System (GSAS)*,**1994**.
26. Kaduk, J. *Acta Crystallographica* Section A **1994**, 50, 259.
27. Von Dreele, R. B.; Jorgensen, J. D.; Windsor, C. G. *Journal of Applied Crystallography* **1982**, *15*, 581.
28. Thompson, P.; Cox, D. E.; Hastings, J. B. *Journal of Applied Crystallography* **1987**, *20*, 79.
29. Toby, B. H., EXPGUI, a graphical user interface for GSAS, **2001**.
30. Blundell, S., *Magnetism in Condensed Matter*, Oxford Master Series in Physics, **2001**.
31. McElfresh, M., Fundamentals of Magnetism and Magnetic Measurements, Quantum Design, Inc., **1994**.

Chapter 3

Synthesis and characterisation of hole doped rare-earth iron oxyarsenides

$Nd_{1-x}Sr_xFeAsO$ ($0 < x \leq 0.2$).

3.1. Introduction.

For a long time, the most famous and well studied high-T_c superconductors were layered copper oxides. Recently there have been extensive studies carried out to discover other types of superconductors. Special interest was taken in 3d and 4d transition metals due to the possibility of strong electronic correlation effects, which could enhance the value of T_c[1]. At the beginning of 2008 a new family of superconductors was reported, generating much excitement in the materials chemistry community[2]. In March 2008 Kamihara[3] announced a discovery of non–cuprate high-T_c superconductors, namely the family of quaternary oxyarsenides $La(O_{1-x}F_x)FeAs$. This was quite surprising, as the presence of Fe should lead to long-range magnetic order, which suppresses superconductivity. The parent compound, LaFeAsO, is not superconducting, but shows anomalies at around 150 K in both resistivity and magnetic susceptibility measurements. These have been explained in terms of a spin–density–wave (SDW) magnetic instability.

Since these discoveries, there has been extensive research on the family of rare–earth quaternary oxypnictides with general formula REFeAsO (RE = La, Sm, Ce, Nd, Pr, Gd, Tb, Dy)[4,5,6,7,8] and T_c reached the value of 55 K for electron doped SmFeAsO[9], being surpassed only by the high-T_c cuprates. All these materials adopt the tetragonal ZrCuSiAs structural type with the space group *P4/nmm* (Figure 3.1). On cooling, the parent compounds display a structural phase transition to orthorhombic crystal symmetry (space group *Cmma*), which is accompanied by the development of a long-range SDW–type antiferromagnetic order observed at temperatures around 150 K. With doping, the parent compound's antiferromagnetic

ordering is surpassed and the superconductivity occurs with the sample showing a metallic behaviour down to the transition temperature.

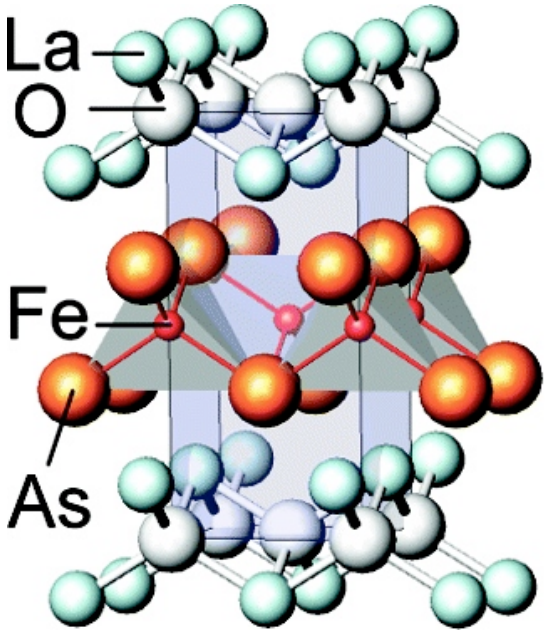

Figure 3.1. Schematic diagram of the room temperature tetragonal structure of the first discovered rare–earth quaternary oxypnictide – LaFeAsO[3].

Recently there have been reports about synthesizing new types of superconductors, which have remarkably similar properties to LaFeAsO. These new materials are AFe_2As_2 (where A = K, Cs, Sr, Ba, Eu)[10,11,12,13,14]. Both LaFeAsO and $BaFe_2As_2$, for example, behave as poor metals and show only weak magnetism. These new compounds show T_c at 3.6 K for KFe_2As_2 and 2.8 K for $CsFe_2As_2$, but after doping them with Sr^{2+} the T_c increases up to 37 K (for doping at level 50 – 60% of Sr^{2+})[12].

In this chapter the structural, electronic and magnetic properties of the family of hole doped quaternary oxyarsenides $Nd_{1-x}Sr_xFeAsO$ is shown. Confirming the existence of superconducting phases, probing how T_c varies with composition, and revealing the influence of doping on the structural and magnetic transitions are of fundamental importance for the understanding of the pairing mechanism in these superconductors.

3.2. Electron and hole doping in REFeAsO.

Partial substitution of O^{2-} with F^- in LaFeAsO leads to the occurrence of superconductivity with a maximum T_c of 26 K. The substitution of O^{2-} with F^- introduces extra electrons to the materials, which are therefore called "electron doped" systems. At the beginning it was claimed that while doping with electrons leads to superconductivity, hole doping does not. Wen later proved otherwise, showing that by substituting La^{3+} with Sr^{2+}, superconductivity can be obtained with the highest transition temperature in this family, of around 25 K[15].

Electron doping of the parent compounds REFeAsO (*e.g.* partial replacement of O^{2-} by F^- or oxygen deficiency) provides extra charge in the conduction plane, suppresses the structural/magnetic instability, and triggers the occurrence of superconductivity.

Theoretical calculations show that LaFeAsO is metallic (electron carriers) at the verge of a transition between a bad metal and a semiconductor, and that the Fermi energy, E_F, is located at the edge of a peak and in a pseudogap region of the density of states (DOS), making the electronic structure strongly electron-hole asymmetric[16,17,18]. The Fermi surfaces of REFeAsO parent compounds are characterized by both electron and hole cylinders. For electron doping the hole cylinders disappear and the electron tubes gradually increase in volume. However, upon hole doping the electron tubes start to decrease in size as the volume of the hole cylinders enlarges.

Hole doping has also been an extremely successful route for the preparation of high-T_c superconductors in the AFe_2As_2 families. However, the issue of whether hole doping in REFeAsO systems produces superconducting compositions is still open. There has been an early report on the substitution of La^{3+} by Ca^{2+} in LaFeAsO that does not induce superconductivity. Subsequent work on Sr^{2+} doping to produce the family of $La_{1-x}Sr_xFeAsO$[15] demonstrated that superconducting phases can be achieved at doping levels $x > 0.08$ and that the evolution of T_c shows a symmetric response to that on the electron doped side. Positive Hall coefficients confirmed that the conduction is through hole charge

carriers[19]. However, these results were not reproduced by other authors[20]. It follows that it is essential to establish the role played by alkaline-earth-doping on the structural, electronic and magnetic behaviour of REFeAsO systems. Confirming the existence of superconducting phases, probing how T_c varies with composition, and revealing the influence of doping on the structural and magnetic transitions are of fundamental importance for the understanding of the pairing mechanism in these high-T_c superconductors.

3.3. Experimental work.

Powder samples of $Nd_{1-x}Sr_xFeAsO$ (where x = 0.05, 0.1, 0.2) were prepared in two-step solid state synthetic procedures according to the reaction below.

$$(1-x)NdAs + xSrO + \frac{1-x}{3}Fe + xFeAs + \frac{1-x}{3}Fe_2O_3 = Nd_{1-x}Sr_xFeAsO$$

Equation 3.1.

In the first step, NdAs and FeAs were prepared. NdAs was prepared by grinding together pure Nd and As pieces and then heating them in evacuated quartz tubes at 500°C for 2 hours (heating rate 250°C/hour), 900°C for 16 hours and then allowing them to cool down slowly. The powder was then reground and heated again at 900°C for 16 hours.

FeAs was made from Fe powder and As pieces ground together, sealed in quartz tubes under vacuum and heated at 500°C for 2 hours (heating rate 250°C/hour), 700°C for 16 hours and cooled to room temperature. After that the powder was reground and heated again for 16 hours at 700°C. The second step was preparing $Nd_{1-x}Sr_xFeAsO$ samples by solid state reaction using stoichiometric amounts of high purity Fe, Fe_2O_3 and SrO (degassed under vacuum at 200°C for 10 hours to remove any traces of moisture) and prepared FeAs and NdAs. All powders were mixed and ground together in an agate mortar and pressed into 10 mm round pellets. The pellets were sealed in evacuated quartz tubes and heated for 48 hours at 1100°C (heating rate 200°C/hour). All the synthesis, except for preparing FeAs, was carried out in a glove box with high pure argon atmosphere due to air-sensitivity of some of the

starting materials (Nd and SrO). The final compounds are stable in air but were found to gradually deteriorate (regardless of the atmosphere) after two months. Increasing doping level of Sr^{2+} above 0.2 results in samples containing secondary phases and it is chemically impossible to produce compounds of satisfactory quality for performing measurements. The masses of reactants used for this synthesis are detailed in Table 3.1.

Table 3.1. Masses of starting materials used to prepare different compositions of $Nd_{1-x}Sr_xFeAsO$.

X (Doping level of Sr^{2+})	Mass of a pellet [g]	Mass of NdAs [g]	Mass of SrO [g]	Mass of Fe [g]	Mass of FeAs [g]	Mass of Fe2O3 [g]
0.05	0.300	0.217	0.005	0.018	0.007	0.053
0.1	0.300	0.207	0.011	0.018	0.014	0.050
0.2	0.300	0.188	0.022	0.016	0.028	0.046

The magnetic properties were measured using a Quantum Design Magnetic Property Measurement System magnetometer following zero field cooled/field cooled (ZFC/FC) protocols at 20 Oe and 10 kOe. The temperature dependence of the electrical resistivity was measured by the four-probe method upon heating between 2 and 300 K. Synchrotron X-ray powder diffraction (XRPD) data were collected on beamline ID31 at the European Synchrotron Radiation Facility (ESRF), Grenoble, France. Diffraction profile analyses were performed using the GSAS suite of Rietveld analysis programs.

3.4. Results.

3.4.1. Structural properties.

Firstly, powder X-ray diffraction measurements on a laboratory D8 Bruker diffractometer were performed on all compositions to check the sample quality. Room temperature diffraction profiles were collected on the three compositions,

revealing that the materials were all highly crystalline (very sharp peaks), with no impurity phases.

The high quality of the produced samples was a motivation to further investigate their structural properties using synchrotron X-ray powder diffraction. High resolution X-ray powder diffraction measurements were collected using a wavelength of 0.4030068 Å. The synchrotron data on powders sealed in 0.5 mm diameter silica capillaries were collected at various temperatures between 5 K and 295 K.

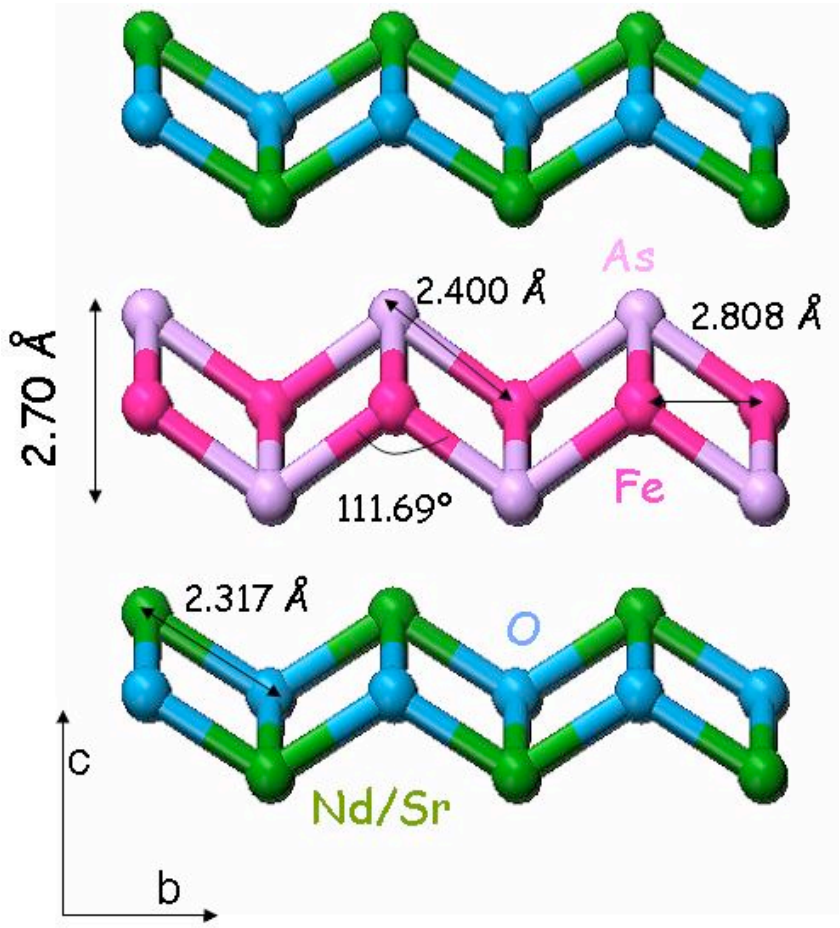

Figure 3.2. Schematic diagram of the room temperature tetragonal structure of the $Nd_{1-x}Sr_xFeAsO$ system.

Rietveld analysis of the room temperature (RT) high statistic diffraction profiles confirmed the successful substitution of Sr^{2+} at the Nd^{3+} sites with the occupancies

refining to 0.052(6), 0.091(6) and 0.21(1) for nominal compositions x = 0.05, 0.1 and 0.2 respectively. Diffraction profiles collected at room temperature show that all members of the series adopt tetragonal *P4/nnm* structures (Figure 3.2). The Rietveld refinements of members of the family at room temperature are shown below (Figures 3.3 to 3.5). Refined structural parameters for $Nd_{1-x}Sr_xFeAsO$ with x = 0.05, 0.1 and 0.2 obtained from Rietveld refinements of the synchrotron X-ray diffraction data at room temperature are shown in Table 3.2.

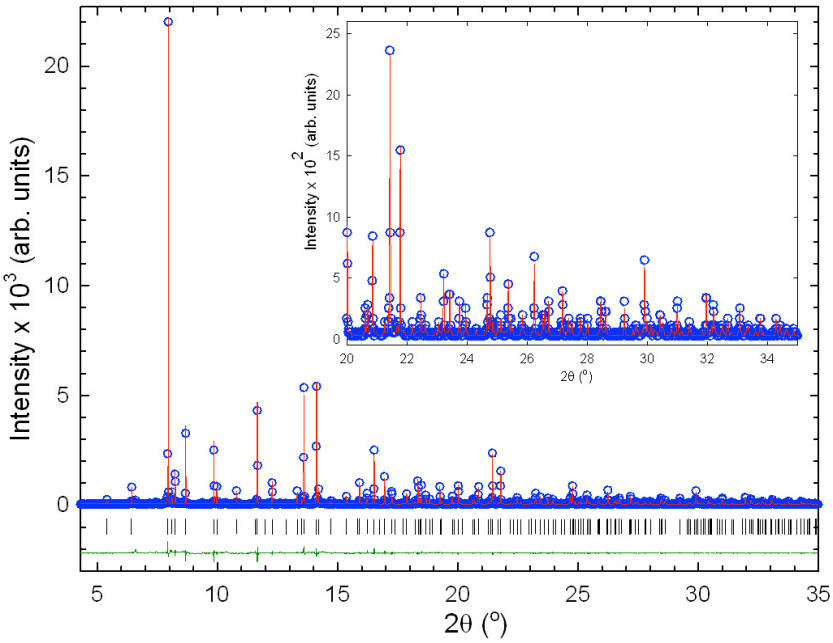

Figure 3.3. Final observed (blue circles), calculated (red solid line), and difference (lower green solid line) plots for the Rietveld refinement of $Nd_{0.948}Sr_{0.052}FeAsO$ at RT. Tick marks show the reflection positions. The refinement proceeded with the main phase in the *P4/nmm* space group. The refined lattice constants are a = 3.97171(2) Å and c = 8.57316(6) Å. The agreement factors are R_{wp} = 6.50%, R_{exp} = 3.80%. The X-ray wavelength is 0.4030068 Å. Inset shows zoom in on the 20 to 35 2θ data range.

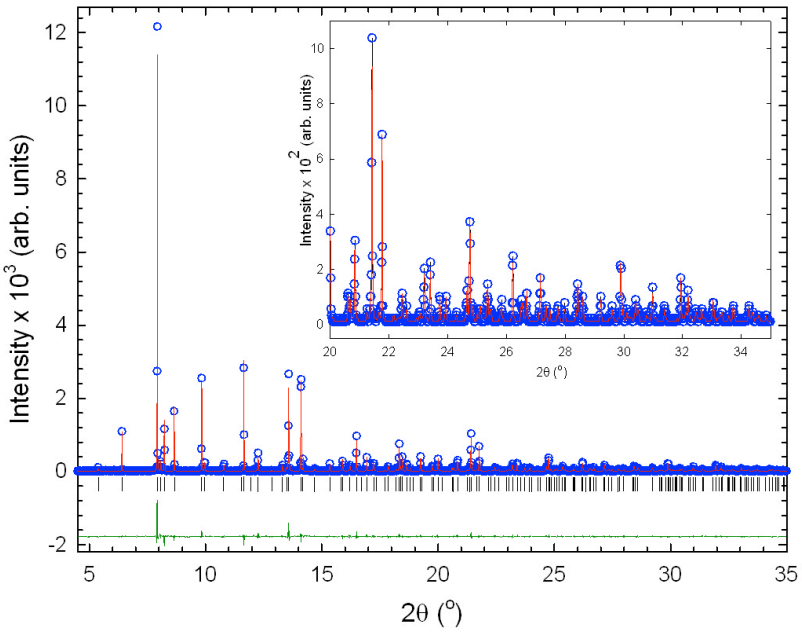

Figure 3.4. Final observed (blue circles), calculated (red solid line), and difference (lower green solid line) plots for the Rietveld refinement of $Nd_{0.909}Sr_{0.091}FeAsO$ at RT. Tick marks show the reflection positions. The refinement proceeded with the main phase in the *P4/nmm* space group. The refined lattice constants are a = 3.97334(2) Å and c = 8.58077(6) Å. The agreement factors are R_{wp} = 6.71%, R_{exp} = 4.34%. The X-ray wavelength is 0.4030068 Å. Inset shows zoom in on the 20 to 35 2θ data range.

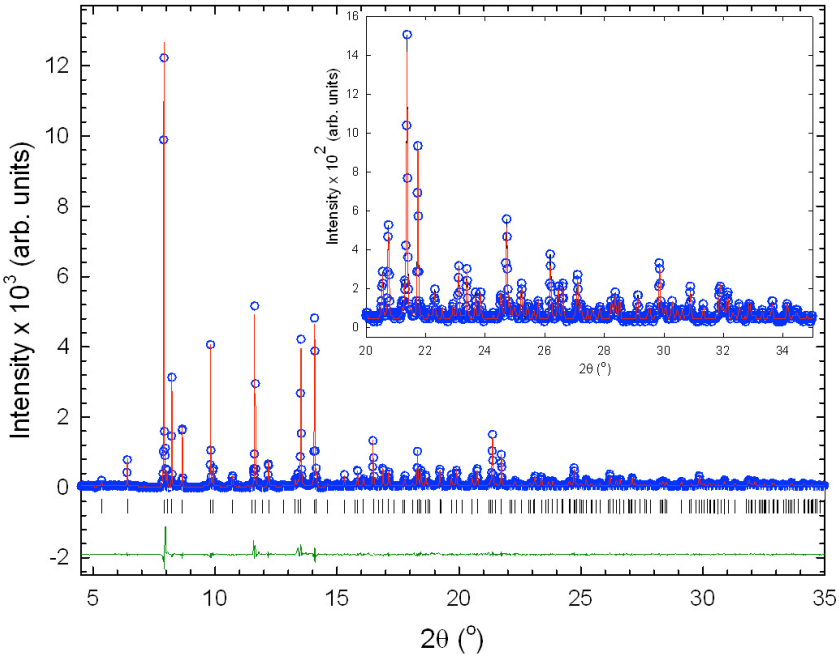

Figure 3.5. Final observed (blue circles), calculated (red solid line), and difference (lower green solid line) plots for the Rietveld refinement of $Nd_{0.79}Sr_{0.21}FeAsO$ at RT. Tick marks show the reflection positions. The refinement proceeded with the main phase in the *P4/nmm* space group. The refined lattice constants are a = 3.97773(2) Å and c = 8.64147(8) Å. The agreement factors are R_{wp} = 6.42%, R_{exp} = 4.11%. The X-ray wavelength is 0.4030068 Å. Inset shows zoom in on the 20 to 35 2θ data range.

Table 3.2. Refined structural parameters and bond lengths (Å) and angles (°) for $Nd_{1-x}Sr_xFeAsO$ with x = 0.05, 0.1 and 0.2 obtained from Rietveld refinements of the synchrotron X-ray diffraction data at room temperature. Estimated errors in the last digits are given in parentheses. The schematic diagram of the structure is shown in Figure 3.1.

		x = 0.05	x = 0.1	x = 0.2
Space group		*P4/nnm*	*P4/nnm*	*P4/nnm*
a (Å)		3.97171(2)	3.97334(2)	3.97773(2)
c (Å)		8.57316(6)	8.58077(6)	8.64147(8)
Volume (Å^3)		135.237(1)	135.469(1)	136.728(1)
Nd	B_{iso} (Å^2)	0.39(1)	0.326(7)	0.45(2)
	Occ.	0.944(6)	0.909(6)	0.79(1)
	z	0.13927(6)	0.13877(5)	0.13719(9)
Sr	B_{iso} (Å^2)	0.39(1)	0.326(7)	0.45(2)
	Occ.	0.052(6)	0.091(6)	0.21(1)
	z.	0.13927(6)	0.13877(5)	0.13719(9)
O	B_{iso} (Å^2)	1.0(3)	0.6(1)	1.1(2)
	Occ	1.00	1.00	1.00
Fe	B_{iso} (Å^2)	0.53(3)	0.41(4)	0.47(5)
	Occ.	1.00	1.00	1.00
As	B_{iso} (Å^2)	0.52(1)	0.42(1)	0.46(3)
	Occ	1.00	1.00	1.00
	z	0.6572(1)	0.6568(1)	0.6563(2)
R_{wp} (%)		6.50	6.71	6.42
R_{exp} (%)		3.80	4.34	4.11
Nd-O (Å)		2.3171(3) x 4	2.3162(2) x 4	2.3151(4) x 4
Nd-O-Nd (º)		117.97(1) x 2	118.12(3) x 2	118.40(4) x 2
		105.39(2) x 4	105.32(2) x 4	105.19(4) x 4
Fe-Fe (Å)		2.80842(1) x 4	2.80958(1) x 4	2.81268(1) x 4
Fe-As (Å)		2.3998(5) x 4	2.3994(4) x 4	2.4045(5) x 4
Fe-As-Fe (º)		111.69(1) x 2 71.63(2) x 4	111.79(4) x 2 71.67(2) x 4	111.62(4) x 2 71.59(2) x 4

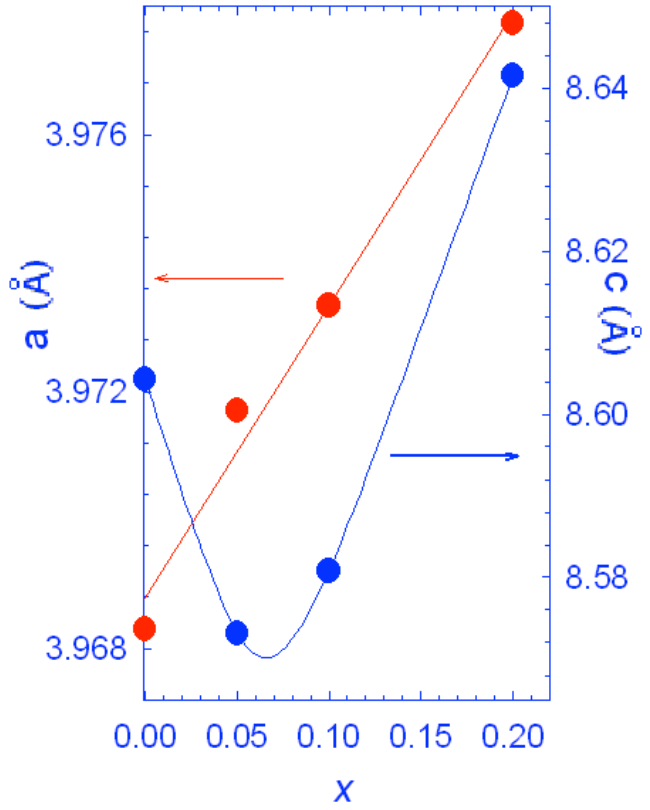

Figure 3.6. Evolution of the room temperature tetragonal lattice constants as a function of Sr^{2+} doping level *x*. Unit cell vector '*a*' is plotted against the left-hand scale; '*c*' against the right-hand scale. The lines are guides to the eye.

The structural analysis also revealed that with increasing doping level the *a* axis increases monotonically, as expected considering the larger ionic radius of Sr^{2+} compared to Nd^{3+} (1.18 Å vs 0.98 Å). The substitution occurs on the RE-O layers, which primarily determines the basal plane lattice dimensions. However, the *c* axis has a different response: it initially contracts slightly at small doping levels before undergoing a considerable expansion for $x > 0.1$ (Figure 3.6). The *c*-axis dimensions are influenced by the geometry of the $FeAs_4$ tetrahedra (Figure 3.7), whose compression first decreases for $0 < x < 0.1$ and then undergoes a large expansion at $x > 0.1$. It is interesting to note that at small levels of Sr^{2+} the evolution of the structural parameters is exactly opposite to what has been reported so far for the F^- doped REFeAsO systems. In those systems the $FeAs_4$ pyramidal units tend to compress monotonically with increasing doping levels without any discontinuities (the Fe-As-Fe angles decrease while the Fe-As distances increase resulting in a total

increase of the thickness of the FeAs layer). However, at higher level of Sr^{2+} substitution the $FeAs_4$ tetrahedra start to expand in analogy with the trend observed for the superconducting electron doped phases (Figure 3.8). It has been discussed that important features of the electronic structure of the REFeAsO systems strongly depend on small changes in interatomic distances and bond angles of the $FeAs_4$ pyramidal units. These structural parameters sensitively control both the Fe near- and next-near-neighbour exchange interactions as well as the width of the electronic conduction band due to the high degree of covalency (strong hybridization) of the Fe-As bond[21]. The observed sudden increase of the Fe-As distance coupled with the larger lattice dimensions for the x = 0.2 composition may lead to a much smaller bandwidth and changes in the electronic behaviour as compared to the small doping level compositions.

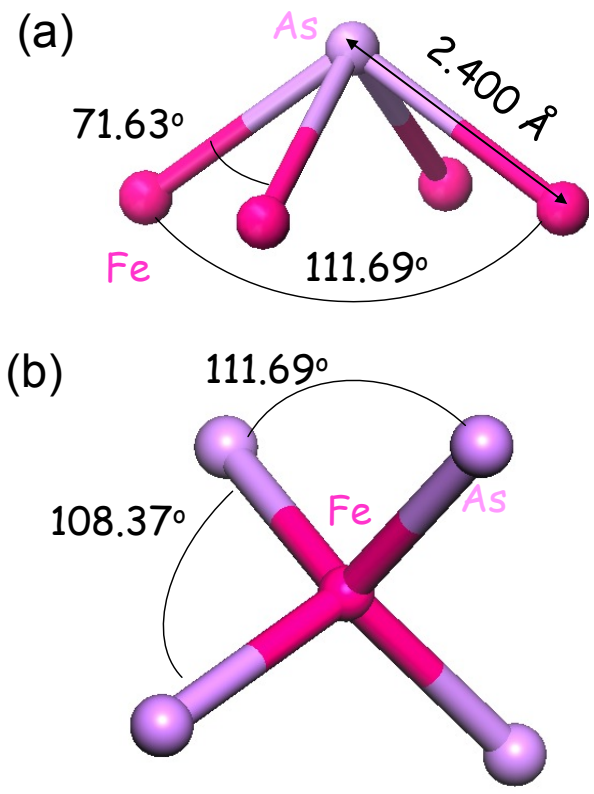

Figure 3.7. Schematic diagram of the **(a)** AsF_4 and **(b)** $FeAs_4$ units. The values of the bond distances and angles reported refer to the x = 0.05 composition.

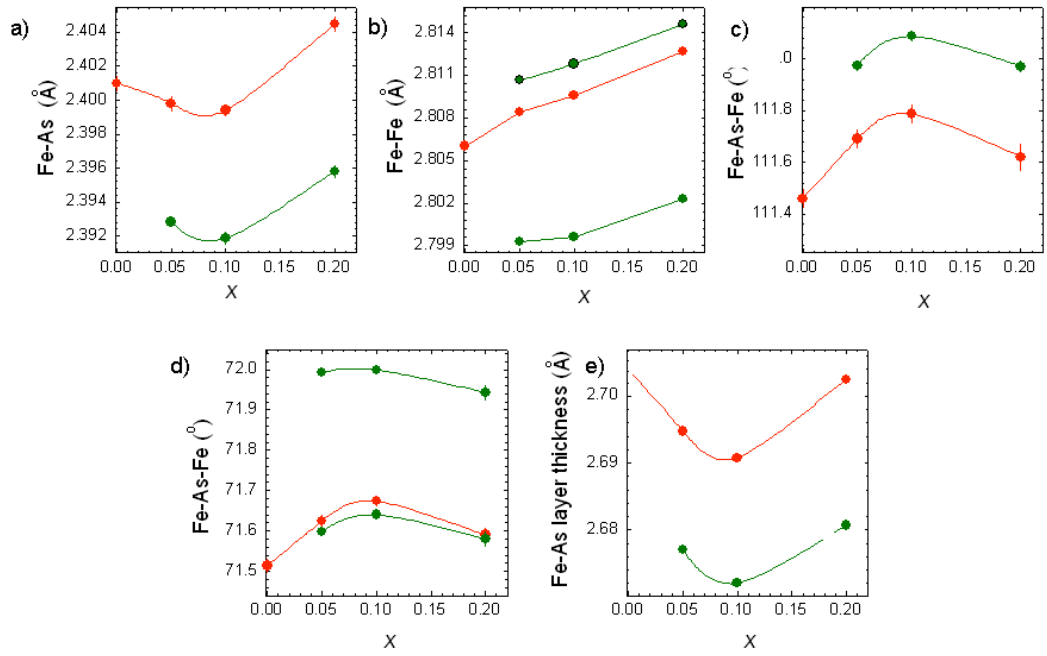

Figure 3.8. Diagram of the evolution of distances between a) Fe-As, b) Fe-Fe and angles between c) Fe-As-Fe, d) Fe-As-Fe and e) thickness of Fe-As layer in $Nd_{1-x}Sr_xFeAsO$.

Diffraction profiles on compositions with x = 0.05, 0.1 and 0.2 were collected during cooling between room temperature and 5 K, and all compositions at around 130 K showed a structural phase transition from tetragonal to orthorhombic (space group *Cmma*) in analogy with the undoped REFeAsO systems. Representative refined lattice constants and structural parameters for $Nd_{1-x}Sr_xFeAsO$ with x = 0.05, 0.1 and 0.2 at 5 K are shown in Table 3.3. The Rietveld refinements of members of the family at 5 K are shown below (Figures 3.9 to 3.11).

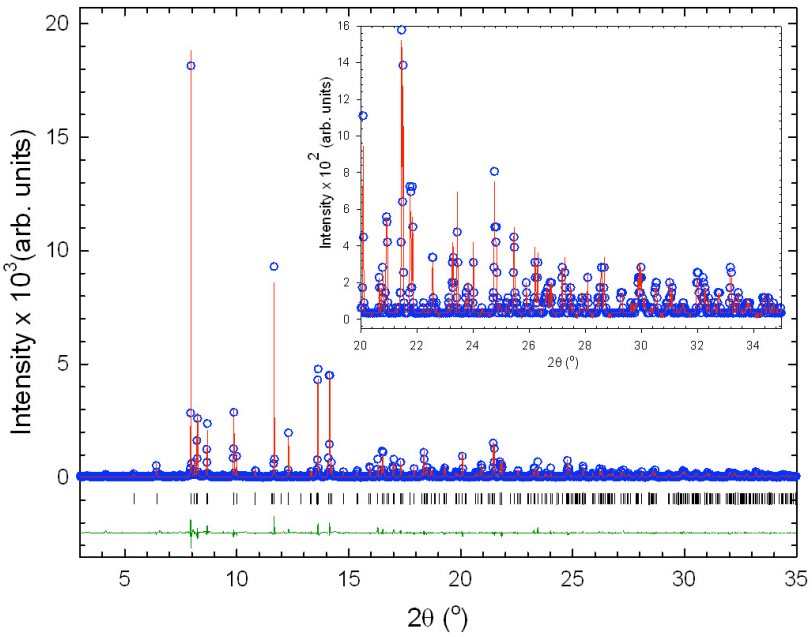

Figure 3.9. Final observed (blue circles), calculated (red solid line), and difference (lower green solid line) plots for the Rietveld refinement of $Nd_{0.948}Sr_{0.052}FeAsO$ at 5 K. Tick marks show the reflection positions. The refinement proceeded with the main phase in the *Cmma* space group. The refined lattice constants are a = 5.59862(1) Å, b = 5.62133(1) Å and c = 8.53437(2) Å. The agreement factors are R_{wp} = 5.25%, R_{exp} = 3.04%. The X-ray wavelength is 0.4030068 Å. Inset shows zoom in on the 20 to 35 2θ data range.

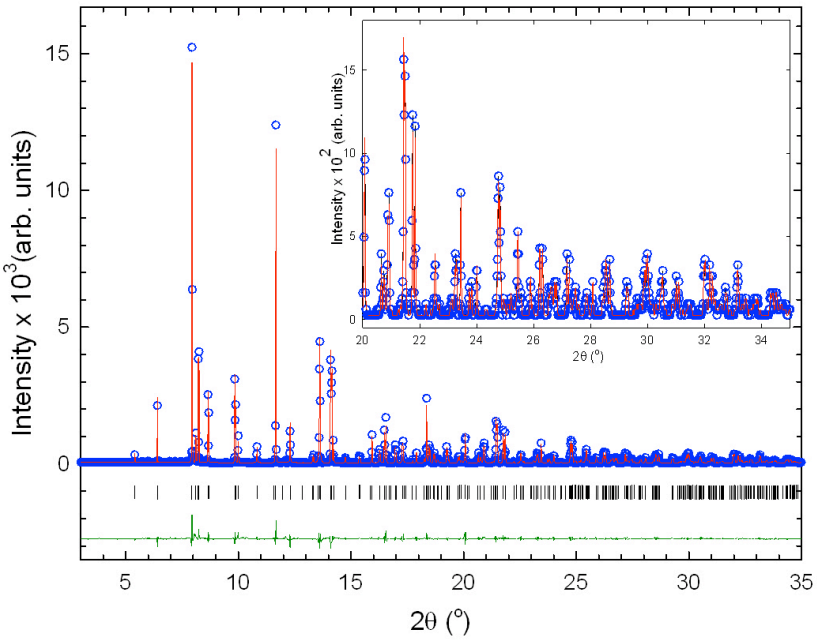

Figure 3.10. Final observed (blue circles), calculated (red solid line), and difference (lower green solid line) plots for the Rietveld refinement of $Nd_{0.909}Sr_{0.091}FeAsO$ at 5 K. Tick marks show the reflection positions. The refinement proceeded with the main phase in the *Cmma* space group. The refined lattice constants are a = 5.59930(2) Å, b = 5.62358(1) Å and c = 8.54437(2) Å. The agreement factors are R_{wp} = 5.87%, R_{exp} = 3.85%. The X-ray wavelength is 0.4030068 Å. Inset shows zoom in on the 20 to 35 2θ data range.

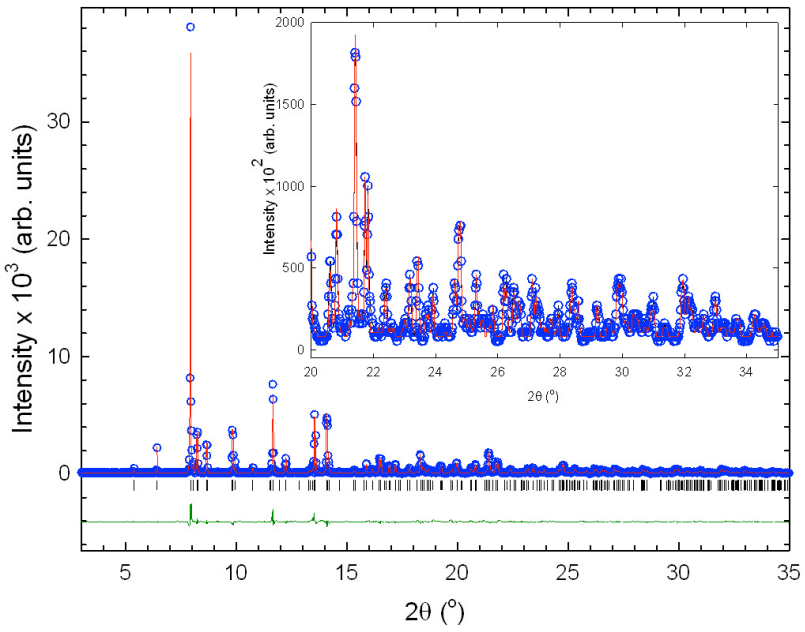

Figure 3.11. Final observed (blue circles), calculated (red solid line), and difference (lower green solid line) plots for the Rietveld refinement of $Nd_{0.79}Sr_{0.21}FeAsO$ at 5 K. Tick marks show the reflection positions. The refinement proceeded with the main phase in the *Cmma* space group. The refined lattice constants are a = 5.60451(2) Å, b = 5.62914(1) Å and c = 8.60519(2) Å. The agreement factors are R_{wp} = 4.99%, R_{exp} = 3.29°%. The X-ray wavelength is 0.4030068 Å. Inset shows zoom in on the 20 to 35 2θ data range.

Table 3.3. Refined structural parameters and bond lengths (Å) and angles (°) for $Nd_{1-x}Sr_xFeAsO$ with x = 0.05, 0.1 and 0.2 obtained from Rietveld refinements of the synchrotron X-ray diffraction data at temperature 5 K. Estimated errors in the last digits are given in parentheses.

		x = 0.05	x = 0.1	x = 0.2
Space group		*Cmma*	*Cmma*	*Cmma*
a (Å)		5.59862(1)	5.59930(2)	5.60451(2)
b (Å)		5.62133(1)	5.62358(1)	5.62914(1)
c (Å)		8.53437(2)	8.54437(2)	8.60519(2)
Volume (Å^3)		268.591(1)	269.046(1)	271.482(1)
Nd	B_{iso} (Å^2)	0.038(4)	0.041(3)	0.10(1)
	Occ.	0.952(5)	0.906(6)	0.805(4)
	z	0.1395(4)	0.13924(3)	0.13842(3)
Sr	B_{iso} (Å^2)	0.038(4)	0.041(3)	0.10(1)
	Occ.	0.048(5)	0.094(3)	0.195(4)
	z.	0.1395(4)	0.13924(3)	0.13842(9)
O	B_{iso} (Å^2)	0.23(6)	0.26(5)	0.8(3)
	Occ	1.00	1.00	1.00
Fe	B_{iso} (Å^2)	0.026(4)	0.014(3)	0.098(4)
	Occ.	1.00	1.00	1.00
As	B_{iso} (Å^2)	0.020(3)	0.030(3)	0.09(3)
	Occ	1.00	1.00	1.00
	z	0.65684(6)	0.65470(5)	0.65576(8)
R_{wp} (%)		5.25	5.87	4.99
R_{exp} (%)		3.04	3.85	3.29
Nd-O (Å)		2.3135(2) x 4	2.3131(4) x 4	2.3157(2) x 4
Nd-O-Nd (º)		118.04(2) x 2	118.09(3) x 2	118.08(4) x 2
		105.54(1) x 4	105.52(2) x 4	105.15(3) x 4
Fe-Fe (Å)		2.81066(1) x 2 2.79931(1) x 2	2.81179(1) x 2 2.79965(1) x 2	2.81456(1) x 4 2.80227(1) x 2
Fe-As (Å)		2.3928(3) x 4	2.3919(4) x 4	2.3958(4) x 4
Fe-As-Fe (º)		111.97(2) x 2 71.60(1) x 2 71.99(1) x 2	112.09(2) x 2 71.64(1) x 2 72.00(2) x 2	111.97(2) x 2 71.58(2) x 2 71.94(2) x 2

At the transition temperatures no discontinuities are observed in either the c lattice constant or the normalized volume, V (Figures 3.12 and 3.13). However, sudden changes are visible in the thermal response of the structural parameters describing the $FeAs_4$ tetrahedra (Fe-As bond distances and Fe-As-Fe exchange angle) for x = 0.05 and 0.1 which could indicate a lattice response to the onset of long range magnetic order (Figure 3.13). These discontinuities are suppressed at x = 0.2, in analogy with the electron doped $SmFeAsO_{1-x}F_x$ ($0 < x < 0.12$) systems where the

influence of the **T→O** (tetragonal to orthorhombic) phase transition on the local geometry of the $FeAs_4$ tetrahedra is only quite subtle[9]. Further differences between the hole and electron doped systems can be found by noticing that increasing the Sr^{2+} content level does not suppress the **T→O** phase transition, and in addition the structural transition temperature, T_s, remain almost constant for all compositions (T_s = 135 K for x = 0, 115 K for x = 0.05 and 130 K for x = 0.1 and 0.2).

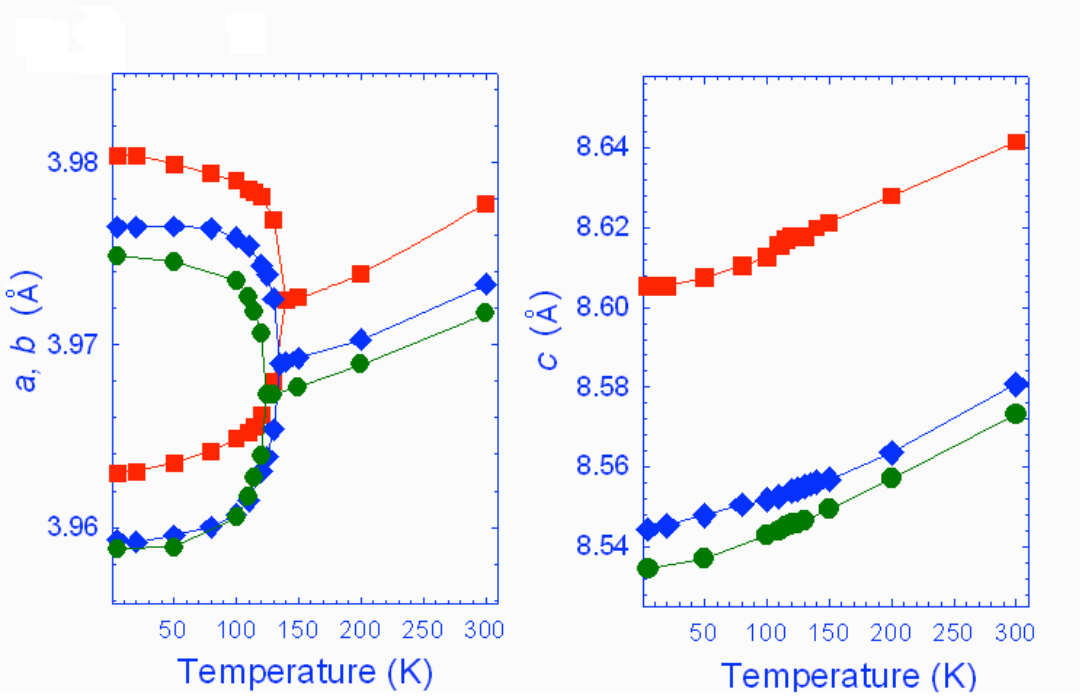

Figure 3.12. Temperature evolution of the lattice constants for $Nd_{1-x}Sr_xFeAsO$: green circles, blue diamonds and red squared refer to compositions with x = 0.05, 0.1 and 0.2, respectively.

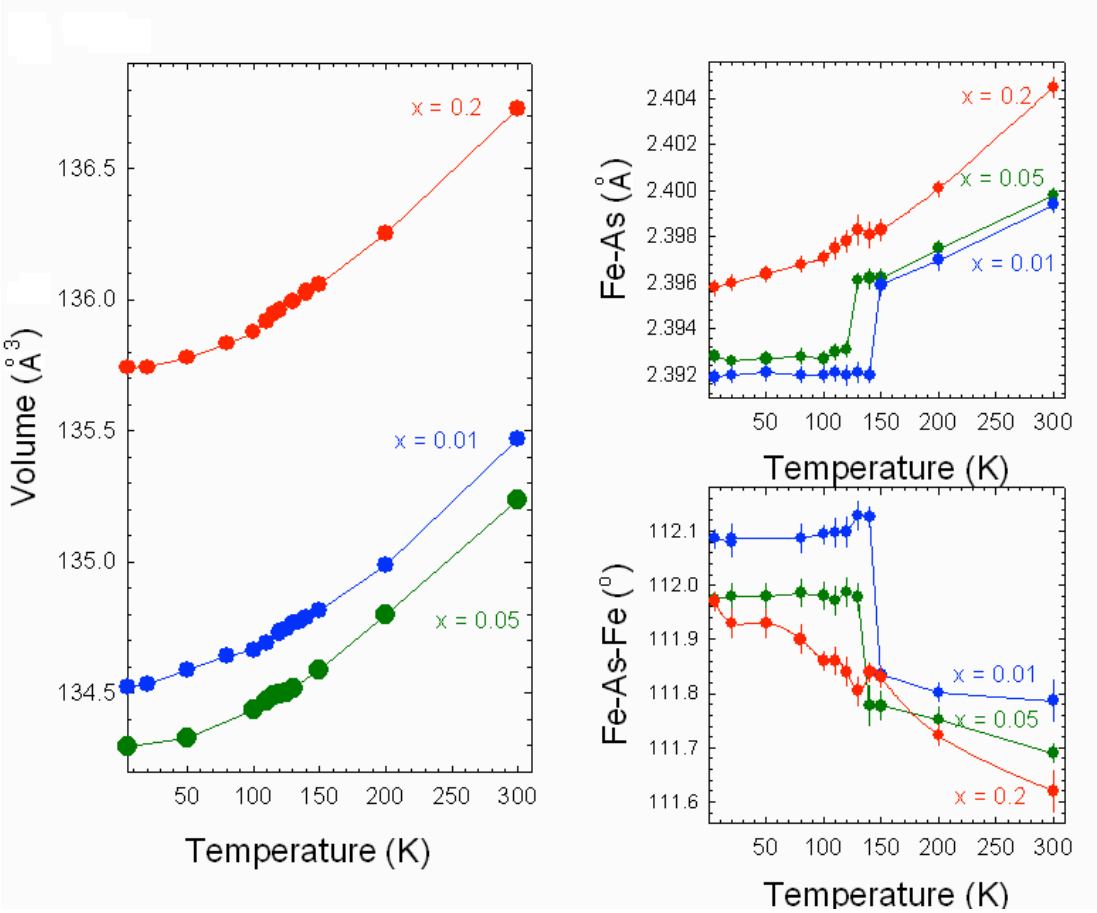

Figure 3.13. On the left: temperature evolution of the volume for $Nd_{1-x}Sr_xFeAsO$: green circles, blue diamonds and red squared refer to compositions with x = 0.05, 0.1 and 0.2, respectively. On the right: thermal response of the structural parameters describing the $FeAs_4$ tetrahedra - Fe-As bond distances and Fe-As-Fe exchange angle.

3.4.2. Magnetic properties.

The magnetic susceptibilities of $Nd_{1-x}Sr_xFeAsO$ for x = 0, 0.05, 0.1 and 0.2 were measured in an applied magnetic field of 10 kOe. For the parent compound, the measured $\chi_M T$ at 300 K (1.96 cm^3 K mol^{-1}) gives a value for the effective magnetic moment μ_{eff} = 3.96 μ_B which is slightly higher then the calculated Nd^{3+} free ion value of 3.62 μ_B. Calculations for the effective magnetic moment for the $Nd_{1-x}Sr_xFeAsO$ series show a decrease of the μ_{eff} value with increasing doping level of Sr (Figure 3.14). The magnetic susceptibility data at 10 kOe smoothly decrease as a function of doping level, as expected from the substitution of Nd^{3+} ($4f^3$, S = 3/2) with non-magnetic Sr^{2+} in the RE-O layer ($\chi_M T$ values at 300 K 1.66, 1.59 and 1.47 cm^3 K

mol^{-1} for x = 0.05, 0.1 and 0.2 respectively) (Figure 3.15). As a first approximation, the Fe^{2+} and Nd^{3+} contribution to the magnetic susceptibility can be considered independently in the high temperature paramagnetic region (180 < T < 300 K). It is then possible to subtract from the total magnetic susceptibility the paramagnetic Nd^{3+} contribution by considering the ground state ($4f^3$, $^4I_{9/2}$). Such a subtraction leaves a temperature-independent component, which can be attributed to Pauli-like susceptibility of the Fe^{2+} spins. At 300 K the value of the susceptibility after subtraction is χ_M = 8.3 x 10^{-4} emu mol^{-1} (LaFeAsO containing non-magnetic La^{3+} has χ_M = 5 x 10^{-4} emu mol^{-1})[22]. Analogous treatment of the 10 kOe data for the other compositions, performed by taking into account the nominal stoichiometry, showed that the values of the temperature-independent component of the magnetic susceptibility first decreases drastically as the Sr content is increased to 5% (9.3 x 10^{-5} emu mol^{-1}) and then smoothly increases up to the maximum doping level of 20% (1.95 and 3.5 x 10^{-4} emu mol^{-1} for x = 0.1 and 0.2 respectively). The observed trend clearly indicates important changes in the electronic properties upon doping.

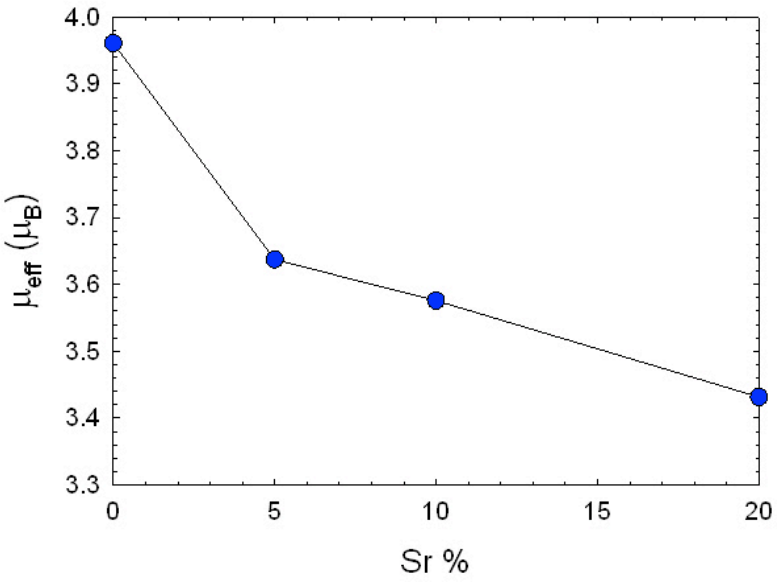

Figure 3.14. Evolution of effective magnetic moment per mol of sample against the doping level of Sr.

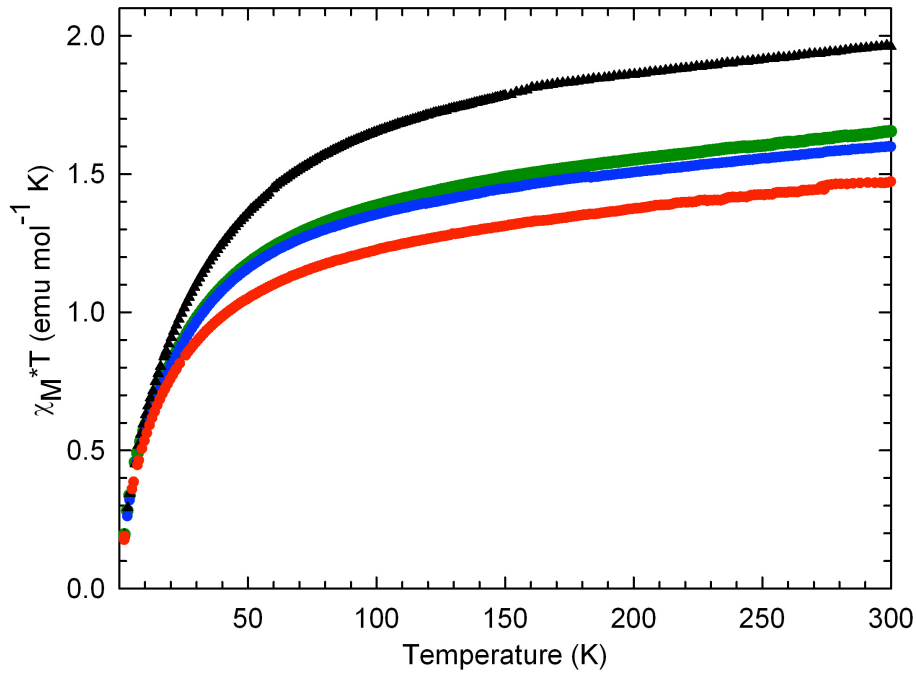

Figure 3.15. Temperature evolution diagram of $\chi_M * T$ for different compositions of $Nd_{1-x}Sr_xFeAsO$: black, green, red and blue marks refer to composition with x = 0, 0.05, 0.1 and 0.2 respectively.

Low temperature measurements of magnetic susceptibility at 20 Oe showed that a superconducting transition is present only for the higher doping level composition x = 0.2. The superconducting transition temperature is 13.5 K with a shielding fraction of 17% (Fig. 3.16).

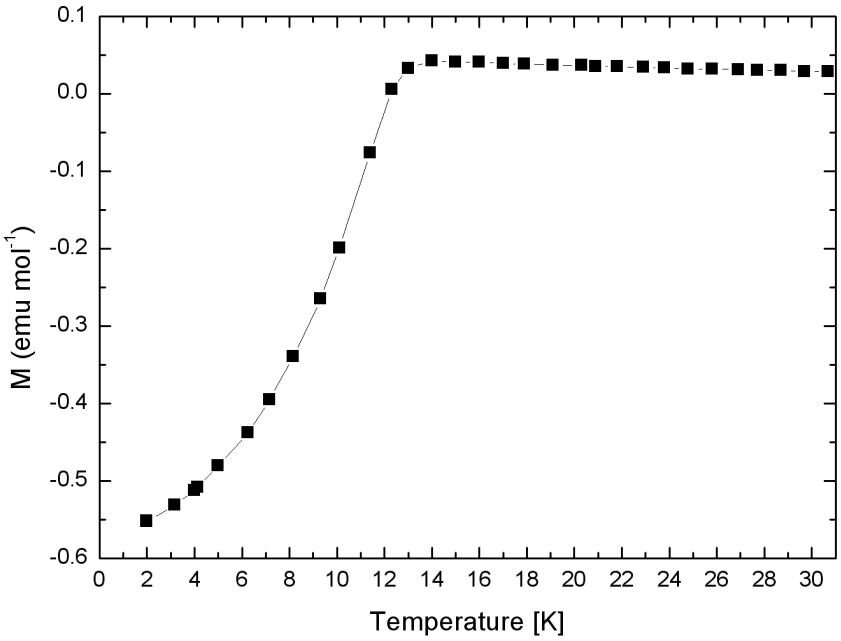

Figure 3.16. Low field superconducting transition of $Nd_{0.8}Sr_{0.2}FeAsO$.

The superconducting shielding fraction was calculated from Equation 3.1, where *M* is the measured value of the magnetization, *m* is the mass of sample in grams, *d* is the density and *H* is the applied magnetic field. In the calculations $d = 7$ g/cm^3 was used.

$$\frac{4\pi \cdot \left(M(30K) - M(4K)\right) \cdot d}{H * m} \cdot 100\%$$

Equation 3.2.

3.4.3. Electrical resistivity.

Resistivity measurements were performed on samples $Nd_{1-x}Sr_xFeAsO$ with $x = 0$, 0.05 and 0.2 (Figure 3.17).

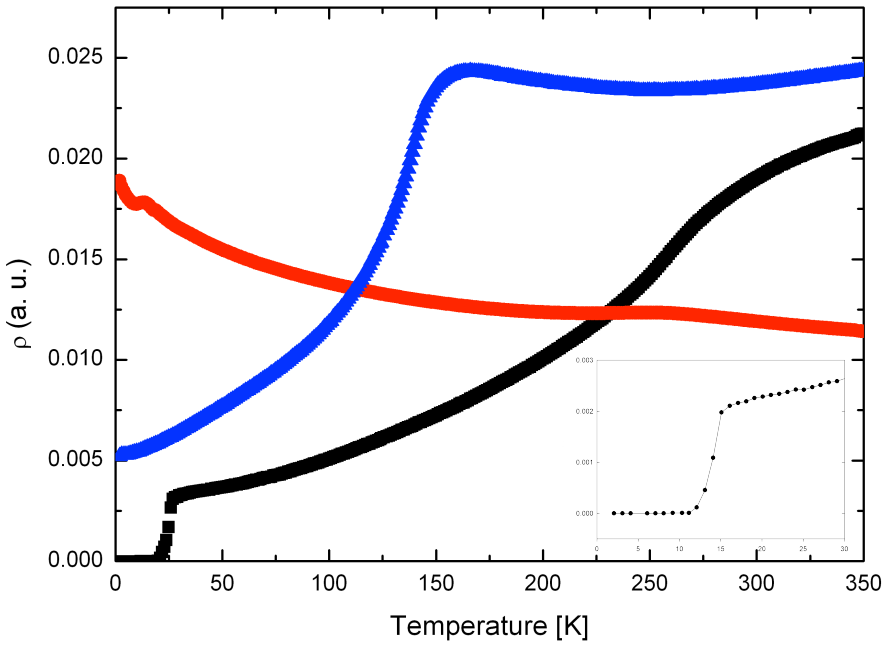

Figure 3.17. The temperature evolution of the resistivity for the different compositions of $Nd_{1-x}Sr_xFeAsO$: blue, red and black marks refer to compositions with $x = 0$, 0.05 and 0.2 respectively. The inset illustrates the superconducting transition.

The parent compound, with $x = 0$, shows the typical behaviour already reported for REFeAsO (displayed as the blue trace on Figure 3.17). Above 250 K, ρ slowly increases. Below 250 K the resistivity increases towards a maximum at 160 K caused by the SDW transition, and then rapidly decreases down to 2 K, but no superconducting transition is observed. The resistivity curve of the 5% doped material (the red trace in Figure 3.17) shows a drastic change with ρ increasing on cooling, implying a semiconducting type of behaviour. There is a small upturn at around 10 K, which can be explained by the ordering of Nd moments, but the SDW is already supressed with this level of doping. A possible reason for such a large change in resistivity with such a small change in doping levels may be that a small

percentage of hole doping depletes the amount of electron type charge carriers available. The electron cylinders of the Fermi surface decrease in volume and this is not immediately compensated by an enlargement of the hole pockets, which would explain the observed behaviour. However, further doping should increase back the amount of hole-type charge carriers and a metallic type of conductivity would be restored (increased volume of the hole-type cylinders). To determine what type of carriers are responsible for the conduction the Hall coefficient measurements are needed, but it has been already demonstrated that Sr^{2+} doping leads to hole type conduction in other systems like $La_{1-x}Sr_xFeAs$[19] or $Sr_{1-x}K_xFe_2As_2$[23]. Indeed, the 20% doped system (the black trace in Figure 3.17) shows a metallic type of behaviour with resistivity: decreasing with temperature and with a superconducting transition at T = 13.5 K, which is in agreement with the magnetic data. It is interesting to note that the derivative of the resistivity curves show maxima at 140, 115 and 130 K for x = 0, 0.05 and 0.2 (Figure 3.18). These maxima correspond exactly to the temperatures of the structural transition.

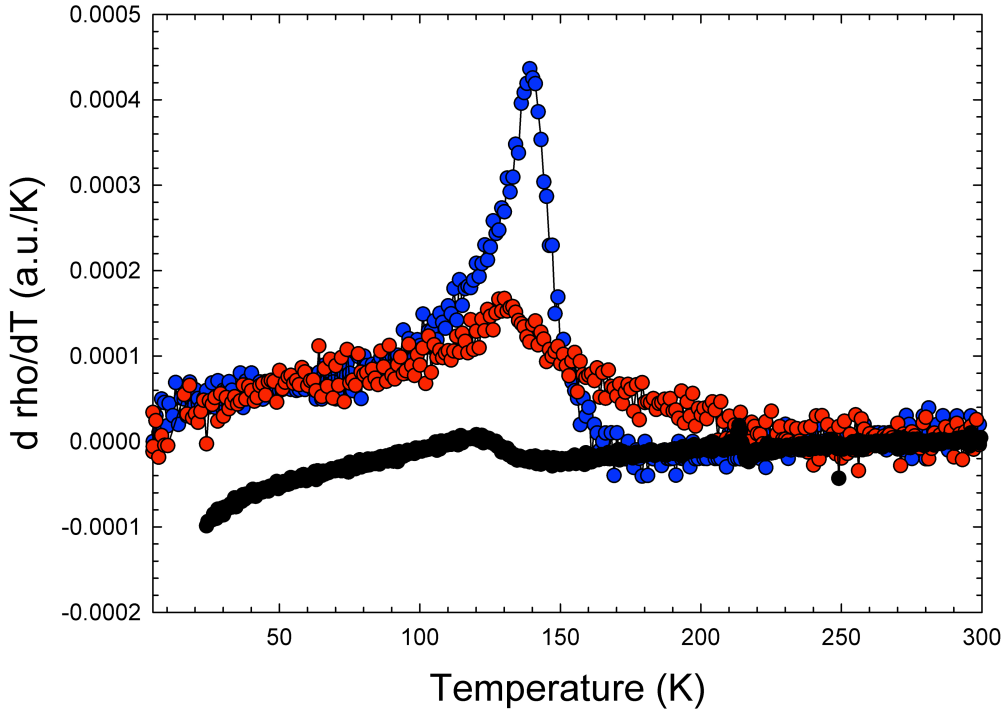

Figure 3.18. Temperature evolution of the derivative of the resistivity curves for different compositions of $Nd_{1-x}Sr_xFeAsO$: black, red and blue marks refer to composition with x = 0.05, 0.1 and 0.2 respectively.

3.5. Discussion.

In this work, it has been proven that partial replacement of Nd^{3+} by Sr^{2+} in the RE-O plane to afford $Nd_{1-x}Sr_xFeAsO$ leads to superconducting phases at $x > 0.1$. However, the electronic and structural behaviour upon hole doping is different and not symmetric to the corresponding electron doped systems where a smooth evolution of the structural and electronic properties is observed (Figure 3.19)[3,4,5]. In the hole doped systems, the **T→O** phase transition is not suppressed up to $x \sim 0.2$ and in addition, T_s varies little in sharp contrast to the structural behaviour of the electron doped analogues. The evolution of the structural parameters of the $FeAs_4$ tetrahedra shows drastic changes at doping levels $x > 0.1$, with a large increase in the Fe-As distances accompanied by a decrease in the thickness of the Fe-As layers. Magnetisation and resistivity measurements also show considerable differences in the electronic behaviour with increasing x. All the experimental observations describe a scenario where at small x, the number of carriers decreases, leading to an accompanying decrease in $N(E_F)$ and initially pushing the system into the semiconducting regime. Higher Sr^{2+} content is necessary for the metallic regime to re-emerge. At $x > 0.1$, the weaker Fe-As hybridisation causes a decrease in the conduction bandwidth, which is accompanied by an increase in $N(E_F)$ and the occurrence of superconducting phases. It appears that for NdFeAsO higher levels of hole doping are necessary to observe a similar phenomenology to the electron doped systems, as an increased number of carriers is necessary to first overcome the initial semiconducting behaviour. This is in contrast to $NdFeAsO_{1-x}F_x$, in which there is a continuous change of the electronic properties upon F doping and superconductivity is obtained for $x > 0.08$ with much higher T_c (*cf.* $NdFeAsO_{0.88}F_{0.12}$, $T_c = 50$ K). It is quite likely that for Sr^{2+} concentrations higher than 20%, a drastic increase in T_c could be achieved. It is noted that also in the hole doped $K_{1-x}Sr_xFe_2As_2$ systems[12], superconductivity is reported at doping levels of 20% ($x = 0.80$) with a T_c of ~15 K. Higher transition temperatures are obtained by increasing the doping level.

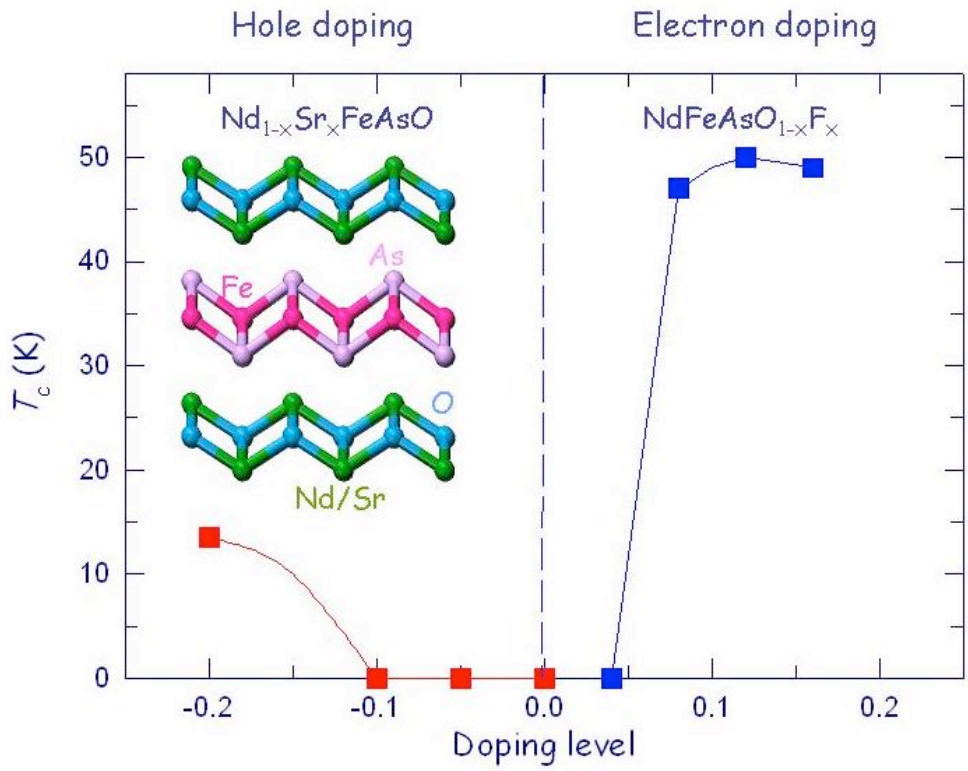

Figure 3.19. Comparison of T_c in electron doped and hole doped NdFeAsO[24,25].

3.6. Conclusions.

A family of hole doped quaternary oxyarsenides $Nd_{1-x}Sr_xFeAsO$ with x = 0, 0.05 and 0.2 was successfully designed and synthesized and the structural, electronic and magnetic properties of these compounds were investigated in depth. Confirming the existence of superconducting phases, it was probed how T_c varies with composition and the influence of doping on the structural and magnetic transitions was revealed. Doped samples produce single phase materials which adopt the tetragonal *P4/nmm* structure at room temperature and undergo a structural phase transition to orthorhombic *Cmma* at the temperatures around 130 K. Low temperature measurements of magnetic susceptibility and resistivity show that samples with small doping levels (x = 0.05) display semiconducting type behaviour. Increasing the doping level leads to metallic conductivity (x = 0.1) and eventually superconductivity for doping level of 20% of Sr^{2+}, with the superconducting transition occurring at T_c = 13.5 K. These results clearly show that hole doping of NdFeAsO can create superconducting phases.

3.7. Bibliography.

1. Wu, M. K.; Ashburn, J. R.; Torng, C. J.; Hor, P. H.; Meng, R. L.; Gao, L.; Huang, Z. J.; Wang, Y. Q.; Chu, C. W. *Physical Review Letters,* **1987**, *58*, 908.
2. Wen, H.-H. *Advanced Materials,* **2008**. 9999, 1-6.
3. Kamihara, Y.; Watanabe, T.; Hirano, M.; Hosono, H. *Journal of the American Chemical Society,* **2008**, *130*, 3296.
4. Xiao, Y.; Su, Y.; Mittal, R.; Chatterji, T.; Hansen, T.; Price, S.; Kumar, C. M. N.; Persson, J.; Matsuishi, S.; Inoue, Y.; Hosono, H.; Brueckel, T., *Physical Review B,* **2009**, 81, 094523.
5. Marcinkova, A.; Grist, D. A. M.; Margiolaki, I.; Hansen, T. C.; Margadonna, S.; Bos, J.-W. G., *Physical Review B,* **2010**, 33.
6. Liu, H.; Chen, G. F.; Zhang, W.; Zhao, L.; Liu, G.; Xia, T.-L.; Jia, X.; Mu, D.; Liu, S.; He, S.; Peng, Y.; He, J.; Chen, Z.; Dong, X.; Zhang, J.; Wang, G.; Zhu, Y.; Xu, Z.; Chen, C.; Zhou, X. J., *Physical Review Letters,* **2010**, 105, 027001.
7. Tegel, M.; Johansson, S.; Weiss, V.; Schellenberg, I.; Hermes, W.; Pöttgen, R.; Johrendt, D., *Europhysics Letters,* **2008**, *84*, 5.
8. Felner, I.; Pal, A.; MNowik, I.; Yamaura, K.; Takayama-Muromachi, E.; Awana, V. P. S., *Physical Review B,* **2010**, *81*, 10.
9. Ren, Z.-A.; Wei, L.; Yang, J.; Yi, W.; Shen, X.-L.; Li, Z.-C.; Che, G.-C.; Dong, X.-L.; Sun, L.-L.; Zhou, F.; Zhao, Z.-X., *Chinese Physics Letters,* **2008**, *25*, 2215.
10. Torikachvili, M. S.; Bud'ko, S. L.; Ni, N.; Canfield, P. C., *Physical Review B* **2008**, *78*, 104527.
11. Tegel, M.; Rotter, M.; Weiss, V.; Schappacher, F. M.; Pöttgen, R.; Johrendt, D., Prof. Dr., *Journal of Physics: Condensed Matter,* **2008**, *20*, 452201.
12. Sasmal, K.; Lv, B.; Lorenz, B.; Guloy, A. M.; Chen, F.; Xue, Y.-Y.; Chu, C.-W., *Physical Review Letters,* **2008**, *101*, 107007.
13. Rotter, M.; Pangerl, M.; Tegel, M.; Johrendt, D., *Angewandte Chemie International Edition,* **2008**, *47*, 7949.
14. Krellner, C.; Caroca-Canales, N.; Jesche, A.; Rosner, H.; Ormeci, A.; Geibel, C. *Physical Review B,* **2008**, *78*, 100504.

15. Wen, H. H.; Mu, G.; Fang, L.; Yang, H.; Zhu, X., *Europhysics Letters,* **82** (2008), 17009.

16. Marsiglio, F.; Hirsch, J. E. *Physica C: Superconductivity* **2008**, *468*, 1047.

17. Miyake, T.; Nakamura, K.; Arita, R.; Imada, M., *Journal of the Physical Society of Japan,* **2009**, 79, 044705.

18. Liu, H.; Zhang, W.; Zhao, L.; Jia, X.; Meng, J.; Liu, G.; Dong, X.; Chen, G. F.; Luo, J. L.; Wang, N. L.; Lu, W.; Wang, G.; Zhou, Y.; Zhu, Y.; Wang, X.; Xu, Z.; Chen, C.; Zhou, X. J. *Physical Review B,* **2008**, *78*, 184514.

19. Mu, G.; Fang, L.; Yang, H.; Zhu, X.; Cheng, P.; Wen, H. H., *Condensed Matter*, arXiv:0806.2104v2, **2008.**

20. Wu, G.; Chen, H.; Xie, Y. L.; Yan, Y. J.; Wu, T.; Liu, R. H.; Wang, X. F.; Fang, D. F.; Ying, J. J.; Chen, X. H.*, Physical Review B,* **2008,** 78, 092503.

21. Vildosola, V.; Pourovskii, L.; Arita, R.; Biermann, S.; Georges, A., *Physical Review B*, **2008**, 78, 064518.

22. Nomura, T.; Kim, S. W.; Kamihara, Y.; Hirano, M.; Sushko, P. V.; Kato, K.; Takata, M.; Shluger, A. L.; Hosono, H., *Superconductor Science and Technology,* **2008**. 21, 125028.

23. Chen, G.-F.; Li, Z.-C.; Li, G.; Hu, W.-Z.; Dong, J.; Zhou, J.; Zhang, X.-D.; Zheng, P.; Wang, N.-L.; Luo, J.-L. *Chinese Physics Letters* **2008**, *25*, 3403.

24. Awana, V. P.S.; Meena, R. S.; Pal, A.; Vajpayee, A.; Rao, K. V.R.; Kishan, H., *The European Physical Journal B*, **2011**, 79 (2), 139-146.

25. Malavasi, L.; Artioli, G. A.; Ritter, C.; Mozzati, M. C.; Maroni, B.; Pahari, B.; Caneschi, A., Journal of the American Chemical Society, 2010, 132 (7), 2417-2420.

Chapter 4

Synthesis and characterisation of $Sr_4M^I_2O_6M^{II}_2As_2$ (M^I = Sc, V, Cr; M^{II} = Fe, Co, Ni).

4.1. Introduction.

The search for superconducting materials with high transition temperatures triggered discoveries of new families of compounds with Fe-Pn layers (Pn = As, P, Se)[1-4]. One of the crucial properties of superconducting materials that would lead to higher superconducting transition temperatures is believed to be the long distance between these Fe-As planes[1,5]. Since the first discovery of LaFeAsP[1] there have been various Fe-Pn based superconducting families reported, starting from the simplest 11 (FeSe)[6], through compounds with an oxide layer between the Fe-Pn slabs like those mentioned in the previous chapter: 1111 (REFeAsO)[1,7-9], 122 ($REFe_2As_2$)[10,11], or 32522 ($Sr_3Sc_2O_5Fe_2As_2$)[12]. These discoveries have catalysed the search for superconducting compositions in related materials in which two-dimensional Fe-Pn slabs are also present, and with even larger distances between neighbouring Fe-Pn layers. This is because it is believed that there are two major parameters that are important to achieve superconductivity in a sample: high symmetry of $Fe-Pn_4$ tetrahedra and the size of the pnictide atoms.

This search has now led to the synthesis of iron-based oxyarsenides with the general formula $Sr_4M^I_2O_6M^{II}_2As_2$ (M^I = Cr, Sc, V; M^{II} = Fe, Co, Ni)[13-19] (abbreviated to 42622) with a perovskite structure layered between Fe-As layers instead of a simple REO layer. This new family of compounds are thought to be good parent materials for achieving superconductivity ($Sr_4Cr_2O_6Fe_2As_2$)[18,20] or are known to be superconducting without any doping ($Sr_4Sc_2O_6Ni_2As_2$)[16]. An important feature of these compounds is the large Fe-As interlayer distance, which is determined by the size of the perovskite block. These are very complex systems

due to the size of these compounds' lattice structures and possible multiple valences of building atoms.

The 42622 system (Figure 4.1) is very different from other Fe-As based systems. In analogy with the REFeAsO systems, these materials adopt a tetragonal crystal structure (space group *P4/nmm*) where the Fe/Co/Ni-As planes are sandwiched between perovskite K_2NiF_4- type oxide layers of $Sr_4M_2O_6$ (M = Sc, V, Cr, Mg/Ti). However, it has one of the biggest unit cell dimensions and does not show the spin density wave ordering in parent compounds or any structural anomalies, which are typical for other systems. Some of the parent compounds also show a superconducting transition without any doping (V, Ni) although in the case of $Sr_4V_2O_6Fe_2As_2$ the exact way of achieving superconductivity is still debatable, as numerous reports show different answers as to what induces the superconducting transition in this compound[14,15,19].

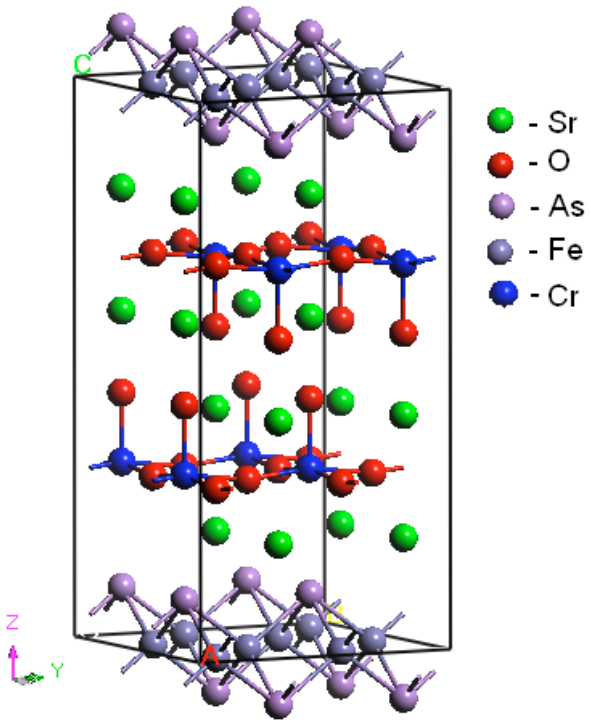

Figure 4.1. Schematic diagram of the room temperature tetragonal structure of $Sr_4Cr_2O_6Fe_2As_2$.

The size of the 42622 compounds makes it difficult to prepare very pure samples, as possible interactions between building atoms are not perfectly known. This also makes it difficult to do magnetic measurements, as magnetism coming from Fe can interfere with other magnetic atoms present in the structure (for example V, Cr). In this work a combination of structural, electronic resistivity and magnetisation measurements has been used to study the family $Sr_4M^I_2O_6M^{II}_2As_2$ (M^I = Sc, V, Cr; M^{II} = Fe, Co, Ni) to investigate the properties of these materials. Synchrotron diffraction data showed a phase transition in $Sr_4V_2O_6Fe_2As_2$, which is unusual for this family, and superconductivity is present in two parent compounds without any doping: $Sr_4V_2O_6Fe_2As_2$ and $Sr_4Sc_2O_6Ni_2As_2$. Neutron diffraction also revealed an antiferromagnetic ordering in $Sr_4Cr_2O_6Fe_2As_2$.

4.2. $Sr_4Sc_2O_6M_2As_2$ (M = Fe, Co, Ni) parent compounds.

4.2.1. Experimental.

All samples were prepared by solid-state synthesis in two steps. The first step was to synthesise SrAs powder by mixing small Sr pieces with As powder and heating it in an evacuated quartz tube for 2 hours at 500°C (heating rate 250°C/hour), followed by 16 hours at 700°C (at the same heating rate). After cooling to 80°C it was then heated again for another 16 hours at 700°C. The quality of the prepared SrAs powder was checked using a D8 Bruker powder diffractometer.

In the next step, pre-made SrAs powder was mixed in an agate mortar with Sc_2O_3, SrO (degassed for 12 hours at 200°C using a vacuum line to remove any traces of moisture), Fe/Co/Ni and As powders according to the general formula $Sr_4Sc_2O_6M_2As_2$ (M = Fe, Co, Ni) in the reaction described by Equation 4.1.

$$Sr_4Sc_2O_6M_2As_2 = SrAs + 3SrO + As + Sc_2O_3 + 2Fe/Co/Ni$$

Equation 4.1.

Mixed powders were pelletized and sealed in quartz tubes with Ar backfilling (0.2 bars). Due to the high air and moisture sensitivity of the starting materials, all

work was carried out in a glovebox with a pure argon atmosphere. Initially reactions were made on a small scale (0.2 g) to prepare the best quality products. Heating treatment was performed at 1200°C for 48 hours with a heating step of 3°C/min, followed by cooling to room temperature slowly, at a rate of around 3°C/min. For the $Sr_4Sc_2O_6Ni_2As_2$ and $Sr_4Sc_2O_6Fe_2As_2$ only one heating was performed as the prepared amounts of both compositions were small (0.2 g), however the second batch of $Sr_4Sc_2O_6Co_2As_2$ powder was prepared in a larger scale of 2 g for neutron powder diffraction measurements. For that synthesis, after the first heating, the tubes containing 2 g samples of $Sr_4Sc_2O_6Co_2As_2$ were cooled down to room temperature, reground, pressed into pellets again and heated in evacuated quartz tubes for 48 hours at 1200°C.

Black polycrystalline samples of $Sr_4Sc_2O_6Ni_2As_2$ and $Sr_4Sc_2O_6Co_2As_2$ were kept in the glovebox due to air-sensitivity of the samples, while $Sr_4Sc_2O_6Fe_2As_2$ is stable in air. The quality of all the samples was firstly checked using X-ray powder diffraction measurements on a laboratory Bruker D8 AXS diffractometer with a Cu $K_{\alpha 1}$ radiation source. Measurements of magnetic properties were done with a Quantum Design Magnetic Property Measurement System magnetometer using Zero field cooled (ZFC) and Field Cooled (FC) DC protocols, with an applied magnetic field (*H*) of 10 Oe and 20 Oe for testing superconductivity. Measurements of temperature dependence of susceptibility with a 10 kOe applied magnetic field were also performed. The electrical resistivity was only measured for $Sr_4Sc_2O_6Fe_2As_2$ due to air-sensitivity of the remaining two samples. High resolution synchrotron X-ray powder diffraction (XRPD) experiments were conducted on the ID31 beamline at the European Synchrotron Radiation Facility (ESRF), Grenoble, France. For the case of $Sr_4Sc_2O_6Co_2As_2$, neutron powder diffraction patterns were also collected at the D2B and D20 beamlines at the Institute Laue - Langevin (ILL) in Grenoble, France. Rietveld analysis of the powder diffraction profiles was performed using the GSAS suite of programs.

4.2.2. Results.

4.2.2.1. Structural properties.

Laboratory powder diffraction measurements showed that the synthesis of the main phases of $Sr_4Sc_2O_6Fe_2As_2$, $Sr_4Sc_2O_6Co_2As_2$ and $Sr_4Sc_2O_6Ni_2As_2$ were successful without any other visible impurity phases. Further measurements were performed using synchrotron high-resolution X-ray diffraction, and also neutron powder diffraction in the case of $Sr_4Sc_2O_6Co_2As_2$.

High resolution X-ray powder diffraction data was collected in 0.5 mm diameter silica capillaries at various temperatures between 20 K and 300 K using the synchrotron radiation wavelength of 0.3994370 Å. In the case of the $Sr_4Sc_2O_6Co_2As_2$, sample synchrotron measurement was performed on a powder mixture of the compound with Si powder to ensure accuracy of the measured temperature. For all samples, the capillary was spun inside a cryostat with liquid helium flow. Rietveld analysis of the high resolution data showed that $Sr_4Sc_2O_6Fe_2As_2$, $Sr_4Sc_2O_6Co_2As_2$ and $Sr_4Sc_2O_6Ni_2As_2$ at room temperature all adopt a tetragonal *P4/nmm* structure. No other phase impurities were seen in $Sr_4Sc_2O_6Fe_2As_2$ and $Sr_4Sc_2O_6Ni_2As_2$, but in the case of $Sr_4Sc_2O_6Co_2As_2$ non-magnetic SrO (10%) and CoAs (5%) impurities were detected. The refined structural parameters obtained by Rietveld analysis of the synchrotron X-ray diffraction data, collected at room temperature, are shown in Table 4.1 and Figure 4.5. The fit to the room temperature datasets of $Sr_4Sc_2O_6Fe_2As_2$, $Sr_4Sc_2O_6Co_2As_2$ and $Sr_4Sc_2O_6Ni_2As_2$ are given in Figures 4.2 to 4.4.

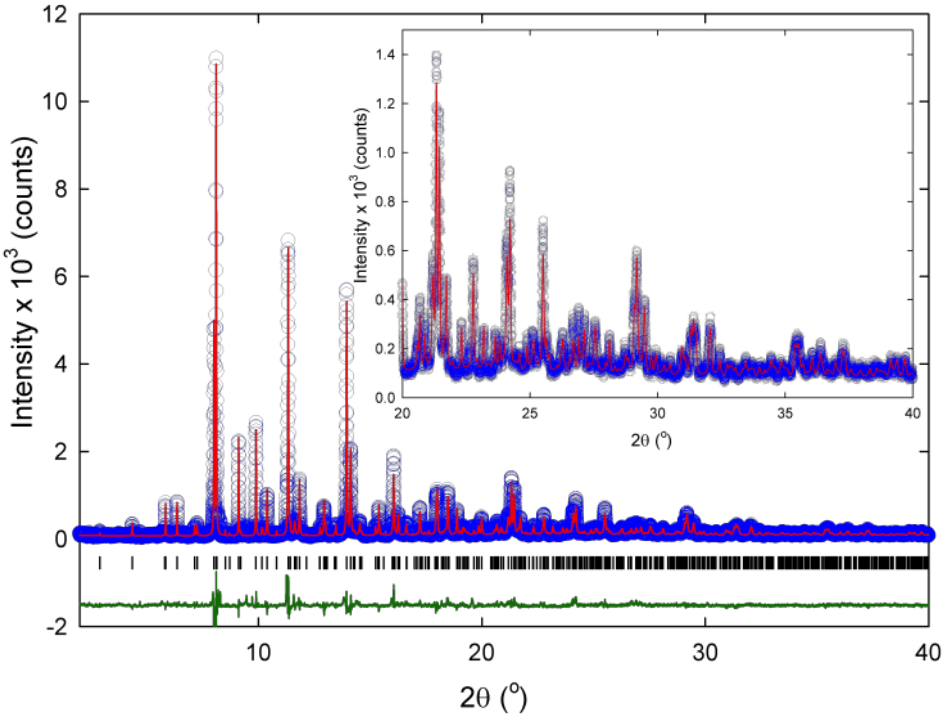

Figure 4.2. Final observed (blue circles), calculated (red solid line), and difference (lower green solid line) plots for the Rietveld refinement of 42622-Fe at RT. Tick marks show the reflection positions. The refinement proceeded with the main phase in the *P4/nmm* space group. The X-ray wavelength is 0.4030068 Å. Inset shows zoom in on the 20 to 40 2θ data range.

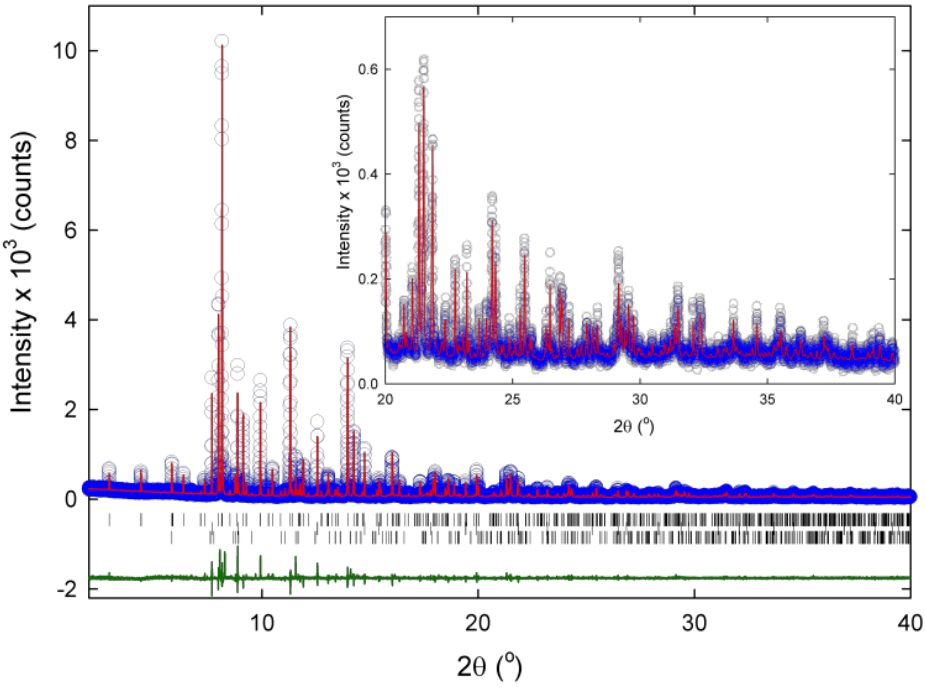

Figure 4.3. Final observed (blue circles), calculated (red solid line), and difference (lower green solid line) plots for the Rietveld refinement of 42622-Co at RT. Tick marks show the reflection positions and are from top to bottom: $Sr_4Sc_2O_6Co_2As_2$, SrO and CoAs. The refinement proceeded with the main phase in the *P4/nmm* space group. The X-ray wavelength is 0.4030068 Å. Inset shows zoom in on the 20 to 40 2θ data range.

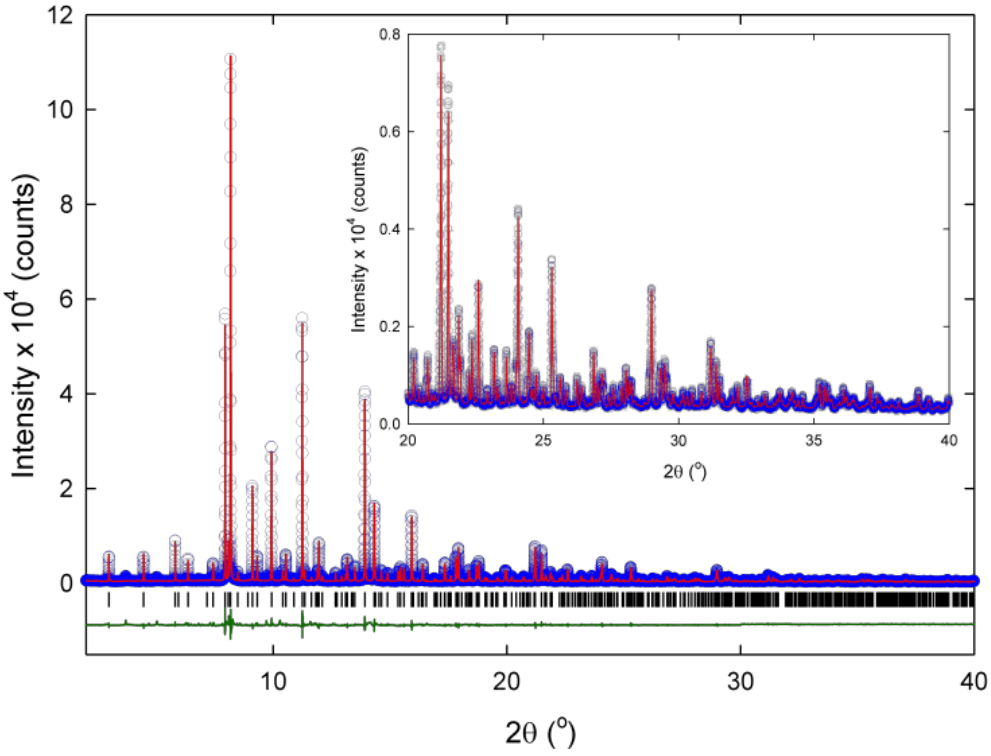

Figure 4.4. Final observed (blue circles), calculated (red solid line), and difference (lower green solid line) plots for the Rietveld refinement of 42622-Ni at RT. Tick marks show the reflection positions. The refinement proceeded with the main phase in the *P4/nmm* space group. The X-ray wavelength is 0.4030068 Å. Inset shows zoom in on the 20 to 35 2θ data range.

Table 4.1. Refined structural parameters and bond lengths (Å) and angles (°) for $Sr_4Sc_2O_6Fe_2As_2$, $Sr_4Sc_2O_6Co_2As_2$ and $Sr_4Sc_2O_6Ni_2As_2$ obtained from Rietveld refinements of the synchrotron X-ray diffraction data at room temperature. Estimated errors in the last digits are given in parentheses.

		Fe	*Co*	*Ni*
Space group		*P4/nnm*	*P4/nnm*	*P4/nnm*
a (Å)		4.05157(6)	4.05257(2)	4.077668(8)
c (Å)		15.8085(6)	15.5764(1)	15.41720(6)
Volume (Å^3)		259.502(3)	255.817(2)	256.348(1)
Sr	B_{iso} (Å^2)	0.61(6)	0.13(7)	0.57(6)
	Occ.	1.02(7)	1.01(2)	1.01(8)
	z	0.18523(4)	0.18828(6)	0.18255(7)
Sr	B_{iso} (Å^2)	1.00(5)	0.37(2)	0.90(2)
	Occ.	1.03(5)	0.99(5)	1.03(5)
	z.	0.41427(4)	0.415718(1)	0.414271(2)
Sc	B_{iso} (Å^2)	0.18(5)	0.1(7)	0.28(7)
	Occ.	0.98(8)	0.96 (4)	1.02(3)
	z	0.30718(5)	0.306589(4)	0.302131(7)
Fe/Ni/Co	B_{iso} (Å^2)	0.4(4)	0.53 (9)	0.71(4)
	Occ.	0.98(5)	0.99(5)	0.98 (8)
As	B_{iso} (Å^2)	0.9360(9)	0.0796(6)	0.8479(2)
	Occ	1.03(8)	1.02(2)	1.01(7)
	z	0.07938(4)	0.086439(4)	0.077310(3)
O	B_{iso} (Å^2)	0.4173(2)	0.1719(5)	0.2713(3)
	Occ.	1.09(3)	1.29(3)	1.07(2)
	z	0.29245(2)	0.286014(5)	0.279302(4)
O	B_{iso} (Å^2)	0.2090(2)	0.1159(4)	0.2413(6)
	Occ	1.03(7)	1.12(3)	1.11(5)
	z	0.43000(6)	0.429508(4)	0.423238(3)
R_{wp} (%)		16.00	14.24	11.67
R_{exp} (%)		7.65	4.34	3.47
d (Sc-O) (Å)		2.0517(2) x 4	2.0392(3) x 4	2.0690(5) x 4
		1.9432(2)	1.9131(2)	1.8671(3)
d (Fe-Fe/Ni-Ni/Co-Co) (Å)		2.8649(7) x 4	2.86560(4) x 4	2.88335(6) x 4
d (Fe/Ni/Co-As) (Å)		2.4436(8) x 4	2.3738(5) x 4	2.3617(7) x 4
∠ As-(Fe/Ni/Co)-As (°)		112.00(6) x 2	117.21(6) x 2	119.38(5) x 2
		108.22(4) x 4	105.77(4) x 4	104.76(5) x 4

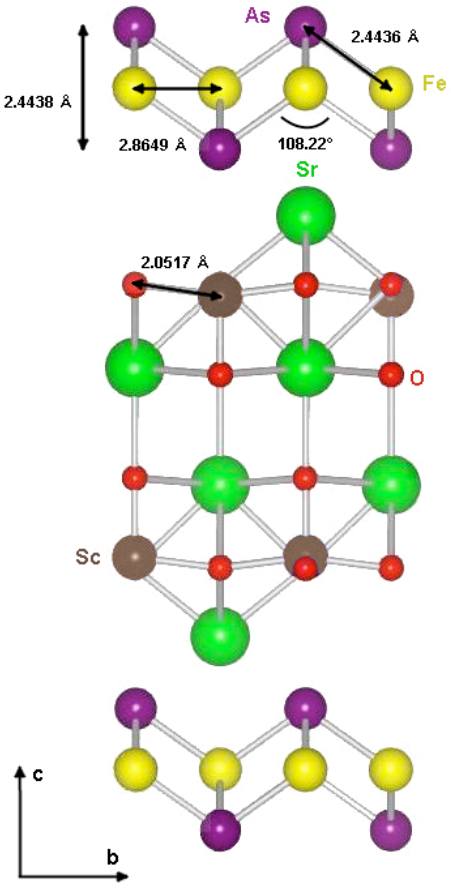

Figure 4.5. Schematic diagram of the room temperature tetragonal structure of the $Sr_4Sc_2O_6Fe_2As_2$ system.

The analysis of lattice constants showed that the *c* axis changes according to the difference in radius of the transition metal used (*c* = 15.8085 Å for Fe, *c* = 15.41739 Å for Ni and *c* = 15.576722 Å for Co), as the ionic radius of Ni^{2+} (0.69 Å) is smaller than Co^{2+} (0.72 Å) and Fe^{2+} (0.77 Å), while the *a* axis shows opposite behaviour (*a* = 4.05157 Å for Fe, *a* = 4.077682 Å for Ni and *a* = 4.0527 Å for Co). These values of the *c* axes are one of the biggest in all Fe-Pn based materials. The different behaviour of the *a* axis is caused by the geometry of $Fe/Co/Ni\text{-}As_4$ (Figure 4.6). The two-fold alpha tetrahedral As-M^{II}-As angle values increase monotonically with the transition metal ion radius (angles versus ionic radii of transition metals are shown in Figure 4.7). Beta tetra-fold As-M^{II}-As

angles values decrease monotonically and are much further in value from the ideal angle of 109.5° than in the ReFeAsO system. Lengths of M^{II}-As bonds also decrease with an increase in the ionic radii of the M^{II} ion. With the described changes in tetrahedra angles, this results in a total decrease of the thickness of M^{II}-As layer, similar to the behaviour observed in 1111 systems.

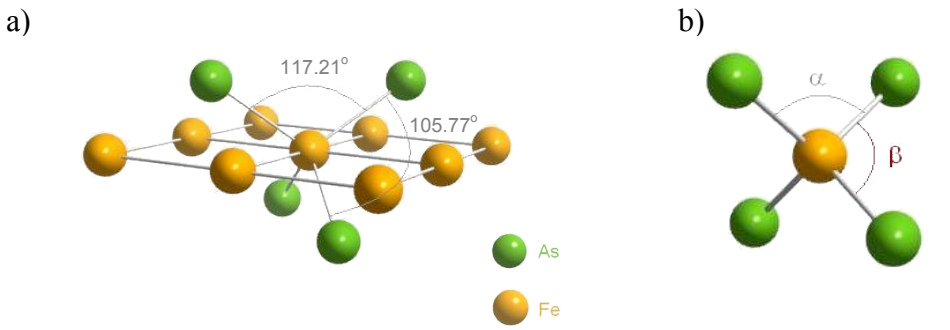

Figure 4.6. Schematic diagram of the **(a)** $FeAs_4$ unit and **(b)** the tetrahedron with detailed two-fold (α) and tetra-fold (β) As-Fe-As angles. The values of the angles reported refer to the $Sr_4Sc_2O_6Co_2As_2$ sample.

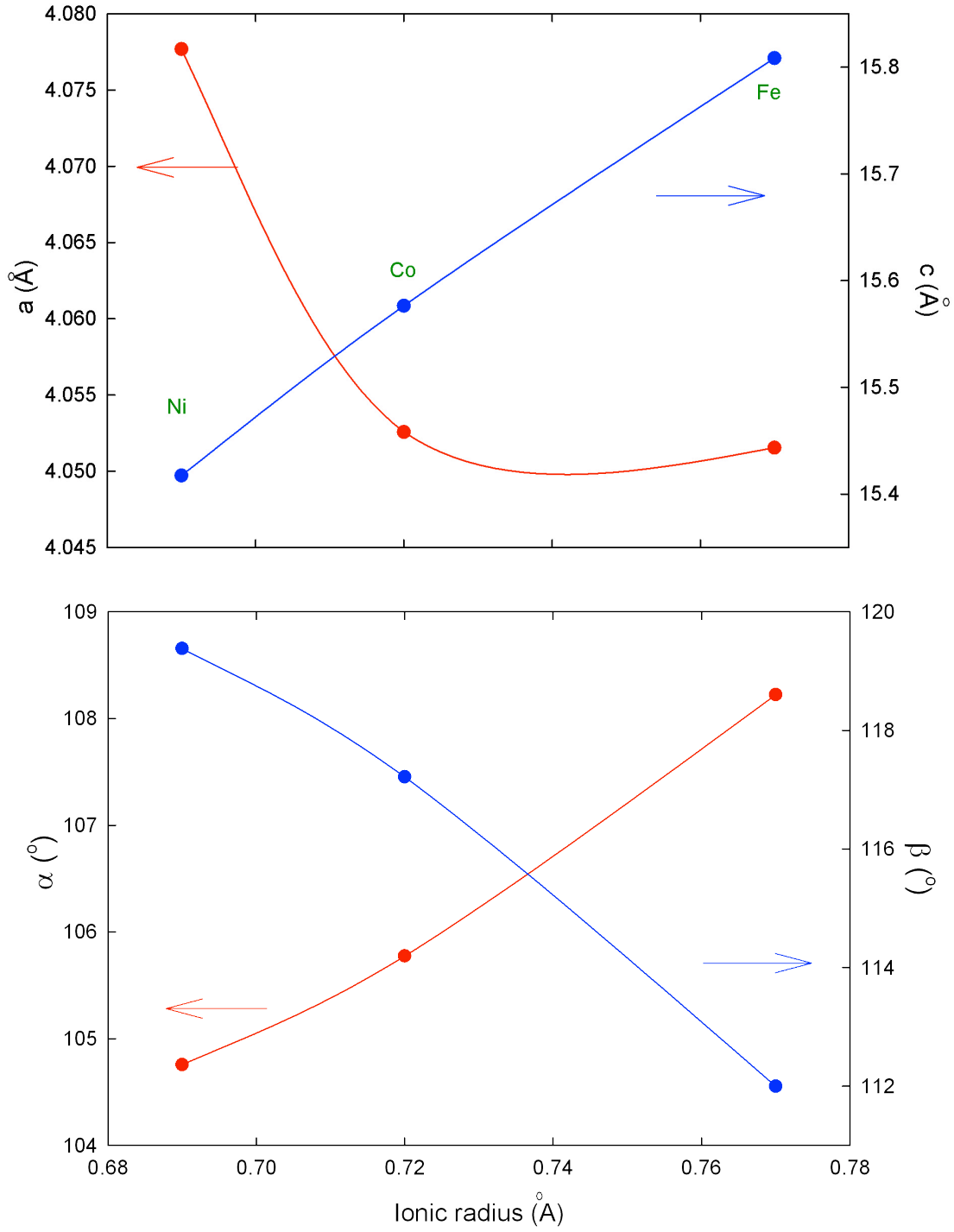

Figure 4.7. Dependence of the *a* and *c* axes and As-M^{II}-As angles versus ionic radii of transition metals (M^{II} = Ni, Co and Fe) in $Sr_4Sc_2O_6Fe_2As_2$, $Sr_4Sc_2O_6Ni_2As_2$ and $Sr_4Sc_2O_6Co_2As_2$.

Synchrotron powder diffraction data was also collected on cooling down to 5 K on all the samples (although only down to 20 K in the case of $Sr_4Sc_2O_6Co_2As_2$ as the capillary used for measurements was filled with argon due to its high air sensitivity). No structural transition was observed during cooling in any of the measured compositions. Representative refined lattice constants and structural parameters for $Sr_4Sc_2O_6Fe_2As_2$, $Sr_4Sc_2O_6Co_2As_2$ and $Sr_4Sc_2O_6Ni_2As_2$ at 20 K are shown in Table 4.2. The Rietveld refinements of members of the family at base temperature are shown below (Figures 4.8 to 4.10). Both *a* and *c* axes values decrease monotonically with decreasing temperature, although at very low temperatures (below 50 K) a slight increase in *c* axis can be seen. It is believed that this is because of negative thermal expansion at low temperatures. The temperature dependence of lattice constants for all compositions is shown in Figures 4.11-4.13. During cooling, Ni-As_4 tetrahedra show in $Sr_4Sc_2O_6Ni_2As_2$ an increase in the Ni-As-Ni angle up to 200 K, and then a decrease up to base temperature. This coincides with the changes in the Ni-As distance, which decreases at higher temperatures and starts increasing at around 150 K. In $Sr_4Sc_2O_6Co_2As_2$ these changes are much less pronounced with the Co-As distance and Co-As-Co angles at almost constant values with minor discrepancies between 100 K and 50 K. In the case of $Sr_4Sc_2O_6Fe_2As_2$, the Fe-As-Fe angles and Fe-As distances also tend to stay reasonably constant upon cooling (Figures 4.14-4.16).

Table 4.2. Refined structural parameters and bond lengths (Å) and angles (°) for $Sr_4Sc_2O_6Fe_2As_2$, $Sr_4Sc_2O_6Co_2As_2$ and $Sr_4Sc_2O_6Ni_2As_2$ obtained from Rietveld refinements of the synchrotron X-ray diffraction data at 20 K. Estimated errors in the last digits are given in parentheses.

		Fe	*Co*	*Ni*
Space group		*P4/nnm*	*P4/nnm*	*P4/nnm*
a (Å)		4.04380(3)	4.04370(1)	4.07026(1)
c (Å)		15.7552(2)	15.5400(1)	15.3682(1)
Volume (Å^3)		257.635(4)	254.102(2)	254.606(2)
Sr	B_{iso} (Å^2)	0.046(4)	0.207(5)	0.556(8)
	Occ.	1.02(6)	1.01(2)	1.01(7)
	z	0.184185(4)	0.188404(5)	0.182549(7)
Sr	B_{iso} (Å^2)	0.09(4)	0.118(6)	0.80(4)
	Occ.	1.03(4)	0.99(5)	1.03(4)
	z.	0.413687(6)	0.415783(5)	0.414271(7)
Sc	B_{iso} (Å^2)	0.03 (7)	0.12(6)	0.37(8)
	Occ.	0.98(7)	0.96(4)	1.03(5)
	z	0.303914(5)	0.307006(4)	0.302131(3)
Fe/Ni/Co	B_{iso} (Å^2)	0.19(9)	0.535(8)	0.96(3)
	Occ.	0.98(4)	0.985(5)	0.98(4)
As	B_{iso} (Å^2)	0.20(7)	0.04(7)	0.93(9)
	Occ	1.03(3)	1.02(4)	1.01(7)
	z	0.079507(6)	0.086325(4)	0.077310(4)
O	B_{iso} (Å^2)	0.15(3)	0.29(5)	0.97(4)
	Occ.	1.09(8)	1.29(4)	1.07(5)
	z	0.283733(7)	0.286178(5)	0.279302(3)
O	B_{iso} (Å^2)	0.36(7)	0.13(5)	1.65(4)
	Occ	1.03(4)	1.12(3)	1.11(6)
	z	0.432091(4)	0.431668(4)	0.423238(2)
R_{wp} (%)		18.00	20.32	14.95
R_{exp} (%)		6.23	4.80	8.00
d (Sc-O) (Å)		2.0484(6) x 4	2.0460(3) x 4	2.0652(5) x 4
		1.9641(3)	1.9919(7)	1.8612(4)
d (Fe-Fe/Ni-Ni/Co-Co) (Å)		2.85944(8) x 4	2.8593(3) x 4	2.8781(4) x 4
d (Fe/Ni/Co-As) (Å)		2.4368(7) x 4	2.3695(7) x 4	2.3566(5) x 4
∠ As-(Fe/Ni/Co)-As (°)		112.15(5) x 2	117.14(3) x 2	119.45(4) x 2
		108.15(5) x 4	105.78(7) x 4	104.73(7) x 4

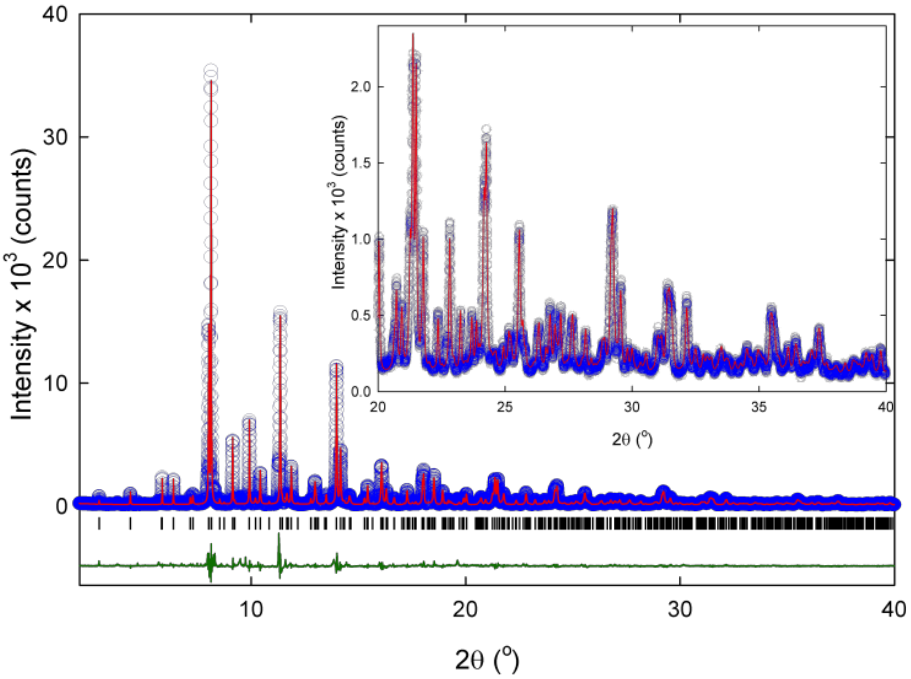

Figure 4.8. Final observed (blue circles), calculated (red solid line), and difference (lower green solid line) plots for the Rietveld refinement of 42622-Fe at 5 K. Tick marks show the reflection positions. The refinement proceeded with the main phase in the *P4/nmm* space group. The X-ray wavelength is 0.4030068 Å. Inset shows zoom in on the 20 to 35 2θ data range.

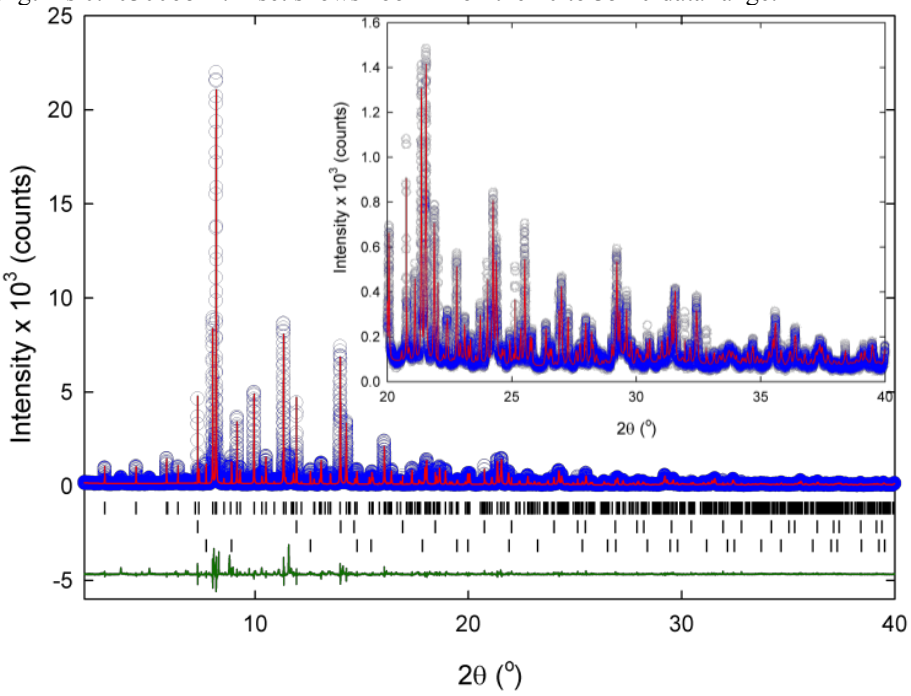

Figure 4.9. Final observed (blue circles), calculated (red solid line), and difference (lower green solid line) plots for the Rietveld refinement of 42622-Co at 20 K. Tick marks show the reflection positions and are from top to bottom: $Sr_4Sc_2O_6Co_2As_2$, SrO and CoAs. The refinement proceeded with the main phase in the *P4/nmm* space group. The X-ray wavelength is 0.4030068 Å. Inset shows zoom in on the 20 to 35 2θ data range.

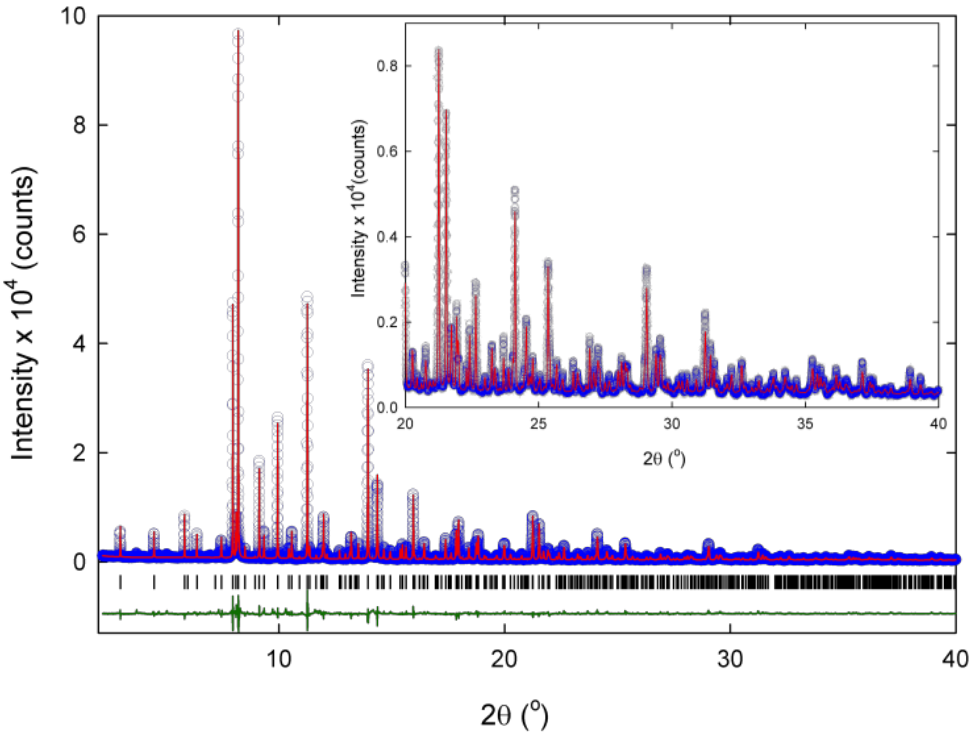

Figure 4.10. Final observed (blue circles), calculated (red solid line), and difference (lower green solid line) plots for the Rietveld refinement of 42622-Ni at 5 K. Tick marks show the reflection positions. The refinement proceeded with the main phase in the *P4/nmm* space group. The X-ray wavelength is 0.4030068 Å. Inset shows zoom in on the 20 to 35 2*θ* data range.

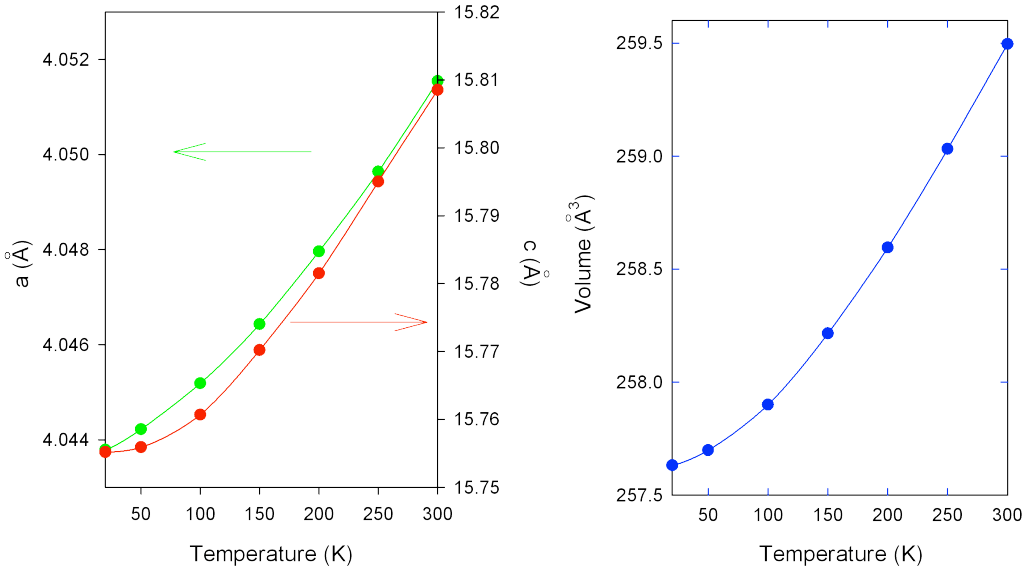

Figure 4.11. On the left: temperature evolution of the lattice constants for 42622-Sc: green and red circles refer to the *a* and *c* lattice constants, respectively. On the right: temperature evolution of the volume of 42622-Sc.

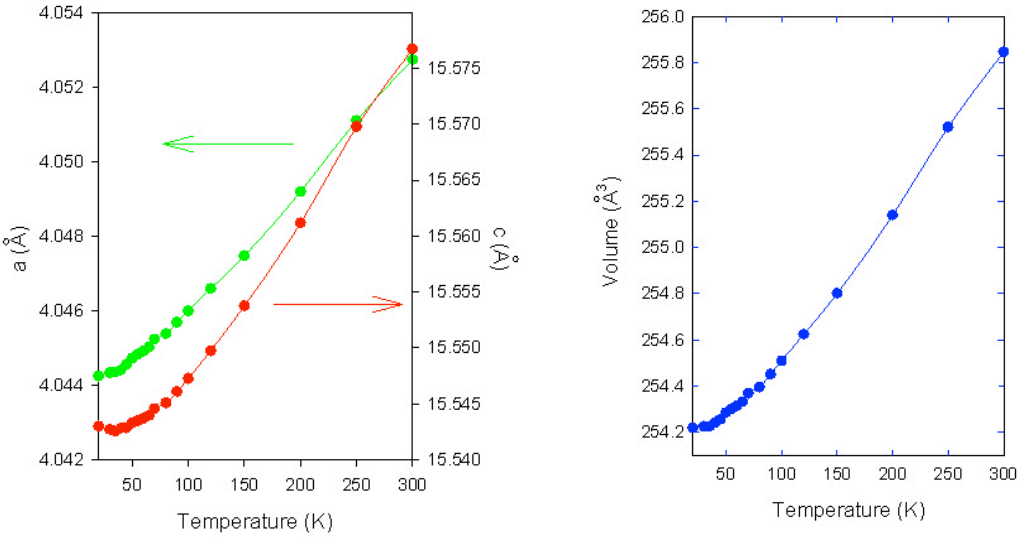

Figure 4.12. On the left: temperature evolution of the lattice constants for 42622-Co: green and red circles refer to the *a* and *c* lattice constants, respectively. On the right: temperature evolution of the volume for 42622-Co.

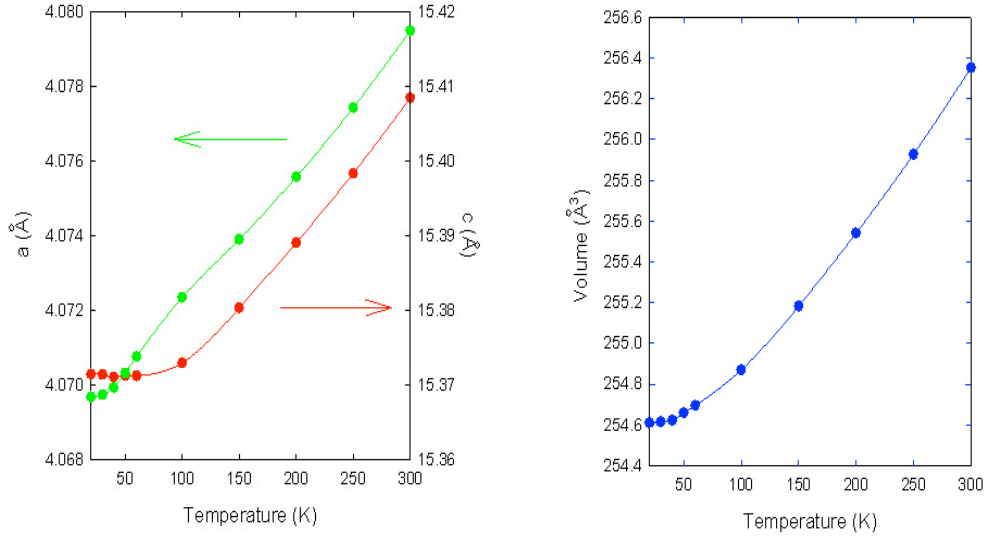

Figure 4.13. On the left: temperature evolution of the lattice constants for 42622-Ni: green and red circles refer to the *a* and *c* lattice constants, respectively. On the right: temperature evolution of the volume for 42622-Ni.

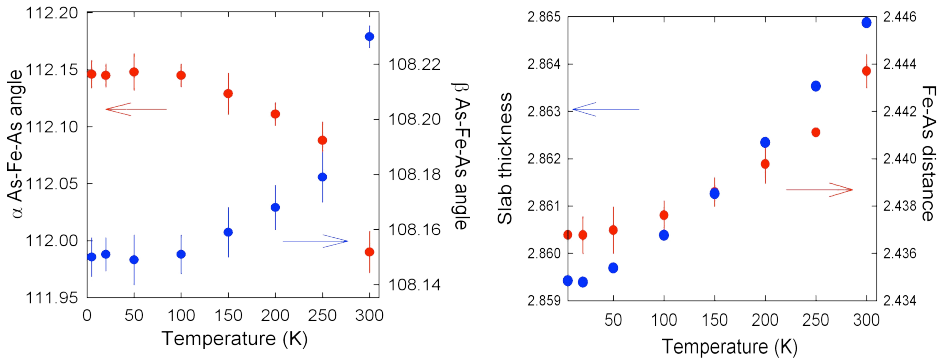

Figure 4.14. On the left: temperature evolution of the two-fold and tetra-fold angles for 42622-Sc: red and blue circles refer to α and β angles, respectively. On the right: temperature evolution of the Fe-As distance and the slab thickness for that composition.

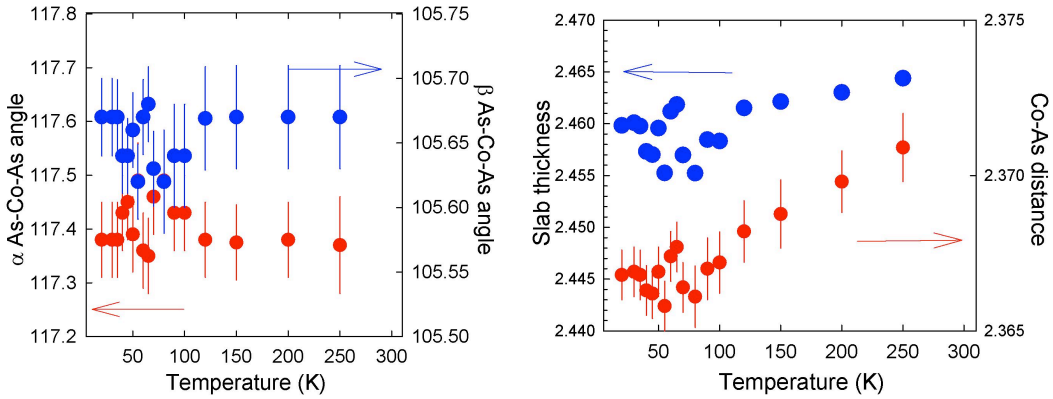

Figure 4.15. On the left: temperature evolution of the two-fold and tetra-fold angles for 42622-Co: red and blue circles refer to α and β angles, respectively. On the right: temperature evolution of the Co-As distance and the slab thickness for that composition.

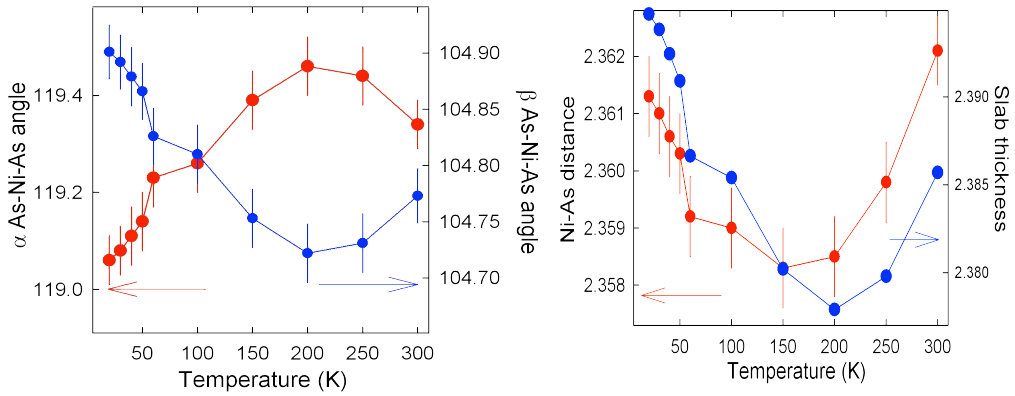

Figure 4.16. On the left: temperature evolution of the two-fold and tetra-fold angles for 42622-Ni: red and blue circles refer to α and β angles, respectively. On the right: temperature evolution of the Ni-As distance and the slab thickness for that composition.

For $Sr_4Sc_2O_6Co_2As_2$, a large amount of powder sample (2 g) was measured using a neutron radiation source at the D2B and D20 beamlines in ILL, Grenoble, France. Firstly, the sample was checked at the D20 beamline in an airtight sealed vanadium can to check for the possibility of any magnetism in the structure. No signs of magnetic peaks were observed between 100 K and 2 K (Figure 4.17).

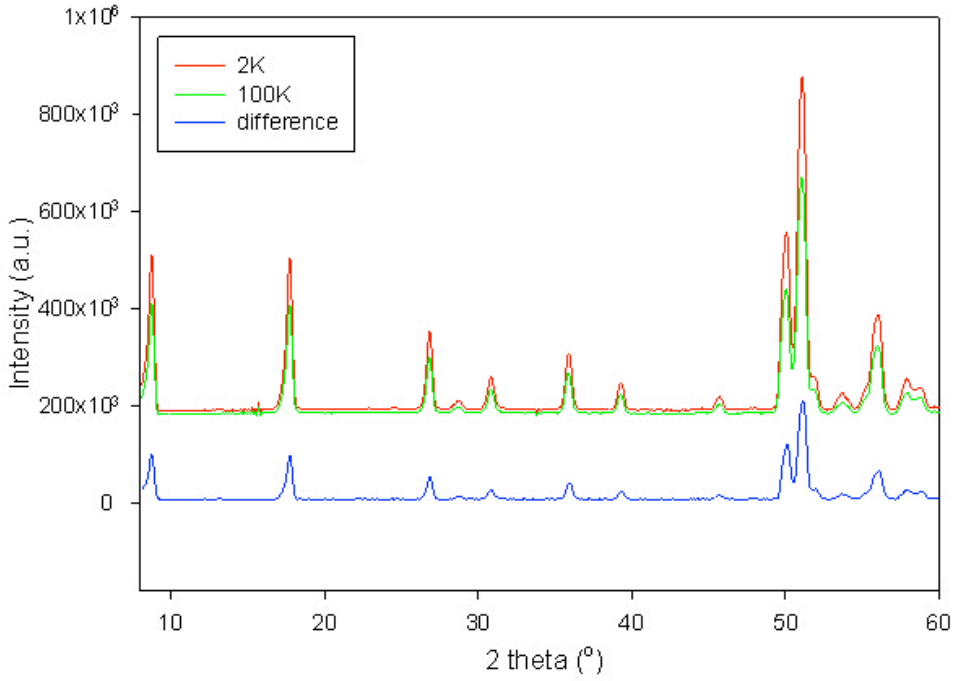

Figure 4.17. Raw neutron data of $Sr_4Sc_2O_6Co_2As_2$ performed at D20 showing the difference between 100 K and 2 K data.

Then measurements using the same vanadium can were performed at D2B to investigate structural features of the composition, as this beamline provides very high intensity and resolution, which are necessary for that structure. Using the same structural model as with synchrotron data, the Rietveld refinement analysis provided corresponding structural parameters to those obtained from the synchrotron radiation source. In order to check a previously reported[20] possibility of mixed atom occupancies in $Sr_4Cr_2O_6Fe_2As_2$ the combined refinement of both synchrotron and neutron data was carried out. There is no sign of atoms mixing between different sites, and both synchrotron and neutron data are in good agreement.

4.2.2.2. *Magnetic properties.*

The DC magnetic susceptibilities of $Sr_4Sc_2O_6Fe_2As_2$, $Sr_4Sc_2O_6Co_2As_2$ and $Sr_4Sc_2O_6Ni_2As_2$ were firstly measured to check for superconductivity in these samples using zero field cooled – field cooled (ZFC/FC) protocol with an applied magnetic field of 10 Oe. Only $Sr_4Sc_2O_6Ni_2As_2$ showed a superconducting transition at very low temperatures while neither $Sr_4Sc_2O_6Fe_2As_2$ nor $Sr_4Sc_2O_6Co_2As_2$ showed any hints of superconductivity. The superconducting transition in $Sr_4Sc_2O_6Ni_2As_2$ occurs at 2.5 K with the calculated shielding fraction of 13%. The magnetic susceptibility of this sample is shown in Figure 4.18.

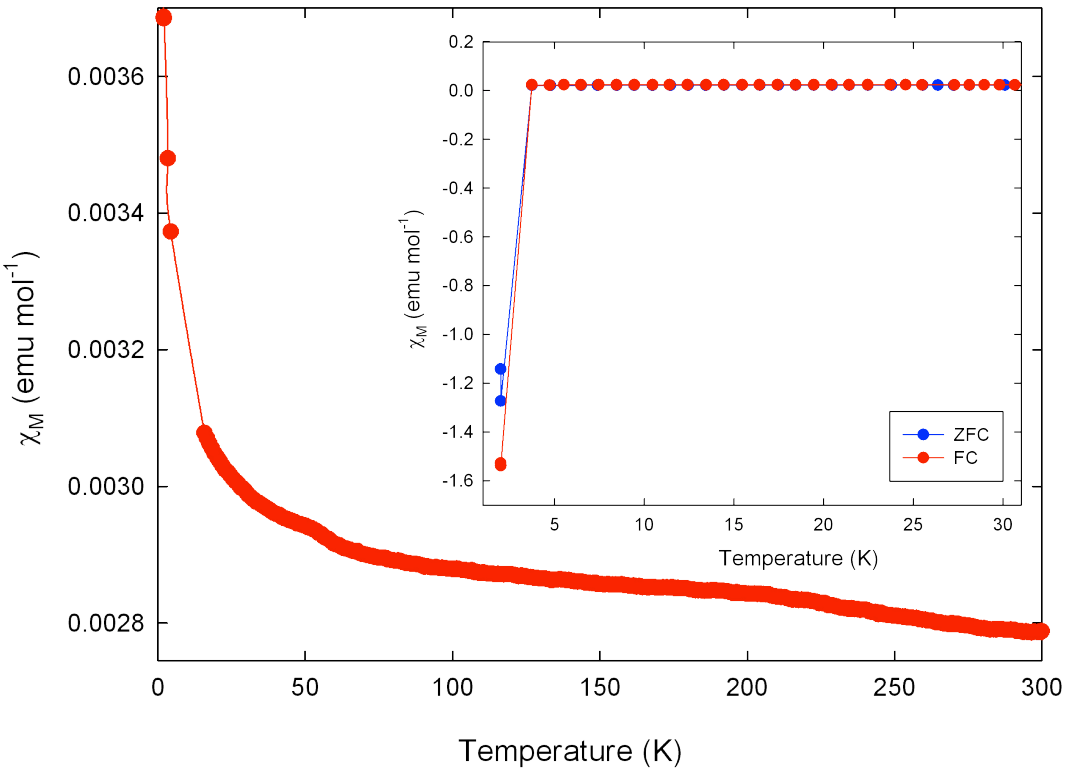

Figure 4.18. Temperature evolution diagram of χ_M for $Sr_4Sc_2O_6Fe_2As_2$ sample. The inset shows the superconducting transition for $Sr_4Sc_2O_6Ni_2As_2$.

Of all of the compositions, neither $Sr_4Sc_2O_6Fe_2As_2$ nor $Sr_4Sc_2O_6Ni_2As_2$ show a Curie-Weiss like behaviour in the whole range of temperatures between 300 K

and 5 K. The $Sr_4Sc_2O_6Co_2As_2$ composition however revealed paramagnetic behaviour in the high temperature range between 70 K and 300 K (Figure 4.19). A fit to $\chi = C/(T-\Theta)$ gives $C = 2.18(1)$ emu $K^{-1}mol^{-1}$ and $\Theta = -146.83(1)$ K. There is no sign of a spin density wave transition observed in any of the compounds, which is very different from other Fe-Pn based families. This fact indicates that increasing the distance between layers of Fe/Co/Ni-As is destructive for the formation of spin density wave transitions.

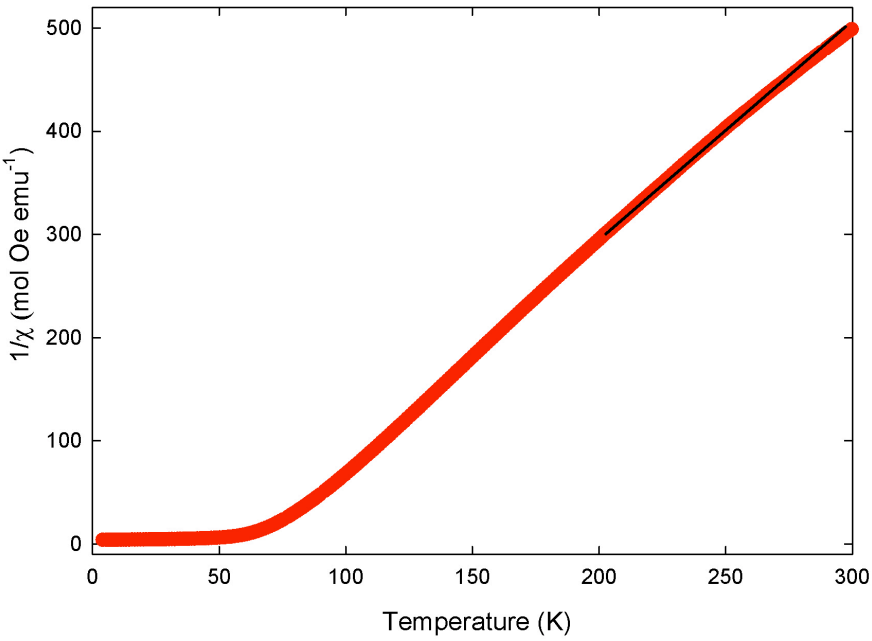

Figure 4.19. Temperature dependence of the inverse magnetic susceptibility for $Sr_4Sc_2O_6Co_2As_2$, the black line corresponds to the fit to Curie-Weiss law.

4.2.2.3. Resistivity measurements.

Resistivity measurements were performed only on the $Sr_4Sc_2O_6Fe_2As_2$ composition, as both other samples were sensitive to air and moisture and thus not able to be prepared for measurement in an open air.

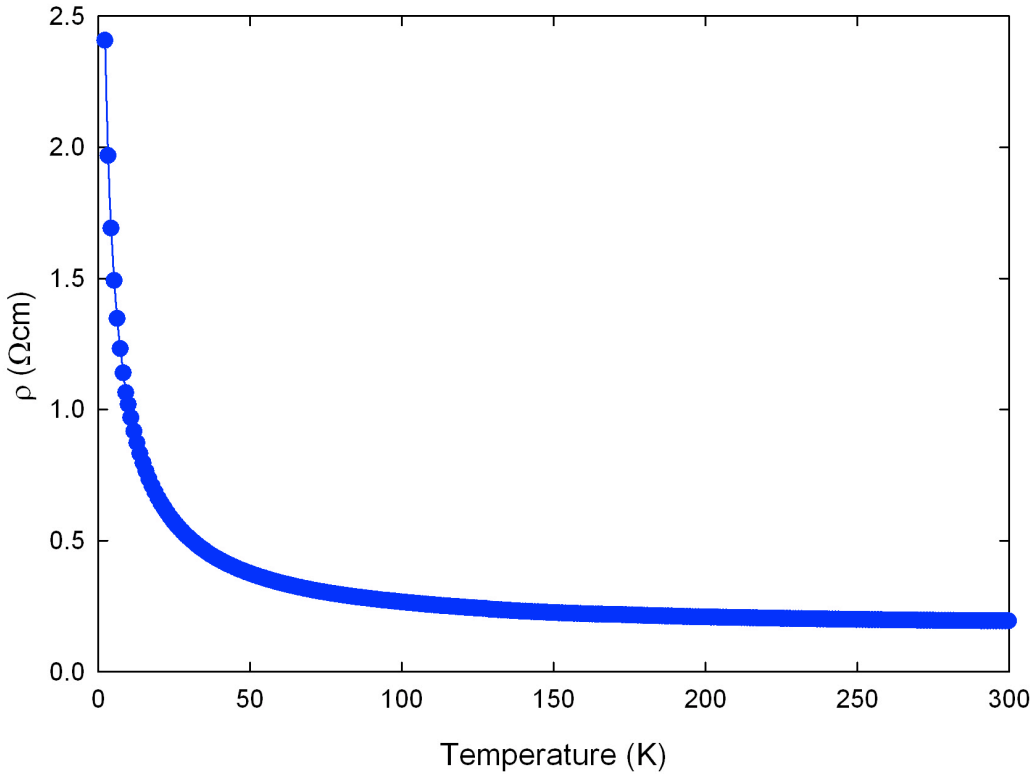

Figure 4.20. Temperature dependence of the resistivity of $Sr_4Sc_2O_6Fe_2As_2$.

As presented in Figure 4.20. $Sr_4Sc_2O_6Fe_2As_2$ shows weak semiconducting type behaviour down to about 50 K and then resistivity increases sharply with decreasing temperature. No anomalies were found in the whole range of temperatures. This is in contrast with other Fe-based superconducting materials where the parent compounds have shown strong changes in electrical resistivity and magnetisation measurements that corresponded to structural and magnetic phase transitions in these samples. This also suggests that an increase in thickness of the layer of the charge reservoir can destroy the spin density wave anomaly seen so commonly in the parent compounds of other families of oxypnictides.

4.3. $Sr_4M_2O_6Fe_2As_2$ (M = Cr, V) parent compounds.

4.3.1. Introduction.

A deeper interest was shown in two other compositions of the 42622 family - $Sr_4Cr_2O_6Fe_2As_2$ and $Sr_4V_2O_6Fe_2As_2$. In the case of the first one, the most interesting feature was the possible magnetic transition in this parent compound and a further check on the way of doping this sample to induce superconductivity. The vanadium sample has already been researched by many scientists[14,21,22,23] and there were still numerous things that are unclear about the mechanism behind its high temperature superconductivity (up to 40 K) in the parent compound state, which was unexpected considering the other compositions in this family.

4.3.2. Experimental.

The polycrystalline samples of $Sr_4Cr_2O_6Fe_2As_2$ and $Sr_4V_2O_6Fe_2As_2$ were prepared in a two-step solid state synthetic procedure. The first step was to prepare starting materials by synthesising the precursor SrAs by grinding pure Sr pieces with As powder from freshly ground arsenic pieces, and sealing them under vacuum in a silica tube. This was heated for 2 hours at 500°C (heating rate 250°C/hour) and then for 16 hours at 700°C (the same heating rate). After cooling to 80°C, the heating process was repeated at 700°C for 16 hours. The compound was prepared in an argon filled glovebox and the resulting powder was kept in the glovebox. The quality of the product was checked using a D8 Bruker powder diffractometer. All oxides (SrO, Cr_2O_3, V_2O_5 and V_2O_3) used in the next step were degassed on a vacuum line at 120°C for 12 hours to remove any traces of moisture.

The second step was to synthesise $Sr_4Cr_2O_6Fe_2As_2$ according to the formula:

$$Sr_4Cr_2O_6Fe_2As_2 = Sr + 3SrO + 2As + Cr_2O_3 + 2Fe$$

Equation 4.2.

Pure powders of SrO, As, Cr_2O_3, Fe and small pieces of Sr were mixed together in an agate mortar and pressed into pellets which were sealed in a silica tube backfilled with 0.2 bar of argon. The tube was then heated at the rate of 3°C/min to 1200°C for 48 hours. After cooling to room temperature, the pellet was ground and heated again in the same conditions. The cooling, grinding and re-heating process was repeated once more. All works were carried out in a glovebox with a protective atmosphere of argon due to the air-sensitivity of some of the starting materials. The product was a black powder, and it was stable in air.

In the case of $Sr_4V_2O_6Fe_2As_2$, two different syntheses were conducted with the use of different starting materials according to formulae:

$$Sr_4V_2O_6Fe_2As_2 = 2SrAs + SrO + Sr + V_2O_5 + 2Fe$$

Equation 4.3.

$$Sr_4V_2O_6Fe_2As_2 = 2As + 3SrO + Sr + V_2O_3 + 2Fe$$

Equation 4.4.

In both synthetic routes, all of the starting materials were mixed thoroughly and grounded together in a mortar and pelletized. Pellets were sealed in quartz tubes filled with 0.2 bar of argon. The heating treatment in both cases was performed at 1050°C for 30 hours with a heating rate of 3°C/min, done twice with an intermediate grounding of the pellets. The preparation of the samples was carried out in a high purity argon-filled glovebox. The final product was dark grey/black pellets and even though the powders seemed to be stable in air they were kept in a glovebox to prevent any contact with oxygen.

In order to check the influence of oxygen content sample pellets of V-42622 were reheated in evacuated quartz tubes with a small amount of Na_2O_2 (during heating it decomposes releasing oxygen) for 4-12 hours at 500°C.

The initial quality of both $Sr_4Cr_2O_6Fe_2As_2$ and $Sr_4V_2O_6Fe_2As_2$ were checked with the use of X-ray powder diffraction measurements on laboratory Bruker D2

Phaser and Bruker D8 AXS diffractometers with a Cu $K_{\alpha 1}$ radiation source. Measurements of magnetic properties were done using a Quantum Design Magnetic Property Measurement System magnetometer using Zero Field Cooled (ZFC) and Field Cooled (FC) DC protocols with an applied magnetic field (*H*) of 10 Oe and 20 Oe for superconductivity testing. The temperature dependence on the susceptibility was also measured with an applied magnetic field of 10 kOe. All of the magnetic susceptibility measurements were performed on the samples sealed in evacuated SQUID quartz tubes to prevent contact with air and moisture, in order to make sure that the measured values were derived from only the samples without any environmental influences. The temperature dependence of the electrical resistivity was measured by the four-probe method on heating between 2 and 300 K. High resolution synchrotron X-ray powder diffraction (XRPD) experiments were conducted on the ID31 beamline at the European Synchrotron Radiation Facility (ESRF), Grenoble, France. In some of these measurements, pure silica powder (99.99%) was mixed with the samples to provide accurate temperature measurements inside the capillaries and to ensure the right conditions during measuring at very low temperatures. This is because silicon has a well defined response to temperature changes, which was important especially below 30 K. Neutron powder diffraction data was collected at the D2B and D20 beamlines at the Institute Laue Langevin (ILL) in Grenoble, France. Diffraction profile analyses were performed using the GSAS suite of the Rietveld analysis program.

4.3.3. Results.

4.3.3.1. Structural properties.

The sample of $Sr_4Cr_2O_6Fe_2As_2$ (abbreviated as Cr-42622) and both samples of $Sr_4V_2O_6Fe_2As_2$ (abbreviated as V-42622) were firstly measured at room temperature on a laboratory diffractometer to check their quality. All the compounds showed very sharp peaks corresponding to the main phase and contained no obvious impurities.

This allowed further investigation of the samples with the use of synchrotron radiation and neutron sources. The high resolution X-ray synchrotron data were collected during a number of experiments on the ID31 beamline at a range of temperatures between 5 K and 300 K with a wavelength 0.3994371 Å and 0.3999912 Å using silica capillaries 0.5 mm diameter, which for low temperature measurements were open on one side for free helium transfer inside the capillaries in order to achieve optimal cooling.

Rietveld analysis of the collected preliminary data at room temperature showed that in all compositions the main phase adopts a tetragonal *P4/nmm* space group, and minor impurity phases of SrO (4% in Cr-42622), Sr_2VO_4 (14% in V-42622 made with V_2O_3) and FeAs (7% in Cr-42622, 4% in V-42622 made with V_2O_3) were also present in two of samples (Figures 4.22-4.24). The *a* axis of the basal plane was determined to be *a* = 3.91343 Å for Cr-42622, *a* = 3.93615 Å for V-42622 made with V_2O_3 and *a* = 3.9364 Å for V-42622 made with V_2O_5. The *c* axis for Cr-42622 was 15.7643 Å, for V-42622 made with V_2O_3 *c* = 15.6888 Å, and *c* = 15.7125 Å for V-42622 made with V_2O_5. The differences in values of *a* axes for Cr-42622 and V-42622 made with V_2O_5 correspond to the different ionic radii of the metal ion in the oxide layer, as the ionic radius of Cr^{3+} is 61.5 pm and V^{5+} is 54 pm, while for V-42622 made with V_2O_3 the value is lower than expected when only taking into account the ionic radius of V^{3+} ion, which is 64 pm. However, the values of *c* axes in all three compounds show completely opposite behaviour with an increase from V-42622 made with V_2O_5 to Cr-42622, and then a rapid drop for V-42622 made with V_2O_3. This can be explained by the fact that only the latter composition shows a superconducting transition due to the structural properties in this system. The refined values of structural parameters of the preliminary data of the three compounds are shown in Table 4.3 and Figure 4.21. The trend in both α and β Fe-As-Fe angles is also dominated by the properties of the compounds with α angle increasing and β angle decreasing with the increasing ionic radii of the main metal. Both angles are changing to reach values very close to the ideal tetrahedral value 109.5°, which is very different to the properties of other superconducting samples in the 42622 family.

Table 4.3. Refined structural parameters and bond lengths (Å) and angles (°) for $Sr_4Cr_2O_6Fe_2As_2$, $Sr_4V_2O_6Fe_2As_2$ made with V_2O_5 and $Sr_4V_2O_6Fe_2As_2$ made with V_2O_3 obtained from Rietveld refinements of the synchrotron X-ray diffraction data at room temperature. Estimated errors in the last digits are given in parentheses.

		Cr	*V-V2O5*	*V-V2O3*
Space group		*P4/nnm*	*P4/nnm*	*P4/nnm*
a (Å)		3.91343(1)	3.9364(8)	3.93615(1)
c (Å)		15.7643(1)	15.7125(6)	15.6888(2)
Volume (Å^3)		241.433(2)	243.479(1)	243.073(2)
Sr	B_{iso} (Å^2)	0.29(5)	0.46(8)	0.55(7)
	Occ.	1.00(2)	1.00(3)	1.02(2)
	z	0.19410(5)	0.19068(4)	0.190172(3)
Sr	B_{iso} (Å^2)	0.56(5)	0.60(5)	0.55(3)
	Occ.	1.00(1)	1.00(2)	1.00(3)
	z.	0.41483(5)	0.41413(4)	0.41380(3)
Cr/V	B_{iso} (Å^2)	0.24(3)	0.30(7)	0.35(7)
	Occ.	0.98(4)	0.99(5)	1.01(6)
	z	0.31073(2)	0.30802(4)	0.30761(3)
Fe	B_{iso} (Å^2)	0.40(9)	0.63(3)	0.27(7)
	Occ.	1.00(3)	0.99(4)	0.97(4)
As	B_{iso} (Å^2)	0.27(8)	0.43(5)	0.56(4)
	Occ	1.00(2)	1.00(4)	1.00(3)
	z	0.08916(2)	0.09055(1)	0.08921(4)
O	B_{iso} (Å^2)	0.37(2)	0.40(3)	1.16(2)
	Occ.	1.02(5)	1.00(3)	1.06(2)
	z	0.29335(3)	0.29290(2)	0.29480(1)
O	B_{iso} (Å^2)	0.33(7)	0.82(5)	1.16(4)
	Occ	1.02(3)	1.06(4)	1.08(2)
	z	0.42701(2)	0.42744(3)	0.42809(4)
R_{wp} (%)		16.77	13.01	20.65
R_{exp} (%)		12.72	7.42	6.49
Cr/V-O (Å)		1.9758(2) x 4	1.9825(2) x 4	1.9783(5) x 4
		1.8331(4)	1.8763(2)	1.8902(3)
Fe-Fe (Å)		2.7672(4) x 4	2.7835(6) x 4	2.7832(5)
Fe-As(Å)		2.4092(2) x 4	2.4287(4) x 4	2.4150(3) x 4
As-Fe-As (º)		108.61(4) x 2	108.27(2) x 2	109.15(3) x 2
		109.89(5) x 4	110.07(4) x 4	109.62(6) x 4

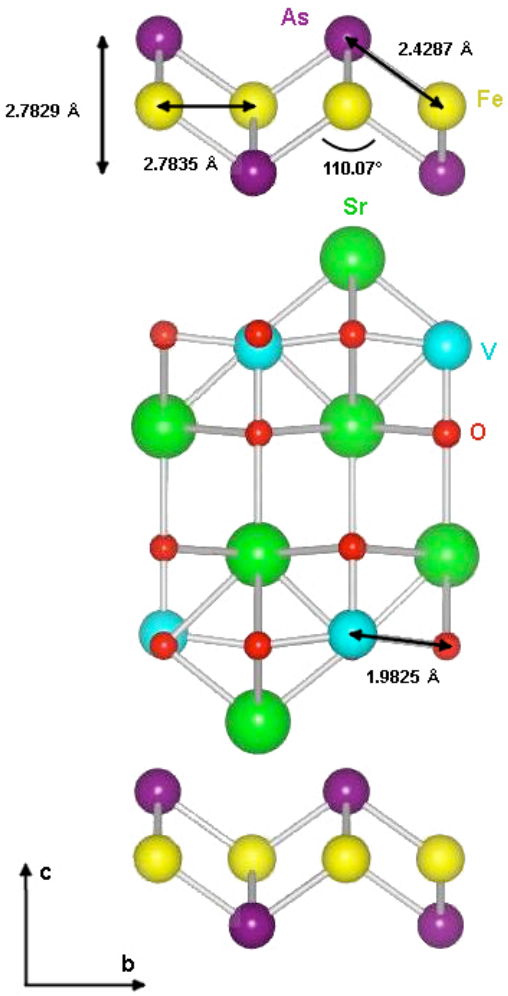

Figure 4.21. Schematic diagram of the room temperature tetragonal structure of the $Sr_4V_2O_6Fe_2As_2$ system.

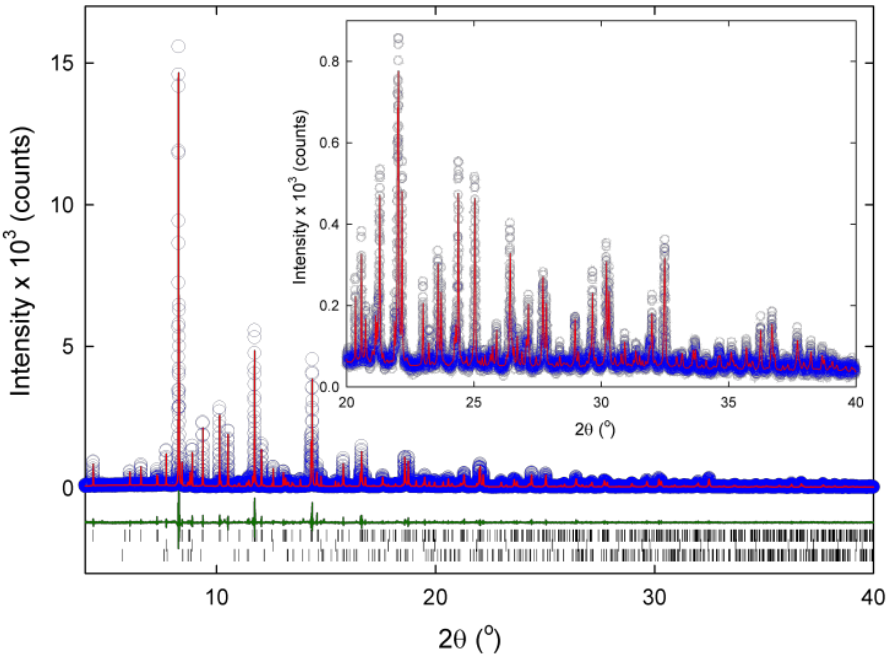

Figure 4.22. Final observed (blue circles), calculated (red solid line), and difference (lower green solid line) plots for the Rietveld refinement of 42622-Cr at RT. Tick marks show the reflection positions and are from top to bottom: $Sr_4Cr_2O_6Fe_2As_2$, SrO and FeAs. The refinement proceeded with the main phase in the *P4/nmm* space group. The X-ray wavelength is 0.4030068 Å. Inset shows zoom in on the 20 to 40 2θ data range.

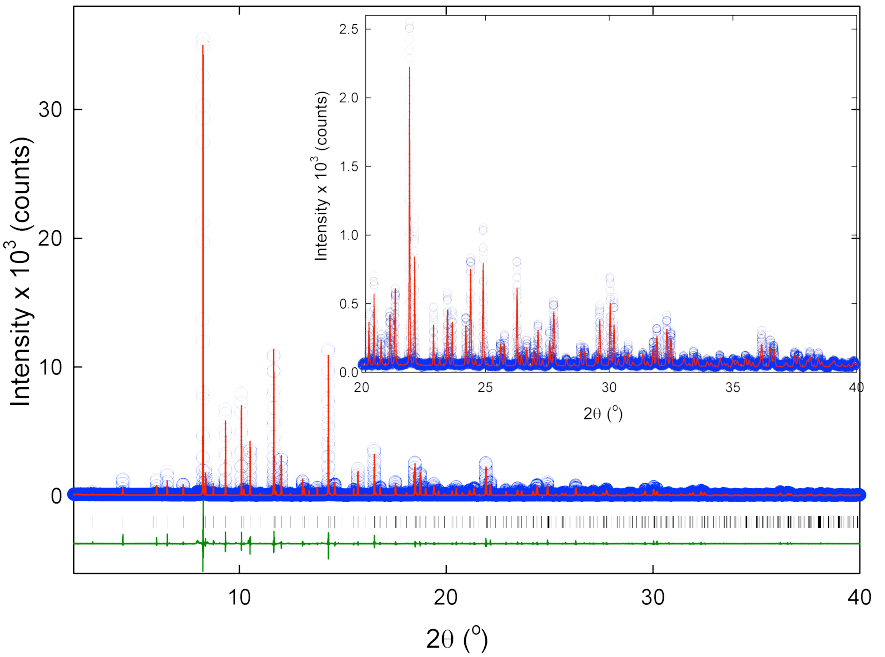

Figure 4.23. Final observed (blue circles), calculated (red solid line), and difference (lower green solid line) plots for the Rietveld refinement of 42622-V made with V_2O_5 at RT. Tick marks show the reflection positions. The refinement proceeded with the main phase in the *P4/nmm* space group. The X-ray wavelength is 0.4030068 Å. Inset shows zoom in on the 20 to 40 2θ data range.

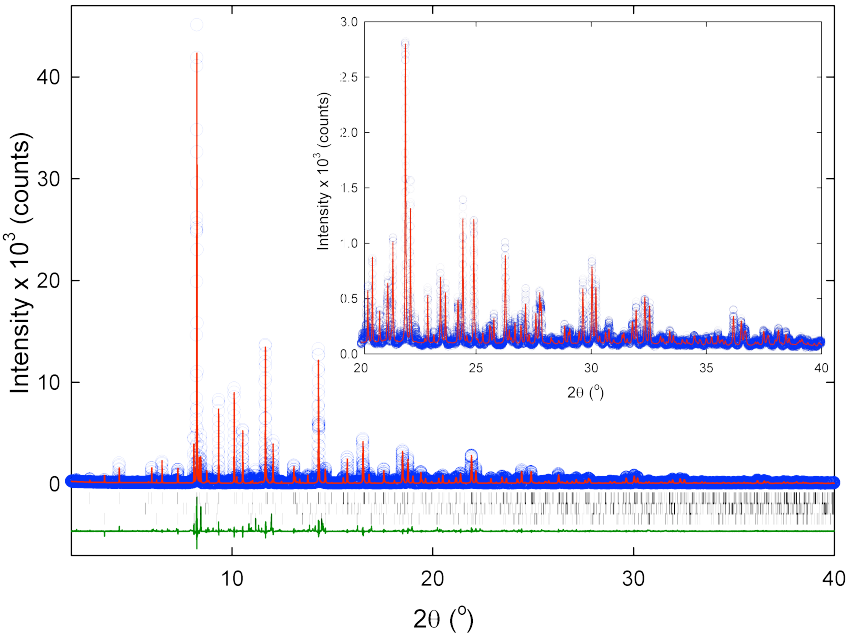

Figure 4.24. Final observed (blue circles), calculated (red solid line), and difference (lower green solid line) plots for the Rietveld refinement of 42622-V made with V_2O_3 at RT. Tick marks show the reflection positions and are from top to bottom: $Sr_4V_2O_6Fe_2As_2$, FeAs and Sr_2VO_4. The refinement proceeded with the main phase in the *P4/nmm* space group. The X-ray wavelength is 0.4030068 Å. Inset shows zoom in on the 20 to 40 2θ data range.

Cr-42622 and V-42622 made with V_2O_5 samples were also measured with synchrotron radiation as a function of temperature between 5 K and 300 K. The refined values of structural parameters of the preliminary data of these two compounds are shown in Table 4.4. The fit to the 5 K datasets of Cr-42622 and V-42622 made with V_2O_5 are given in Figures 4.27 to 4.28. Cr-42622 does not show any sign of peaks splitting or change in shape, which means that no structural phase transition is observed and the sample retains its tetragonal *P4/nmm* crystal structure throughout the whole range of temperatures. The value of the *a* axis decreases monotonically with temperature down to 20 K and then remains stable while the *c* axis decreases with cooling down to 50 K and then remains stable. The values of lattice constants for this composition at base temperature (5 K) are: a = 3.90813 Å and c = 15.6847 Å and their temperature dependence is shown in Figure 4.25. Values of the Fe-As-Fe angles' dependencies on temperature are shown in Figure 4.26, where a minimum and a maximum, in the α and β angles

respectively, are seen at around 40 K, which corresponds to the magnetic transition.

Table 4.4. Refined structural parameters and bond lengths (Å) and angles (°) for $Sr_4Cr_2O_6Fe_2As_2$ and $Sr_4V_2O_6Fe_2As_2$ obtained from Rietveld refinements of the synchrotron X-ray diffraction data at 5 K. Estimated errors in the last digits are given in parentheses.

		Cr	*V-V_2O_5*
Space group		*P4/nnm*	*P4/nnm*
a (Å)		3.90813(1)	3.93007(2)
b (Å)			3.92717(2)
c (Å)		15.6847(4)	15.6254(8)
Volume (Å^3)		239.561(2)	241.165(1)
Sr	B_{iso} (Å^2)	0.20(7)	0.19(3)
	Occ.	1.00(4)	1.00(3)
	z	0.19372(2)	0.18962(1)
Sr	B_{iso} (Å^2)	0.197(3)	0.193(2)
	Occ.	1.00(2)	0.99(4)
	z.	0.41375(1)	0.41343(4)
Cr/V	B_{iso} (Å^2)	0.11(8)	0.46(4)
	Occ.	1.02(2)	1.02(5)
	z	0.30933(5)	0.30663(2)
Fe	B_{iso} (Å^2)	0.12(3)	0.01(2)
	Occ.	1.00(3)	0.99(1)
As	B_{iso} (Å^2)	0.53(8)	0.30(8)
	Occ	1.00(4)	1.01(3)
	z	0.08866(3)	0.08996(1)
O	B_{iso} (Å^2)	1.61(9)	0.69(5)
	Occ.	1.04(1)	0.98(3)
	z	0.29677(3)	0.28914(2)
O	B_{iso} (Å^2)	1.61(4)	0.70(8)
	Occ	1.04(3)	1.09(2)
	z	0.42896(7)	0.42708(1)
O	B_{iso} (Å^2)		0.30(5)
	Occ		1.10(2)
	z		0.29604(3)
R_{wp} (%)		16.77	14.22
R_{exp} (%)		9.39	8.77
Cr/V-O (Å)		1.9639(5) x 4	1.9825(5) x 4
		1.8763(4)	1.8820(3)
Fe-Fe (Å)		2.7634(2) x 4	2.7768(4) x 4
Fe-As(Å)		2.3984(5) x 4	2.3966(2) x 2
			2.4346(3) x 2
As-Fe-As (º)		109.12(2) x 2	110.02(3)
			109.78(2) x 4
		109.64(2) x 4	107.63(3)

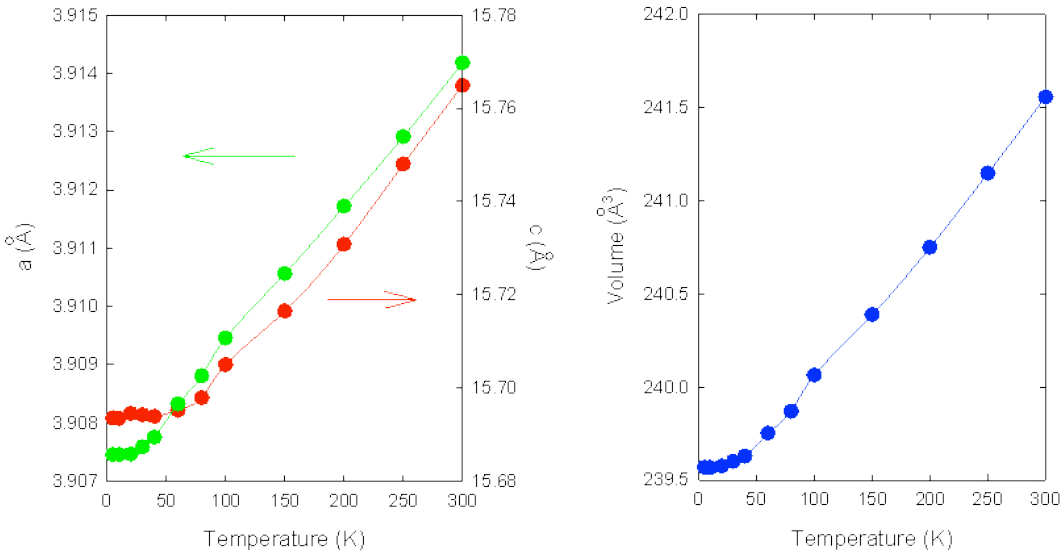

Figure 4.25. On the left: temperature evolution of the lattice constants for 42622-Cr: green and red circles refer to the *a* and *c* lattice constants, respectively. On the right: temperature evolution of the volume for 42622-Cr.

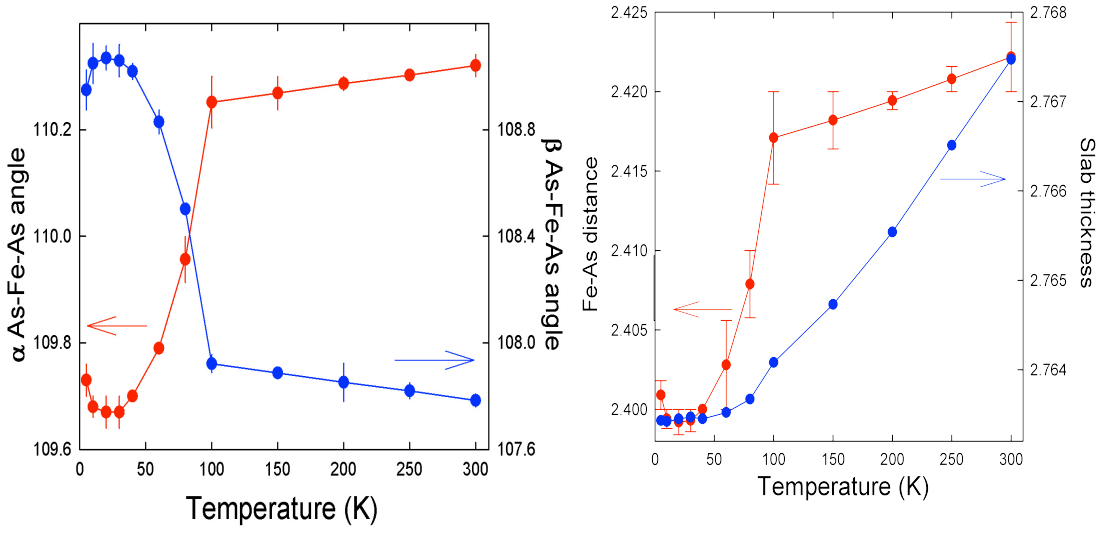

Figure 4.26. On the left: temperature evolution of the two-fold and tetra-fold angles for 42622-Cr: red and blue circles refer to α and β angles, respectively. On the right: temperature evolution of the Fe-As distance and the slab thickness for that composition.

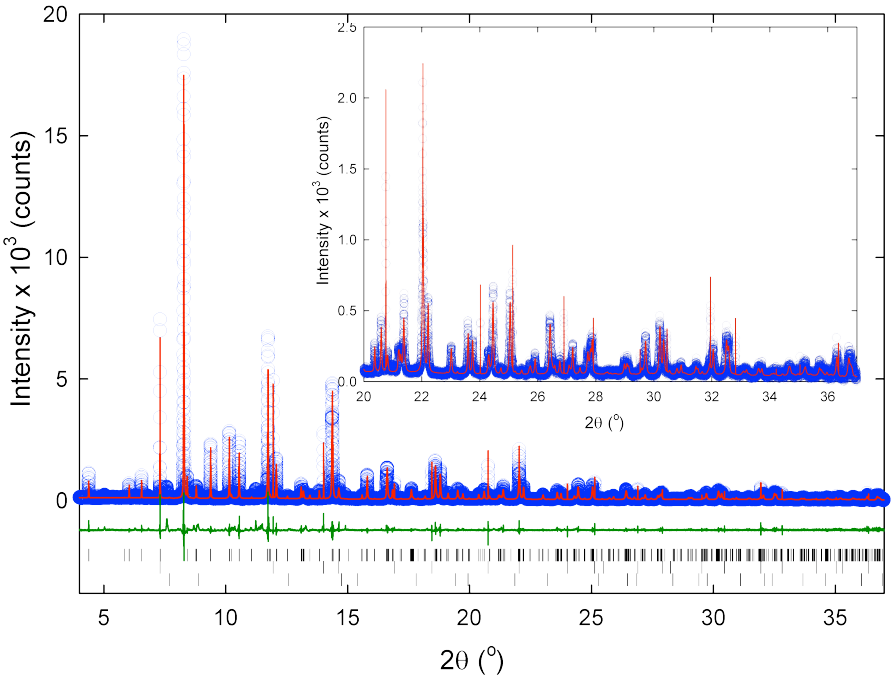

Figure 4.27. Final observed (blue circles), calculated (red solid line), and difference (lower green solid line) plots for the Rietveld refinement of 42622-Cr at 5 K. Tick marks show the reflection positions and are from top to bottom: $Sr_4Cr_2O_6Fe_2As_2$, SrO and Si powder. The refinement proceeded with the main phase in the *P4/nmm* space group. The X-ray wavelength is 0.4030068 Å. Inset shows zoom in on the 20 to 37 2θ data range.

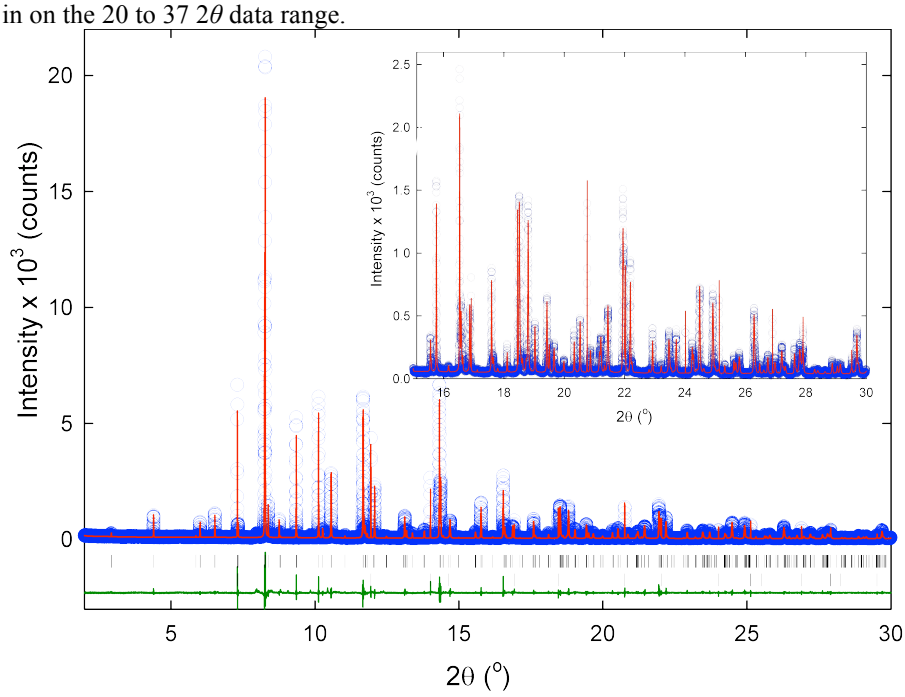

Figure 4.28. Final observed (blue circles), calculated (red solid line), and difference (lower green solid line) plots for the Rietveld refinement of 42622-V at 5 K. The tick marks show the reflection positions and are from top to bottom: $Sr_4V_2O_6Fe_2As_2$ and Si powder. The refinement proceeded with the main phase in the *Cmma* space group. The X-ray wavelength is 0.4030068 Å. Inset shows zoom in on the 15 to 30 2θ data range.

In the V-42622 compound made with V_2O_5, however, there are visible peak splittings indicating a phase transition below 100 K. Various space groups were investigated to establish which one was the best fit for this preliminary result. The new structure can be described with an orthorhombic *Cmma* space group and the lattice parameters at 5 K are a = 3.93007 Å, b = 3.92717 Å and c = 15.6254 Å. On cooling, the c lattice decreases monotonically down to around 50 K and then starts increasing slightly, but no discontinuities are visible at the phase transition temperature. The basal plane lattice constants monotonically decrease with temperature (Figure 4.29). The temperature dependence of the As-Fe-As angles and Fe-As distances is shown in Figure 4.30. Upon reaching 100 K the phase transition starts, reaching its maximum at around 80 K, and as the temperature decreases further, the splittings of the peaks get smaller (Figure 4.31).

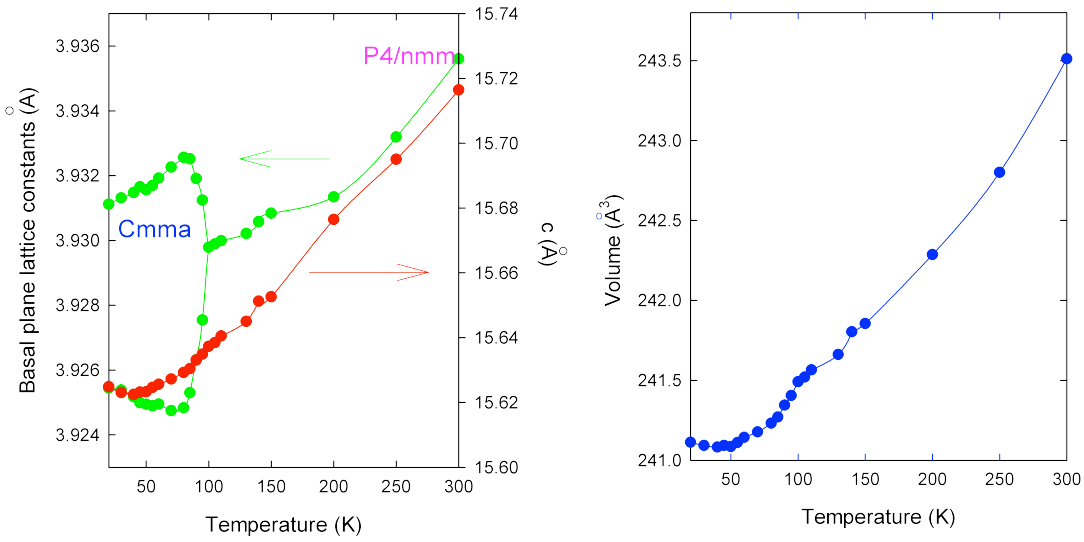

Figure 4.29. On the left: temperature evolution of the lattice constants for 42622-V: green and red circles refer to the a and c lattice constants, respectively. On the right: temperature evolution of the volume for 42622-V.

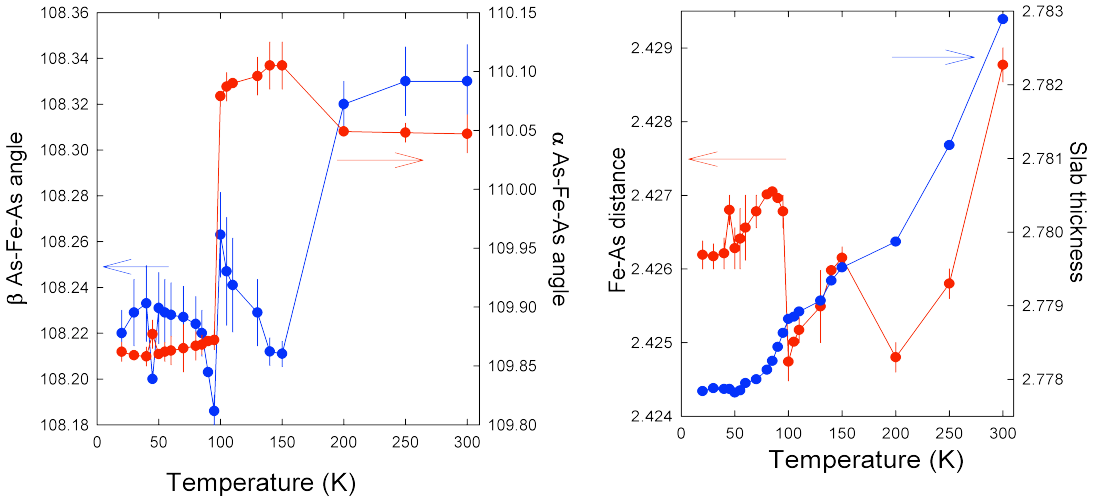

Figure 4.30. On the left: temperature evolution of the two-fold and tetra-fold angles for 42622-V: red and blue circles refer to α and β angles, respectively. On the right: temperature evolution of the Fe-As distance and the slab thickness for that composition.

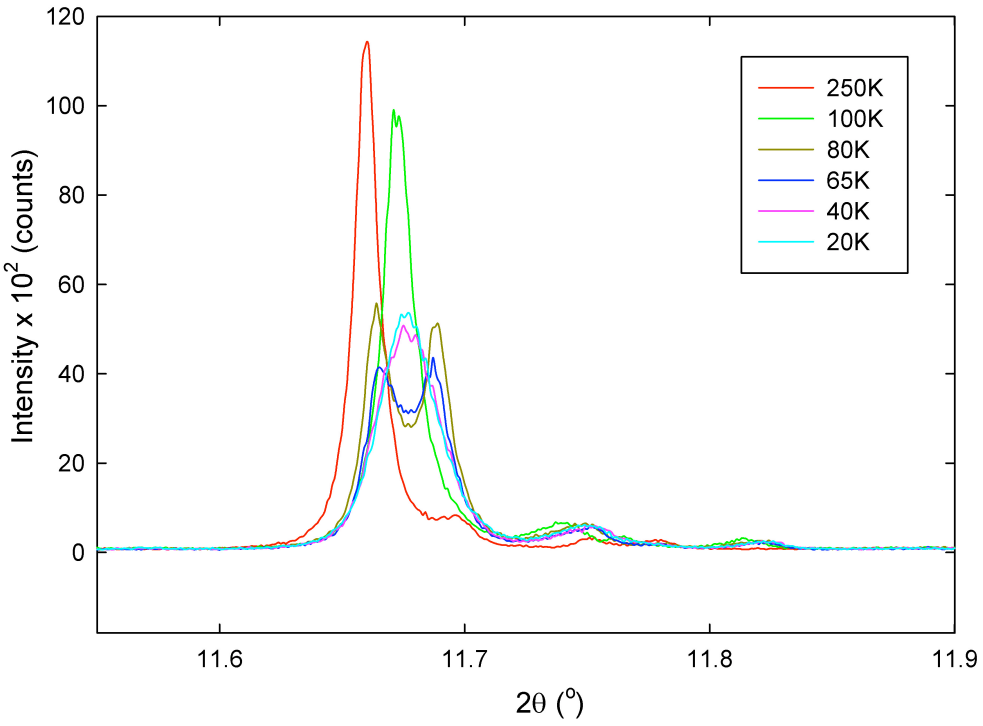

Figure 4.31. Example of peak splitting evolution with temperature observed in synchrotron X-ray experiment for sample 42622-V.

On cooling, the Fe-As_4 tetrahedral angles are decreasing towards the ideal value of 109.5°. The temperature dependence of the α angle shows a steady value and

then a sharp drop at 100 K, which is the structural transition temperature, while for the β angle two drops can be seen – the first one at the higher temperature of about 150 K with a slight increase in the value afterwards, and then another drop at 100 K. The overall slab thickness is monotonically decreasing with decreasing temperature, suggesting that the Fe-As_4 tetrahedra are transforming towards the ideal shape.

For all the samples neutron diffraction measurements were also conducted on the D2B and D20 beamlines at ILL, Grenoble. Use of beamline D20 was necessary to observe magnetism in the samples in detail. No sign of magnetism was found in any of the V-42622 samples (Figure 4.32), while Cr-42622 showed a magnetic phase transition at around 70 K, which indicates long-range antiferromagnetic ordering in Cr^{3+} (Figures 4.33 and 4.34).

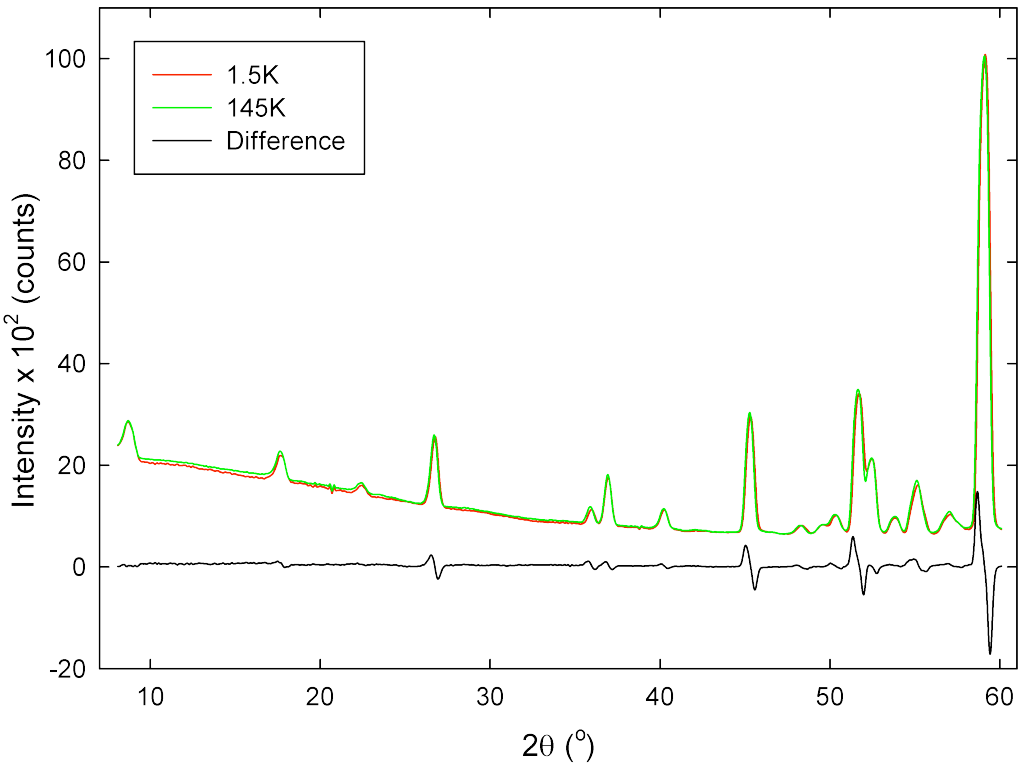

Figure 4.32. Raw neutron data of $Sr_4V_2O_6Fe_2As_2$ performed at D20 showing the difference between 100 K and 2 K data.

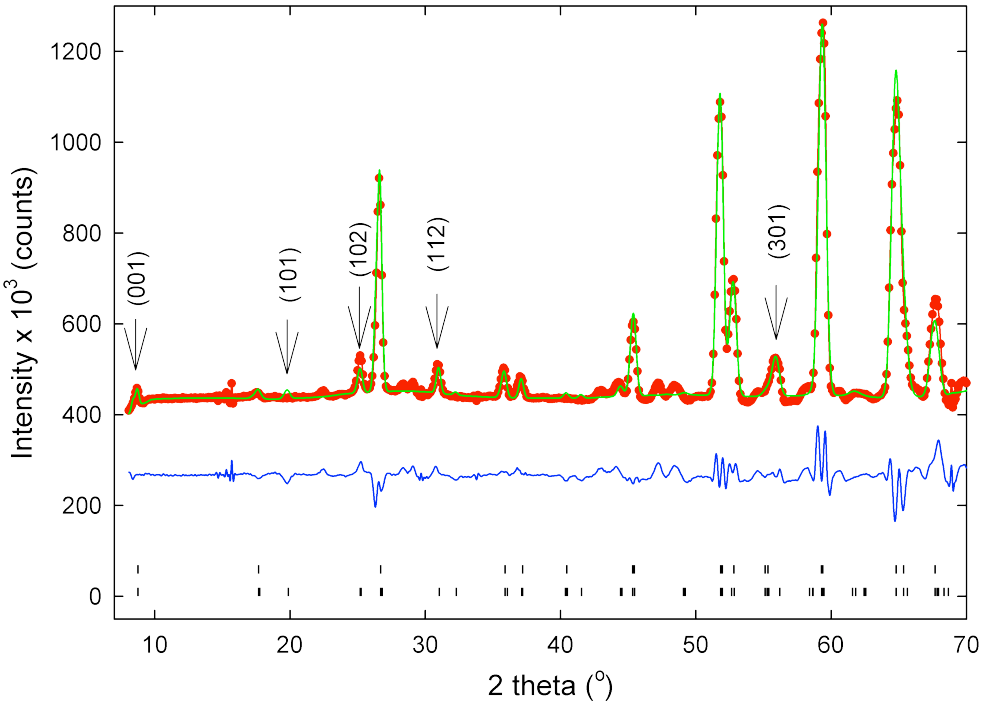

Figure 4.33. Neutron powder diffraction data of Cr-42622 collected on the D20 beamline at 2 K, showing magnetic peaks.

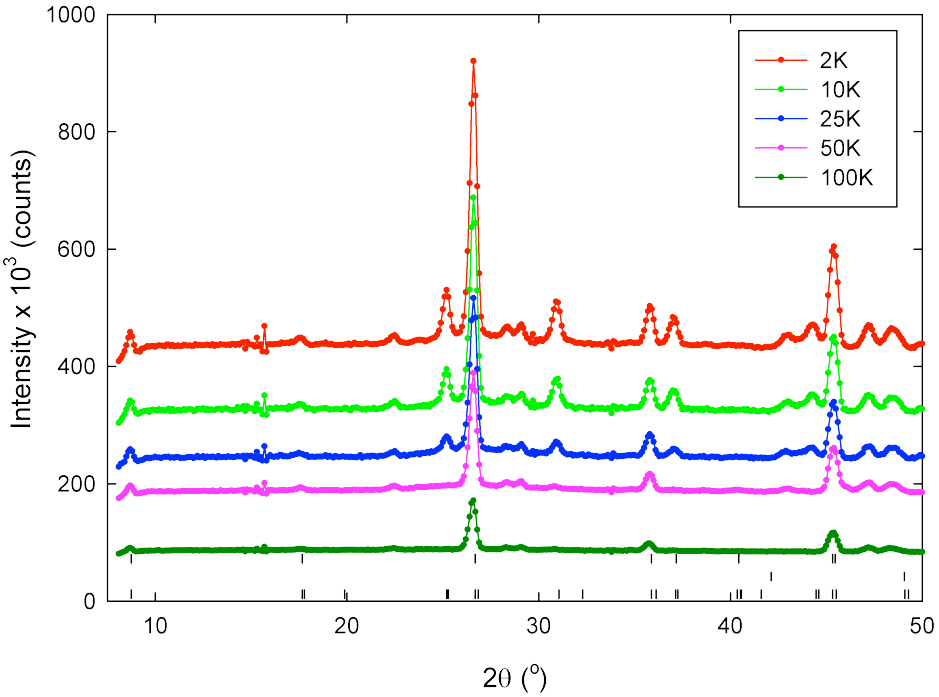

Figure 4.34. Temperature evolution of magnetic peaks from neutron powder diffraction data on Cr-42622, collected on the D20 beamline between 2 K and 100 K.

The experiments using the high-resolution D2B beamline allowed analysis of structural data with the use of synchrotron (Figure 4.35 and 4.36) and neutron combined Rietfield refinements. The refined lattice constants were taken from the previously refined synchrotron radiation data, and neutron data was used to refine the positions and occupancies of atoms in the samples. No sign of mixed atom occupancies were observed in any of the measured samples. In the case of Cr-42622 this fact is in disagreement with previously published data that suggested mixed occupancies on both Fe and Cr sites[20].

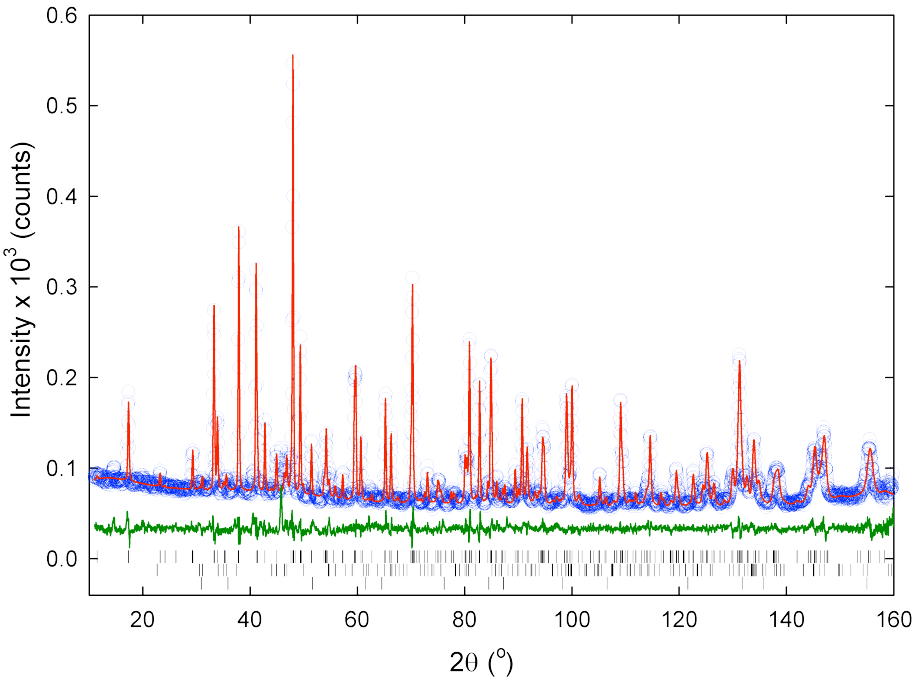

Figure 4.35. Final observed (blue circles), calculated (red solid line), and difference (lower green solid line) plots for the Rietveld refinement of neutron data of 42622-Cr at RT collected on D2B beamline. Tick marks show the reflection positions and are from top to bottom: $Sr_4Cr_2O_6Fe_2As_2$, SrO and FeAs. The refinement proceeded with the main phase in the *P4/nmm* space group. The wavelength used is 1.5943 Å.

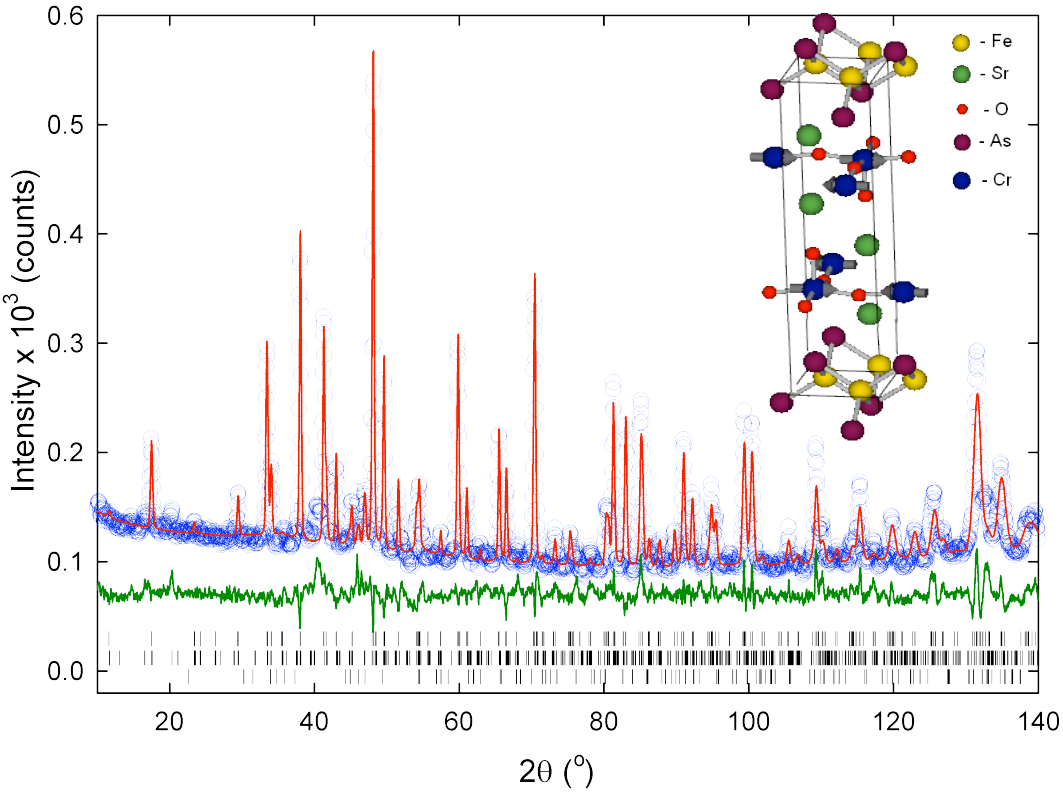

Figure 4.36. Final observed (blue circles), calculated (red solid line), and difference (lower green solid line) plots for the Rietveld refinement of neutron data of 42622-Cr at 2 K collected on D2B beamline. Tick marks show the reflection positions and are from top to bottom: $Sr_4Cr_2O_6Fe_2As_2$, SrO and FeAs. The refinement proceeded with the main phase in the *P4/nmm* space group. The wavelength used is 1.5943 Å. Inset shows the graphic representation of the fitted magnetic structure.

4.3.3.2. Magnetic properties.

The temperature dependence of magnetisation of $Sr_4Cr_2O_6Fe_2As_2$ and both $Sr_4V_2O_6Fe_2As_2$ samples was measured under an applied field of 10 kOe. The resulting data are shown in Figures 4.37-4.38. In Cr-42622 the magnetic susceptibility shows a broad magnetisation peak at around 70 K with a maximum at $T_N \sim 70$ K, which can be explained by antiferromagnetic ordering of Cr^{3+} in the oxide layer. The data show no Curie-Weiss type behaviour in the whole range of measured temperatures. Measured under a magnetic field of 10 Oe, this sample showed no signs of superconductivity.

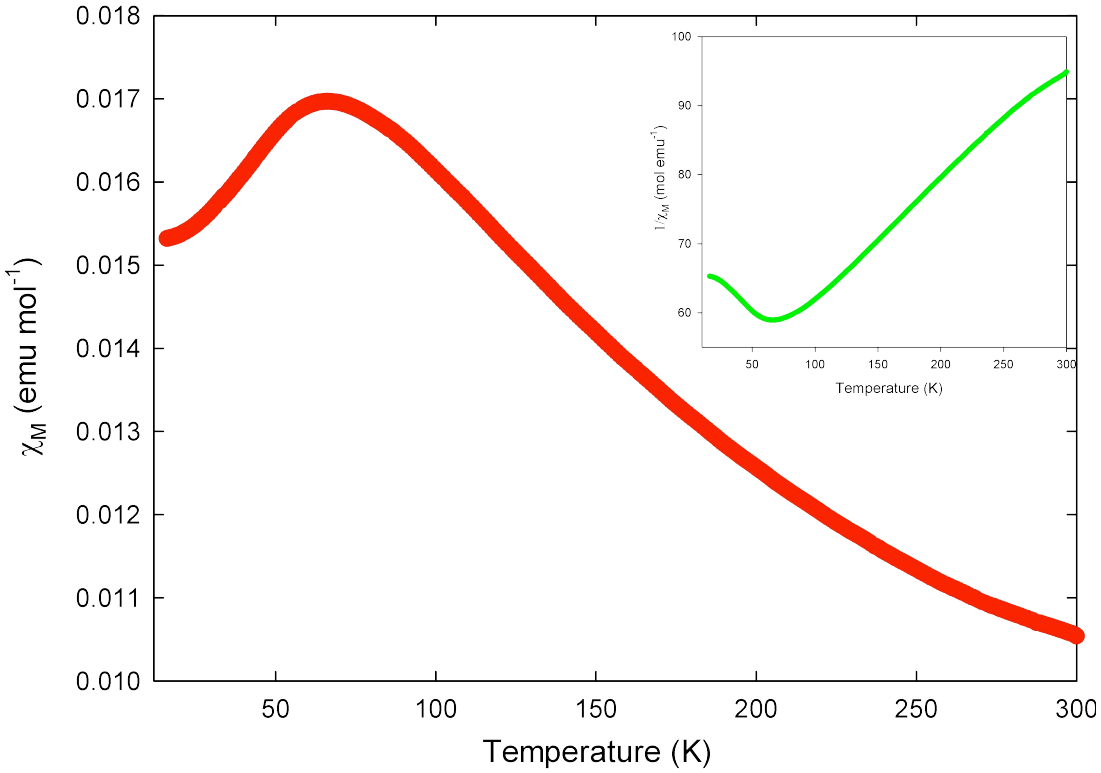

Figure 4.37. Temperature evolution diagram of χ_M for $Sr_4Cr_2O_6Fe_2As_2$. Inset shows the temperature dependence of inverse magnetic susceptibility.

In the case of the V-42622 compounds, the one made with V_2O_5 shows an upturn peak at around 120 K in the magnetic susceptibility data, which corresponds to the temperature of a structural phase transition. The zero-field cooled (ZFC) and field cooled (FC) magnetization data under 10 Oe of V_2O_5 V-42622 showed no signs of a superconducting transition, whereas the preliminary result for V_2O_3 V-42622 showed a superconducting transition at 28 K. The superconducting fraction was calculated to be around 34%. This sample was then reheated in an evacuated quartz tube for 6 hours in the presence of Na_2O_2 pellets to try to check if the oxygen content in the compound could be changed and, if so, to ascertain how that would that affect the superconducting properties. When measured, the same sample after this treatment showed a decrease in T_c to 15 K, and the value of the superconducting fraction also decreased (Figure 4.38 inset). The superconducting transition also broadened substantially. This suggests that

both oxygen concentration and the valency of the vanadium ions play a crucial role in the mechanism behind superconductivity for this compound.

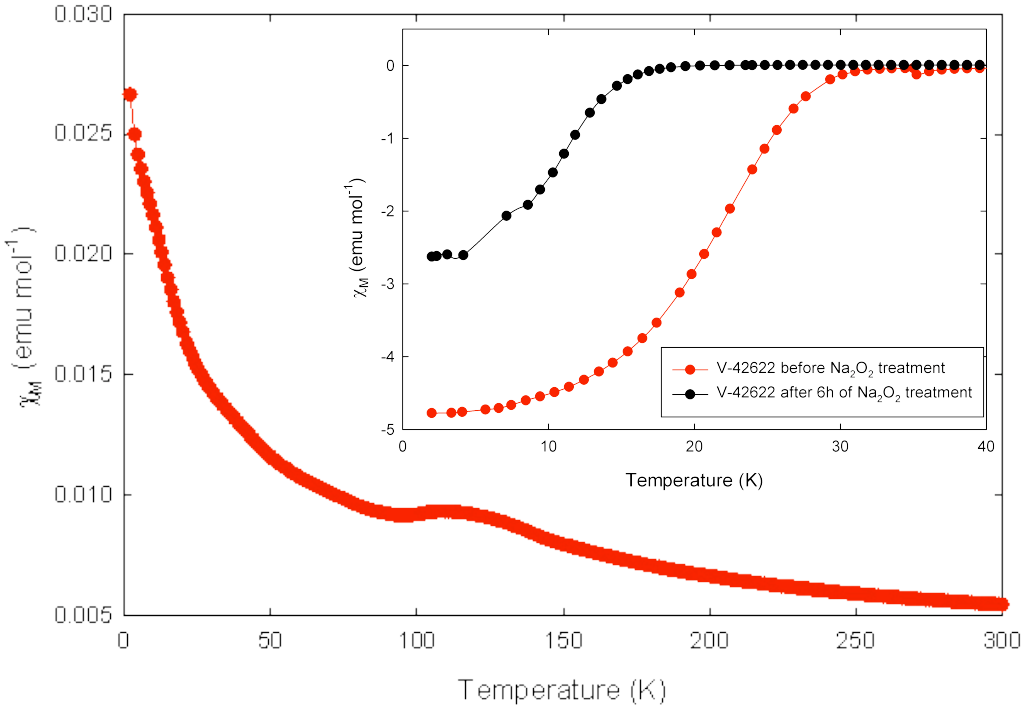

Figure 4.38. Temperature evolution diagram of χ_M for $Sr_4V_2O_6Fe_2As_2$ sample made with V_2O_5. The inset shows the superconducting transitions in V-42622 sample made with V_2O_3 with and without oxygenation of the sample.

4.3.3.3. Electrical properties.

The conducting pastes used to mount samples on PPMS pucks caused the pellets of the Cr-42622 compound to disintegrate into powder (although the chemical composition remained unchanged), so the measurement results are not accurate above 100 K. The measurements were taken on warming from base temperature 2 K to 300 K, and while the pellet piece was still intact at low temperature, after increasing the temperature above 100 K the sample was observed to become more porous and finally became a powder. On the graph there is a clear anomaly at around 70 K that corresponds to the temperature at which the magnetization peak appears in the magnetic susceptibility data. Due to the

inability to measure the resistivity accurately with the standard puck, the sample was measured with the use of high pressure cells, starting with a very low applied pressure. The pressure was as low as possible to provide measurements relatively close to ambient conditions, and the achieved starting pressure for this composition was 22 kbar. The graph shows insulating behaviour and the same anomaly as observed in the ambient resistivity measurement, but at a slightly higher temperature this time due to the applied pressure. When compared the two graphs seem to be in agreement (Figure 4.39). Further experiments were conducted with the use of higher pressures up to 200 kbar. It is clear that the anomaly is suppressed by increasing pressure. Also, the overall resistivity values are decreasing with increasing pressure (Figure 4.40).

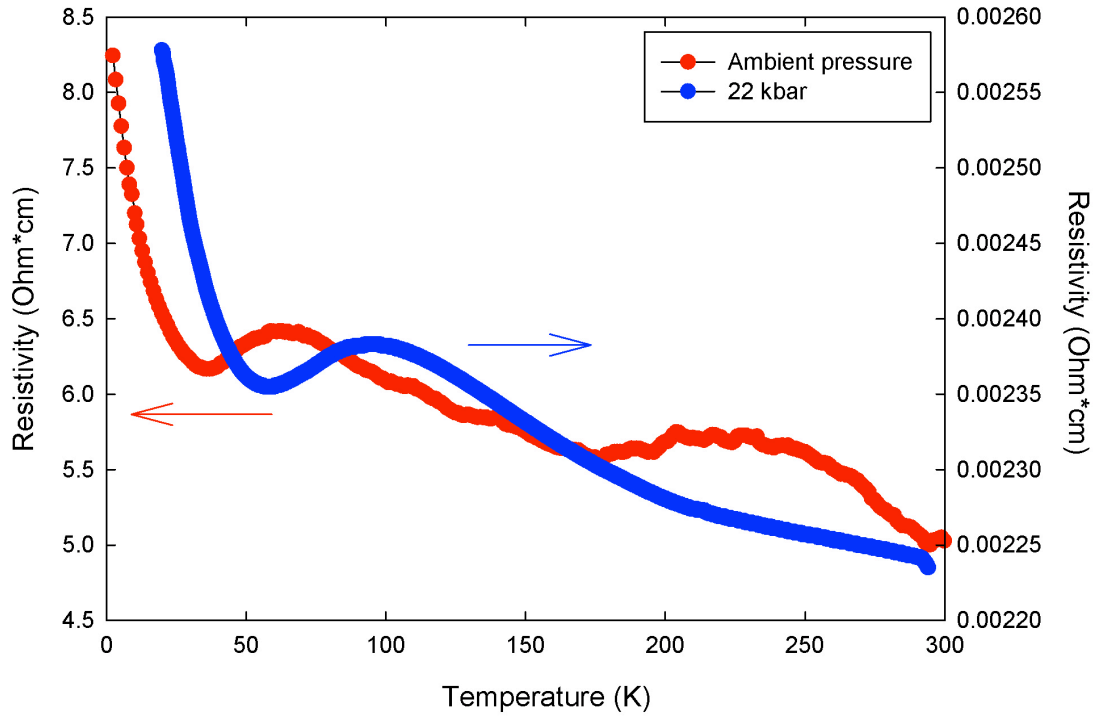

Figure 4.39. Temperature dependence of resistivity of $Sr_4Cr_2O_6Fe_2As_2$ in ambient pressure and at 22 kbar.

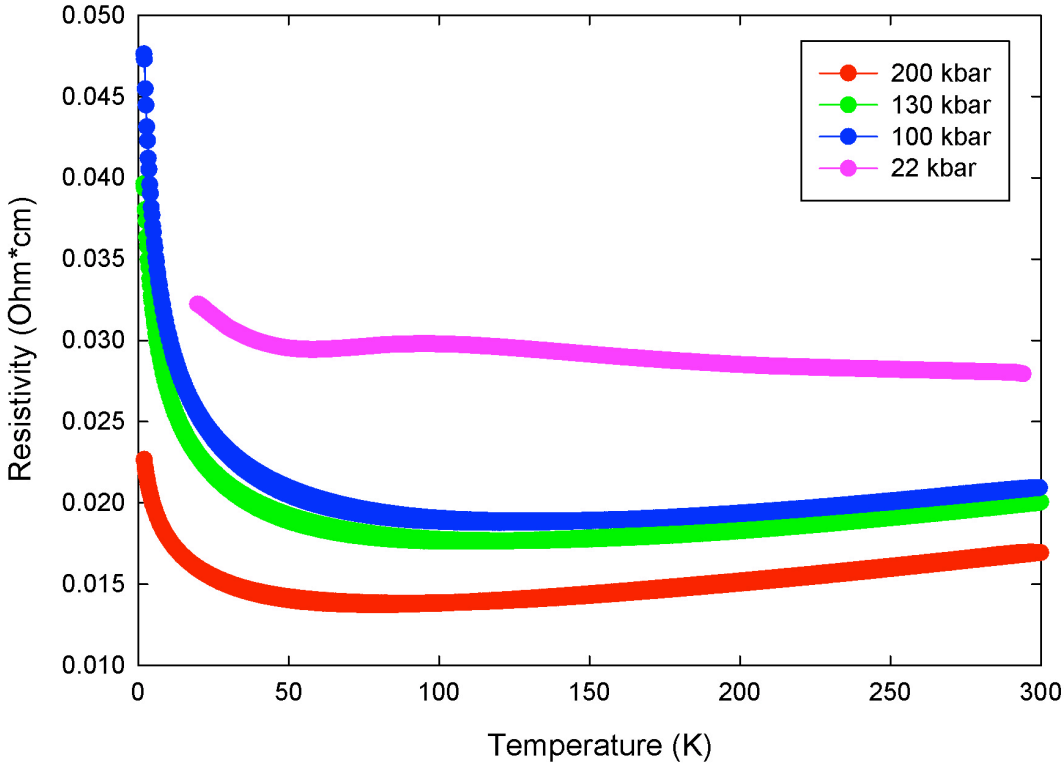

Figure 4.40. An overview of the temperature dependence on resistivity for $Sr_4Cr_2O_6Fe_2As_2$ at different pressures.

In the case of V-42622, the sample made from V_2O_5 was measured with the use of PPMS in the range of temperatures 2 K – 300 K. The measured sample shows semiconducting-type behaviour throughout the measured temperature range, with no anomaly observed at any point (Figure 4.41).

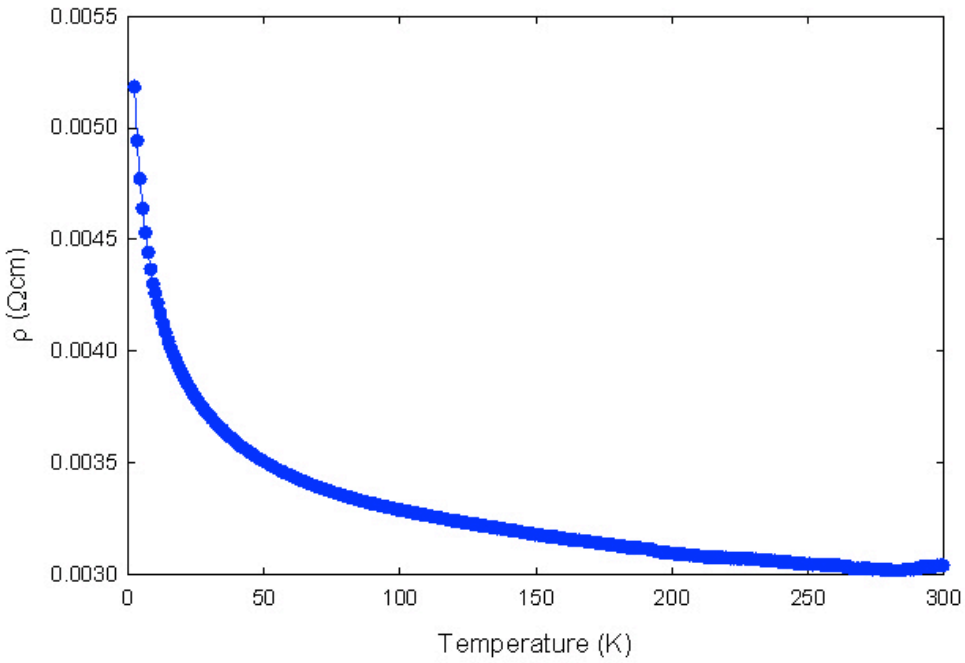

Figure 4.41. Temperature dependence of resistivity for $Sr_4V_2O_6Fe_2As_2$.

4.4. Discussion.

The 42622 family is a very intriguing one due to the size of the compounds' lattice structures and the possibility of many interactions between building atoms. It may be a promising starting point for discovering more about the nature of the superconducting mechanism. Compounds of this type can be easily modified using a number of transition metals to try to achieve higher superconducting transition temperatures.

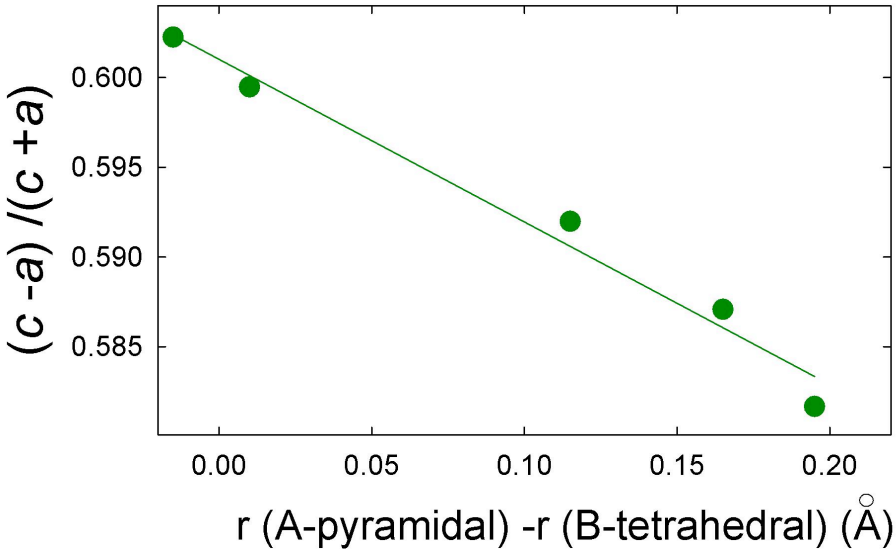

Figure 4.42. Comparison of all 42622 samples' lattice strain as a function of the transition metals size difference-from left to right the data represents samples made with these metals respectively: Cr-Fe, V-Fe, Sc-Fe, Sc-Co, Sc-Ni.

All measured compounds show a clear trend in the structural values when compared to the ionic radii of the transition metals used. The ionic radii values are not in direct correlation as both M^{I} and M^{II} transition metals vary between the different samples. By taking the difference between the ionic radius of the metal on the pyramidal site and the ionic radius of the metal on the tetrahedral site in the compound, this takes into account both transition metals involved and allows them to be easily compared. While analysing lattice constants, a clear relationship can be seen between the lattice strain, *(c-a)/(c+a)*, and the aforementioned ionic radii difference. This relationship shows a linear dependence with the highest ratio value for the Cr-Fe compound, gradually decreasing down to the Sc-Ni composition (Figure 4.42).

The α angle shows a slight decrease in value from Cr-Fe to V-Fe compositions and then a steady increase for Sc-Fe, then Sc-Co and finally up to Sc-Ni. For the β angle the trend is opposite, with the maximum for V-Fe (Figure 4.43). When plotted, the graphs for overall slab thickness and the distance between main transition metal (V, Cr or Sc) and the other transition metal (Fe,

Co or Ni) both follow similar pattern as that of the β angle, although Sc-Fe has a slightly higher value in the distance measurements (Figure 4.44).

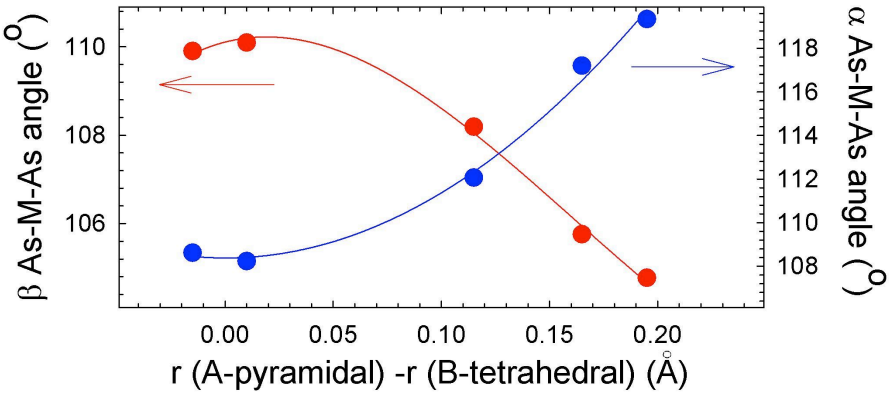

Figure 4.43. Comparison of all 42622 samples' α and β angles as a function of the transition metals size difference-from left to right the data represents samples made with these metals respectively: Cr-Fe, V-Fe, Sc-Fe, Sc-Co, Sc-Ni.

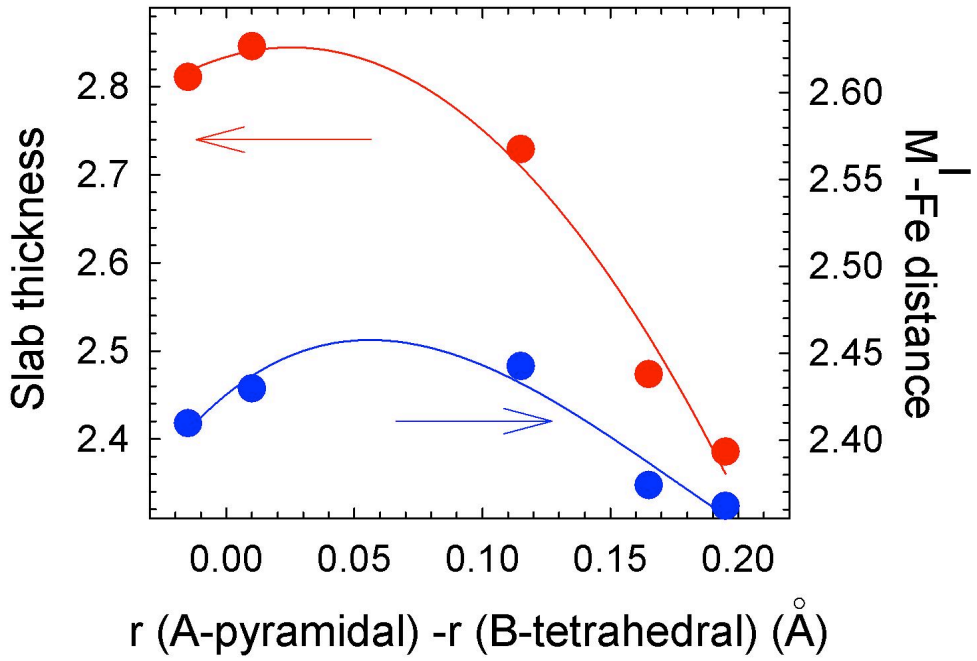

Figure 4.44. Comparison of all 42622 samples' slab thickness and transition metals distances as a function of the transition metals size difference-from left to right the data represents samples made with these metals respectively: Cr-Fe, V-Fe, Sc-Fe, Sc-Co, Sc-Ni.

The shape of the $FeAs_4$ tetrahedra in some of the previously mentioned compositions in the 42622 family tend to have a different nature than in other Fe-based superconductors, as the material can show superconductivity despite relatively big differences in the tetrahedral angles from the ideal value of 109.5°. It was shown empirically amongst other Fe-based superconductors that materials with the least distorted $FeAs_4$ tetrahedron exhibit the highest T_c among all the families. In the case of some compounds in the 42622 family it seemed that this new trend in the behaviour of Fe-As planes' structure might lead to a different approach towards achieving materials with higher T_c. The V-42622 sample made with V_2O_3, which shows one of the biggest transition temperatures among all the Fe-based families, indicates that the ideal tetrahedron might still be the key for achieving superconducting materials. This fact also shows how complex the 42622 family is and how different the properties of members of the same family can be.

4.5. Conclusions.

The structural, electronic and magnetic properties of the parent compounds of new Fe-based superconducting family have been discussed. Five different compositions were made to examine the possibility of being a starting point for developing new high temperature superconducting materials. Two compounds, namely $Sr_4V_2O_6Fe_2As_2$ made with V_2O_3 and $Sr_4Sc_2O_6Ni_2As_2$, showed superconducting transitions as parent compounds before any doping had taken place. All of the compositions show no spin density wave anomaly, which is commonly present in other superconducting families. Only one composition, $Sr_4Cr_2O_6Fe_2As_2$, showed a magnetic transition, which is due to the transition metal used. It is also the first known family where the structural transition upon cooling in the parent compounds is not usually observed. The only exception in this family is $Sr_4V_2O_6Fe_2As_2$, which undergoes a transition from tetragonal *P4/nnm* crystal structure into orthorhombic *Cmma* at 100 K.

This system is a good start point for researching new superconducting materials. The largest cell volume among all known structures up to now, and also one of the highest transition temperatures achieved indicates the importance of these compounds in the race for making high temperature superconductors. The unusual possibility of doping on different sites in this family could lead to a new approach in the making of superconductors. Also, different trends in bond lengths and angles and the lack of the spin density wave anomaly makes this system very interesting and important for understanding the mechanism of superconductivity better, as well as providing routes that may lead to achieving materials with higher transition temperatures.

4.6. Bibliography.

1. Miyake, T.; Nakamura, K.; Arita, R.; Imada, M., *Journal of the Physical Society of Japan,* **2009**, 79, 044705.
2. Rozsa, S.; Schuster, H.-U. *Zeitschrift für Naturforschung,* **1981**, *86b*, 1668.
3. Xia, Y.; Huang, F.; Xie, X.; Jiang, M.*, Europhysics Letters,* **2009**, *86*, 37008.
4. Yang, Y.; Hu, X., *arXiv:1003.0592,* **2010**.
5. Ogino, H.; Matsumura, Y.; Katsura, Y.; Ushiyama, K.; Horii, S.; Kishio, K.; Shimoyama, J.-i., *Superconductor Science and Technology,* **2009**, 22, 075008.
6. Margadonna, S.; Takabayashi, Y.; Ohishi, Y.; Mizuguchi, Y.; Takano, Y.; Kagayama, T.; Nakagawa, T.; Takata, M.; Prassides, K. *Physical Review B* **2009**, *80*, 064506.
7. Marcinkova, A.; Grist, D. A. M.; Margiolaki, I.; Hansen, T. C.; Margadonna, S.; Bos, J.-W. G., *Physical Review B,* **2010**, 81, 064511.
8. Monni, M.; Bernardini, F.; Profeta, G.; Sanna, A.; Sharma, S.; Dewhurst, J. K.; Bersier, C.; Continenza, A.; Gross, E. K. U.; Massidda, S. *Physical Review B,* **2010**, 81, 104503.
9. Xiao, Y.; Su, Y.; Mittal, R.; Chatterji, T.; Hansen, T.; Price, S.; Kumar, C. M. N.; Persson, J.; Matsuishi, S.; Inoue, Y.; Hosono, H.; Brueckel, T., *Physical Review B,* **2009**, 81, 094523.
10. Krellner, C.; Caroca-Canales, N.; Jesche, A.; Rosner, H.; Ormeci, A.; Geibel, C. *Physical Review B* **2008**, *78*, 100504.
11. Mewis, A.; Distler, A. *Zeitschrift für Naturforschung,* **1980**, *35*, 391.
12. Zhu, X.; Han, F.; Mu, G.; Zeng, B.; Cheng, P.; Shen, B.; Wen, H.-H. *Physical Review B* **2009**, *79*, 5.
13. Chen, G. F.; Xia, T.-L.; Yang, H. X.; Li, J. Q.; Zheng, P.; Luo, J. L.; Wang, N. L., *Superconductor Science and Technology,* **2009**, 22, 072001.
14. Kotegawa, H.; Kawazoe, T.; Tou, h.; Murata, K.; Ogino, H.; Kishio, K.; Shimoyama, J.-I. *Journal of the Physical Society of Japan* **2009**, *78*, 4.
15. Lee, K.-W.; Pickett, W. E, *Europhysics Letters,* **2010**, 89, 57008.
16. Matsumura, Y.; Ogino, H.; Horii, S.; Katsura, Y.; Kishio, K.; Shimoyama, J.-I., *Applied Physics Express,* **2009**, 2, 063007.

17. Ogino, H.; Katsura, Y.; Horii, S.; Kishio, K.; Shimoyama, J.-I. *Superconductor Science and Technology,* **2009**, *22*, 13.
18. Tegel, M.; Hummel, F.; Lackner, S.; Schellenberg, I.; Pöttgen, R.; Johrendt, D., *Zeitschrift für anorganische und allgemeine Chemi,e* **2009**, *635*, 2242.
19. Xie, Y. L.; Liu, R. H.; Wu, T.; Wu, G.; Song, Y. A.; Tan, D.; Wang, X. F.; Chen, H.; Ying, J. J.; yan, Y. J.; Li, Q. J.; Chen, X. H., *Europhysics Letters,* **2009**, *86*, 9.
20. Tegel, M.; Hummel, F.; Su, Y.; Chatterji, T.; Brunelli, M.; Johrendt, D., *Europhysics Letters,* **2010**, *89*, 37006.
21. Zhu, X.; Han, F.; Mu, G.; Cheng, P.; Shen, B.; Zeng, B.; Wen, H.-H. *arXiv:0904.1732,* **2010**.
22. Zhu, X.; Han, F.; Mu, G.; Cheng, P.; Shen, B.; Zeng, B.; Wen, H.-H. *Physical Review B* **2009**, *79*, 220512.
23. Han, F.; Zhu, X.; Mu, G.; Cheng, P.; Shen, B.; Zeng, B.; Wen, H.-H., *Science China Physics,* **2009**, 53,7 (1202-1206).

Chapter 5

Synthesis and characterisation of

$Sr_4Cr_2O_6Fe_{2-x}Co_xAs_2$ ($0 < x < 2$).

5.1. Introduction.

Previous research on different families of Fe-As based superconductors showed that chemical doping, both hole and electron doping, is a successful route to induce superconductivity in non-superconducting parent compounds. Such doping can be achieved either by partially replacing oxygen with fluorine ($LaFeAsO_{1-x}F_x$ with T_c = 26 K for x = 0.11)[1], by producing oxygen deficient samples (the highest T_c was achieved for $SmFeAsO_{1-y}$ with T_c = 55 with y = 0.15)[2,3], by doping directly on the Fe site with Co, Ni, Rh, Ru, Mn, Ir, Pd[4-7], or by hole doping by substitutions on the RE metal site ($La_{1-x}Sr_xFeAsO$ with T_c = 25 K or, as mentioned in *Chapter 3*, $Nd_{1-x}Sr_xFeAsO$ with T_c = 13.5 K for x = 0.2) the latter of which is the least common method of chemical doping. The other way to induce superconductivity is with the use of hydrostatic pressure, which also very often leads to an increase in T_c in already superconducting materials (for example, in $LaFeAsO_{1-x}F_x$, T_c rises under pressure from 26 K to 43 K)[8-11].

Electron doping by means of cobalt substitution on the Fe site has been proven to lead to superconductivity in various families of Fe-As based materials. The first reported case was in the 1111 family in $LaFe_{1-x}Co_xAsO$ where T_c reached 14.3 K for x = 0.11. After that discovery came other cobalt doped superconductors in the 1111 family including $CaFe_{1-x}Co_xAsF$ (T_c = 22 K for x = 0.1)[1], $NdFe_{1-x}Co_xAsO$ (T_c = 16.5 K for x = 0.12)[4] and $SmFe_{1-x}Co_xAsO$ (T_c = 17.2 K for x = 0.1)[2] and in the 122 family, $Ca(Fe_{1-x}Co_x)_2As_2$ (T_c = 17 K for x = 0.06)[1] and $Ba(Fe_{1-x}Co_x)_2As_2$ (T_c = 22 K for x = 0.2)[4]. From a chemical point of view, cobalt substitution should be a very good means of electron doping as the charge carriers are doped directly into the conducting Fe-As plane. Most other ways of chemical doping tend to reduce the

two-fold tetrahedral As-Fe-As angle, which plays a crucial role in achieving high temperature superconductivity with higher T_c as the angle reaches values close to the ideal 109.5°.

The 42622 family is very intriguing as the compounds in their undoped state have one of the largest unit cells among all Fe-As based materials and they show unusual physical and magnetic properties compared to other Fe-As based materials. There are various possibilities of doping in this system, from doping in the perovskite layer, like partial substitution on the M^I site as reported in the mixed Mg-Ti compound $Sr_4Mg_{1-x}Ti_{1+x}O_6Fe_2As_2$ with highest T_c at 39 K for $x = 0.6$[12], on the oxygen site, either with fluoride or by making oxygen deficient samples ($Sr_4V_2O_{6-x}Fe_2As_2$ with T_c at 36 K for $x = 0.2$)[13] to partial doping on Fe site with Co, Ni. There has been a report of self doping within the compound by mixed Cr-Fe occupancies but this did not lead to changes in the resulting properties[14].

The $Sr_4Cr_2O_6Fe_2As_2$ compound was chosen for further investigation as it shows a magnetic ordering in its undoped structure and a route for synthesising very pure samples of the parent compound was found, as proven in Chapter 4, which is necessary to make doped compounds of high quality. Herein a successful electron doping on the Fe^{2+} site by Co^{3+} in $Sr_4Cr_2O_6Fe_2As_2$ is shown, along with the structural, electronic and magnetic properties of the synthesised samples. The main interest of this investigation was in how doping with cobalt changes the structure of the parent compound, and whether it can induce superconductivity in this system.

5.2. Experimental.

Polycrystalline samples of $Sr_4Cr_2O_6Fe_{2-x}Co_xAs_2$ (where $0 < x < 2$) were prepared in a two-step solid state synthetic procedure according to the reaction below.

$$SrAs + 3SrO + (2-x)Fe + As + Cr_2O_3 + xCo = Sr_4Cr_2O_6Fe_{2-x}Co_xAs_2$$

Equation 5.1.

In the first step, SrAs was prepared by grinding together Sr pieces and As powder. Then the mixture was sealed in an evacuated quartz tube and heated at 500°C for 2 hours (with heating step 250°/hour), then it was heated up to 700°C where it was kept for 16 hours and cooled down at pace of 300°C/h. At room temperature the tube was shaken and heated again for 16 hours at 700°C and cooled to room temperature. Then the quality of the product was checked with a use of laboratory Bruker D8 Powder Diffractometer.

The second step of the synthesis was to prepare $Sr_4Cr_2O_6Fe_{2-x}Co_xAs_2$ sample with various *x* content. It was made by a solid state reaction using high purity powders of pre-prepared SrAs, SrO, Fe, As, Co and Cr_2O_3. Both oxides of SrO and Cr_2O_3 were prepared for the synthesis by degassing them under vacuum in a tube at 120°C for 12 hours to prevent any traces of moisture reacting with any of the starting materials in the process. The starting materials were mixed thoroughly in an agate mortar and pressed in the form of pellets, put in alumina crucibles and sealed in quartz tubes with 0.2 bar atmosphere of argon. The tubes were then heated at a rate of 3°/min up to 900°C where they were kept for 60 hours and cooled slowly to room temperature. Then the pellets were reground and pelletized again, and heated in evacuated quartz tubes at 1050°C for 60 hours (using the same heating rate). After a slow cooling down to room temperature, the initial quality phase analysis was done on Bruker D2 and Bruker D8 powder diffractometers. All of the procedures were performed in a glovebox filled with high purity argon due to air- and moisture-sensitiveness of some of the starting materials. The final products were also kept in a glovebox due to deterioration of pellets in air.

The masses of reactants used for this synthesis are detailed in Table 5.1.

Table 5.1. Masses of starting materials used to prepare different compositions of $Sr_4Cr_2O_6Fe_{2-x}Co_xAs_2$.

***X* (Doping level of Co)**	**Mass of a pellet [g]**	**Mass of SrAs [g]**	**Mass of SrO [g]**	**Mass of Fe [g]**	**Mass of As [g]**	**Mass of Cr2O3 [g]**	**Mass of Co [g]**
0.05	0.300	0.060	0.115	0.040	0.028	0.056	0.001
0.1	0.300	0.060	0.115	0.039	0.028	0.056	0.002
0.15	0.300	0.060	0.115	0.038	0.028	0.056	0.003
0.2	0.300	0.060	0.115	0.037	0.028	0.056	0.004
0.25	0.300	0.060	0.115	0.036	0.028	0.056	0.005
1	0.300	0.060	0.115	0.021	0.028	0.056	0.022
1.5	0.300	0.060	0.115	0.010	0.028	0.056	0.032
2	0.300	0.060	0.115	0	0.028	0.056	0.043

The magnetic properties were measured using a Quantum Design Magnetic Property Measurement System magnetometer following ZFC/FC protocols at 10 Oe and 10 kOe. Produced samples in the form of pellets tend to degrade with time very quickly when not kept in airtight containers, or when any type of silver or graphite paste was used in order to attach conducting wires for experiments. This does not affect the crystallinity of the samples, but prevents the obtaining of electrical resistivity measurements on those samples. High pressure resistivity measurements were conducted using Quantum Design Physical Property Measurement System (PPMS) between 2 K and 300 K with the range of pressures used between 5 kbar and 76 kbar. Synchrotron X-ray powder diffraction (XRPD) was collected on samples with x = 0.05, 0.1, 0.15, 0.25, 1, 1.5 and 2 (the doping levels chosen were more concentrated at lower levels in order to examine the superconductivity in this system, the higher doping level measurements were to check if a full Fe – Co exchange is possible, and to see the properties of the compound with full cobalt doping) on beamline ID31 at the European Synchrotron Radiation Facility (ESRF), Grenoble, France. The X-ray wavelength used was 0.4001 Å and the data were binned between $0 \leq 2\theta \leq 40°$ with a 0.02° step size. All measured samples were sealed in 0.5 mm diameter silica capillaries and room temperature measurements were collected.

Rietveld analyses were performed on the collected data using the GSAS suite programs with a pseudo-Voigt function to describe the peak shape.

5.3. Results.

5.3.1. Structural properties.

Synchrotron X-ray Rietveld refinement was used to examine the structural properties with increased levels of Co doping. Analysis of the high resolution data showed that all samples of $Sr_4Cr_2O_6Fe_{2-x}Co_xAs_2$ (x = 0.05, 0.1, 0.15, 0.25, 1, 1.5 2) adopt a tetragonal structure (*P4/nmm*) at room temperature. The Rietveld fits of these data are shown in Figures 5.1 - 5.7 and the Rietveld refined parameters of the preliminary data are summarized in Table 5.2 and Figure 5.8. Some minor impurities of SrO, FeAs, CoAs and Co_2As_3 (the last one only in the sample with full Co replacement) can be seen.

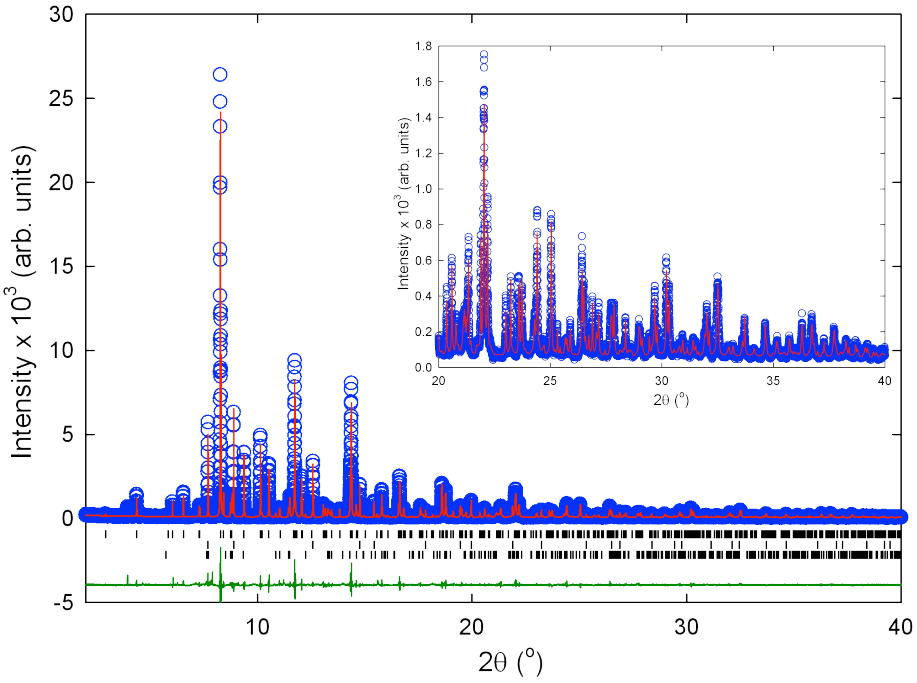

Figure 5.1. Final observed (blue circles), calculated (red solid line), and difference (lower green solid line) plots for the Rietveld refinement of $Sr_4Cr_2O_6Fe_{1.95}Co_{0.05}As_2$ at RT. Tick marks show the reflection positions and are from top to bottom: the main phase, 8% SrO and 12% FeAs. The refinement proceeded with the main phase in the *P4/nmm* space group. The X-ray wavelength is 0.4030068 Å. Inset shows zoom in on the 20 to 40 2θ data range.

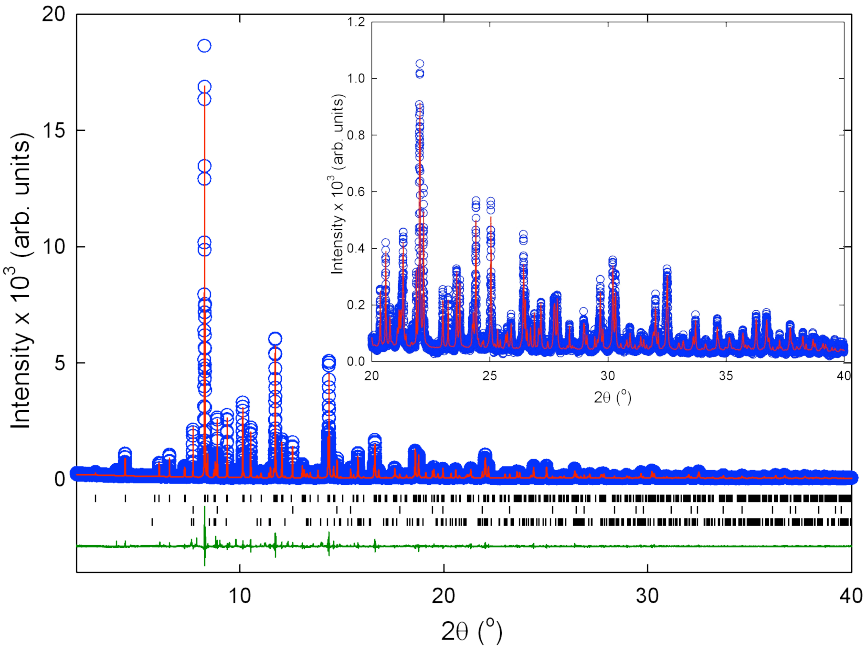

Figure 5.2. Final observed (blue circles), calculated (red solid line), and difference (lower green solid line) plots for the Rietveld refinement of $Sr_4Cr_2O_6Fe_{1.9}Co_{0.1}As_2$ at RT. Tick marks show the reflection positions and are from top to bottom: the main phase, 6% SrO and 8% FeAs. The refinement proceeded with the main phase in the *P4/nmm* space group. The X-ray wavelength is 0.4030068 Å. Inset shows zoom in on the 20 to 40 2θ data range.

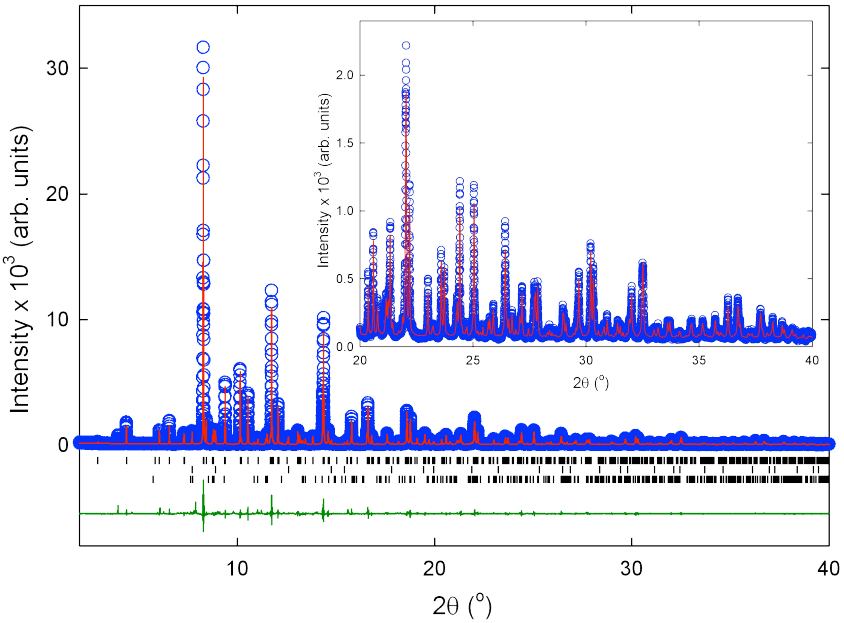

Figure 5.3. Final observed (blue circles), calculated (red solid line), and difference (lower green solid line) plots for the Rietveld refinement of $Sr_4Cr_2O_6Fe_{1.85}Co_{0.15}As_2$ at RT. Tick marks show the reflection positions and are from top to bottom: the main phase, 2.5% SrO and 8.5% FeAs. The refinement proceeded with the main phase in the *P4/nmm* space group. The X-ray wavelength is 0.4030068 Å. Inset shows zoom in on the 20 to 40 2θ data range.

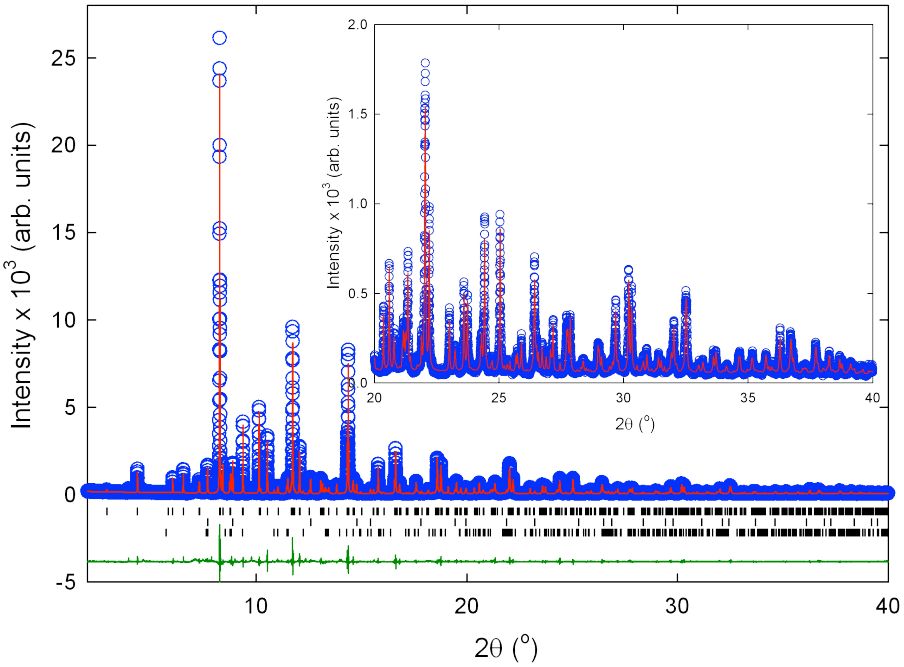

Figure 5.4. Final observed (blue circles), calculated (red solid line), and difference (lower green solid line) plots for the Rietveld refinement of $Sr_4Cr_2O_6Fe_{1.75}Co_{0.25}As_2$ at RT. Tick marks show the reflection positions and are from top to bottom: the main phase, 4% SrO and 10% FeAs. The refinement proceeded with the main phase in the *P4/nmm* space group. The X-ray wavelength is 0.4030068 Å. Inset shows zoom in on the 20 to 40 2θ data range.

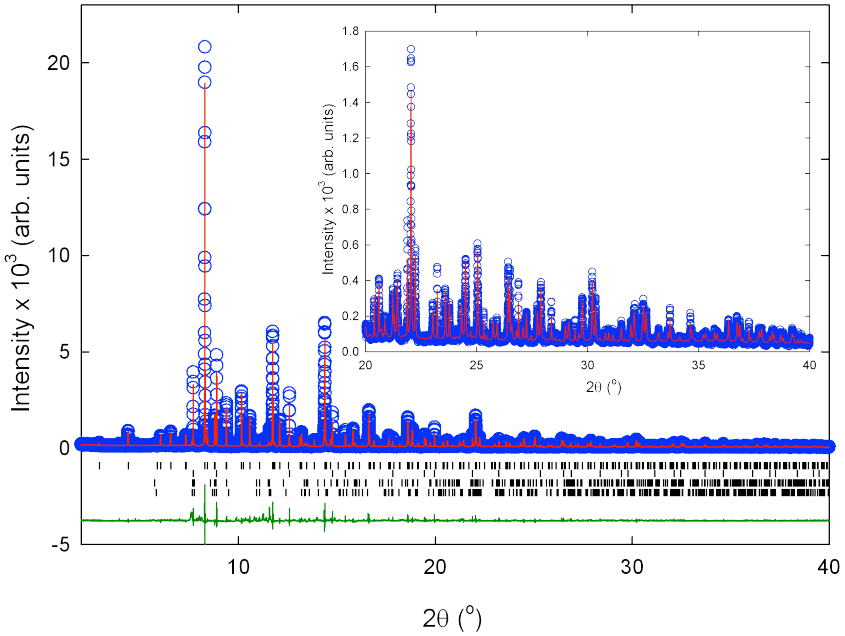

Figure 5.5. Final observed (blue circles), calculated (red solid line), and difference (lower green solid line) plots for the Rietveld refinement of $Sr_4Cr_2O_6FeCoAs_2$ at RT. Tick marks show the reflection positions and are from top to bottom: the main phase, 8% SrO, 4% FeAs and 3% CoAs. The refinement proceeded with the main phase in the *P4/nmm* space group. The X-ray wavelength is 0.4030068 Å. Inset shows zoom in on the 20 to 40 2θ data range.

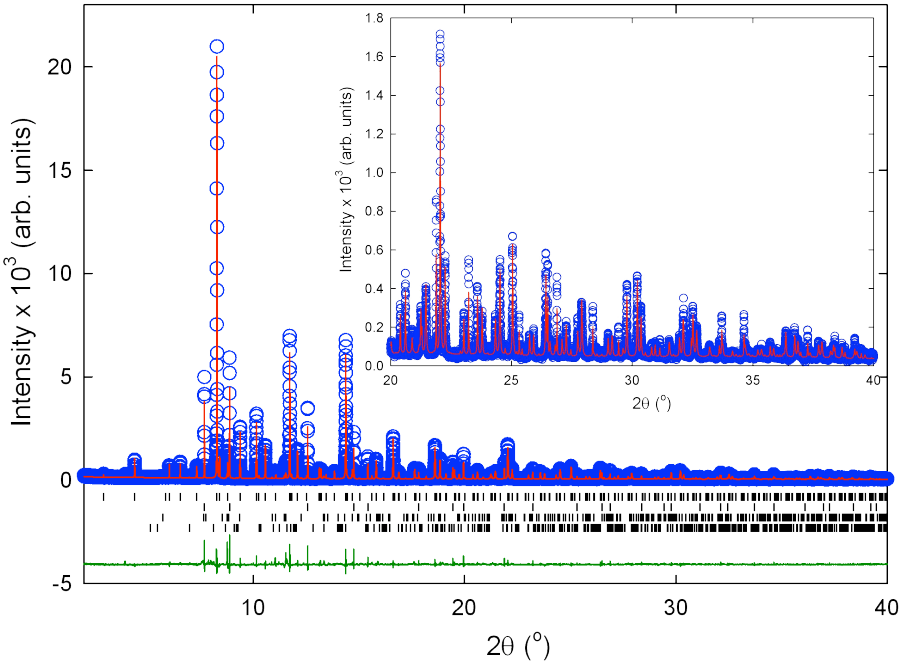

Figure 5.6. Final observed (blue circles), calculated (red solid line), and difference (lower green solid line) plots for the Rietveld refinement of $Sr_4Cr_2O_6Fe_{0.5}Co_{1.5}As_2$ at RT. Tick marks show the reflection positions and are from top to bottom: the main phase, 10% SrO, 5% FeAs and 3% CoAs. The refinement proceeded with the main phase in the *P4/nmm* space group. The X-ray wavelength is 0.4030068 Å. Inset shows zoom in on the 20 to 40 2θ data range.

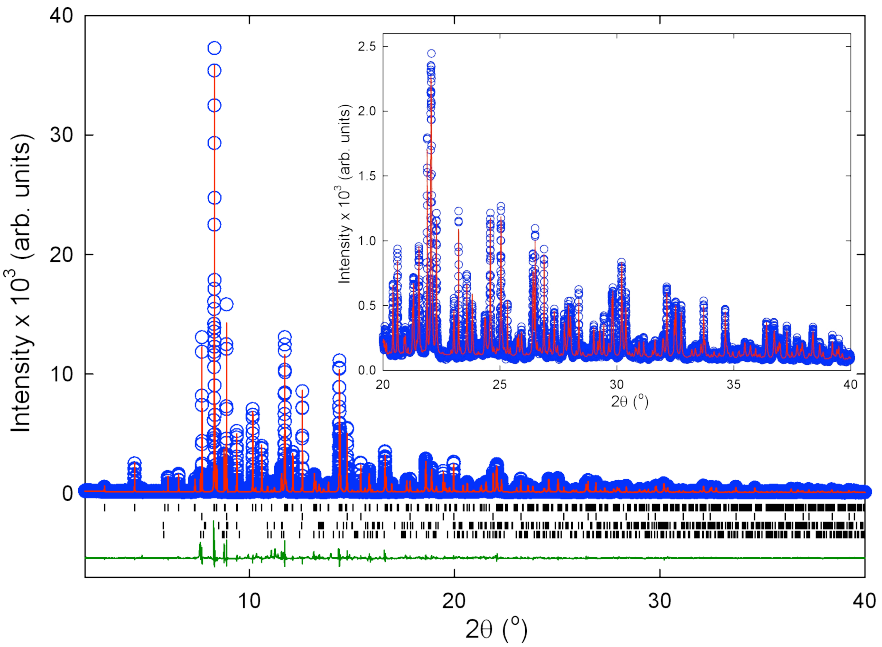

Figure 5.7. Final observed (blue circles), calculated (red solid line), and difference (lower green solid line) plots for the Rietveld refinement of $Sr_4Cr_2O_6Co_2As_2$ at RT. Tick marks show the reflection positions and are from top to bottom: the main phase, 12% SrO, 7% CoAs and 2% Co_2As_3. The refinement proceeded with the main phase in the *P4/nmm* space group. The X-ray wavelength is 0.4030068 Å. Inset shows zoom in on the 20 to 40 2θ data range.

Table 5.2. Refined structural parameters and bond lengths (Å) and angles (°) for chosen samples of $Sr_4Cr_2O_6Fe_{2-x}Co_xAs_2$ with x = 0.05, 0.15, 0.25, 1 and 2 obtained from Rietveld refinements of the synchrotron X-ray diffraction data at room temperature. Estimated errors in the last digits are given in parentheses.

		x = 0.05	x = 0.15	x = 0.25	x = 1	x = 2
Space group		*P4/nnm*	*P4/nnm*	*P4/nnm*	*P4/nnm*	*P4/nnm*
a (Å)		3.91430(1)	3.91504(0)	3.91511(1)	3.91378(1)	3.91660(1)
c (Å)		15.7475(1)	15.74927(1)	15.74564(1)	15.66827(0)	15.58850(1)
Volume (Å^3)		241.281(2)	241.398(1)	241.351(2)	240.002(2)	239.125(4)
Sr	B_{iso} (Å^2)	0.48(7)	0.48(7)	0.43(5)	0.61(6)	0.41(3)
	Occ.	0.98(3)	0.98(5)	0.96(7)	1.01(3)	0.98(3)
	z	0.19432(2)	0.19460(4)	0.19460(1)	0.19300(3)	0.19097(2)
Sr	B_{iso} (Å^2)	0.21(5)	0.21(5)	0.17(5)	0.34(7)	0.14(4)
	Occ.	0.94(2)	0.96(4)	0.93(9)	0.99(7)	0.93(5)
	z.	0.41513(3)	0.41465(4)	0.41473(6)	0.41383(4)	0.41361(5)
Cr	B_{iso} (Å^2)	0.35(5)	0.35(4)	0.30(6)	0.48(4)	0.28(5)
	Occ.	0.89(9)	0.91(1)	0.90(4)	0.93(2)	0.92(1)
	z	0.31027(4)	0.31025(1)	0.31067(3)	0.30985(1)	0.30918(1)
Fe	B_{iso} (Å^2)	0.79(5)	0.84(6)	0.81(6)	0.66(5)	-
	Occ.*	0.98	0.92	0.87	0.5	-
Co	B_{iso} (Å^2)	0.79(6)	0.84(6)	0.81(6)	0.66(7)	0.55(8)
	Occ.*	0.02	0.07	0.12	0.49	1.01
As	B_{iso} (Å^2)	0.31(4)	0.36(4)	0.33(7)	0.18(6)	0.66(5)
	Occ	0.94(3)	0.97(3)	0.94(3)	0.98(4)	0.94(2)
	z	0.08980(1)	0.08921(2)	0.08916(1)	0.08465(2)	0.08499(1)
O1	B_{iso} (Å^2)	0.38(7)	0.38(7)	0.33(4)	0.50(6)	1.86(3)
	Occ.	0.95(3)	1.00(8)	0.96(6)	0.98(7)	0.96(5)
	z	0.29364(1)	0.29190(2)	0.29398(1)	0.29009(1)	0.29065(1)
O2	B_{iso} (Å^2)	0.38(7)	0.38(7)	0.33(4)	0.50(4)	1.86(6)
	Occ	0.97(1)	1.00(4)	1.02(7)	0.93(4)	0.80(3)
	z	0.42445(1)	0.42342(1)	0.42514(2)	0.42492(1)	0.42738(1)
R_{wp} (%)		15.74	16.06	16.22	18.95	20.01
R_{exp} (%)		7.18	7.62	8.15	8.81	6.70
Cr-O (Å)		1.9747(5) x 4	1.9787(4) x 4	1.9751(5) x 4	1.9773(5) x 4	1.9794(6) x 4
		1.7981(3)	1.7823(4)	1.8023(2)	1.7500(5)	1.8426(3)
Fe/Co-Fe/Co (Å)		2.7680(3) x 4	2.7683(3) x 4	2.7684(2) x 4	2.7674(5) x 4	2.7694(2) x 4
Fe/Co-As(Å)		2.4148(6) x 4	2.4095(6) x 4	2.4089(4) x 4	2.3788(5) x 4	2.3643(3) x 4
Fe/Co-As-Fe/Co (°)		108.29(2) x 2	108.66(3) x 2	108.70(3) x 2	108.86(2) x 2	108.30(2) x 2
		110.06(2) x 4	109.87(3) x 4	109.85(3) x 4	110.70(2) x 4	111.83(3) x 4

*The total Fe/Co occupancies were obtained from a Rietveld fit to the synchrotron X-ray data, but the Fe/Co ratio was restrained to the nominal values.

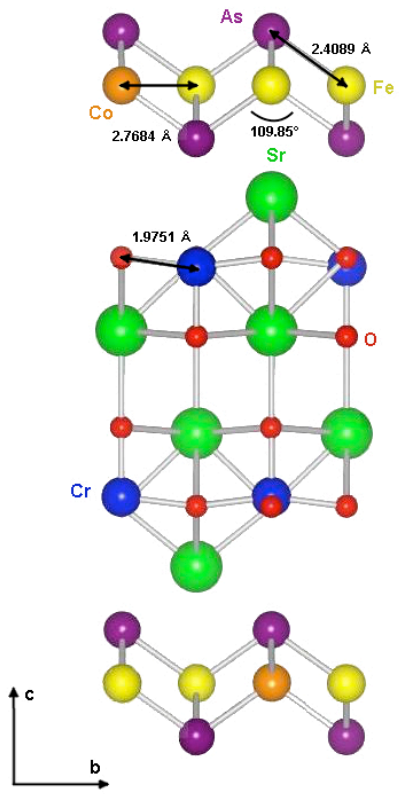

Figure 5.8. Schematic diagram of the room temperature tetragonal structure of the $Sr_4Cr_2Fe_{2-x}Co_xAs_2O_6$ system. The particular arrangement shown is $Sr_4Cr_2Fe_{1.75}Co_{0.25}As_2O_6$.

Refinement of the occupancies of the atomic sites confirms the nominal composition for most of the samples. It can also be seen clearly when both *a* and *c* values are plotted as a percentage of the corresponding axes in the parent compound. In the case of $Sr_4Cr_2O_6Fe_{1.75}Co_{0.25}As_2$, however, the refinement shows a large deviation from the nominal composition. Further data analysis shows that the doping level reached is lower than assumed, and thus the compositions used in this chapter are the ones calculated from the fit to the percentage of the parent compound (Figure 5.11), which indicates a composition of $Sr_4Cr_2O_6Fe_{1.8}Co_{0.2}As_2$. The refined values of *a* and *c* axes are shown in Figure 5.9.

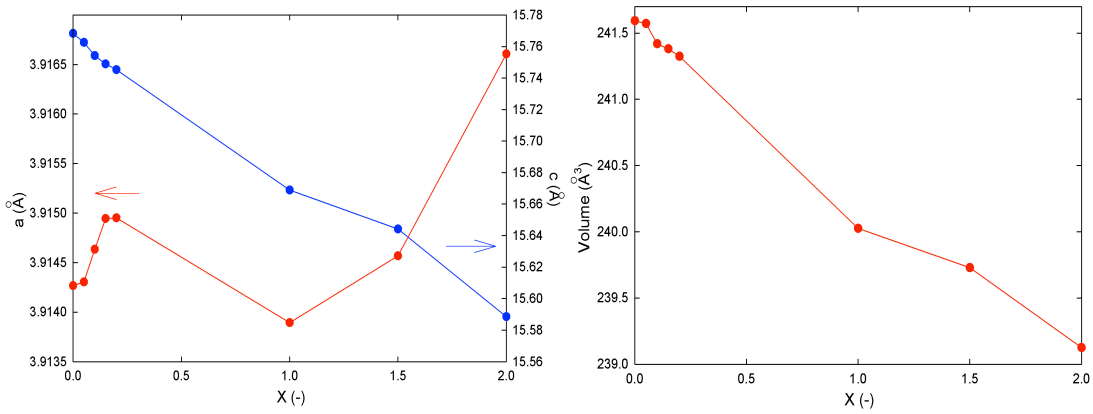

Figure 5.9. Evolution of the room temperature tetragonal lattice constants as a function of Co^{3+} doping level *x* in $Sr_4Cr_2O_6Fe_{2-x}Co_xAs_2$**.** The lines are guides to the eye.

The *ab* plane lattice constants are increasing slightly with increasing content of Co at low levels of doping, and then it is dropping to a minimum for Fe-Co doping level ratio 1:1. This is consistent with the larger ionic radius of Fe compared to Co. For higher cobalt content the *ab* plane values are increasing smoothly, which can be explained by gradual contraction of the Fe/Co-As bond lengths, and expansion of the tetrahedral angle from 110.70° for $x = 1$ to 111.83° for the sample with full cobalt substitution (Figure 5.10). On the other hand the *c* axis decreases gradually with an increasing level of Co substitution. This results in a decrease in cell volume across all measured samples.

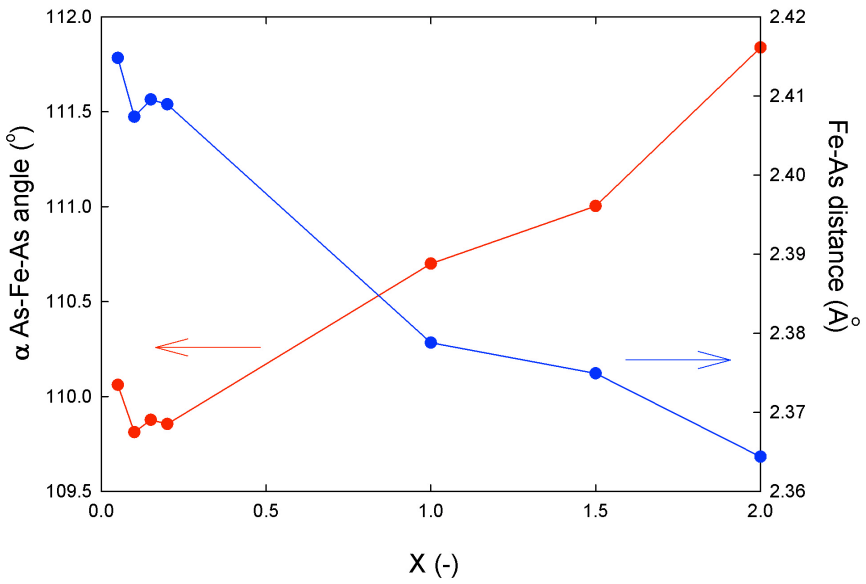

Figure 5.10. Evolution of the room temperature tetrahedral angle and Fe-As bond as a function of Co^{3+} doping level *x* in $Sr_4Cr_2O_6Fe_{2-x}Co_xAs_2$**.** The lines are guides to the eye.

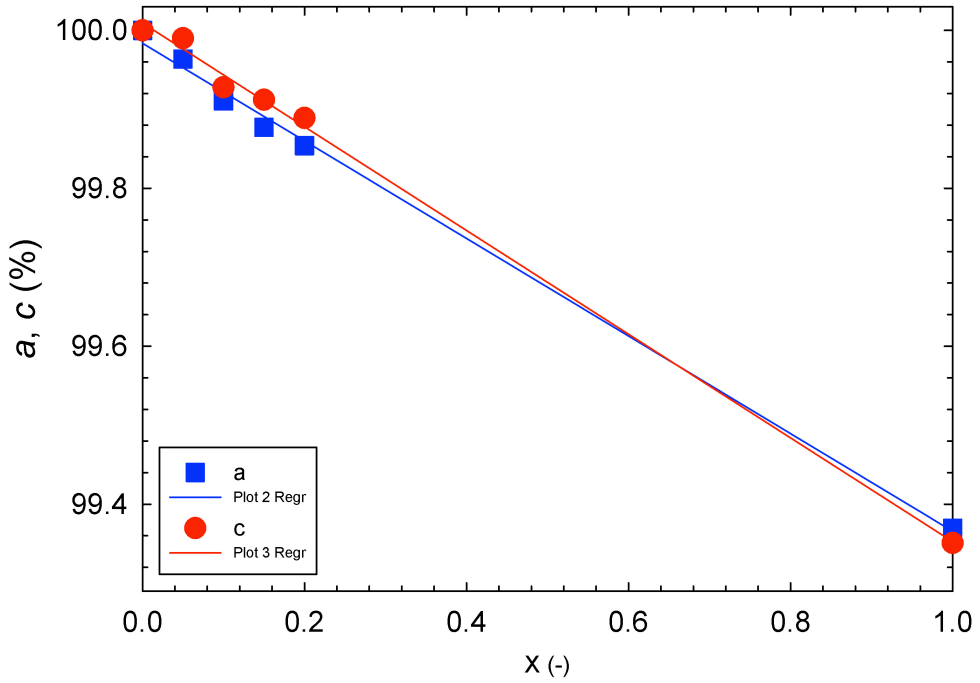

Figure 5.11. Evolution of the room temperature tetragonal lattice constants as a function of percentage of parent lattice constants in $Sr_4Cr_2O_6Fe_{2-x}Co_xAs_2$**.** The lines are guides to the eye.

5.3.2. Magnetic susceptibility.

The magnetic susceptibility of the $Sr_4Cr_2O_6Fe_{2-x}Co_xAs_2$ samples was measured at applied field of 10 kOe (Figure 5.12). The data show a maximum at around 70 K, which corresponds to the one seen in the parent compound. At low temperatures there is another visible upturn, which corresponds to the superconducting transition temperatures. The temperature dependence of χ is Curie-Weiss between RT and 120 K, and is dominated by the paramagnetic contribution of Cr^{3+}. The inverse ($1/\chi$) magnetic susceptibilities are shown in Figure 5.13. The effective magnetic moments are much lower (μ_{eff} = 1.31 μ_B, θ = -72.4(2) K for x = 0.05; μ_{eff} = 1.30 μ_B, θ = -68.3(1) K for x = 0.10 and μ_{eff} = 1.26 μ_B, θ = -65.8(2) K for x = 0.15) than the parent compound (μ_{eff} = 5.03 μ_B) and they are all decreasing in value with increasing Co doping level, while the Weiss temperatures are negative, which suggests antiferromagnetic interactions, and they are increasing with increasing doping levels. This indicates that doping with cobalt successfully suppresses the magnetic contribution from Fe and Cr.

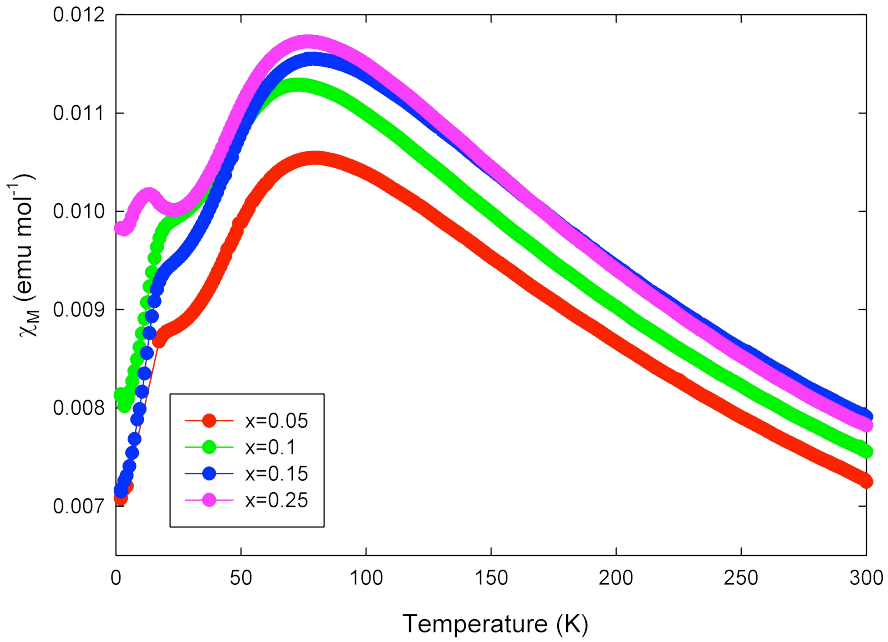

Figure 5.12. Temperature dependence of magnetic susceptibility measured at 10 kOe for the $Sr_4Cr_2O_6Fe_{2-x}Co_xAs_2$ series.

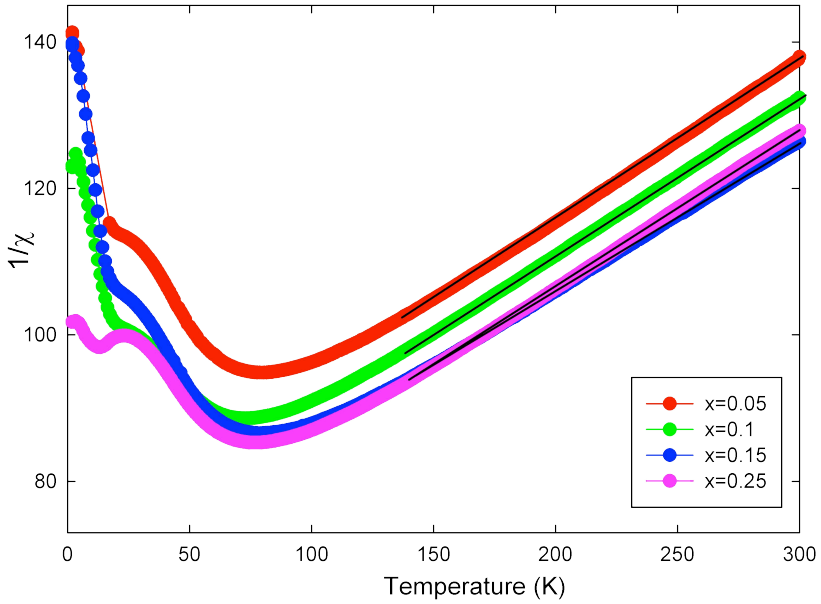

Figure 5.13. Temperature dependence of inverse magnetic susceptibility for the $Sr_4Cr_2O_6Fe_{2-x}Co_xAs_2$ series. The solid line is a fit to the Curie-Weiss law.

Samples with a low doping level of Co were also measured with use of a field of 10 Oe (Figure 5.14). The data show a clear drop and superconducting transition for all samples with the doping level up to $x = 0.25$. The transition temperature increases for samples with $x = 0.05$, reaching a maximum for $x = 0.1$ and then dropping for $x = 0.15$, $x = 0.2$ and finally for $x = 0.25$, which indicates the borderline for superconductivity in this composition (Figure 5.15). The maximum T_c achieved is 17.5 K for $x = 0.1$, and the calculated diamagnetic shielding fractions are shown in Table 5.3.

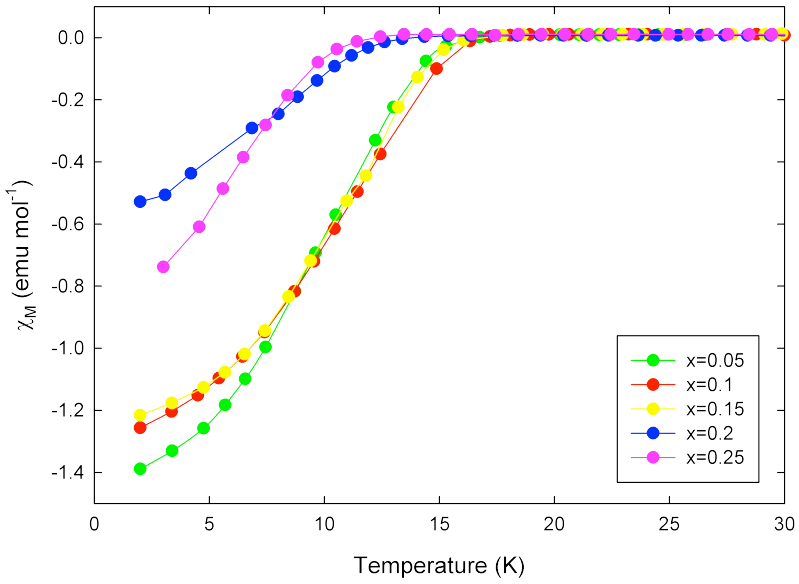

Figure 5.14. Evolution of the superconducting transition with the doping level in $Sr_4Cr_2O_6Fe_{2-x}Co_xAs_2$.

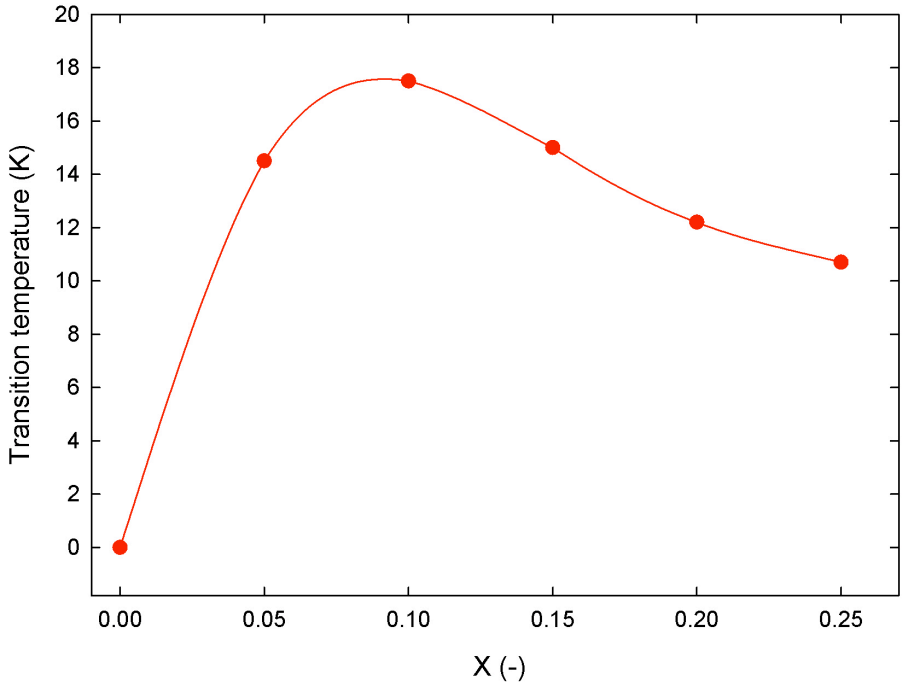

Figure 5.15. Evolution of the superconducting transition temperatures with the doping level in $Sr_4Cr_2O_6Fe_{2-x}Co_xAs_2$. The lines are guides to the eye.

Table 5.3. Values of superconducting transition temperatures and diamagnetic shielding fractions with increased cobalt doping level in $Sr_4Cr_2O_6Fe_{2-x}Co_xAs_2$.

X (doping level of cobalt)	Superconducting transition temperature (K)	Diamagnetic shieding fractions (%)
0.05	14.5	15.1
0.1	17.5	15.4
0.15	15	13.3
0.2	12.2	9.1
0.25	10.7	8.1

5.3.3. Electrical resistivity.

The resistivity measurements of $Sr_4Cr_2O_6Fe_{2-x}Co_xAs_2$ compounds were not possible at ambient pressure in a traditional PPMS puck, as the samples are sensitive to air and moisture. Instead, high pressure measurements were conducted in an air-tight pressure cell. The range of pressures used was between 5 kbar and 76 kbar. The measured samples were $Sr_4Cr_2O_6Fe_{1.9}Co_{0.1}As_2$ and $Sr_4Cr_2O_6Fe_{1.85}Co_{0.15}As_2$. In both samples there is a maximum followed by a steep drop in resistivity at temperatures corresponding to the superconducting transition, although it does not drop to zero value. This can be explained by the superconducting transition not occurring throughout the sample due to insufficient homogeneity. The pressures used seem to play a role, as the aforementioned peak is decreasing and smoothing down for higher pressures used.

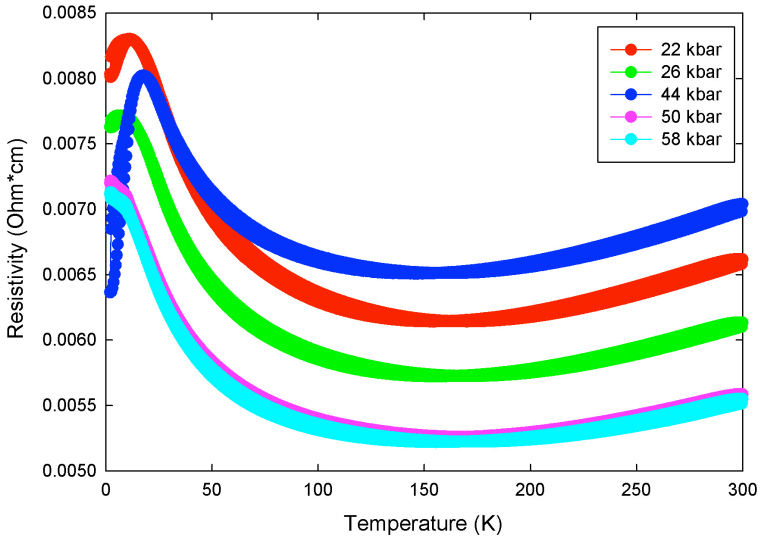

Figure 5.16. Temperature dependence of the resistivity for $Sr_4Cr_2O_6Fe_{1.9}Co_{0.1}As_2$ measured at different pressures.

The measurements of $Sr_4Cr_2O_6Fe_{1.9}Co_{0.1}As_2$ sample show a slight decrease in resistivity and at around 150 K the values start to increase, reaching the maximum at a transition temperature (Figure 5.16). That maximum also shifts to higher temperatures for higher pressures, with the biggest shift being at 44 kbar before almost disappearing with further increase in pressure.

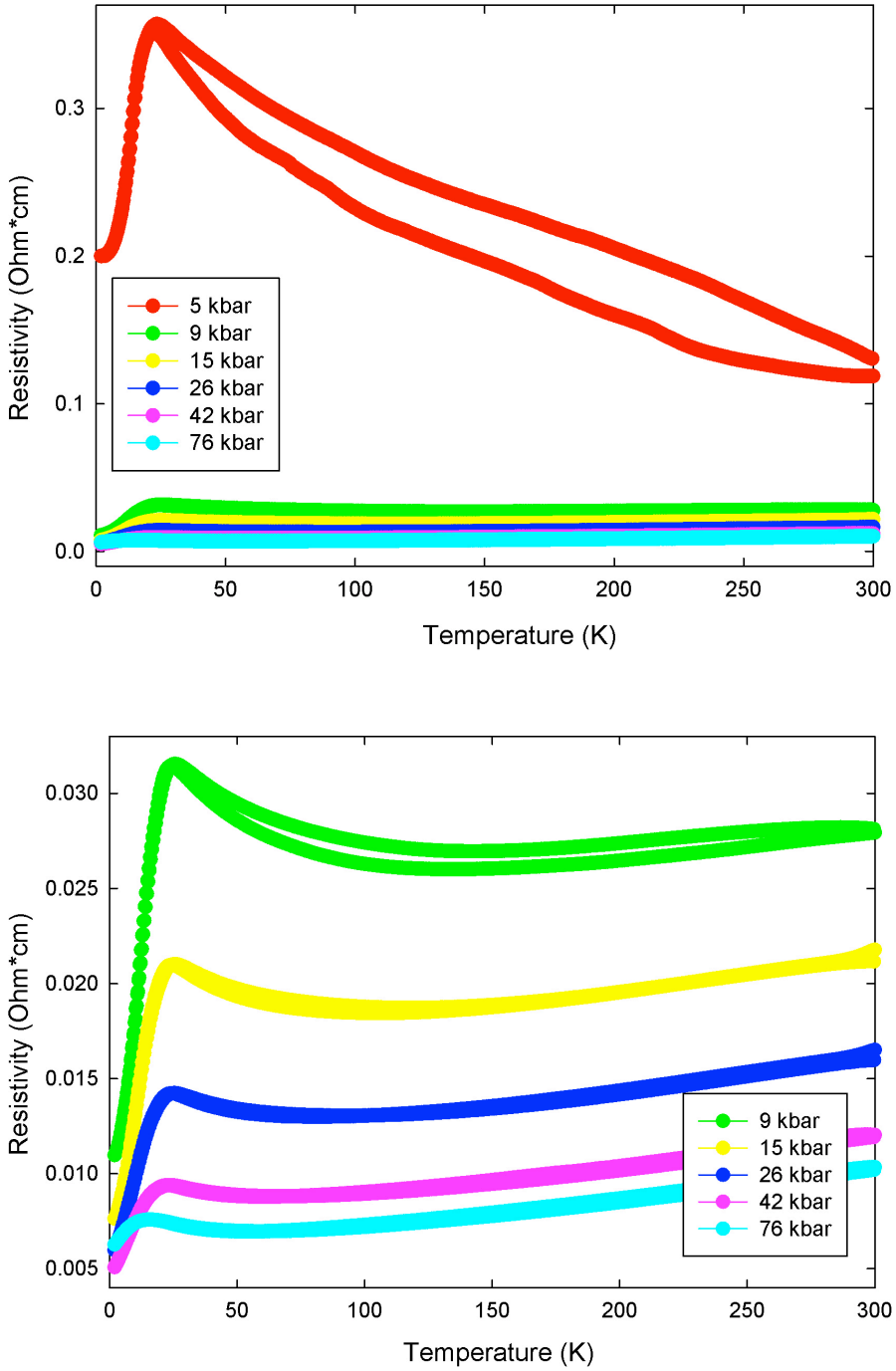

Figure 5.17. Temperature dependence of the resistivity for $Sr_4Cr_2O_6Fe_{1.85}Co_{0.15}As_2$ measured at different pressures. The bottom picture shows a close-up of measurements done at higher pressures.

The $Sr_4Cr_2O_6Fe_{1.85}Co_{0.15}As_2$ sample shows a steady increase in resistivity for 5 kbar with the aforementioned peak for the superconducting transition (Figure 5.17 top and bottom). There is however a huge decrease in overall resistivity between 5 kbar and 9 kbar, and for those higher pressures the data shows a very

small decrease in values down the way to the temperature of the peak, which for this composition decreases with higher pressure.

When compared to the parent compound, the overall resistivity values are much lower for doped samples (Figure 5.18). The parent compound shows a local maximum at a magnetic transition temperature, while none of the doped samples show that property. All doped samples measured are bad metals compared to the semiconducting parent compound, and there is a clear drop in the doped compounds at the superconducting transition temperatures, which is not seen at all in the parent compound.

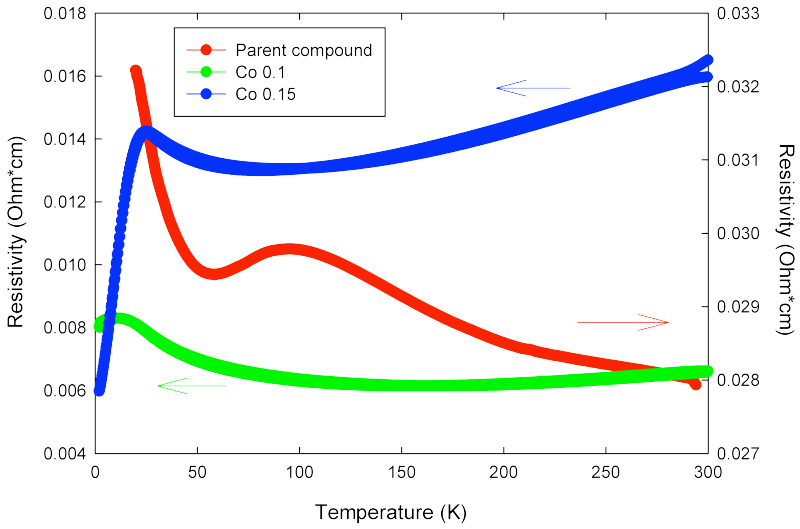

Figure 5.18. Comparison of different temperature dependence of the resistivities for different samples of $Sr_4Cr_2O_6Fe_{2-x}Co_xAs_2$ measured at 22 kbar for the parent compound and $x = 0.1$ and 26 kbar for $x = 0.15$.

5.4. Conclusion.

The structural, magnetic and electric properties of polycrystalline $Sr_4Cr_2O_6Fe_{2-x}Co_xAs_2$ were investigated. The experimental study showed that a parent compound $Sr_4Cr_2O_6Fe_2As_2$ is a good starting compound for doping and achieving materials that have a superconducting transition. Successful doping on the Fe site with Co triggers superconductivity and changes some properties seen in the pure parent compound. The lattice constants, angles and distances between atom change gradually with Co doping, and also the percentage of the original values of the *a* and *c* axes can be used as an experimental way of measuring the actual composition achieved in synthesis. A full doping range was achieved between the parent compound with full Fe level to a complete interchange of Fe with Co. The experimental data showed that for the highest level of Fe/Co mixing it is difficult to produce very pure samples. With Co doping the magnetic moment is suppressed, showing that Fe plays an important role in the magnetic structure of this composition. The maximum temperature of the superconducting transition was 17.5 K for the composition with $x = 0.1$ and the maximum Co doping showing signs of superconductivity is for $x = 0.25$.

The $Sr_4Cr_2O_6Fe_{2-x}Co_xAs_2$ series is a good starting point for examining the correlation between magnetism and superconductivity in this type of materials. More detailed investigation of the structural and magnetic properties with changing temperature would be beneficial to fully understand this family of superconductors.

5.5. Bibliography.

1. Kamihara, Y.; Watanabe, T.; Hirano, M.; Hosono, H., *Journal of the American Chemical Society,* **2008**, *130*, 3296.
2. Ren, Z.-A.; Wei, L.; Yang, J.; Yi, W.; Shen, X.-L.; Li, Z.-C.; Che, G.-C.; Dong, X.-L.; Sun, L.-L.; Zhou, F.; Zhao, Z.-X. *Chinese Physics Letters,* **2008**, *25*, 2215.
3. Aswathy, P. M.; Anooja, J. B.; Sarun, P. M., *Superconductor Science and Technology,* **2010,** 23(7), 073001.
4. Marcinkova, A.; Grist, D. A. M.; Margiolaki, I.; Hansen, T. C.; Margadonna, S.; Bos, J.-W. G., *Physical Review B,* **2010**, 81(6), 064511.
5. Ning, F. L.; Ahilan, K.; Imai, T.; Sefat, A. S.; McGuire, M. A.; Sales, B. C.; Mandrus, D.; Cheng, P.; Shen, B.; Wen, H.-H., *Physical Review Letters*, **2009**, 104(3), 037001.
6. Paular, S.; Sharma, S.; Bharathi, A.; Satya, A. T.; Chandra, S.; Hariharan, Y.; Sundar, C. S. *Physical Review B,* **2010,** 81(17), 174512.
7. Shi, H. Y.; Wang, X. L.; Xia, T.-L.; Zhang, Q. M.; Wang, X. Q.; Zhao, T.-S., *Rapid Research Letters*, **2010**, 4(3-4), 67-69.
8. Gooch, M.; Lv, B.; Lorenz, B.; Guloy, A. M.; Chu, C.-W. *Physical Review B*, **2008**, 78(18), 180508.
9. Margadonna, S.; Takabayashi, Y.; Ohishi, Y.; Mizuguchi, Y.; Takano, Y.; Kagayama, T.; Nakagawa, T.; Takata, M.; Prassides, K. *Physical Review B* **2009**, *80*, 064506.
10. Torikachvili, M. S.; Budko, S. L.; Ni, N.; Canfield, P. C. *Physical Review B* **2008**, *78*, 104527.
11. Yang, Y.; Hu, X., *arXiv:1003.0592*, **2010.**
12. Sato, S.; Ogino, H.; Kawaguchi, N.; Katsura, Y.; Kishio, K.; Shimoyama, J.-I., *Superconductor Science and Technology* **2010**, 23(4), 045001.
13. Han, F.; Zhu, X.; Mu, G.; Cheng, P.; Shen, B.; Zeng, B.; Wen, H.-H., *Science China Physics*, **2010**, 53(7), 1202-1206.
14. Tegel, M.; Hummel, F.; Su, Y.; Chatterji, T.; Brunelli, M.; Johrendt, D., *Europhysics. Letters,* **2010**, *89*, 37006.

Chapter 6

Conclusions and future directions.

This thesis describes an investigation into two families of transition metal-based oxyarsenides: 1111-type and 42622-type. This led to the discovery of several materials that may form bases for high temperature superconductors, and are a good starting point for further research. Several of them had unique properties, which with further study may provide useful insights into the nature of superconductivity itself.

During this research, a variety of different compounds were synthesised, and their properties were measured in order to produce new high-temperature superconductors and materials that might lead to them. The 1111-type oxyarsenides researched were the family of $Nd_{1-x}Sr_xFeAsO$, with the Sr content being between 5 and 20%. In the 42622 family a number of different materials were produced based on the general formula $Sr_4M^I{}_2O_6M^{II}{}_2As_2$ (M^I = Sc, Cr, V; M^{II} = Fe, Co, Ni) and also the Co-doped family of $Sr_4Cr_2Fe_{2-x}O_6Co_xAs_2$ was synthesised. A variety of measurements were conducted and analysed in order to understand the materials produced. Laboratory- and synchrotron-based powder X-ray diffraction techniques were used to determine the crystal structure, and neutron powder diffraction was employed to describe magnetic structures and detailed atom positions within the samples. SQUID and PPMS measurements were conducted to gather data about the electric and magnetic properties of the researched compounds, and to check how those properties change with doping in the parent compounds. Both families investigated showed a large number of interesting properties, including a change from semiconducting behaviour to metallic type conductivity with increased doping levels ($Nd_{1-x}Sr_xFeAsO$), lack of structural transition in 42622 family members (the only exception being $Sr_4V_2O_6Fe_2As_2$) and superconductivity alongside magnetic transition ($Sr_4Cr_2O_6Fe_{2-x}Co_xAs_2$). These behaviours are unusual both within their families and for superconductors in general. A detailed comparison of the different compositions within these families may illuminate the connections between a material's structure and superconducting properties.

The synthesis of the 1111 family of $Nd_{1-x}Sr_xFeAsO$ proved to be a successful route for hole doping in this system. Although the maximum level of doping achieved was 20%, these low level doped compounds showed a remarkable change in structural and physical properties. The *a* axis showed a steady increase with doping, which can be explained by the fact that the Sr^{2+} ions are larger than the replaced Nd^{3+}. The *c* axis, however, shows a completely different behaviour – firstly decreasing and then increasing again with higher doping levels, which is in contrast to electron doped members of 1111 family. The same behaviour was observed for the $FeAs_4$ pyramidal units, which expand for low doping levels and contract for the higher Sr^{2+} substitution. It is opposite from electron doped compounds, where $FeAs_4$ tetrahedra usually compress with increasing doping level, without any discontinuities. Structural studies showed that all members of $Nd_{1-x}Sr_xFeAsO$ family adopt a tetragonal *P4/nnm* structure and upon cooling undergo a structural phase transition, which lowers the symmetry from tetragonal to orthorhombic *Cmma*, in analogy with the undoped parent compound.

The structural analysis of the synthesised 42622-type showed a different behaviour to any other members of transition metal-based oxyarsenides. All of the members of this family adopt a tetragonal *P4/nmm* structure that remains unchanged upon cooling, as no structural phase transition was observed down to 2 K. The only exception was $Sr_4V_2O_6Fe_2As_2$, which undergoes a symmetry lowering transition from tetragonal to orthorhombic *Cmma* crystal structure. Another unusual property of this family is its large lattice dimensions, much bigger than other known types. This, along with the mixed valencies of atoms involved and the possibility of doping these structures using a large variety of elements at different locations, makes the 42622 family an important step towards synthesising high temperature superconducting materials with and without doping.

Both types of transition metal-based oxyarsenides, 1111-type and 42622-type, were investigated with SQUID and PPMS to reveal their magnetic and electronic properties. One of the important factors to study was how different compounds' properties change with partial or full substitution of their constituent atoms with other elements.

The NdFeAsO was known to be an antiferromagnet with poor metallic behaviour. Successful hole-doping of this material with strontium on the neodymium site led to a change in these properties – the 5% doped material shows a semiconducting type of behaviour and further doping leads to metallic behaviour with a superconducting transition, with a T_c of 13.5 K for a 20% doping level. Also with the doping the spin-density-wave antiferromagnetism is suppressed. The changes in structural and physical properties in the 1111-type upon hole doping were proven not to show symmetrical behaviour to those seen in analogous electron doped compounds, and higher levels of hole doping will be required in order to achieve similar behaviours. Further research on the hole doped $Nd_{1-x}Sr_xFeAsO$ compounds would be beneficial to fully understand the behaviour of this family in comparison to the electron doped analogous materials.

The researched electronic and magnetic properties of 42622 family showed a variety of different behaviours in the studied parent compounds. Neither of them exhibits the spin-density-wave anomaly, which is so common in other known families. Two of the synthesised parent compounds show a superconducting transition without any doping: $Sr_4V_2O_6Fe_2As_2$ and $Sr_4Sc_2O_6Ni_2As_2$, which again is something not commonly seen in other types of oxyarsenides. Finally, one of the members of 42622-type, $Sr_4Cr_2O_6Fe_2As_2$, exhibits a magnetic phase transition, and this parent compound was chosen for further research upon doping with Co on the Fe site.

The $Sr_4Cr_2O_6Fe_{2-x}Co_xAs_2$ system was successfully synthesised across the full range of doping levels, from the $Sr_4Cr_2O_6Fe_2As_2$ parent compound to the fully substituted iron by cobalt compound in $Sr_4Cr_2O_6Co_2As_2$. This doping was shown to suppress the magnetic transition, proving the contribution towards magnetism not only from Cr, but also from Fe. Also with the low levels of doping these compounds show a superconducting transition, with the highest temperature of 17.5 K for 5% doping level.

The research in this thesis showed a successful way of synthesising new superconducting materials and new parent compounds for further superconducting materials. Although neither of the superconductors synthesised reached a very high

superconducting transition temperature, they may prove to be good starting points for the further development of new high-temperature superconductors based upon these structures. In addition, these materials exhibited interesting superconducting properties that should be researched deeper and may provide useful data points for theoretical research into fully understanding the mechanisms behind superconductivity and its relationship to structural composition. Additional work is required to follow on from the results presented in this thesis to develop a full understanding of the mechanism behind the superconductivity in these systems. This work could include more detailed low temperature structural investigations as well as complete magnetic measurements using a variety of magnetic fields and temperatures. It is also worth considering that during this research, the $Sr_4Cr_2Fe_{2-x}O_6Co_xAs_2$ system was doped only using Co. There is a possibility that other elements may yield more interesting results. More detailed research is also required on the V-42622 family to confirm the preliminary data gathered during this investigation, and to better understand the mechanisms at play in this system. This could include alternative synthesis routes, using different starting materials or developing oxygen deficient samples to find out which factors are important for gaining the highest T_c. The theoretical understanding gained from such research could well lead to the design of structures that display superconducting behaviour at higher temperatures than ever before.

List of conferences and experiments attended:

- ESRF experiment on ID31 beamline – July 2008
- ILL experiment on D2B beamline – July 2008
- ILL experiment on D2B beamline – November 2008
- ILL experiment on D2B beamline – April 2009
- Diamond Light Source, IO8 beamline – May 2009
- ILL experiment on D20 beamline – May 2009
- ESRF experiment on ID31 beamline – June 2009
- ILL experiment on D20 beamline – June 2009
- ESRF experiment on ID31 beamline – July 2009
- 42nd IUPAC CONGRESS, 2-7 August 2009 – poster '**The oxyarsenides $Sr_4M_2O_6Fe_2As_2$ (M = Sc, Cr, V) as parent compounds of new superconducting materials'**
- ESRF experiment on ID31 beamline – July 2010
- ILL experiment on D2B beamline – July 2010
- ILL experiment on D20 beamline – July 2010

Reprint of Publications

Crystal structure of the new $FeSe_{1-x}$ superconductor†

Serena Margadonna,*[a] Yasuhiro Takabayashi,[b] Martin T. McDonald,[b] Karolina Kasperkiewicz,[a] Yoshikazu Mizuguchi,[c] Yoshihiko Takano,[c] Andrew N. Fitch,[d] Emmanuelle Suard[e] and Kosmas Prassides*[b]

Received (in Cambridge, UK) 29th July 2008, Accepted 5th September 2008
First published as an Advance Article on the web 26th September 2008
DOI: 10.1039/b813076k

The newly discovered superconductor $FeSe_{1-x}$ ($x \approx 0.08$, $T_c^{onset} \approx 13.5$ K at ambient pressure rising to 27 K at 1.48 GPa) exhibits a structural phase transition from tetragonal to orthorhombic below 70 K at ambient pressure—the crystal structure in the superconducting state shows remarkable similarities to that of the $REFeAsO_{1-x}F_x$ (RE = rare earth) superconductors.

Superconductivity at the surprisingly high temperature of 55 K has been recently reported in fluorine-doped rare-earth iron oxyarsenides, $REFeAsO_{1-x}F_x$.[1] The magnitude of T_c and the apparent similarities with the high-T_c cuprate superconductors—layered structural motifs of the conducting FeAs slabs and proximity to antiferromagnetic (AFM) and structural instabilities—have made these systems an intensely studied research field. The parent REFeAsO materials possess a simple tetragonal crystal structure (ZrCuSiAs-type, space group $P4/nmm$) comprising layers of edge-sharing $FeAs_4$ tetrahedra interleaved with REF layers. On cooling, a structural phase transition to orthorhombic crystal symmetry (space group *Cmma*) accompanied by the development of long range AFM order occurs.[2] The magnetic instability is suppressed upon fluorine-doping before the onset of superconductivity,[3] while orthorhombic symmetry survives well within the superconducting compositions.[4] Superconductivity can also be induced by oxygen vacancies in the $REFeAsO_{1-\delta}$ systems.[5] The family of FeAs-based superconductors has now further expanded to include the related alkali-doped superconductors, $A_{1-x}A'_xFe_2As_2$ (A = alkaline earth, A′ = alkali metal)[6] and the ternary LiFeAs phase.[7]

These discoveries have catalysed the search for superconducting compositions in related materials in which two-dimensional FeQ (Q = non-metal ions) slabs are also present. This search has now led to the report that superconductivity at ~8 K occurs in the simple binary α-$FeSe_{1-x}$ phase field for $x = 0.12$ and 0.18.[8] Subsequent work has revealed resistivity onsets for the superconducting transition at temperatures as high as 13.5 K at ambient pressure.[9] Quite remarkably, T_c is extremely sensitive to applied pressure and rises rapidly at a rate of 9.1 K GPa^{-1}, reaching a value of 27 K at 1.48 GPa.[9] α-FeSe crystallises at room temperature with the tetragonal PbO-type structure (Fig. 1) and comprises stacks of edge-sharing $FeSe_4$ tetrahedra—the FeSe packing motif is essentially identical to that of the FeAs layers in the iron oxyarsenides. On cooling, it was reported that a structural phase transition occurs near 105 K to an unidentified low-temperature structure with possible triclinic symmetry.[8] At present, little else is known about the electronic properties of the superconducting α-$FeSe_{1-x}$ phases but it is reasonable to assume that Se non-stoichiometry is accompanied by the introduction of charge carriers in the 2D FeSe layers. At this stage, precise structural information on the superconducting phase of α-$FeSe_{1-x}$ is needed and this should be the cornerstone for all subsequent understanding of the origin of superconductivity in this intriguing system.

Here we report the structural determination of the α-$FeSe_{1-x}$ ($x \approx 0.08$) binary superconductor by high-resolution synchrotron X-ray and neutron powder diffraction at temperatures between 5 and 295 K. We find that below $T_s = 70$ K, the crystal structure becomes metrically orthorhombic (space group *Cmma*), displaying an identical distortion of the FeSe slabs to that observed for the FeAs layers in the iron oxyarsenide family. The structural transition coincides with the temperature at which the temperature-dependent resistivity, ρ, shows an anomaly.

Powder samples of $FeSe_{1-x}$ were prepared as described before.[9] SQUID measurements (ZFC/FC protocols, 10 Oe) reveal the onset of bulk superconductivity below ~8 K.

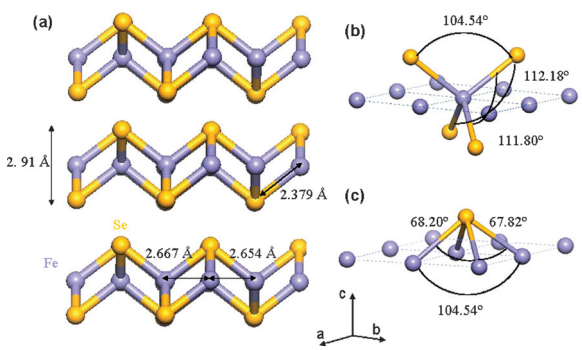

Fig. 1 (a) Schematic diagram of the low-temperature orthorhombic crystal structure of α-$FeSe_{0.92}$. Fe and Se ions are depicted as blue and yellow spheres, respectively. (b), (c) Geometry of the $FeSe_4$ tetrahedra and the $SeFe_4$ pyramids with the three distinct Se–Fe–Se and Fe–Se–Fe bond angles indicated.

[a] *School of Chemistry, University of Edinburgh, Edinburgh, UK EH9 3JJ. E-mail: serena.margadonna@ed.ac.uk*
[b] *Department of Chemistry, University of Durham, Durham, UK DH1 3LE. E-mail: K.Prassides@durham.ac.uk*
[c] *National Institute for Materials Science, 1-2-1 Sengen, Tsukuba, 305-0047, Japan*
[d] *European Synchrotron Radiation Facility, 38043 Grenoble, France*
[e] *Institut Laue Langevin, 38042 Grenoble, France*
† Electronic supplementary information (ESI) available: Results of the structural refinements. See DOI: 10.1039/b813076k

Resistivity measurements by the four-probe method show the onset of superconductivity at 13.5 K with the zero-resistance state obtained at ~7.5 K. In addition, two small humps in $\rho(T)$ are evident near 200 and 50 K.[9] High-resolution synchrotron X-ray diffraction experiments were carried out on the ID31 beamline at the ESRF. The samples were sealed in 0.7 mm diameter thin-wall glass capillaries and diffraction profiles (λ = 0.40301 Å) were collected at various temperatures between 5 and 295 K. The data were binned in the 2θ range 1–40° to a step of 0.002°. Higher statistics diffraction profiles were also recorded at 5, 100, 200 and 295 K over a longer angular range (2θ = 1° to 50°). Complementary neutron powder diffraction data were collected with the high-resolution diffractometer D2b (λ = 1.5944 Å) at the ILL. The sample (149 mg), from the same batch used for the synchrotron X-ray diffraction measurements, was loaded in a cylindrical vanadium can (diameter = 5 mm) and then placed in a standard ILL "orange" liquid helium cryostat. The instrument was operated in its high-flux mode and the data were collected in the angular range, 2θ = 0–164.5° in steps of 0.05°. Full diffraction profiles were measured with counting times of 8 h at 5 and 295 K. The raw data were merged and normalised to standard vanadium runs using local ILL programmes. Analysis of the diffraction data was performed with the GSAS suite of Rietveld programmes.

Inspection of the synchrotron X-ray and neutron diffraction profiles of α-$FeSe_{1-x}$ at ambient temperature confirmed the primitive tetragonal (T) unit cell (a = 3.77376(2) Å, c = 5.52482(5) Å; space group $P4/nmm$, R_{wp} = 7.87% (SXRPD) and 5.80% (NPD), χ^2 = 2.743, Fig. 1S, Table 1S†). The Se content refines to a value of 0.91(1). Additional peaks were also evident in the profiles and these could be accounted for by the presence of a minority hexagonal β-$FeSe_{1-x}$ phase (space group $P6_3/mmc$, 22% fraction as revealed by the combined Rietveld refinements). Based on the evolution of the diffraction profiles down to 90 K the refined structure remained strictly tetragonal with both lattice constants, a and c decreasing smoothly (Fig. 2). The rate of contraction at 13.5 and 30.0 ppm K^{-1} for a and c, respectively, is considerably anisotropic and leads to a gradual decrease of the (c/a) ratio with decreasing temperature. However, the lattice response to further decrease in temperature below 90 K is dramatically different—the hkl (h, $k \neq 0$) reflections in the diffraction profile first develop a characteristic broadening, followed by a clear splitting at $T_s \approx 70$ K (Fig. 3) signifying a lowering in symmetry of the high-temperature tetragonal structure and the onset of a structural transition. The magnitude of the splitting increases monotonically as the sample is cooled further down to 5 K.

Combined Rietveld refinements of the synchrotron X-ray and neutron powder diffraction data of α-$FeSe_{1-x}$ at 5 K were performed successfully with the same orthorhombic (O) superstructure model (space group $Cmma$, $b > a \sim \sqrt{2}a_T$, $c \approx c_T$, where a_T and c_T are the lattice constants of the high-temperature tetragonal unit cell) employed for the low-temperature phases of $REFeAsO_{1-x}F_x$.[2,4] At 5 K, the Se content refines to 0.92(1) and the refined lattice constants are a = 5.30781(5) Å, b = 5.33423(5) Å and c = 5.48600(5) Å (R_{wp} = 8.34% (SXRPD) and 3.77% (NPD), χ^2 = 2.750, Fig. 4, Table 1S†). The temperature evolution of the lattice constants and of the unit cell volume is shown in Fig. 2. The structural phase transition below

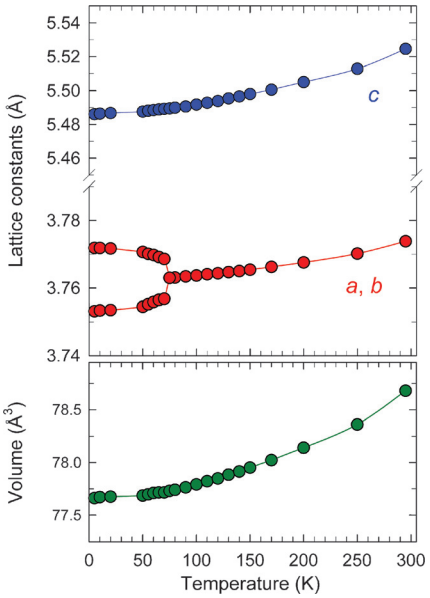

Fig. 2 Temperature evolution of the lattice constants (top) and the unit cell volume, V (bottom) in α-$FeSe_{0.92(1)}$. The a and b lattice constants are divided by $\sqrt{2}$ at temperatures below the tetragonal-to-orthorhombic phase transition.

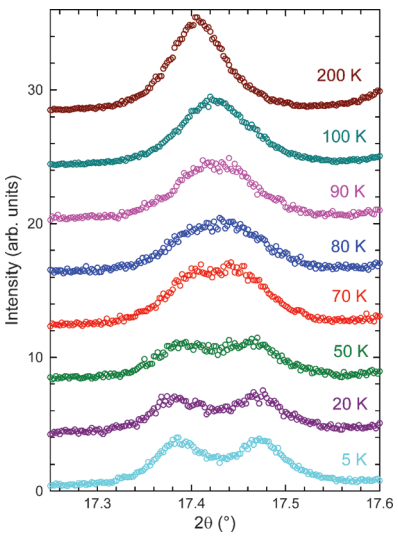

Fig. 3 Selected region of the synchrotron X-ray diffraction profile of α-$FeSe_{0.92(1)}$ showing the temperature evolution of the $(220)_T$ Bragg reflection which on cooling splits into a doublet [$(040)_O$, $(400)_O$] (λ = 0.40301 Å).

70 K is accompanied by the development of orthorhombic strain in the ab basal plane—this increases continuously on cooling, approaching a value of $s = (b - a)/(b + a) = 2.5 \times 10^{-3}$ at 5 K. However, the structural transition has no influence on the magnitude of either the interlayer c lattice constant or the unit cell volume, V as both decrease smoothly on cooling across the tetragonal–orthorhombic phase boundary. The influence of the T → O phase transition on the local geometry of the $FeSe_4$ tetrahedra in the SeFeSe slabs is only quite subtle (Fig. 1)—while at high T, there is a single Fe–Fe distance (at 295 K: 2.668 Å), below T_s, there are two symmetry inequivalent Fe–Fe distances

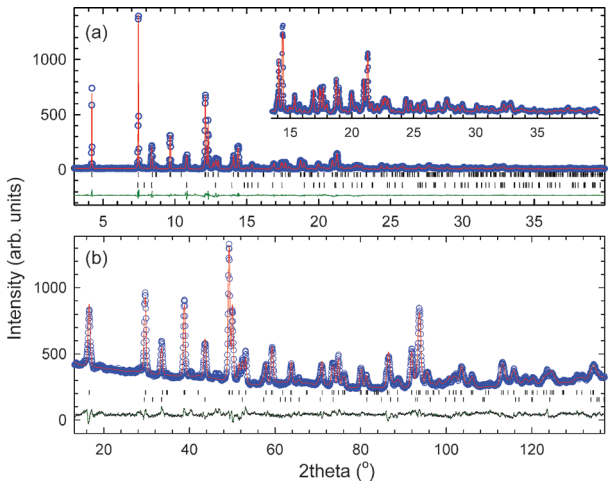

Fig. 4 Final observed (circles) and calculated (solid lines) (a) synchrotron X-ray (λ = 0.40301 Å) and (b) neutron (λ = 1.5944 Å) powder diffraction profiles for the α-$FeSe_{0.92(1)}$ sample (78% fraction) at 5 K. The lower solid lines show the difference profiles and the tick marks show the reflection positions of the α- (top) and β-$FeSe_{1-x}$ (bottom) phases. The inset in (a) shows an expanded view of the diffraction profile at high Bragg angles.

(at 5 K: 2.667 and 2.654 Å). Similarly, one set of the Fe–Se–Fe angles remains unaltered (at 295 K: 104.3°, at 5 K: 104.5°), while the second set (at 295 K: 112.1°) splits into two (at 5 K: 111.8° and 112.2°). On the other hand, there is a single Fe–Se bond distance both in the tetragonal and orthorhombic phases (at 295 K: 2.389 Å, at 5 K: 2.379 Å).

An important point arising from the present structural refinements is that the crystal structure of the superconducting state at ambient pressure in α-$FeSe_{0.92}$ is metrically orthorhombic. Moreover, there is a signature of the structural transformation in the electronic properties as T_s coincides with the observation of a hump in the temperature dependence of $\rho(T)$. This is reminiscent of the structural behaviour in the $SmFeAsO_{1-x}F_x$ oxyarsenide family in which an isostructural orthorhombically distorted structure is also adopted for the superconducting compositions with F doping levels $x \leq 0.12$, while the T → O phase transition is only suppressed at doping levels $x \geq 0.15$.[4] It is quite likely that an analogous suppression may occur for higher levels of Se non-stoichiometry in the present system. Certainly it is intriguing to conjecture that application of pressure may also lead to suppression of the low-temperature T → O phase transition, thereby accounting for the remarkable enhancement of T_c upon pressurisation.

Fig. 1 shows a schematic view of the orthorhombic structure of α-$FeSe_{0.92}$. It comprises SeFeSe slabs of ~2.91 Å thickness made of edge-sharing distorted $FeSe_4$ tetrahedra and separated from each other by an interlayer distance of ~2.58 Å. The $SmFeAsO_{1-x}F_x$ superconductors adopt a similar packing geometry made of AsFeAs slabs of ~2.7 Å thickness interleaved with Sm(F,O) layers which are absent in α-$FeSe_{0.92}$. The absence of the charge reservoir layers leads to a drastically reduced c lattice constant of ~5.5 Å for α-$FeSe_{0.92}$ (*cf.* $c \approx 8.5$ Å for $SmFeAsO_{1-x}F_x$). The basal plane lattice constants of α-$FeSe_{0.92}$ are also somewhat smaller than those in $SmFeAsO_{1-x}F_x$ reflecting the shorter Fe–Se bond lengths (2.38 Å *vs.* 2.40 Å for the Fe–As bond lengths).

Finally, it has been argued before for the iron oxypnictide superconductors that the geometry of the $AsFe_4$ pyramidal units (Fig. 1) sensitively controls both the Fe near- and next-near-neighbour exchange interactions[10] and the width of the electronic conduction band.[3,11] As a result, the superconducting transition onset T_c of $REFeAsO_{1-x}F_x$ increases as the Fe–As–Fe angles become progressively smaller and the rare earth series is traversed with the RE^{3+} ionic radius decreasing. At present, there is no information available on the electronic structure of the iron selenide superconductors and the corresponding influence of the local geometry on the conduction bandwidth. Nonetheless we note that for α-$FeSe_{1-x}$, the two small Fe–Se–Fe angles at ~68° (Fig. 1c) are comparable to those in $SmFeAsO_{1-x}F_x$ (~71°), while the larger Fe–Se–Fe angle of the $SeFe_4$ pyramids at ~105° is considerably smaller that those of the iron oxyarsenides (>111°).

In conclusion, we have found that the α-$FeSe_{0.92}$ superconductor adopts at low temperatures an orthorhombic superstructure of the high-temperature tetragonal PbO-type structure. The structural transition at ~70 K is evidenced in the electronic properties *via* a hump in the temperature dependence of the resistivity. Given the very large positive pressure coefficient of T_c (~9 K GPa^{-1}) in this material, it will be intriguing to follow the structural behaviour and the response of the orthorhombic distortion as a function of applied external pressure.

We thank the ESRF and the ILL for synchrotron X-ray and neutron beamtime, respectively.

Notes and references

1 Y. Kamihara, T. Watanabe, M. Hirano and H. Hosono, *J. Am. Chem. Soc.*, 2008, **130**, 3296; X. H. Chen, T. Wu, G. Wu, R. H. Liu, H. Chen and D. F. Fang, *Nature*, 2008, **453**, 761; R. H. Liu, G. Wu, T. Wu, D. F. Fang, H. Chen, S. Y. Li, K. Liu, Y. L. Xie, X. F. Wang, R. L. Yang, L. Ding, C. He, D. L. Feng and X. H. Chen, *Phys. Rev. Lett.*, 2008, **101**, 087001; Y. Takabayashi, M. T. McDonald, D. Papanikolaou, S. Margadonna, G. Wu, R. H. Liu, X. H. Chen and K. Prassides, *J. Am. Chem. Soc.*, 2008, **130**, 9242.
2 C. de la Cruz, Q. Huang, J. W. Lynn, J. Li, W. Ratcliff, J. L. Zarestky, H. A. Mook, G. F. Chen, J. L. Luo, N. L. Wang and P. Dai, *Nature*, 2008, **453**, 899; T. Nomura, S. W. Kim, Y. Kamihara, M. Hirano, P. V. Sushko, K. Kato, M. Takata, A. L. Shluger and H. Hosono, arXiv:0804.3569, 2008.
3 J. Zhao, Q. Huang, C. de la Cruz, S. Li, J. W. Lynn, Y. Chen, M. A. Green, G. F. Chen, G. Li, Z. Li, J. L. Luo, N. L. Wang and P. Dai, arXiv:0806.2528, 2008.
4 S. Margadonna, Y. Takabayashi, M. T. McDonald, M. Brunelli, G. Wu, R. H. Liu, X. H. Chen and K. Prassides, arXiv:0806.3962, 2008.
5 Z. A. Ren, G. C. Che, X. L. Dong, J. Yang, W. Lu, W. Yi, X. L. Shen, Z. C. Li, L. L. Sun, F. Zhou and Z. X. Zhao, *Europhys. Lett.*, 2008, **83**, 17002.
6 M. Rotter, M. Tegel, D. Johrendt, I. Schellenberg, W. Hermes and R. Pottgen, *Phys. Rev. B: Condens. Matter Mater. Phys.*, 2008, **78**, 020503.
7 M. J. Pitcher, D. R. Parker, P. Adamson, S. J. C. Herkelrath, A. T. Boothroyd, S. J. Clarke, arXiv:0807.2228, 2008; J. H. Tapp, Z. Tang, B. Lv, K. Sasmal, B. Lorenz, P. C. W. Chu and A. M. Guloy, *Phys. Rev. B: Condens. Matter Mater. Phys.*, 2008, **78**, 060505(R).
8 F.-C. Hsu, J.-Y. Luo, K.-W. Yeh, T.-K. Chen, T.-W. Huang, P. M. Wu, Y.-C. Lee, Y.-L. Huang, Y.-Y. Chu, D.-C. Yan and M.-K. Wu, arXiv:0807.2369, 2008.
9 Y. Mizuguchi, F. Tomioka, S. Tsuda, T. Yamaguchi and Y. Takano, arXiv:0807.4315.
10 T. Yildirim, *Phys. Rev. Lett.*, 2008, **101**, 057010.
11 T. M. McQueen, M. Regulacio, A. J. Williams, Q. Huang, J. W. Lynn, Y. S. Hor, D. V. West, M. A. Green and R. J. Cava, *Phys. Rev. B: Condens. Matter Mater. Phys.*, 2008, **78**, 024521.

Structural and electronic response upon hole doping of rare-earth iron oxyarsenides $Nd_{1-x}Sr_xFeAsO$ ($0 < x \leq 0.2$)†

Karolina Kasperkiewicz,[a] Jan-Willem G. Bos,[a] Andrew N. Fitch,[b] Kosmas Prassides[c] and Serena Margadonna*[a]

Received (in Cambridge, UK) 10th September 2008, Accepted 24th November 2008
First published as an Advance Article on the web 19th December 2008
DOI: 10.1039/b815830d

Hole doping of NdFeAsO *via* partial replacement of Nd^{3+} by Sr^{2+} is a successful route to obtaining superconducting phases (T_c = 13.5 K for a Sr^{2+} content of 20%); however, the structural and electronic response with doping is different from and non-symmetric to that in the electron-doped side of the phase diagram.

Upon electron doping, the family of rare-earth quaternary oxyarsenides with general formula REFeAsO (RE = rare earth) displays superconductivity with transition temperatures, T_c as high as 55 K, being surpassed only by the high-T_c cuprates.[1] The oxyarsenides adopt a tetragonal layered structure (space group *P*4/*nmm*) featuring alternating insulating RE–O and conducting Fe–As planes (Fig. 1a). On cooling, a structural phase transition to orthorhombic crystal symmetry (space group *Cmma*), accompanied by the development of long range AFM order occurs. Electron doping of the parent compounds REFeAsO (*e.g.* partial replacement of O^{2-} by F^- or oxygen deficiency) provides extra charge in the conduction plane, suppresses the structural/magnetic instability and triggers the occurrence of superconductivity. Theoretical calculations show that LaFeAsO is metallic (electron carrier) at the verge of a transition between a bad metal and a semiconductor[2] and that the E_F is located at the edge of a peak and in a pseudogap region of the density of states (DOS), making the electronic structure strongly electron–hole asymmetric.[3,4] The Fermi surfaces of the REFeAsO parent compounds are characterised by the presence of both electron and hole pockets.[4] The family of Fe-based superconductors has now further expanded to include the related hole-doped superconductors, $A_{1-x}A'_xFe_2As_2$ (A = alkaline earth, A′ = alkali metal)[5] as well as the ternary LiFeAs and the binary $FeSe_{1-x}$ phases.[6]

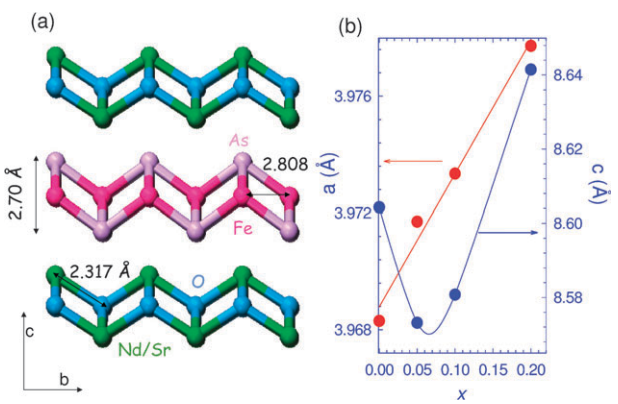

Fig. 1 (a) Schematic diagram of the room temperature tetragonal structure of $Nd_{1-x}Sr_xFeAsO$. The values of bond distances and angles shown refer to the composition with x = 0.05. (b) Evolution of the room temperature tetragonal lattice constants as a function of Sr^{2+} doping level, x. The lines are guides to the eye.

Hole doping has been an extremely successful route for the preparation of high-T_c superconductors in the AFe_2As_2 families. However, the issue of whether hole doping in REFeAsO produces superconducting compositions is still open. There has been an early report on the substitution of La^{3+} by Ca^{2+} in LaFeAsO that does not induce superconductivity.[1] Subsequent work on Sr^{2+} doping to afford $La_{1-x}Sr_xFeAsO$ demonstrated that superconductivity can be achieved at $x > 0.08$ and that the evolution of T_c shows a symmetric response to that on the electron-doped side. Positive Hall coefficients confirmed that the conduction is through hole charge carriers.[7] However, these results were not reproduced by other authors.[8] At this stage, it is essential to establish the role played by alkaline-earth-doping on the structural, electronic and magnetic behaviour of REFeAsO systems. Confirming the existence of superconducting phases, probing how T_c varies with composition and revealing the influence of doping on the structural and magnetic transitions are of fundamental importance for the understanding of the pairing mechanism in these high-T_c superconductors.

Here we report on the electronic and structural behaviour of a new family of hole-doped systems, $Nd_{1-x}Sr_xFeAsO$ (x = 0.05, 0.1, 0.2). We find that introduction of Sr^{2+} at the Nd^{3+} site affords single phase materials adopting the *P*4/*nmm* structure at 300 K. Low temperature resistivity and susceptibility measurements reveal that compositions with small doping levels (x = 0.05) show semiconducting behaviour. Increased doping leads to the emergence of metallic conductivity and superconductivity is observed at the maximum doping level, x = 0.20 with T_c = 13.5 K. The results clearly demonstrate that hole doping of NdFeAsO affords superconducting phases. In addition, the evolution of the electronic and structural properties is drastically different and non-symmetric to the electron-doped side of the phase diagram.

Powder samples of $Nd_{1-x}Sr_xFeAsO$ (x = 0, 0.05, 0.1, 0.2) were prepared by reaction of stoichiometric quantities of high-purity Fe, Fe_2O_3 and SrO with pre-synthesised FeAs and NdAs. All powders were mixed, grounded together and

[a] *School of Chemistry, University of Edinburgh, Edinburgh, UK EH9 3JJ. E-mail: serena.margadonna@ed.ac.uk*
[b] *European Synchrotron Radiation Facility, 38043 Grenoble, France*
[c] *Department of Chemistry, University of Durham, Durham, UK DH1 3LE*

† Electronic supplementary information (ESI) available: Results of the structural refinements at 5 and 300 K. See DOI: 10.1039/b815830d

pressed into pellets in an Ar atmosphere glovebox and then heated for 48 h at 1100 °C in evacuated quartz tubes. Increasing x above 0.2 leads to samples containing secondary phases. The magnetic susceptibilities were measured using a Quantum Design MPMS magnetometer and the electrical resistivity with a Quantum Design PPMS instrument by the four-probe method. High-resolution synchrotron X-ray diffraction experiments (λ = 0.40301 Å) were performed between 5 and 300 K on the ID31 beamline, ESRF, France.‡

Inspection of the diffraction profiles of all $Nd_{1-x}Sr_xFeAsO$ compositions at room temperature readily reveals the tetragonal unit cell (*P*4/*nmm*) established before for the REFeAsO systems.[9,10] Rietveld analysis of the room temperature high statistics diffraction profiles confirmed the successful substitution of Sr^{2+} at the Nd^{3+} sites with the occupancies refining to 0.052(6), 0.091(6) and 0.21(1) for the nominal compositions x = 0.05, 0.1 and 0.2, respectively (Table S1, Fig. S1, ESI†). The structural analysis also revealed that the *a*-axis increases monotonically as expected considering the larger ionic radius of Sr^{2+} (1.18 Å *vs.* 0.98 Å for Nd^{3+}) (Fig. 1b). Sr^{2+} substitution occurs within the RE–O layers which determine the basal plane dimensions. However, the *c*-axis shows a different response: it initially contracts before undergoing a considerable expansion at $x > 0.1$ (Fig. 1b). The *c*-axis dimensions are influenced by the geometry of the $FeAs_4$ tetrahedra (Fig. 2a and b) whose compression first decreases for $0 < x < 0.1$ and then increases at $x > 0.1$ (Fig. 2c). It is important to note that for small Sr^{2+} content, the evolution of the structural parameters is exactly opposite to what is found for the electron-doped systems where the $FeAs_4$ pyramidal units tend to compress monotonically with increasing doping level—the Fe–As–Fe angles decrease, while the thickness of the FeAs layer increases. However, at higher levels of Sr^{2+} substitution, the compression of the $FeAs_4$ tetrahedra increases in analogy with the trend observed for the superconducting electron-doped phases (Fig. S2, ESI†). It has been argued that the electronic structure of the REFeAsO systems strongly depends on small changes in interatomic distances and bond angles of the $FeAs_4$ pyramidal units. These structural parameters sensitively control both the Fe near- and next-near-neighbour exchange interactions as well as the width of the electronic conduction band due to the high degree of covalency (strong hybridisation) of the Fe–As bond.[11] The observed sudden increase in the Fe–As distance coupled with the larger lattice dimensions for the x = 0.2 composition may lead to a much smaller bandwidth and changes the electronic behaviour as compared to the small doping level compositions.

Diffraction profiles of compositions with x = 0.05, 0.1, 0.2 were collected on cooling between 300 and 5 K. All samples show a structural phase transition from tetragonal to orthorhombic (space group *Cmma*) in analogy with the undoped and electron-doped REFeAsO systems (Fig. 3 and S3, Table S2, ESI†).[9,10] At the transition temperature, T_s, no discontinuities are observed in either the *c* lattice constant or the normalised volume, *V*. Increasing the Sr^{2+} content level does not suppress the T → O transition and T_s remains almost constant for all compositions (T_s = 115 K for x = 0.05 and 130 K for x = 0.1 and 0.2, *cf.* T_s = 135 K for NdFeAsO this work and ref. 12).

The zero-field-cooled magnetic susceptibilities, χ_M of $Nd_{1-x}Sr_xFeAsO$ for x = 0, 0.05, 0.1 and 0.2 were measured in an applied magnetic field of 1 T. The values of χ_M smoothly decrease as a function of doping level as expected from the substitution of Nd^{3+} ($4f^3$, S = 3/2) by the non-magnetic Sr^{2+} in the RE–O layer ($\chi_M T$ at 300 K: 1.66, 1.59 and 1.47 emu K mol^{-1} for x = 0.05, 0.1 and 0.2, respectively) (Fig. 4). As a first approximation, the Fe^{2+} and Nd^{3+} contribution to the magnetic susceptibility can be considered independently in the high temperature paramagnetic region ($180 < T < 300$ K). It is then possible to subtract from the total magnetic susceptibility the paramagnetic Nd^{3+} contribution by considering the ground state ($4f^3$, $^4I_{9/2}$) and a van Vleck contribution due to the first excited state ($^4H_{7/2}$). Such a subtraction leaves for NdFeAsO a temperature independent component which is assigned to Pauli-like susceptibility of the Fe^{2+} spins. At 300 K, the susceptibility after subtraction is $\chi_M = 8.3 \times 10^{-4}$ emu mol^{-1} (*cf.* χ_M of LaFeAsO[10] with non-magnetic La^{3+} is 5×10^{-4} emu mol^{-1}). Analogous treatment of the 1 T data of the other compositions showed that the values of the temperature independent component of the susceptibility first decreases for a Sr content of 5% (9.3×10^{-5} emu mol^{-1}) and then smoothly increases up to the maximum doping level of 20% (1.95×10^{-4} and 3.5×10^{-4} emu mol^{-1} for x = 0.1 and 0.2, respectively). As the Pauli magnetic susceptibility is directly related to the DOS at the Fermi level, $N(E_F)$, the observed trend clearly indicates

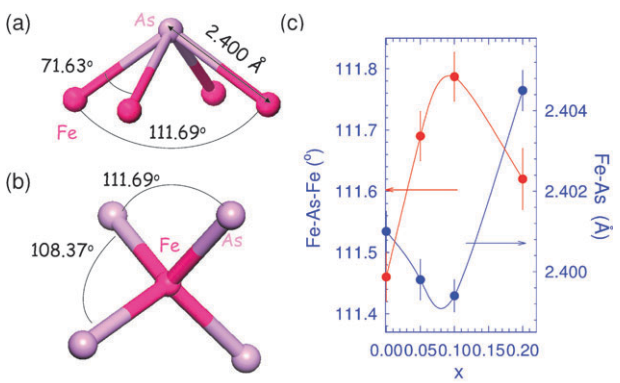

Fig. 2 Schematic diagram of the (a) $AsFe_4$ and (b) $FeAs_4$ units. Bond distances and angles refer to x = 0.05. (c) Evolution of the room temperature Fe–As distance and of the Fe–As–Fe angle as a function of Sr^{2+} doping level x. Lines are guides to the eye.

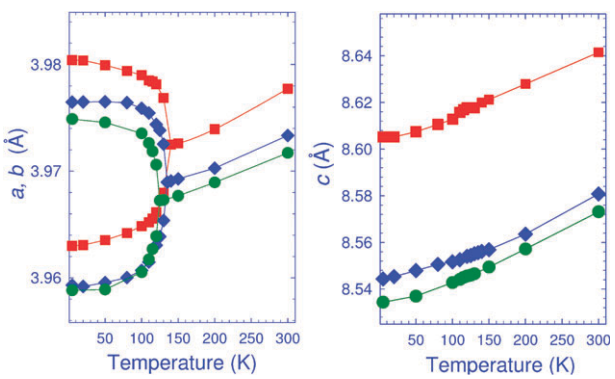

Fig. 3 Temperature evolution of the lattice constants for $Nd_{1-x}Sr_xFeAsO$: green circles, blue diamonds and red squares refer to compositions with x = 0.05, 0.1 and 0.2, respectively.

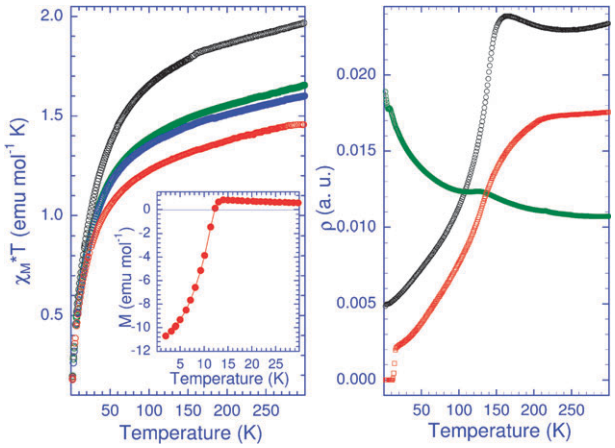

Fig. 4 Left panel: temperature evolution of $\chi_M T$ for $Nd_{1-x}Sr_xFeAsO$: black, green, blue and red circles refer to compositions with $x = 0$, 0.05, 0.1 and 0.2, respectively. Right panel: temperature evolution of the resistivity for $x = 0$ (black), $x = 0.05$ (green) and $x = 0.2$ (red).

changes in the electronic properties upon increasing doping. Low-field (20 Oe) magnetic measurements showed that a superconducting transition is present only for the highest doping level composition, $x = 0.2$ with a T_c of 13.5 K and a superconducting fraction of 17% (Fig. 4 inset).

Such a trend was confirmed by resistivity measurements on samples with $x = 0$, 0.05 and 0.2 (Fig. 4). The parent compound shows the typical behaviour reported for REFeAsO.[1] The resistivity curve of the 5%-doped material shows a drastic change with ρ increasing on cooling. It thus appears that upon low levels of hole doping, the electron charge carriers in NdFeAsO are initially depleted. This is consistent with the electron cylinders of the Fermi surface[4] decreasing in volume—this is not immediately compensated by an enlargement of the hole pockets[4] pushing the system through a transition from a bad metal to semiconductor. Further hole doping increases the amount of hole-type charge carriers, inflates the volume of the hole pockets and metallic conductivity is restored.§ Indeed, the 20%-doped system shows metallic behaviour with ρ decreasing with temperature and a superconducting transition at $T_c = 13.5$ K in agreement with the magnetisation data. The derivatives of the temperature-dependent resistivity, $d\rho/dT$, show maxima at 140, 115 and 130 K for $x = 0$, 0.05 and 0.2. These correspond exactly to the temperatures at which the T → O structural transition occurs.

There are many important points arising from the present results. Partial replacement of Nd^{3+} by Sr^{2+} to afford $Nd_{1-x}Sr_xFeAsO$ leads to superconducting phases at $x > 0.1$. However, the electronic and structural behaviour upon hole doping is different and non-symmetric to the corresponding electron-doped systems where a smooth evolution of the structural and electronic properties is observed. In the hole-doped systems, the T → O phase transition is not suppressed up to $x \sim 0.2$ and in addition, T_s varies little in sharp contrast to the structural behaviour of the electron-doped analogues.[9] The evolution of the structural parameters of the $FeAs_4$ tetrahedra shows drastic changes at doping levels $x > 0.1$ with a large increase in the Fe–As distances which is accompanied by a decrease in the thickness of the Fe–As layers. Magnetisation and resistivity measurements also show considerable differences in the electronic behaviour with increasing x. All our experimental observations describe a scenario where at small x, the number of carriers decreases, leading to an accompanying decrease in $N(E_F)$ and initially pushing the system into the semiconducting regime. Higher Sr^{2+} content is necessary for the metallic regime to re-emerge. At $x > 0.1$, the weaker Fe–As hybridisation causes a decrease in the conduction bandwidth which is accompanied by an increase in $N(E_F)$ and the occurrence of superconducting phases. It appears that for NdFeAsO higher levels of hole doping are necessary to observe a similar phenomenology to the electron-doped systems as an increased number of carriers is necessary to first overcome the initial semiconducting behaviour. This is in contrast to $NdFeAsO_{1-x}F_x$, in which there is a continuous change of the electronic properties upon F doping and superconductivity is obtained for $x > 0.08$ with much higher T_c (*cf.* $NdFeAsO_{0.88}F_{0.12}$, $T_c = 50$ K).[13] It is likely that if it were chemically possible to obtain levels of Sr^{2+} doping higher than 20%, a further increase in T_c could be achieved. We note that in hole-doped $K_{1-x}Sr_xFe_2As_2$, superconductivity is also reported at doping levels of 20% ($x = 0.80$) with a T_c of ~15 K.[5] Higher transition temperatures ($T_c \sim 37$ K) are obtained by increasing the doping level to 40–50%.

Notes and references

‡ Structural analysis of NdFeAsO is in agreement with earlier work.[12]
§ Hall coefficient measurements are necessary to determine the type of charge carriers. It has been shown that Sr^{2+} doping leads to hole-type conduction in $La_{1-x}Sr_xFeAs$[7] and $Sr_{1-x}K_xFe_2As_2O$.[5]

1 Y. Kamihara, T. Watanabe, M. Hirano and H. Hosono, *J. Am. Chem. Soc.*, 2008, **130**, 3296; R. H. Liu, G. Wu, T. Wu, D. F. Fang, H. Chen, S. Y. Li, K. Liu, Y. L. Xie, X. F. Wang, R. L. Yang, L. Ding, C. He, D. L. Feng and X. H. Chen, *Phys. Rev. Lett.*, 2008, **101**, 087001; Y. Takabayashi, M. T. McDonald, D. Papanikolaou, S. Margadonna, G. Wu, R. H. Liu, X. H. Chen and K. Prassides, *J. Am. Chem. Soc.*, 2008, **130**, 9242.
2 K. Haule, J. H. Shim and G. Kotliar, *Phys. Rev. Lett.*, 2008, **100**, 226402.
3 Z. P. Yin, S. Legebue, M. J. Han, B. Nea, S. Y. Savrasov and W. E. Pickett, *Phys. Rev. Lett.*, 2008, **101**, 047001.
4 D. J. Singh and M. H. Du, *Phys. Rev. Lett.*, 2008, **100**, 237003.
5 M. Rotter, M. Pangerl, M. Tegel and D. Johrendt, *Angew. Chem.*, 2008, **47**, 7949; K. Sasmal, B. Lv, B. Lorenz, A. Guloy, F. Chen, Y. Xue and C. W. Chu, *Phys. Rev. Lett.*, 2008, **101**, 107007.
6 M. J. Pitcher, D. R. Parker, P. Adamson, S. J. C. Herkelrath, A. T. Boothroyd and S. J. Clarke, *Chem. Commun.*, 2008, DOI: 10.1039/b813153h; S. Margadonna, Y. Takabayashi, M. T. McDonald, K. Kasperkiewicz, Y. Mizuguchi, Y. Takano, A. N. Fitch, E. Suard and K. Prassides, *Chem. Commun.*, 2008, 5607.
7 H. Wen, G. Mu, L. Fang, H. Yang and X. Zhu, *Europhys. Lett.*, 2008, **82**, 117009; G. Mu, L. Fang, H. Yang, X. Zhu, P. Cheng and H. Wen, *J. Phys. Soc. Jpn.*, 2008, **77**, 15.
8 G. Wu, H. Chen, Y. L. Xie, Y. J. Yan, T. Wu, R. H. Liu, X. F. Wang, D. F. Fang, J. J. Ying and X. H. Chen, *Phys. Rev. B: Condens. Matter*, 2008, **78**, 092503.
9 S. Margadonna, Y. Takabayashi, M. T. McDonald, M. Brunelli, G. Wu, R. H. Liu, X. H. Chen and K. Prassides, *Phys. Rev. B*, 2009, in press, arXiv:0806.3962.
10 T. Nomura, S. W. Kim, Y. Kamihara, M. Hirano, P. V. Susko, K. Kato, M. Takata, A. L. Shluger and H. Hosono, *Supercond. Sci. Technol.*, 2008, **21**, 125028.
11 V. Vildosola, L. Pourovskii, R. Arita, S. Biermann and A. Georges, *Phys. Rev. B*, 2008, **78**, 064518.
12 M. Fratini, R. Caivano, A. Puri, A. Ricci, Z.-A. Ren, X.-L. Dong, J. Yang, W. Lu, Z.-X. Zhao, L. Barba, G. Arrighetti, M. Polentarutti and A. Bianconi, *Supercond. Sci. Technol.*, 2008, **21**, 092002.
13 G. F. Chen, Z. Li, D. Wu, J. Dong, G. Li, W. Z. Hu, P. Zheng, J. L. Luo and N. L. Wang, *Chin. Phys. Lett.*, 2008, **25**, 2235.